

Centro Brasileiro de Pesquisas Físicas

**NMR relaxation on porous media:  
a superstatistical approach with  
application to petrophysics**

Maury Duarte Correia

January 2015

Supervised by Ivan S. Oliveira

Submitted as a partial fulfilment of the requirements  
for obtaining the degree of Doctor of Philosophy  
from the Centro Brasileiro de Pesquisas Físicas

Bottomless wonders spring from  
simple rules, which are repeated  
without end.

---

Benoit Mandelbrot

## Acknowledgement

I would like to thank my supervisor Ivan for creating a pleasant environment in CBPF where we could apply basic physics ideas on problems of industrial interest. He gave to me great examples of how to behave in a scientific career and I am grateful for he share some guitar riffs in the rock/blues band “Queda Livre”. I also thank the group of nonextensive statistical mechanics of CBPF that took part of my training in the early years of my Ph.D., especially Professor Constantino Tsallis and my friends Leonardo Cirto, Max and Mauricio. My friend Pablo Diniz, from Goiás like me and that fortuitously we met in CBPF, was very important in philosophical and conceptual discussions. Doctor Rafael that helped me to get psychic stability but for professional ethics we can not be friends. The Milrian for being by my side at the beginning of this journey. The Mariza for giving me so many joys Rio. The Tamires to helped me many times getting to my side. I am extremely grateful to Petrobras in particular to CENPES and my managers, Mauro Becker, Daniel and Rosalba, who had the sensitivity to allow me to advance in new ideas for the company. All my friends from CMR, specially Luiz Fernando, Eldues, Xingu and George who always defended me and supported me to continue the doctorate. My Petrobras friends, Surmas, Bernardo and Willian was very important to help me to conclude this work. The Petrobras petrophysics class of 2014. My bands were very important in this period, Fox Brothers, Hortifrutigranjeiros, Till the bone and Queda Livre. To my friends Waguinho, Branquinho, Letícia and Leo, the Goiás fellows in the Rio. My former housemates Doug Funny, Clarissa and Fernando. My brothers that I love so much Vitor and Hiury, my niece Maitê and his mother Rebecca. My Mother by praying for me, poor lady. My friend João Lucas Crepaldi, which unveiled with me the corners of the universe. The Black Sabbath for coming in apotheosis in 2013 and sang to me the music Black Sabbath. My friend Alexandre Cotait who had the courage to let

me guide you in his monograph. The CBPF/CAT image group that share with me the adventure of understand the world of rock images, Marcio, Marcelo, Clécio, Elisângela and Heitor. My comrades of the titanic apartment, Gabo, Ceci, Adrianete, Bruno, Oswaldo, Rafael and François. The crowd of javalismo that keeping this flame alive, Joaquim, Marquinho, Gersinho, Rafael, Jorlandio, Gigi, Fracassado, He-man and Muso. A special thanks to Roberta that showed me a new way in my life and that I love so much.

# Abstract

The superstatistics has been applied to interpret Nuclear Magnetic Resonance (NMR) data on transverse relaxation on porous media with application in petrophysics. Porous media are very important kind of structures, and many areas in Science and Technology have studied these materials [1], including mathematics, physics, chemistry, engineering, biology, medicine, and industrial areas such as Oil & Gas. The NMR technique has raised many interesting questions about porous media through the study of the transverse relaxation of fluids in these materials [2]. This thesis aims to contribute to the discussion about the ill-posed problem of the inversion of transverse relaxation  $T_2$  decay measured with the standard CPMG sequence, by the application of mathematical tools and ideas from superstatistics and nonextensive statistics. The  $T_2$  time decay of one single pore is a statistical sum of the time evolution of spins states inside it. One pore yields a well defined  $T_2$  time that is a solution of diffusion equation with boundary conditions. If the porous media is a statistical sum of pores, the total  $T_2$  time will be given by a distribution of values rather than a single value. We show that the NMR transverse decay can be modelled by  $q$ -exponential functions, represented by the distribution  $f_i(T_2) \propto T_2^{-2} \chi^2(T_2^{-1})$ . To test the validity of these parametric statistical model, we perform high-field NMR  $T_2$  relaxation measurements on porous media built from glass microsphere with different ranges of two different companies, the Multiesferas and Cospheric, and three samples of outcrop rocks.

The Multiesferas set is of soda lime glass and the spheres radii are in the following ranges: A (425-600 $\mu m$ ); B (250-425 $\mu m$ ); C (106-212 $\mu m$ ); D (75-125 $\mu m$ ); and E (45-90 $\mu m$ ). The Cospheric's microspheres are in the following ranges: A (710-850 $\mu m$ ); B (425-500 $\mu m$ ); C (212-250 $\mu m$ ); D (106-125 $\mu m$ ); and E (45-53 $\mu m$ ). The outcrops rocks used were the Berea and the Buff Berea sandstone, and the Indiana Limestone. This new model for NMR petrophysics includes statistical assumptions for the constitution of rocks and porous media and can be very useful to estimate petrophysical parameters like, water saturation ( $S_w$ ), clay bound water ( $CBW$ ), bound volume index ( $BVI$ ), free fluid ( $FF$ ),  $T_{2cutoff}$  and even a pore size distribution. We show the mathematical formulation to find these petrophysical parameters without inversion and use experimental data to evaluate the applicability of the model.

# Contents

<b>1. Introduction</b>	<b>23</b>
1.1. Petrophysics . . . . .	25
1.2. Petrophysical models and concepts . . . . .	26
1.3. Wireline logging Petrophysics . . . . .	36
<b>2. Superstatistics</b>	<b>41</b>
2.1. Nonextensive Statistical Mechanics . . . . .	46
<b>3. Nuclear Magnetic Resonance</b>	<b>52</b>
3.1. Fundamentals of NMR . . . . .	52
3.1.1. Spin in a static magnetic field . . . . .	52
3.1.2. Applying radio frequency . . . . .	54
3.1.3. Relaxation: Bloch-Torrey equations . . . . .	57
3.1.4. Spin echo and CPMG pulse sequence . . . . .	60
3.2. NMR on Porous Media . . . . .	62
3.2.1. Single spherical pore . . . . .	65
3.2.2. Two spherical pores . . . . .	70
3.2.3. Spherical pore in slow and fast regimes . . . . .	74
3.2.4. Cubic pore . . . . .	75
3.2.5. Bimodal distribution of spherical pores . . . . .	76
3.3. NMR Petrophysics . . . . .	77
3.3.1. The inversion of $T_2$ decay . . . . .	82

<b>4. Results</b>	<b>84</b>
4.1. $q$ -Exponential model for magnetization decay . . . . .	84
4.2. NMR High-field experiments . . . . .	89
4.2.1. Microesferas A: 425-600 $\mu m$ range diameter . . . . .	93
4.2.2. Microesferas B: 250-425 $\mu m$ range diameter . . . . .	101
4.2.3. Cospheric A: 710-850 $\mu m$ range diameter . . . . .	106
4.2.4. Cospheric B: 425-500 $\mu m$ range diameter . . . . .	110
4.2.5. Berea Sandstone . . . . .	114
4.2.6. Buff Berea Sandstone . . . . .	118
4.2.7. Indiana Limestone . . . . .	122
<b>5. Conclusions and Discussions</b>	<b>126</b>
5.1. Prediction of pore sizes . . . . .	126
5.2. Concluding remarks . . . . .	131
<b>A. Microesferas samples C, D and E</b>	<b>137</b>
A.1. Microesferas C: 106-212 $\mu m$ range diameter . . . . .	137
A.2. Microesferas D: 75-125 $\mu m$ range diameter . . . . .	142
A.3. Microesferas E: 45-90 $\mu m$ range diameter . . . . .	146
<b>B. Cospheric samples C, D and E</b>	<b>150</b>
B.1. Cospheric C: 212-250 $\mu m$ range diameter . . . . .	150
B.2. Cospheric D: 106-125 $\mu m$ range diameter . . . . .	154
B.3. Cospheric E: 45-53 $\mu m$ range diameter . . . . .	158

# List of Tables

4.1. Statistical parameters of three q-exponentials model for Microesferas sample A. . . . .	97
4.2. Statistical parameters of three q-exponentials model for Microesferas sample B. . . . .	101
4.3. Statistical parameters of two q-exponentials model for Cospheric sample A. . . . .	106
4.4. Statistical parameters of three q-exponentials model for Cospherisample C B. . . . .	110
4.5. Statistical parameters of three q-exponentials model for Berea Sandstone. . . . .	114
4.6. Statistical parameters of three q-exponentials model for Buff Berea Sandstone. . . . .	118
4.7. Statistical parameters of three q-exponentials model for Indiana Limestone. . . . .	122
A.1. Statistical parameters of three q-exponentials model for Microesferas sample C. . . . .	137
A.2. Statistical parameters of three q-exponentials model for Microesferas sample D. . . . .	142
A.3. Statistical parameters of three q-exponentials model for Microesferas sample E. . . . .	146

B.1. Statistical parameters of three q-exponentials model for Co-spheric sample C. . . . .	150
B.2. Statistical parameters of three q-exponentials model for Co-spheric sample D. . . . .	154
B.3. Statistical parameters of three q-exponentials model for Co-spheric sample E. . . . .	158

# List of Figures

1.1. The dynamics of spins in one pore drive its NMR relaxation $T_2$ time. The porous media is composed by a sum of different pore sizes and geometries with different $T_2$ time each. To describe $T_2$ time of porous media it is necessary to consider two statistical behaviors in two different length scales, one in a pore scale and other in a sample scale. . . . .	25
1.2. First resistivity log measurement made by Schlumberger brothers: Pechelbronn field, Alsace-Lorraine, France, 1927 [3]. The vertical axis is the well depth in meters and horizontal axis is resistivity given in $\Omega.m$ . . . . .	27
1.3. The picture shows a logging well operation near Bakersfield, California, in 1933 [3]. . . . .	28
1.4. The figure above is the Flow Zone Indicator (FZI) classification proposed by Amaefule <i>et al.</i> [4] applied to plugs of one pre-salt well. The second image is the optical microscopic images of one representative sample of each petrofacies set. The blue color represent the pores and decreases from $A$ to $D$ . Possibly the FZI is a good definer of unit flows for this well [5]. . . . .	31

1.5.	Prediction of BVI and FFI from NMR $T_2$ distribution $f(T_2)$ . The area under $T_2$ curve is calibrated to predict the total porous volume ( $V_\phi = BVI + FFI$ ) and with a cut off in this curve ( $T_{2cutoff}$ ) is possible to infer these quantities. . . . .	32
1.6.	Image of cryo-scanning electron microscopy (backscattered electrons) of a fragment of bioclastic limestone showing complex structural formation. Water (light gray) is in the middle of pore and oil (dark gray) is adsorbed on calcitic matrix (white). This rock is strongly wettable to oil and is a quite rare case in oil reservoirs [6]. . . . .	33
1.7.	Homogeneous distribution for cementation $m$ needs parameter in Archie law. All values of $m$ needs to be considered to generalize Archie law in a supestatistical approach. . . . .	35
1.8.	Comparison between Archie equation with fixed values for $m$ , Eq.(1.7) and superstatistical generalized Archie equation with homogeneous distribution of $m$ , Eq(1.9). The formation factor is $F = \frac{R}{R_w}$ and $aS_w^{-n} = 1$ . . . . .	36
1.9.	Schematic of wireline log: a cable with the tool is lowered into the well and makes measurements of rock formation [7]. . . . .	38
1.10.	Examples of wireline log data. The first image shows gamma ray, photoelectric, caliper, sonic, density, neutron, and resistivity logs [8]. The second figure shows the modern high resolution wireline imaging tools. (a) The FMI resistivity imager (Schlumberger). (b) The STAR resistivity imager (Baker Atlas). (c) The CBIL acoustic imager Baker Atlas. . . . .	40
2.1.	Representation of system in which the $\beta$ parameter fluctuates locally. To describe correctly the particle dynamics or the global behavior of the system, all possible values of $\beta$ must be considered.	42

2.2. One hundred values for a Gaussian random variable and their respective histogram and probability density function (PDF) in vertical axis. . . . .	43
2.3. One hundred values for a sum of ten square Gaussian random variable and their respective histogram and probability density function (PDF) in vertical axis. . . . .	43
2.4. Comparison between $\chi^2$ , inverse $\chi^2$ and log-normal distributions fitting data of turbulent flow. Details can be seen in [9]. .	46
2.5. The function $W(N)$ is the probability of occurrence of a microstate configuration. Systems with $W(N) \propto \mu^N$ , are described by $S_{BG}$ , and systems with microstates dependence like $W(N) \propto N^\rho$ are described by $S_q$ entropy [10]. . . . .	49
2.6. Example of system where the entropy is extensive ( $S_q \propto N$ ) for $q \neq 1$ . Details of the model can be found in [11]. In this case the $q$ parameter is suggested to be $q = 1 - \frac{1}{d}$ , where $d$ is an important parameter to generate the $\pi_{N,n}$ values. The figures <b>a)</b> and <b>b)</b> , shows the results of $S_q$ versus $N$ for $d = 1$ and $d = 2$ , respectively. . . . .	50
2.7. The figure on top shows $S_q$ versus the size of system $L$ of one-dimensional spin-1/2 ferromagnetic chain with an exchange coupling and subjected to an external transverse magnetic field [12]. The figure on bottom shows a model based on fractal geometry of porous media, details can be see in [13]. . . . .	51
3.1. Bloch sphere representation of a quantum state $ \psi\rangle$ . Observe that for a time dependent azimuthal angle such as $\phi(t) = \gamma B_0 t$ , the state precess around z-axis. . . . .	54

3.2. Representation of spin state on the Bloch sphere in a resonance experiment. The states precess around z-axis due static magnetic field and rotates around x-axis due radiofrequency field. . . . .	56
3.3. The absorption and dispersion modes. . . . .	60
3.4. Representation of a component of free induction decay (FID). . . . .	61
3.5. Representation of spin echo that is a phase recovery due application of a $\frac{\pi}{2}$ - $\pi$ pulse sequence. . . . .	61
3.6. Representation of spins in a Bloch sphere of phase recovery in a $\frac{\pi}{2}$ - $\pi$ pulse sequence: (A) initial state; (B) $\frac{\pi}{2}$ -pulse; (C) and (D) lost of phase; (E) $\pi$ -pulse; (F) and (G) phase recovery. . . . .	62
3.7. Representation of CPMG pulse sequence. The $T_2$ time is the mean lifetime of the transverse relaxation decay. . . . .	62
3.8. Usual geometries to analytically solve diffusion equation with boundary conditions, and obtain a solution for transverse NMR relaxation [14]. . . . .	65
3.9. Spherical geometry representation. This geometry has analytical solution for $T_2$ relaxation. Considering a special sum of spherical pores is possible to predict a q-exponential decay for $T_2$ . . . . .	66
3.10. The left figure shows the graphical solution for $\zeta_n$ eigenvalues transcendental equation in spherical pores Eq.(3.33) for $D = 10^{-9}m/s$ , $K = 10^{-6}m^2/s$ and $l < 1mm$ . The right figure shows variations in curves intersection by change pore size $l$ . The first eigenvalue will be always $0 \leq \zeta_0 \leq \pi$ . . . . .	68

3.11. The left figure shows the $T_{2n}$ spectrum and the intensities modes $I_n$ for a single spherical pore for $D = 10^{-9}m/s$ , $K = 10^{-6}m^2/s$ , $l = 0.5mm$ and $\Gamma = 0$ . The right figure shows the first four magnetization modes given by Eq.(3.37); the first one is the most important. . . . .	69
3.12. Plots of the intensities $I_n$ , Eq. (3.35) as function of $\zeta_n$ . If the pore radius is $l \leq 0.5mm$ the first mode is $I_0 \geq 98.6\%$ . . . . .	71
3.13. Representation of two spherical pores with different radii with analytical solution for transverse relaxation. The total magnetization of this system will be a sum of the contribution from the two spheres. . . . .	72
3.14. Representation of cubic geometry. This kind of boundary for a pore surface has analytical solution for transverse NMR magnetization. . . . .	75
3.15. Representation of a system with one big pore and many small pores. Depending of the number of small pores, the relaxation can be dominated by them. . . . .	77
3.16. The three figures on the left show the behavior of the magnetization, $T_2$ and pore radius distributions for $n = 1$ . The three figures on the right show the behavior of the magnetization, $T_2$ and pore radius distribution for $n = 1000$ . It is necessary three orders of magnitude in the number of small pores, relative to the big pore, for fast relaxation to be evident in magnetization signal and consequently in $T_2$ distribution. . . . .	78

3.17. The figure on the top is from Kenyon [15] and shows the longitudinal NMR data to extract $T_1$ time. When water is in the Berea sandstone the $T_1$ value is 214ms and their bulk value is 3.9s. The second figure [16] shows relaxation time as a function of the ratio viscosity/temperature. When water is present in sandstone the relaxation time is smaller. . . . .	80
3.18. Schematic representation of diffusive spin inside a pore. The relaxation is due three mechanisms, surface, bulk and diffusion (see text). . . . .	81
4.1. Geometrical model of Brownstein and Tarr 1979 [14] applied to explain data of rat gastronemius muscle NMR decay. An annular cylinder geometry is assumed and the ratio of radius $R = b/a$ is tuned to give the best fit. . . . .	85
4.2. Geometrical model of Tangyan <i>et. al.</i> 2012 [17] to describe porous rock saturated by oil and water. . . . .	86
4.3. Analytical function for $T_2$ distribution used in NMR experiments on porous media. In the limit of $q \rightarrow 1$ , $f_{q,\beta_0}(T_2)$ tends to a distribution highly concentrated around in $\langle T_2 \rangle$ , and recovers one single exponential for the magnetization. The inset a log-log plot showing the tail behavior of distributions. . . . .	88
4.4. The area under each curve in the graphics is equal to one, and the $q$ parameter is chosen $q = 1.5$ for this example. Because the logarithm scale, the peak of the distribution becomes smaller as $\langle T_2 \rangle$ increases. . . . .	90
4.5. Example of typical NMR log well data with a large amount of noise. . . . .	91

4.6.	The colored bars represent the diameter size range of ten samples of soda lime glass microsphere from two different companies. The Cospheric's microspheres have the follow ranges: A (710-850 $\mu m$ ); B (425-500 $\mu m$ ); C (212-250 $\mu m$ ); D (106-125 $\mu m$ ); and E (45-53 $\mu m$ ); and the Microesferas sample have the follow ranges: A (425-600 $\mu m$ ); B (250-425 $\mu m$ ); C (106-212 $\mu m$ ); D (75-125 $\mu m$ ); and E (45-90 $\mu m$ ). . . . .	92
4.7.	Outcrop rocks used in high-field NMR experiments. From left to right is the Buff Berea Sandstone, Berea Sandstone and Indiana Limestone. . . . .	92
4.8.	The figure on top shows the soda-lime glass microspheres set of samples with five different diameter ranges inside 10mm tubes, imbibed on water for perform NMR experiments. The figure on the bottom shows one raw image of the x-ray microtomography of the glass microsphere sample of range 106-212 $\mu m$ diameter of Microesfera. . . . .	94
4.9.	The figure on top shows the rendered 3D volume of microtomography images of soda-lime glass microspheres from Cospheric with range of 710-850 $\mu m$ . The figure on the bottom shows one horizontal 2D slice of the first image. . . . .	95
4.10.	Analyses of the regularization parameter effect, $\alpha$ , on the $T_2$ distribution for Microesferas sample A. . . . .	96
4.11.	The figure on top shows the spectrum decay in CPMG pulse sequence. The figure on bottom shows the comparison between the q-exponential and multiexponential models decay to prediction of $T_2$ distribution in Microesferas sample A. . . . .	98
4.12.	Comparison of $T_2$ distribution given by q-exponential model and multiexponential model in Microesferas sample A. . . . .	99

4.13. The figure on top shows the spectrum decay in CPMG pulse sequence. The figure on bottom shows the comparison between the q-exponential and multiexponential models for the of $T_2$ distribution in Microesferas sample B. . . . .	102
4.14. Analyses of the regularization parameter effect, $\alpha$ , on the $T_2$ distribution for Microesferas sample B. . . . .	103
4.15. Comparison of $T_2$ distribution given by q-exponential model and multiexponential model decay. . . . .	104
4.16. The figure on top shows the spectrum decay in CPMG pulse sequence. The figure on bottom shows the comparison between the q-exponential and multiexponential models for the of $T_2$ distribution in Cospheric sample A. . . . .	107
4.17. Analyses of the regularization parameter effect, $\alpha$ , on the $T_2$ distribution for Cospherisample C A. . . . .	108
4.18. Comparison of the $T_2$ distributions given by q-exponential and multiexponential models. . . . .	109
4.19. The figure on top shows the spectrum decay in CPMG pulse sequence. The figure on bottom shows the comparison between the q-exponential and multiexponential models for the of $T_2$ distribution in Cospheric sample B. . . . .	111
4.20. Analyses of the regularization parameter effect, $\alpha$ , on the $T_2$ distribution for Cospherisample C B. . . . .	112
4.21. Comparison of $T_2$ distribution given by q-exponential model and multiexponential model. . . . .	113
4.22. The figure on top shows the spectrum decay in CPMG pulse sequence. The figure on bottom shows the comparison between the q-exponential and multiexponential models for the of $T_2$ distribution in Berea Sandstone. . . . .	115

4.23. Analyses of the regularization parameter effect, $\alpha$ , on the $T_2$ distribution for Berea Sandstone. . . . .	116
4.24. Comparison of the $T_2$ distributions given by q-exponential and multiexponential models. . . . .	117
4.25. The figure on top shows the spectrum decay in CPMG pulse sequence. The figure on bottom shows the comparison between the q-exponential and multiexponential models for the of $T_2$ distribution in Buff Berea Sandstone. . . . .	119
4.26. Analyses of the regularization parameter effect, $\alpha$ , on the $T_2$ distribution for Buff Berea Sandstone. . . . .	120
4.27. Comparison of the $T_2$ distributions given by q-exponential and multiexponential models. . . . .	121
4.28. The figure on top shows the spectrum decay in CPMG pulse sequence. The figure on bottom shows the comparison between the q-exponential and multiexponential models for the of $T_2$ distribution for Indiana Limestone. . . . .	123
4.29. Analyses of the regularization parameter effect, $\alpha$ , on the $T_2$ distribution for Indiana Limestone. . . . .	124
4.30. Comparison of $T_2$ distribution q-exponential model and multiexponential model decay. . . . .	125
5.1. The figure on top show the model fit of six exponentials and three q-exponentials. The bottom figure show the ratio <i>model/data</i> to analyse the quality of fit. All models fit well with less than 0.4% of error. . . . .	129

5.2. Discrete distribution of six exponentials model in function of eigenvalue $\zeta_0$ . The blue lines are the distribution of pore diameters for $\zeta_0 = 0.1\pi$ , the black lines for $\zeta_0 = 0.1\pi$ and red is for $\zeta_0 = 0.9\pi$ . The pore size diameter is linear with the eigenvalue $\zeta_0$ . . . . .	130
5.3. Low-field NMR transverse data decay for Indiana Limestone sample. We have fitted four curves, three multiexponentials with different values for Tikhonov regularization, and a two $q$ -exponentials curves. . . . .	134
5.4. Normalised four distributions of $T_2$ NMR low-field data decay of Indiana Limestone. The squares obtained from the multiexponential model with low value of regularization, and exhibits a nonphysical oscillating behavior. . . . .	135
A.1. The figure on top shows the spectrum decay in CPMG pulse sequence. The figure on bottom shows the comparison between the $q$ -exponential and multiexponential models for the $T_2$ distribution in Microesferas sample C. . . . .	138
A.2. Analyses of the regularization parameter effect, $\alpha$ , effect on the $T_2$ distribution for Microesferas sample C. . . . .	140
A.3. Comparison of the $T_2$ distributions given by $q$ -exponential and multiexponential models. . . . .	141
A.4. The figure on top shows the spectrum decay in CPMG pulse sequence. The figure on bottom shows the comparison between the $q$ -exponential and multiexponential models for the of $T_2$ distribution in Microesferas sample D. . . . .	143
A.5. Analyses of the regularization parameter effect, $\alpha$ , on the $T_2$ distribution for Microesferas sample D. . . . .	144

A.6. Comparison of the $T_2$ distributions given by q-exponential and multiexponential models. . . . .	145
A.7. The figure on top shows the spectrum decay in CPMG pulse sequence. The figure on bottom shows the comparison between the q-exponential and multiexponential models for the of $T_2$ distribution in Microesferas sample E. . . . .	147
A.8. Analyses of the regularization parameter effect, $\alpha$ , on the $T_2$ distribution for Microesferas sample E. . . . .	148
A.9. Comparison of the $T_2$ distributions given by q-exponential and multiexponential models. . . . .	149
B.1. The figure on top shows the spectrum decay in CPMG pulse sequence. The figure on bottom shows the comparison between the q-exponential and multiexponential models for the of $T_2$ distribution in Cospheric sample C. . . . .	151
B.2. Analyses of the regularization parameter effect, $\alpha$ , on the $T_2$ distribution for Cospheric sample C. . . . .	152
B.3. Comparison of the $T_2$ distributions given by q-exponential and multiexponential models. . . . .	153
B.4. The figure on top shows the spectrum decay in CPMG pulse sequence. The figure on bottom shows the comparison between the q-exponential and multiexponential models for the of $T_2$ distribution in Cospheric sample D. . . . .	155
B.5. Analyses of the regularization parameter effect, $\alpha$ , on the $T_2$ distribution for Cospheric sample D. . . . .	156
B.6. Comparison of the $T_2$ distributions given by q-exponential and multiexponential models. . . . .	157

B.7. The figure on top shows the spectrum decay in CPMG pulse sequence. The figure on bottom shows the comparison between the q-exponential and multiexponential models for the of $T_2$ distribution in Cospheric sample E. . . . .	159
B.8. Analyses of the regularization parameter effect, $\alpha$ , on the $T_2$ distribution for Cospheric sample E. . . . .	160
B.9. Comparison of the $T_2$ distributions given by q-exponential and multiexponential models. . . . .	161

# 1. Introduction

Nuclear Magnetic Resonance (NMR) was discovered in the first half of 20th century and is a technique widely used in both, industry and basic science [18–24]. NMR has been applied to studies and characterization of chemical molecules [25–27], proteins [28–30], implementation of quantum computational algorithms [31–35] and prediction of petrophysical properties, such as pore distribution and fluid contents [36–39]. Other areas have benefited from NMR, such as medicine [40–42], mainly from the techniques of Magnetic Resonance Imaging (MRI) [43].

Superstatistics theory, on the other hand, was proposed and developed at the beginning of the 21th century. The theory was created to describe nonequilibrium systems with complex dynamics in stationary states with large fluctuations of intensive quantities (e.g. the temperature, chemical potential or energy dissipation) over long time scales [44]. Many areas of research have used superstatistics [45–55].

The third subject that we will explore in this thesis is Petrophysics, the study of properties of rocks and their interactions with fluids [56]. Petrophysics also appeared on the first half of 20th century, with well log measurements of resistivity by the Schlumberger brothers [57, 58], and theoretical studies of Archie [56]. Today petrophysics is a very important area in Oil & Gas Industry [59]. The petrophysicist is responsible, among other things, for evaluating the saturation of hydrocarbons and water in rock reservoirs and quantifying

the hydrocarbon reserves, based on well log, laboratory measurements and petrophysical models. It is common that a petrophysical evaluation to decide whether a reserve is economically feasible. There are many companies that offer well log services and plug laboratory measurements for Oil & Gas industry [60].

The central thesis presented here is that superstatistics is a good theory to describe phenomena in rocks, in particular the transverse relaxation in NMR experiments in porous media. With this approach a new model emerges to interpret NMR petrophysical data. The superstatistical petrophysical model is based on the idea that the fundamental properties of rocks can be given by an analytical distribution of values. For example, if we consider that a sample of rock is a porous media with a random distribution of porous sizes we can construct a statistical model for these porous sizes. It is natural to apply superstatistics to the NMR  $T_2$  decay in rocks because in the length scale of one spin state, the relevant dynamics of this spin, inside one single pore, is the reflected Brownian motion, so in the pore scale, the statistical sum of all spins is described by the diffusion equation with boundary conditions. Therefore in the scale of the sample, the total relaxation is composed by a statistical sum of each pore, see Fig 1.1. In the NMR relaxation of fluids in rocks we can identify two relevant statistical behaviours in two different length scales: i) the scale of a single pore size; ii) and the scale of sample size. The main objective of this thesis is to evaluate the applicability of this new conceptual model, based on statistical assumptions, to describe NMR transverse decay experiments in porous media.

The thesis is organized as follows: Chapter 1 review briefly the petrophysics concepts to introduce the subject. The Chapter 2 show the fundamentals of superstatistics theory and q-statistics, with some examples of application. The Chapter 3 shows the basics theory of NMR phenomena, experiments and the

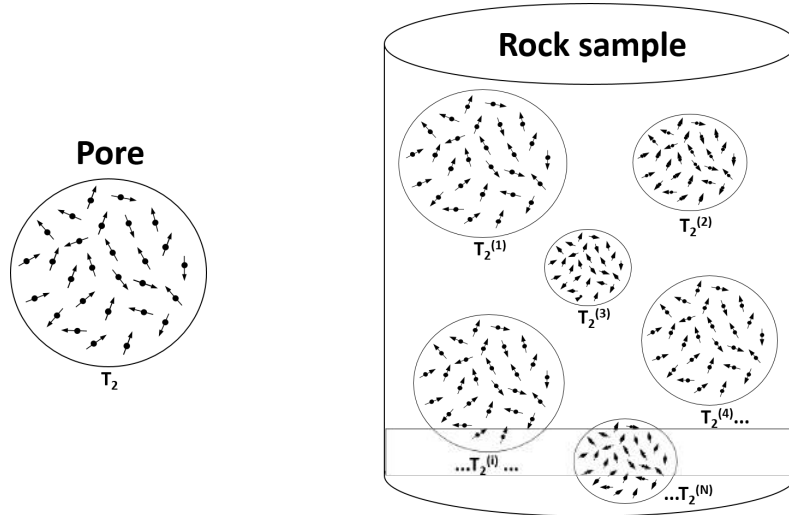


Figure 1.1.: The dynamics of spins in one pore drive its NMR relaxation  $T_2$  time. The porous media is composed by a sum of different pore sizes and geometries with different  $T_2$  time each. To describe  $T_2$  time of porous media it is necessary to consider two statistical behaviors in two different length scales, one in a pore scale and other in a sample scale.

application of NMR on porous media. The Chapter 4 show the main results of the thesis. The superstatistical model to describe the transverse magnetization decay is developed. The high-field NMR data from ten samples of unconsolidated microsphere packing and three different rocks are explained using the proposed model. In the Chapter 5 show the discussions and concluding remarks.

## 1.1. Petrophysics

The term *Petrophysics* was coined by G. E. Archie in 1940's [61] but the first log measure was made, in 1927, by H. Doll, R. Jost and C. Scheibli, employees of a small geophysical exploration company [3] founded in 1926 by two brothers, Conrad and Marcel Schlumberger, to map the geological subsurface with electrical methods. These first steps on wireline techniques showed that it is possible to correlate geological features in subsurface (Fig.1.2). A field team

in the year of 1933 can be seen in Fig.1.3.

A porous media, in general, is a very complex structure constituted by the solid part and the pores, which are empty spaces that can stock and conduct fluids. The porous media is a research subject in many areas, from basic sciences, mathematics, physics and chemistry to petrophysics, biology, and medicine [1]. Petrophysics, in particular, is the study of rock properties and their interactions with fluids (gases, liquid hydrocarbons, and aqueous solutions) [62]. The various kind of rocks, fluids and the correlation between properties has made the petrophysical world a very rich subject to study. Many elements and processes are present in a rock sample, since the basic constituents mineral until secondary post-depositional diagenetic features, like cementation, compression and dissolution. Based on models, experiments and their geological expertise, the petrophysicist tries to draw conclusions about absolute and relative permeability, porosity, resistivity, fluid saturation, nuclear radiation features, bulk modulus and many other properties [63].

In general, a rock reservoir is sedimentary, despite of existing reservoirs of fractured igneous rock. The sedimentary rocks can be divided in two classes, the sandstones, that are composed by quartz and others minerals, and the carbonates that have as major constituent calcium carbonate. The sediments of sandstones come mainly from mechanical weathering, while the carbonates can be constructed by biological structures or chemical deposition. Other important kind of rock is the shale, but in general it is not a reservoir, although nowadays some shale formations can be considered as non-conventional reservoirs, that is, produced by fracking process [64].

## **1.2. Petrophysical models and concepts**

For the Oil & Gas Industry, some important petrophysical properties are the permeability and porosity, because the hydrocarbons production are very de-

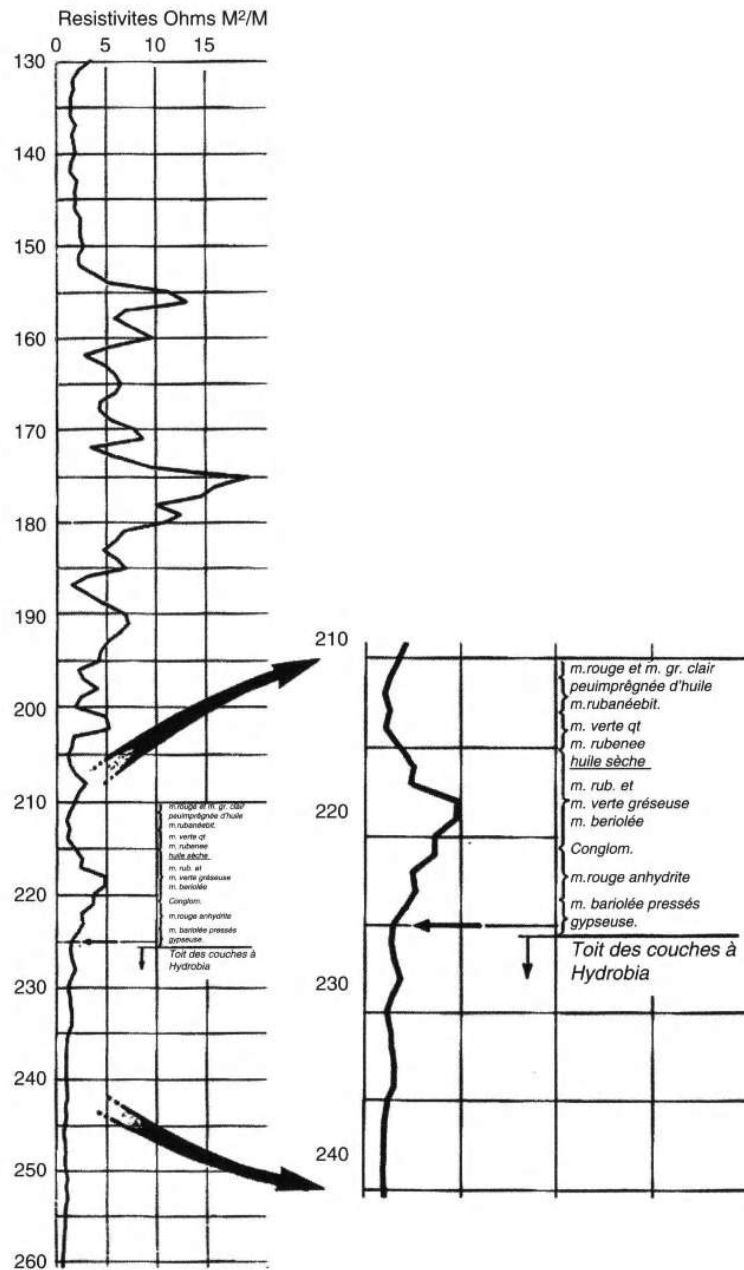


Figure 1.2.: First resistivity log measurement made by Schlumberger brothers: Pechelbronn field, Alsace-Lorraine, France, 1927 [3]. The vertical axis is the well depth in meters and horizontal axis is resistivity given in  $\Omega.m$ .

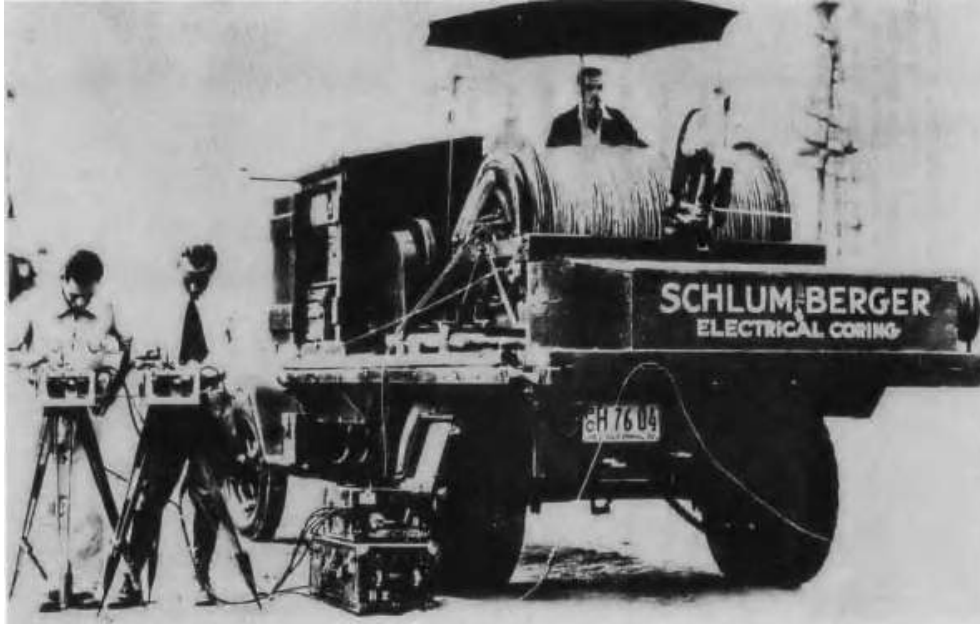


Figure 1.3.: The picture shows a logging well operation near Bakersfield, California, in 1933 [3].

pendent on them. For a rock reservoir to present high values of permeability and porosity a three-dimensional network of interconnected pores is necessary in order to store the fluids and allow hydraulic connection for their movement. The storage capacity, driven by porosity, is a necessary condition for hydrocarbon production but is not sufficient. It is important that the rock has hydraulic connections and it allow fluid mobility, and this is the essence of permeability. The fluid properties and its interaction with rocks are essential to petrophysics too; for example the wettability and saturation affect directly the fluid transport properties [63].

The porosity of a rock is defined as the ratio of the empty volume space on a sample ( $V_p$ ), and the total volume  $V_T$ , that is the the volume of pores plus the volume of grains:

$$\phi = \frac{V_p}{V_T}. \quad (1.1)$$

From Equation (1.1) the maximum theoretical value of porosity is  $\phi = 1$ ,

but for structural reasons, a rock never reaches values too high. For packed spheres in cubic arrangement the porosity is 47.6% and for rhombohedral (close-packed) is 25.9% [65], for random packing of spheres the porosity is around 36% [66, 67]. In general for rock reservoirs the porosity ranges from 5% to 40%. Basically there are two forms to rate porosity: i) the engineering classification (connected or not connected) or ii) the geological classification (primary and secondary porosity). The connected porosity is called effective porosity and is responsible for the fluid transport. The sum of all porosity is called total porosity. The primary porosity occurs when the depositional process happens, and the secondary porosity in a posteriori process such as diagenetic process.

The permeability is the capacity of a piece of rock to conduct fluid. The standard fluid flow equation in petroleum engineering is the Darcy equation [68]:

$$v = -\frac{k}{\mu} \frac{dp}{dl}, \quad (1.2)$$

where  $v$  is the fluid velocity,  $k$  is the permeability,  $\mu$  is the viscosity and  $\frac{dp}{dl}$  is the pressure gradient in the direction of the flow. The permeability given by Eq.(1.2) is the absolute permeability if the rock is fully saturated with one single fluid. In the presence of more than one fluid, the permeability of each fluid is called effective permeability. The ratio of effective permeability of one single fluid phase to the absolute permeability is called relative permeability [63].

The fluid flow studies of porous rocks began with Kozeny works in 1927 [69], who solved the Navier-Stokes equation for fluid flow by considering a porous media as an assembly of pores of the same length, and obtained a relationship between permeability, porosity, and surface porous area:

$$k = \left( \frac{1}{2s_{gr}^2} \right) \frac{\phi^3}{(1 - \phi)^2}, \quad (1.3)$$

where  $s_{gr}$  is the specific surface area of a porous material or the total area exposed within the pore space per unit of grain volume [63].

An important concept in petrophysics is that of flow units. Several authors have defined flow units for description of reservoir zones as storage containers and reservoir conduits for fluid flow. The concept of unit flow has the following characteristics [63]: *i*) it is a specific volume of reservoir and can be composed by one or more lithologies types (ex: sandstone, limestone, shale, dolomite etc.); *ii*) it is mapable and correlative at the interval scale; *iii*) it is recognizable on wire-line log; *iv*) it may be in communication with other flow units.

Amaefule *et al.*, based on Kozeny permeability-porosity relationship, proposed the concept of reservoir quality index (RQI) [4], that is

$$RQI = 0.0314 \sqrt{\frac{k}{\phi}}. \quad (1.4)$$

The flow zone indicator concept (FZI) can be defined as

$$RQI = FZI \times \phi_z, \quad (1.5)$$

where  $\phi_z = \frac{\phi}{1-\phi}$  is the ratio of pore volume to grain volume. The Kozeny Equation (1.3) can be rewritten as

$$\sqrt{\frac{k}{\phi}} = FZI \frac{\phi}{1-\phi}. \quad (1.6)$$

An application of these concepts in Brazilian presalt rocks can be viewed in Fig. 1.4.

Other important concepts, in particular to NMR petrophysics, are the bound volume index (BVI) and free fluid index (FFI). The BVI yields the total irreducible water in a rock, and is defined by the product of porosity and

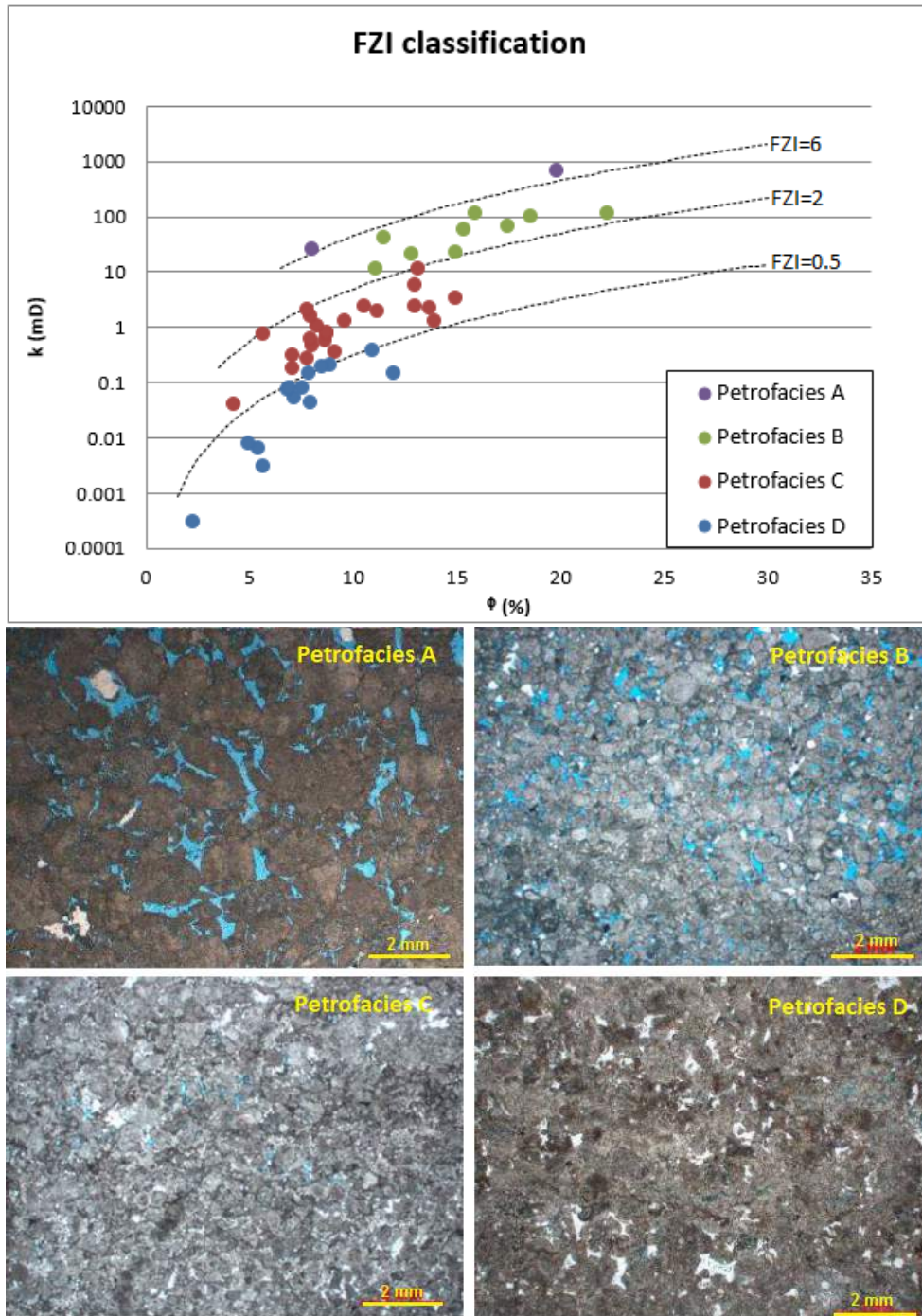


Figure 1.4.: The figure above is the Flow Zone Indicator (FZI) classification proposed by Amaefule *et al.* [4] applied to plugs of one pre-salt well. The second image is the optical microscopic images of one representative sample of each petrofacies set. The blue color represent the pores and decreases from *A* to *D*. Possibly the FZI is a good definer of unit flows for this well [5].

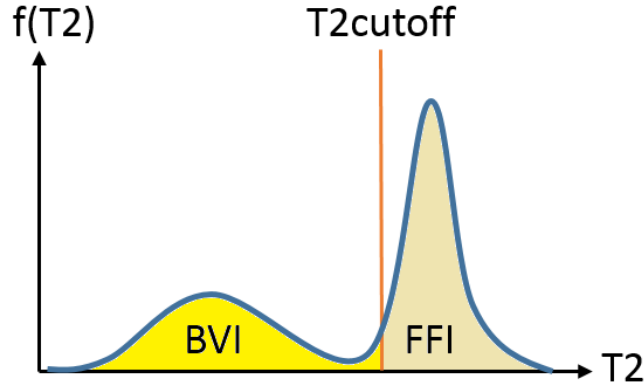


Figure 1.5.: Prediction of BVI and FFI from NMR  $T_2$  distribution  $f(T_2)$ . The area under  $T_2$  curve is calibrated to predict the total porous volume ( $V_\phi = BVI + FFI$ ) and with a cut off in this curve ( $T_{2cutoff}$ ) is possible to infer these quantities.

water irreducible saturation ( $S_{wi}$ ),  $BVI = \phi S_{wi}$ . The  $FFI$  is a measure of movable liquids and is expressed as  $FFI = \phi(1 - S_{wi})$ . Some NMR models of permeability and hydrocarbons storage are based on inference of these quantities from  $T_2$  distribution. In this case it is important the concept of  $T_{2cutoff}$ , as illustrated in Fig. 1.5, see Ref.[70].

Due the complexity involved in porous media, see Fig. 1.6, many petrophysical models are based on exponents like power laws. In general, it is necessary to calibrate these parameters of the model with a set of samples to be analysed. One of the important aspects of laboratory experiments in plug samples, is to give more reliability for these parameters. For one reservoir of one particular field the petrophysical parameters can change if we compared with a reservoir of other field. One example of power law is the Archie law for rock resistivity, see Ref.[61]

$$R = aR_w\phi^{-m}S_w^{-n}, \quad (1.7)$$

where  $a$  is called tortuosity factor,  $R_w$  is the brine water resistivity,  $\phi$  is poros-

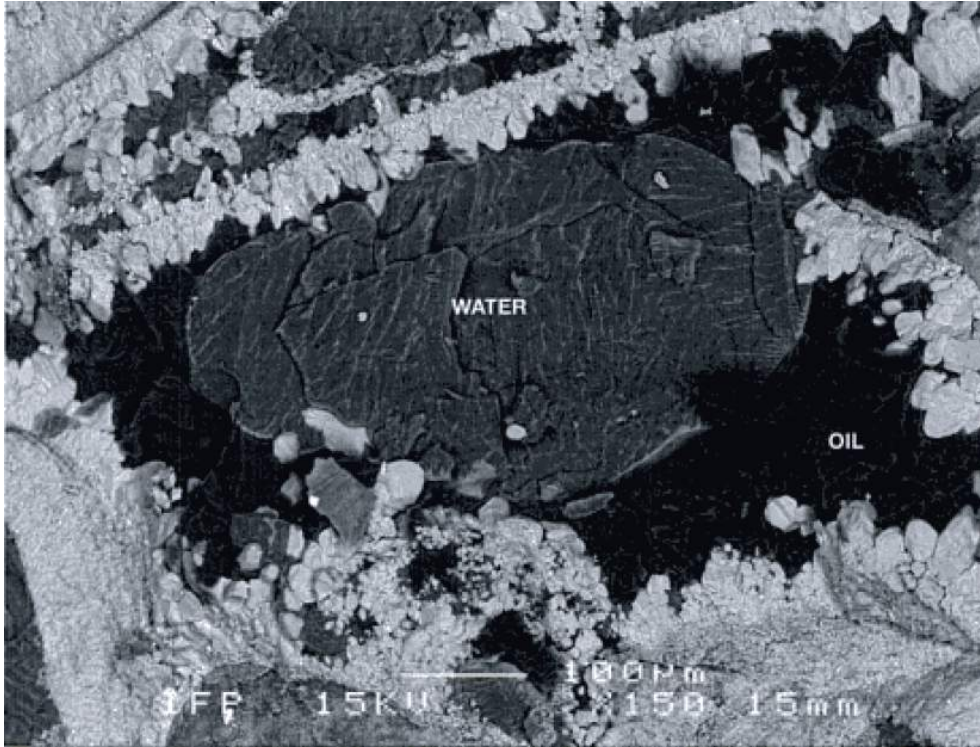


Figure 1.6.: Image of cryo-scanning electron microscopy (backscattered electrons) of a fragment of bioclastic limestone showing complex structural formation. Water (light gray) is in the middle of pore and oil (dark gray) is adsorbed on calcitic matrix (white). This rock is strongly wettable to oil and is a quite rare case in oil reservoirs [6].

ity,  $S_w$  is saturation of brine water in rock and  $m$  is the cementation factor (usually in the range 1.8-2.0 for sandstones in literature [63]) and  $n$  is the saturation exponent (usually close to 2 [63]). For the application of Archie law, it is necessary to perform laboratory measurements to calibrate  $m$  and  $n$ .

A plug from one well is an attempt to sampling the reservoir. By petrophysics experimental methods and modelling, it is possible to obtain knowledge about the reservoir. The procedure to infer properties of reservoir based on petrophysics is called upscaling [71]. Of course the values of the physical properties of sampled plugs may differ depending on the position in the reservoir. Our proposal to circumvent this problem is to use the superstatistical approach that will be better explained in Chapter 2, but we can illustrate the idea using Archie law.

Consider the Archie equation for prediction of resistivity of rock Eq.(1.7). The literature considers that cementation index  $m$  may fluctuate between two values. This means that given two different sample sets, each set can belong to different universality class. Suppose that the two boundary values are  $m_1$  and  $m_2$ . To describe the resistivity of one random sample, we have to use one value of  $m$  between  $m_1$  and  $m_2$ . Suppose now that the  $m$  value that we want is not described by only one single parameter but by an equiprobable distribution  $f(m)$ , such as Fig.(1.7). Since we do not know the real value of  $m$ , we have to consider all possible values, so the rock resistivity will be an integral of Archie equation and a probability density function  $f(m)$ :

$$R = aR_w S_w^{-n} \int_{m_1}^{m_2} dm f(m) \phi^{-m}. \quad (1.8)$$

Eq.(1.8) reminds a superstatistics generalization of Boltzmann factor [72], where all values of fluctuating parameter are considered. The result for Archie

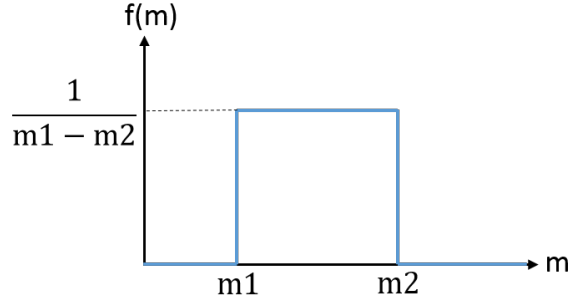


Figure 1.7.: Homogeneous distribution for cementation  $m$  needs parameter in Archie law. All values of  $m$  needs to be considered to generalize Archie law in a supestatistical approach.

law considering all possible values of  $m$  given by distribution  $f(m)$  is

$$R = aR_w S_w^{-n} \frac{\phi^{-m_2} - \phi^{m_1}}{\sqrt{12}\sigma_m \log \phi}, \quad (1.9)$$

where  $\sigma_m$  is the variance of  $f(m)$  distribution. The ratio of rock resistivity saturated with fluid and fluid resistivity is called formation factor ( $F = \frac{R}{R_w}$ ) and is plotted in Fig. 1.8, where  $aS_w^{-n} = 1$ .

Equation (1.9) is an example of generalization Archie law considering a distribution of values of  $m$  parameter. Other kind of generalization can be found in [73]. It is possible to calculate a standard deviation to resistivity  $R$  due  $f(m)$  distribution:

$$\sigma_R = \left| \frac{\partial R}{\partial \bar{m}} \right| \sigma_m, \quad (1.10)$$

where  $\bar{m}$  is the mean of  $m$ . If we suppose another  $f(m)$  parameter distribution the result will be different. The validity of statistical assumptions to predict  $f(m)$  will give a better petrophysical model, and this validity can be tested empirically by experiments. This example is just for introducing the main argument of this thesis: in NMR relaxation of porous media, the fluctuating quantity is  $T_2$ , and a similar argument is therefore applicable. We hypothesized and successfully tested a specific statistical distribution  $f(T_2)$  with different

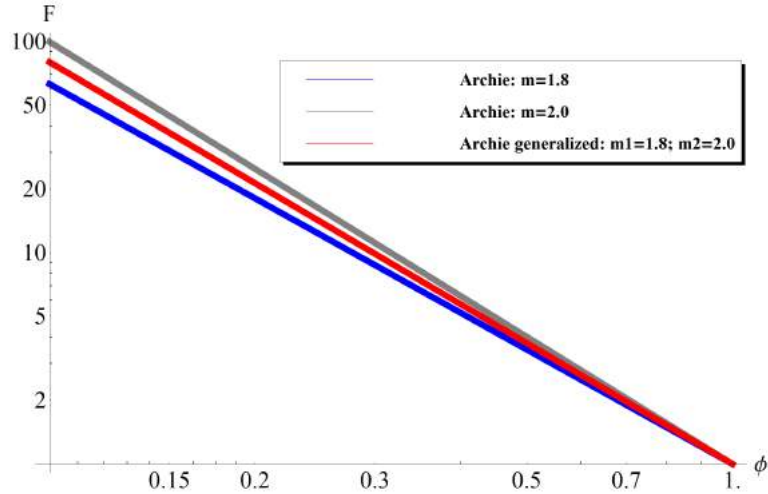


Figure 1.8.: Comparison between Archie equation with fixed values for  $m$ , Eq.(1.7) and superstatistical generalized Archie equation with homogeneous distribution of  $m$ , Eq(1.9). The formation factor is  $F = \frac{R}{R_w}$  and  $aS_w^{-n} = 1$ .

kinds of samples in high- and low-field NMR experiments and well log data too. The advantage of this method is to take into account all possibilities of fluctuating parameter, even if the range of fluctuation is very large. The drawback can be the emergence of new parameters such as the variance of the distribution  $f(m)$ . However, new parameters can be useful if the statistical assumption about the  $f(m)$  is valid.

### 1.3. Wireline logging Petrophysics

The wireline logging petrophysics is the standard way to gather information about a well, such as location in depth, the amount and the producibility of hydrocarbons. The technology is based on a cable with a tool lowered into the well which perform active and passive measurements of the rock formation, such as resistivity, sonic measurements, gamma ray, neutron density, NMR and

others. A schematic wireline can be view in Fig. 1.9. In the next paragraphs we will explain quickly some wireline log tools and measurements principles.

The gamma ray log (GR) is a shale indicator, it is a passive tool and detects the natural emission of gamma-ray photons of isotopes in reservoir rock. The feldspar and micas, minerals presents in sandstones, contains Potassium, Thorium and Uranium. The clay minerals like illite, smectite and chlorite, are main constituents of shales and have content of radioactive isotopes, which are detected by GR log. The GR measurements are used to calculate the amount of shale as a function of depth. The vertical resolution of GR tools is approximately 0.3m with a depth of investigation of 0.4-0.6m depending on the density of the rock.

Another gamma ray tool is the density log tool and is a porosity indicator. It emits medium gamma ray and the 100-300 keV range interacts with rock by Compton scattering and is, therefore, an indicative for the electron density of the rock. The bulk density of rock is closely related to electron density, so upon calibration, a porosity value can be derived. The low energy photons are dominated by the photoelectric effect, and with these two phenomena it is possible to determine the porosity and lithology, such as sand, limestone, anhydrite and dolomite. The vertical resolution is approximately 0.25m and the depth of investigation of the density tool is about 0.15m.

The neutron log is an indicator of porosity, shale and gas. The neutron tool emits high-energy neutrons into the formation from a radioactive source, most often plutonium-beryllium, and a single detector, or an electrically powered accelerator source called a minitron. The neutrons interact first with hydrogen, and for formation filled by fluid is possible to quantify porosity. The formations with gas have less content of hydrogen than water or oil, so due to a low measurements of neutrons, this log is a good indicator of regions of the reservoir with hydrocarbon gas. The depth of investigation of the neutron

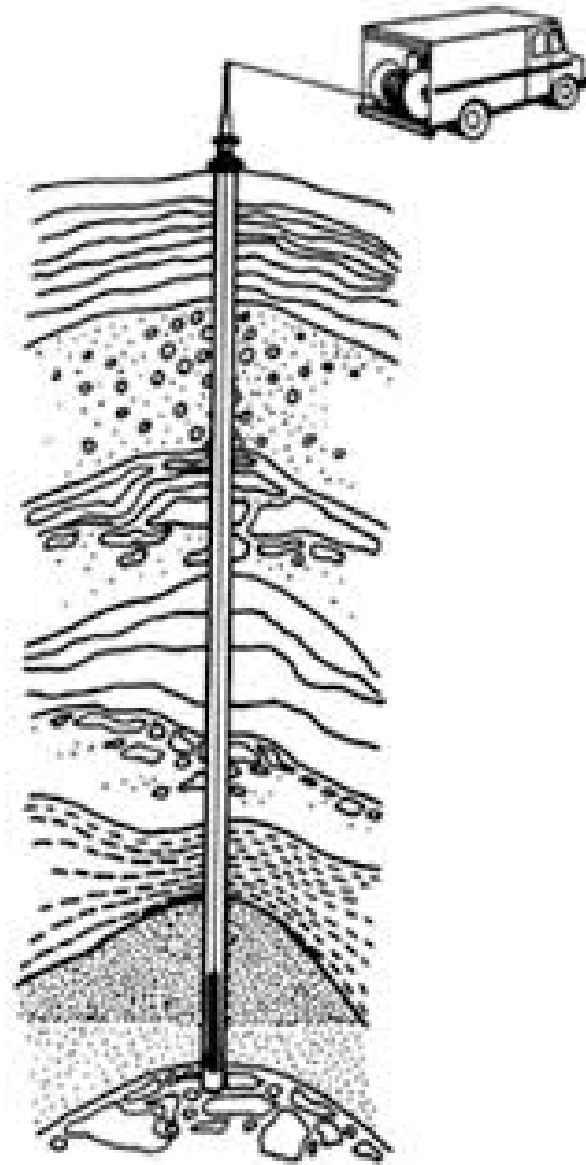


Figure 1.9.: Schematic of wireline log: a cable with the tool is lowered into the well and makes measurements of rock formation [7].

log is approximately 0.25m with some 0.4m depth resolution. Neutron tool readings are very sensitive to clays too and vary from one clay kind to the other.

The resistivity log is an indicator of hydrocarbon saturation. Electrical currents are sent to formation and resistivity is measured. The resolution of resistivity tools depends on the depth of investigation. Shallow reading tools can have resolutions down to 2.5 centimetres while the deeper reading tools have resolutions of approximately one metre.

Sonic (acoustic) log is an indicator of porosity. The tool emits an acoustical stimulus to the formation and measures the interval transit time, which is the time that rock formation transmits a seismic wave. The velocity of transmission of seismic wave in geological formation depends of the effective porosity and if the velocity of the rock matrix and pore fluid is known the porosity can be estimated. Two other important logs are the imaging logs, made from acoustical or resistivity measurements, an example is given in Fig. 1.10.

The NMR log are indicators of porosity and permeability. The NMR tool has one magnet to apply a static field, and one probe with radiofrequency to measures relaxation. The NMR experiment accesses only the fluid in the formation and because of this it is the only log that allows a permeability model, despite its limitations.

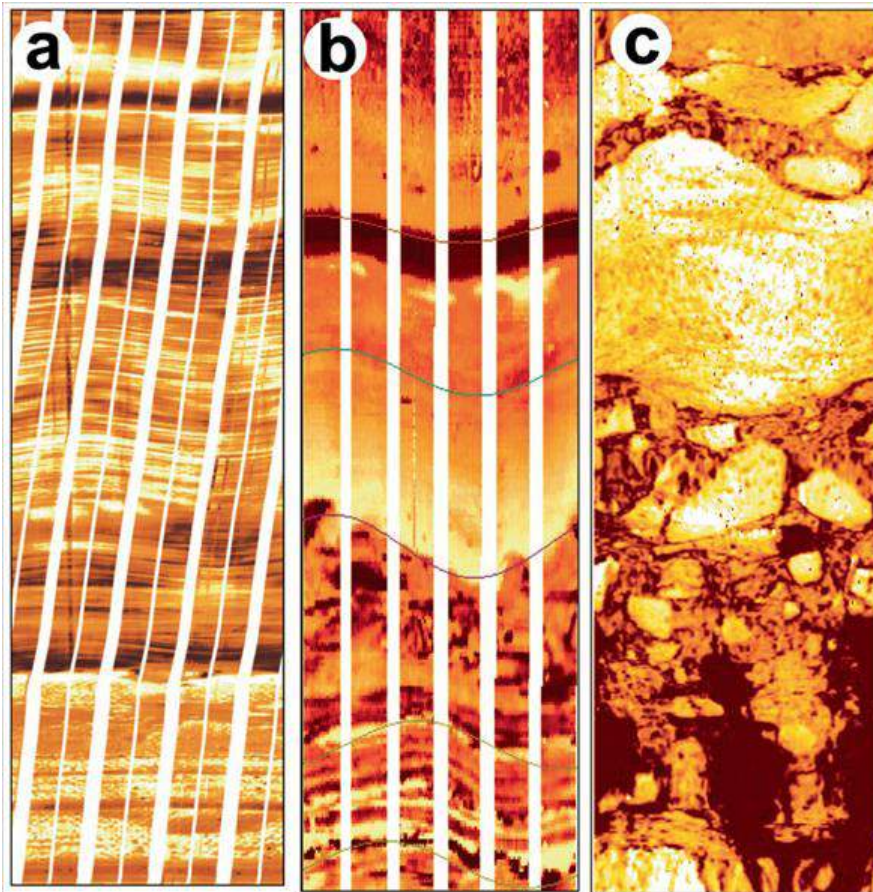
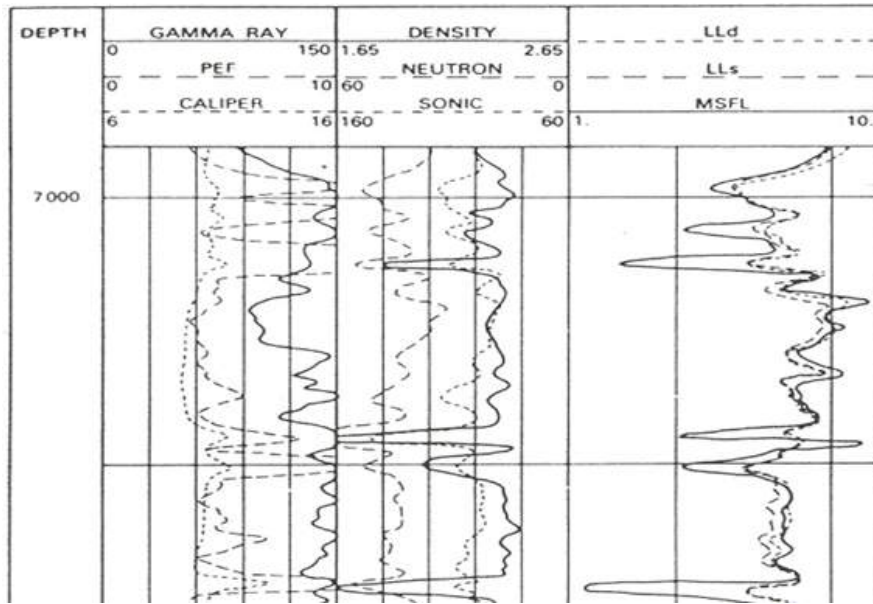


Figure 1.10.: Examples of wireline log data. The first image shows gamma ray, photoelectric, caliper, sonic, density, neutron, and resistivity logs [8]. The second figure shows the modern high resolution wireline imaging tools. (a) The FMI resistivity imager (Schlumberger). (b) The STAR resistivity imager (Baker Atlas). (c) The CBIL acoustic imager Baker Atlas.

## 2. Superstatistics

Superstatistics was proposed by Beck and Cohen to describe nonequilibrium systems with complex dynamics in stationary states with large fluctuations of intensive quantities (e.g. the temperature, chemical potential or energy dissipation) on long time scales [74]. After that, many applications and interesting developments have appeared in the literature [75].

The superstatistics approach applies to situations in which an intensive thermodynamical parameter, such as the temperature of the system, fluctuates (Fig. 2.1), in such a way that the probability of occurrence of a microstate is not a Boltzmann weight, but rather a sum of Boltzmann weights [53]. This approach leads to a density function concept of the fluctuating intensive parameter. In this way, the generalized Boltzmann weight or *Beck-Cohen weight* is similar to a Laplace transform of that density function:

$$B(E) = \int_0^\infty e^{-\beta E} f(\beta) d\beta \quad (2.1)$$

where  $E$  is the energy of a microstate,  $\beta$  is the inverse of temperature and  $f(\beta)$  is the distribution function of  $\beta$ 's divided by partition function.

One of the most important derivation of superstatistics occurs if  $f(\beta)$  is a  $\chi^2$ -distribution. In this case the microstate of the system is the  $q$ -exponential function or *Tsallis weight*, [72]:

$$B(E) = \int_0^\infty e^{-\beta E} \chi_{q,\beta_0}^2(\beta) d\beta, \quad (2.2)$$

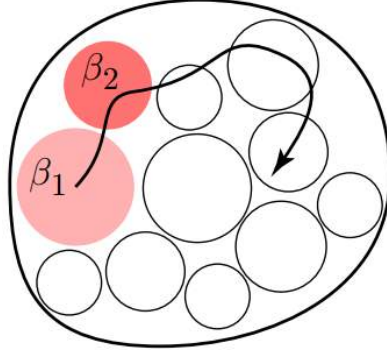


Figure 2.1.: Representation of system in which the  $\beta$  parameter fluctuates locally. To describe correctly the particle dynamics or the global behavior of the system, all possible values of  $\beta$  must be considered.

where  $\chi_{q,\beta_0}^2(\beta)$  is the  $\chi^2$ -distribution, which after integration leads to

$$B(E) = (1 - (1 - q)\beta_0 E)^{\frac{1}{1-q}}, \quad (2.3)$$

which, in turn, is the definition of  $q$ -exponential function [10]:

$$B(E) = e_q^{-\beta_0 E}, \quad (2.4)$$

Therefore, a  $q$ -exponential can be represented as a particular infinite sum of exponentials.

Let us introduce how to generate a  $\chi^2$ -distribution. If we get some values, about one hundred for example, of one Gaussian random variable ( $X_j$ ) the result can be seen in Figure 2.2. The  $\chi^2$ -distribution is the distribution of a random variable given by a sum of squares of Gaussian variables ( $\beta = \sum_{j=1}^{\nu} X_j^2$ ) and is specially important to generate random variables with strictly positive values. Here, the superscript  $\nu$  is the number of degrees of freedom. The result of a hundred values of one random variable given by a sum of ten square Gaussian random variable can be see in Figure 2.3.

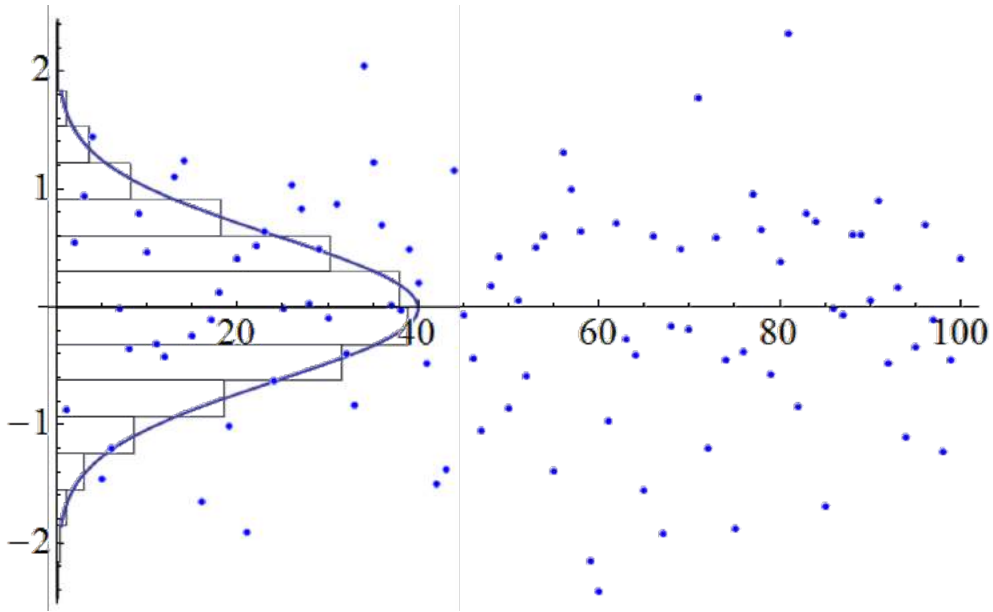


Figure 2.2.: One hundred values for a Gaussian random variable and their respective histogram and probability density function (PDF) in vertical axis.

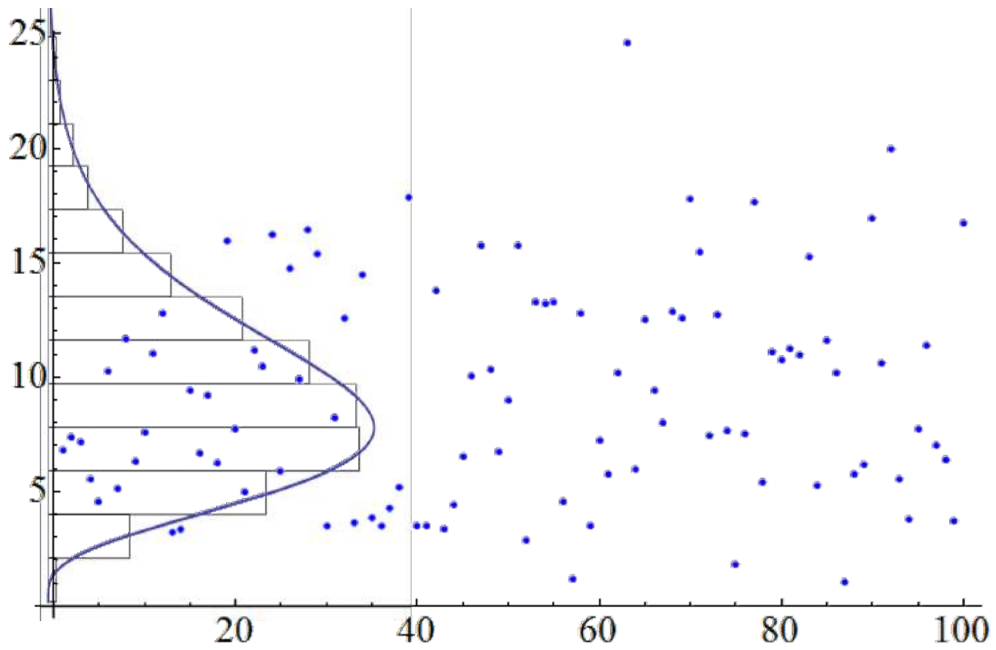


Figure 2.3.: One hundred values for a sum of ten square Gaussian random variable and their respective histogram and probability density function (PDF) in vertical axis.

The relationship between  $\nu$  and  $q$  is

$$q = 1 + \frac{2}{\nu}, \quad (2.5)$$

so when  $\nu \rightarrow \infty$  is the same that  $q \rightarrow 1$ . The probability density function (PDF) of  $\chi^2$ -distribution is

$$\chi_{q,\beta_0}^2(\beta) = \frac{\left(\frac{1}{(q-1)\beta_0}\right)^{\frac{1}{q-1}}}{\Gamma\left(\frac{1}{q-1}\right)} \beta^{\frac{1}{q-1}-1} e^{-\frac{\beta}{(q-1)\beta_0}}, \quad (2.6)$$

where  $\beta_0$  is the mean of the distribution and  $q$  is the so-called nonextensive parameter in q-statistics. This parameter is related to the mean,  $\beta_0$ , and standard deviation,  $\sigma^2$ , of  $\chi_{q,\beta_0}^2(\beta)$ :

$$q = 1 + \frac{\sigma^2}{\beta_0^2}. \quad (2.7)$$

Equation (2.7) shows that the  $q$  parameter cannot be smaller than unit, so the superstatistics is a generalization of q-statistics only for  $q > 1$  [74].

In Equation (2.1),  $f(\beta)$  distribution cannot be Gaussian, because  $\beta$  is strictly positive by construction. For practical applications of superstatistical distributions, Beck (2005) [76] and Kiyono (2013) [77] pointed out that there are three physically relevant universality classes in experiments: *i*) the  $\chi^2$  superstatistics; *ii*) the inverse- $\chi^2$ ; and *iii*) the log-normal. The  $\chi^2$  and inverse- $\chi^2$  are associated to additive process and log-normal to multiplicative ones. We show in this thesis that the  $\chi^2$  distribution of  $\beta$ s is adequate to describe transverse relaxation in porous media, because the porous sample can be viewed like a large random sum of  $\beta$ s positive values, i.e., each pore of sample has a specific positive and random  $\beta_i$  and the  $\beta$  sample is the sum of them all.

We see above, that if many squared random Gaussian variable ( $X_j^2$ ) contribute in additive way to  $\beta = \sum_{j=1}^{\nu} X_j^2$  variable, the result of this approach

leads to a  $\chi^2$ -distribution, Eq.(2.6). We will suppose the following assumption for  $T_2$  in porous media:

$$\frac{1}{T_2} = \sum_{j=1}^{\nu} X_j^2, \quad (2.8)$$

and because of this the distribution for the inverse of  $T_2$  will be given by a  $\chi^2$ -distribution.

The other two universality classes that appear in experiments analysed by superstatistics, the inverse  $\chi^2$  and log-normal distribution, are associated to additive stochastic processes and multiplicative stochastic processes respectively. If the same consideration made for obtain  $\chi^2$  is applied to the inverse of  $\beta$ , i.e. the  $\beta^{-1} = \sum_{i=1}^N X_i^2$ , which now can represent the temperature ( $T$ ) or  $T_2$  time in NMR, the result will be the inverse  $\chi^2$ -distribution:

$$\text{inv}\chi_{q,\beta_0}^2(\beta) = \beta_0 \frac{\left(\frac{1}{(q-1)\beta_0}\right)^{\frac{1}{q-1}}}{\Gamma\left(\frac{1}{q-1}\right)} \beta^{\frac{1}{1-q}-2} e^{-\frac{\beta_0}{(q-1)\beta}}. \quad (2.9)$$

Finally, there are situations in which the  $\beta$  variable can be given by a multiplicative process  $\beta = \prod_{i=1}^{\nu} X_i$  of Gaussian random variables, which leads to  $\log \beta = \sum_{j=1}^{\nu} \log X_j$  and  $\beta$  will be log-normally distributed:

$$f(\beta) = \frac{a}{\beta} e^{-c(\log \beta - b)^2}, \quad (2.10)$$

where  $a$ ,  $b$  and  $c$  are constants. This type of log-normal superstatistics is particularly relevant for turbulent flows. In Figure 2.4 it is possible to see the comparison between  $\chi^2$ , inverse  $\chi^2$  and log-normal distributions fitting data of turbulent flow.

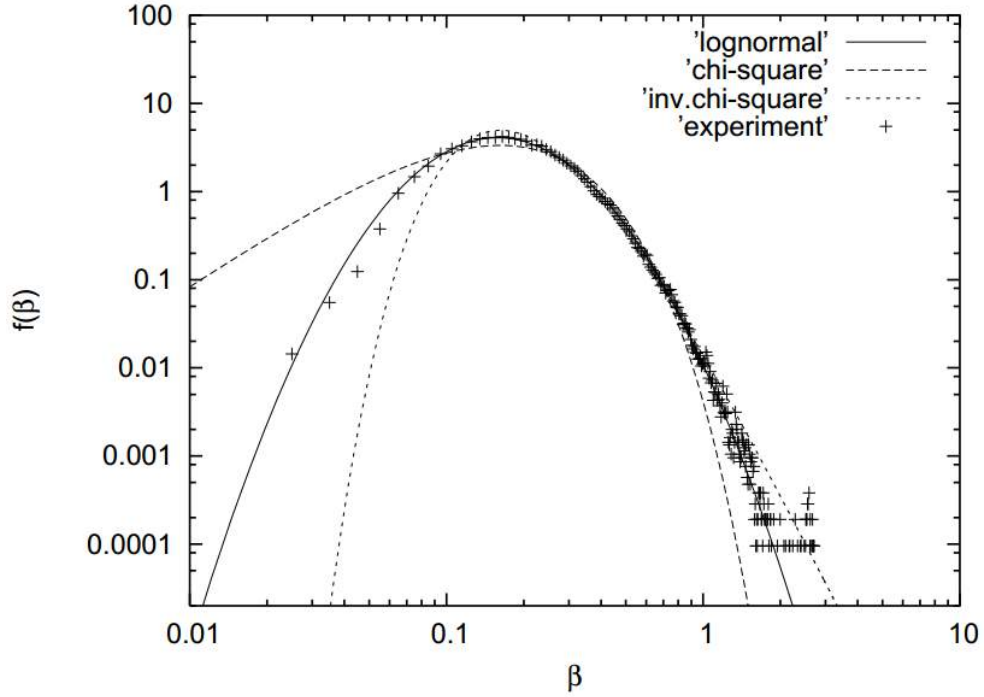


Figure 2.4.: Comparison between  $\chi^2$ , inverse  $\chi^2$  and log-normal distributions fitting data of turbulent flow. Details can be seen in [9].

## 2.1. Nonextensive Statistical Mechanics

The nonextensive statistical mechanics was proposed by Tsallis in 1988 [78]. The new entropic form proposed, as a possible generalization of Boltzmann-Gibbs statistical mechanics, is nonadditive and the energy is nonextensive.

The Boltzmann-Gibbs entropy is:

$$S_{BG} = -k \sum_i p_i \log p_i, \quad (2.11)$$

where  $k$  is the Boltzmann constant and  $p_i$  is a probability function of a microstate of the system. The entropy has a maximum when  $p_i$  is an equiprobable function like  $p_i = 1/W$ , where  $W$  is the total number of microstates. The  $S_{BG}$  function is additive, and this means that when the whole system is partitioned

in subsystems, the total entropy is the sum of entropies of each subsystem:

$$S_{BG}(A + B) = S_{BG}(A) + S_{BG}(B). \quad (2.12)$$

The Tsallis entropy, or  $q$ -entropy, is based on a generalization of logarithm function:

$$S_q = -k \sum_i p_i \ln_q p_i, \quad (2.13)$$

where  $q$ -logarithm is  $\ln_q x = \frac{x^{1-q}-1}{1-q}$ . The  $S_q$  entropy is a nonadditive function:

$$S_q(A + B) = S_q(A) + S_q(B) + \frac{(1-q)}{k} S_q(A) S_q(B). \quad (2.14)$$

Detailed discussion about  $S_{BG}$  and  $S_q$  properties and concepts can be found in [10].

The concept of extensivity applies for a quantity linear with the size of the system, or the number of particles. The thermodynamical entropy, for instance, is an extensive quantity, i.e.:

$$S(N) \propto N, \quad (2.15)$$

where  $S$  is the entropy and  $N$  is the number of particles. In nonextensive statistical mechanics, the functional form of entropy is changed and the  $q$  parameter is introduced to preserve the extensivity property of entropy  $S_q$ . This will be explained below.

In Figure 2.5 it is possible to see the relation between additivity and extensivity properties of Boltzmann-Gibbs ( $S_{BG}$ ) and Tsallis ( $S_q$ ) functional entropies and  $W(N)$  function, that is the probability of occurrence of a microstate configuration. If  $W(N) \propto \mu^N$ , when one particle is introduced in the system, and so  $N$  becomes  $N + 1$ , the probability of a microstate configuration is given by all possibilities of arrangements with this new particle. For example, in a

system of  $N$  coins, or any system with two levels, the probability of occurrence of one microstate configuration is given by  $W(N) = 2^N$ , but if one more coin is introduced in the system, the probability will be  $W(N + 1) = 2^{N+1}$ . This kind of system has equiprobable distribution of microstates, and is closely related to the concept of ergodicity. Systems with  $W(N) \propto \mu^N$  will have  $S(N) \propto \log(W(N)) \propto \log(\mu^N) \propto N$ , so  $S(N) \propto N$ . This is the reason why  $S_{BG}$  is the most appropriate function form for classical thermodynamic systems.

There are many thermodynamical systems in nature for which the function  $W(N)$  is polynomial rather than exponential function, i.e.  $W(N) \propto N^\rho$ . Introducing the  $q$ -logarithm function  $\ln_q x = \frac{x^{1-q}-1}{1-q}$ , with  $q = 1 - 1/\rho$ , it is easy to see that the entropy based on  $q$ -logarithm will be extensive when  $W(N) \propto N^\rho$ :  $S(N) \propto \ln_q(W(N)) \propto \ln_q(N^\rho) \propto \frac{N^\rho(1-q)-1}{1-q} \propto N$ . The polynomial dependence of  $W(N)$  is the microscopic reason to use  $S_q$  entropy. However it is very difficult to predict the  $q$  value from first principle. The physical meaning of  $W(N) \propto N^\rho$  is supported by long range interactions, fractal behavior, correlations, non-ergodicity or many other considerations [10, 79].

The following example show a theoretical set of correlated probabilities that suggest it has  $W(N) \propto N^d$ , and in this case the  $q = 1 - 1/d$  turns the  $S_q$  functional an extensive quantity. The system is the *Leibniz triangle rule* to generate a marginal probability function with  $N$ -subsystems. The rule is the sum of two successive joint probabilities of the  $N$ -system coincides or asymptotically approaches the corresponding joint probability of the  $(N - 1)$ -system. This idea can be better see in Fig.2.6, where:

$$\pi_{N,n} + \pi_{N,n+1} = \pi_{N-1,n}, \quad (2.16)$$

with  $n = 0, 1, \dots, N - 1$ ; and  $N = 2, 3, \dots$ . Figure 2.6 shows one specific

	ENTROPY	
$W(N)$ ( $N \rightarrow \infty$ )	$S_{BG}$  (ADDITIVE)	$S_q$ ( $q \neq 1$ )  (NONADDITIVE)
$\sim \mu^N$ ( $\mu > 1$ )	EXTENSIVE	NONEXTENSIVE
$\sim N^\rho$ ( $\rho > 0$ )	NONEXTENSIVE	EXTENSIVE  ( $q = 1 - 1/\rho$ )

Figure 2.5.: The function  $W(N)$  is the probability of occurrence of a microstate configuration. Systems with  $W(N) \propto \mu^N$ , are described by  $S_{BG}$ , and systems with microstates dependence like  $W(N) \propto N^\rho$  are described by  $S_q$  entropy [10].

model for generating the  $\pi_{N,n}$  probabilities that the entropy  $S_q$  is extensive for  $q \neq 1$ . Details about the model can be seen in Tsallis et al. 2005 [11].

A physical example where nonadditive entropy  $S_q$  is extensive for a special value of  $q$  can be view in Fig 2.7. The system studied in [12] is a one-dimensional spin-1/2 ferromagnetic chain with an exchange coupling and subjected to an external transverse magnetic field, i.e., the quantum XY model.

There are many geological, geophysical and petrophysical models there are based on fractal geometry [13, 80–91] (Fig. 2.7). The  $q$ -Gauss solutions for porous media equation can be found in [92]. We advocate that  $q$ -statistics is applicable to model and explain NMR transverse decay due  $T_2$  of a porous sample, in special rocks, are associated to a random additive process, and therefore the  $\chi^2$ -distribution is appropriated to be a statistical model. Physically, the porous sample is constituted by a sum over all pores and each pore has a random value of  $T_2$  due to random geometrical properties of each one. The  $T_2$  distribution of sample will be a sum over all pores.

$(N = 0)$	1
$(N = 1)$	$\pi_{10} \ \pi_{11}$
$(N = 2)$	$\pi_{20} \ \pi_{21} \ \pi_{22}$
$(N = 3)$	$\pi_{30} \ \pi_{31} \ \pi_{32} \ \pi_{33}$
$(N = 4)$	$\pi_{40} \ \pi_{41} \ \pi_{42} \ \pi_{43} \ \pi_{44}$

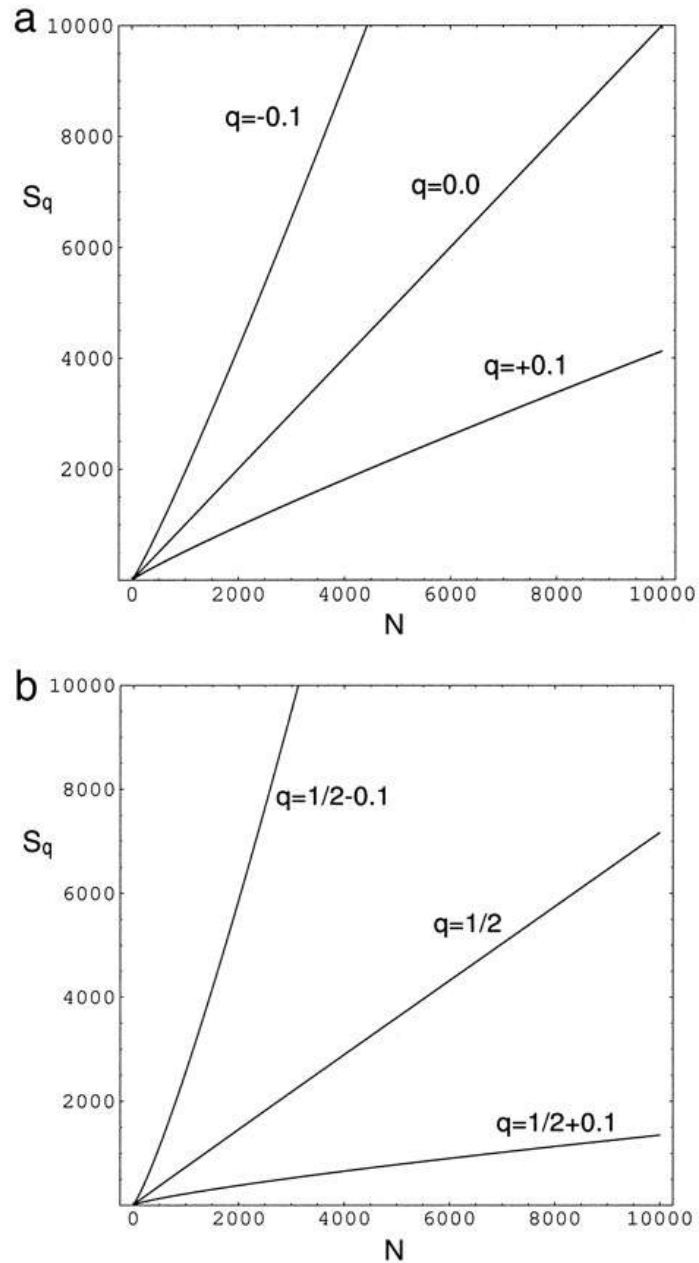


Figure 2.6.: Example of system where the entropy is extensive ( $S_q \propto N$ ) for  $q \neq 1$ . Details of the model can be found in [11]. In this case the  $q$  parameter is suggested to be  $q = 1 - \frac{1}{d}$ , where  $d$  is an important parameter to generate the  $\pi_{N,n}$  values. The figures **a**) and **b**), shows the results of  $S_q$  versus  $N$  for  $d = 1$  and  $d = 2$ , respectively.

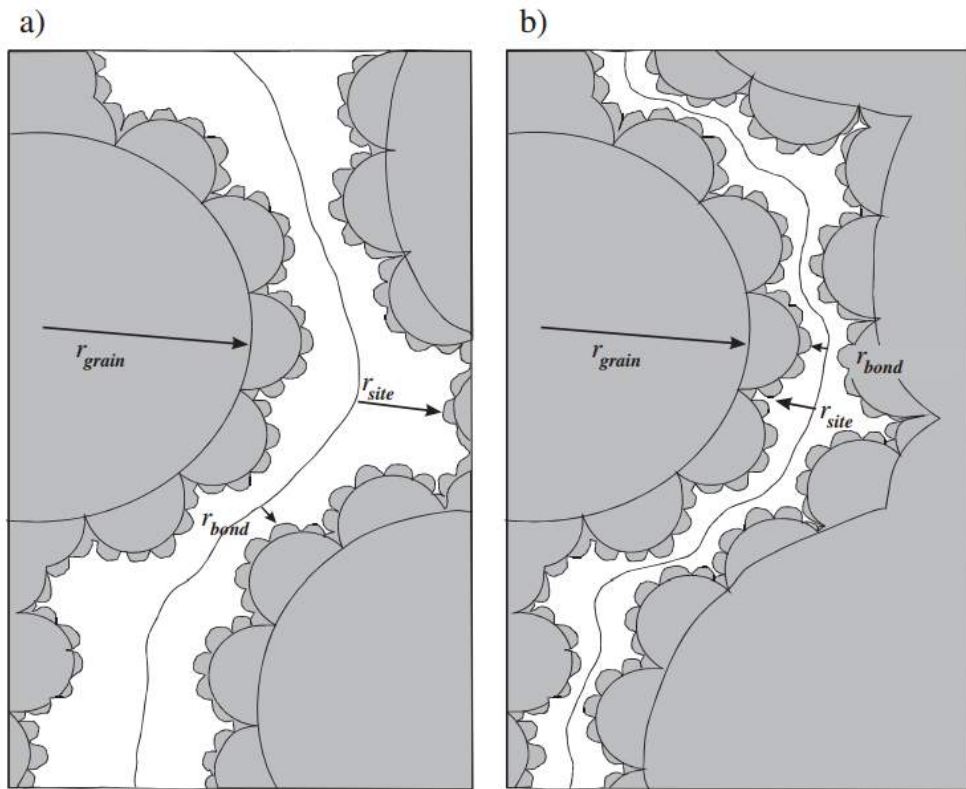
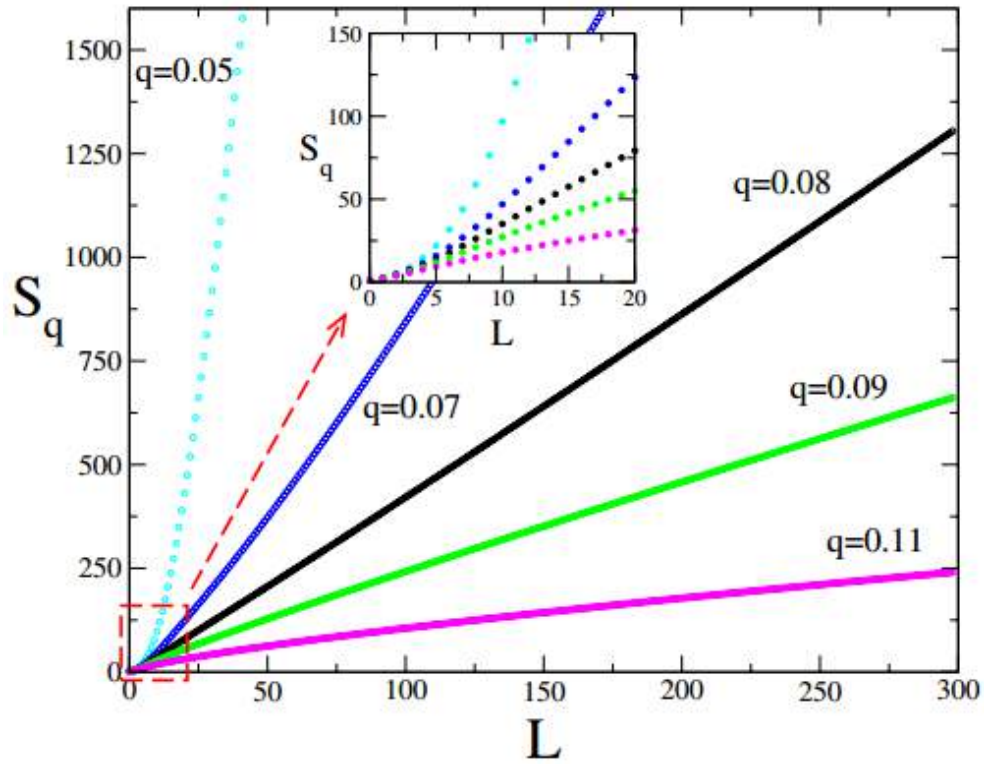


Figure 2.7.: The figure on top shows  $S_q$  versus the size of system  $L$  of one-dimensional spin-1/2 ferromagnetic chain with an exchange coupling and subjected to an external transverse magnetic field [12]. The figure on bottom shows a model based on fractal geometry of porous media, details can be see in [13].

## 3. Nuclear Magnetic Resonance

### 3.1. Fundamentals of NMR

#### 3.1.1. Spin in a static magnetic field

The basic of a NMR experiment is an ensemble of nuclear spins in a static magnetic field, given by a magnet, and the application of an orthogonal radiofrequency field produced in a sample probe. The spins will precess in the region of static magnetic field with a Larmor Frequency, and for the resonance to occur, the frequency of electromagnetic field applied needs to be tuned to be the same as the Larmor frequency. In this section we will show that one isolated magnetic moment aligned with a static magnetic field will rotate if an orthogonal oscillating magnetic field is applied in a resonance condition [24].

The spin is an intrinsic angular moment of particles and is a quantum property. The magnetic properties of particles are defined by their magnetic moments, a quantity closely related to the spin. When one magnetic moment ( $\vec{\mu}$ ) is placed in a magnetic field ( $\vec{B}$ ) the energy of interaction is described by the Hamiltonian

$$H = -\vec{\mu} \cdot \vec{B}. \quad (3.1)$$

When the magnetic moment ( $\vec{\mu}$ ) is proportional to the  $\frac{1}{2}$ -spin, it is convenient to represent it in terms of the Pauli matrices,  $\vec{\mu} = \frac{\hbar\gamma}{2}\vec{\sigma}$ , where the  $\hbar$  is the Planck constant and  $\gamma$  is the gyromagnetic ratio. The gyromagnetic ratio appear due quantum-relativistic effects and emerges naturally from Dirac

equation for fundamental particles like electron, but not for protons that are constituted by two quarks up and one quark down. The solution of Dirac equation for half-integer spin particles and discussion about gyromagnetic ratio can be found in the reference [93].

A particle of  $\frac{1}{2}$ -spin can stay in one of two quantum pure states or in an arbitrary superposition of both. To analyse the evolution of a spin with Hamiltonian (3.1) given by Schroedinger equation, let us consider the initial quantum state,  $|\psi(0)\rangle = \frac{1}{\sqrt{2}}(|\uparrow\rangle + |\downarrow\rangle)$ ,

$$i\hbar \frac{d}{dt} |\psi(t)\rangle = H |\psi(t)\rangle. \quad (3.2)$$

The time evolution can be calculated by the propagator  $U(t)$  applied in  $|\psi(0)\rangle$ ,

$$|\psi(t)\rangle = U(t) |\psi(0)\rangle = e^{-\frac{i}{\hbar} H t} |\psi(0)\rangle. \quad (3.3)$$

Suppose that the static and constant magnetic field aligned on z-axis, the Hamiltonian is

$$H = \frac{\hbar\gamma}{2} B_0 \sigma_z, \quad (3.4)$$

and the calculation of  $|\psi(t)\rangle$  is

$$\begin{aligned} |\psi(t)\rangle &= e^{-\frac{i\gamma B_0}{2} \sigma_z} \left( \frac{1}{\sqrt{2}} (|\uparrow\rangle + |\downarrow\rangle) \right) \\ &= \frac{1}{\sqrt{2}} \left( e^{-\frac{i\gamma B_0}{2} t} |\uparrow\rangle + e^{\frac{i\gamma B_0}{2} t} |\downarrow\rangle \right) \\ &= \frac{1}{\sqrt{2}} (|\uparrow\rangle + e^{i\gamma B_0 t} |\downarrow\rangle). \end{aligned} \quad (3.5)$$

Let us have a closer look on the state  $|\psi(t)\rangle$  of Eq.(3.5). One general quantum state can be represented on the Bloch sphere [94] by

$$|\psi\rangle = \cos(\theta/2) |\uparrow\rangle + \sin(\theta/2) e^{i\phi} |\downarrow\rangle,$$

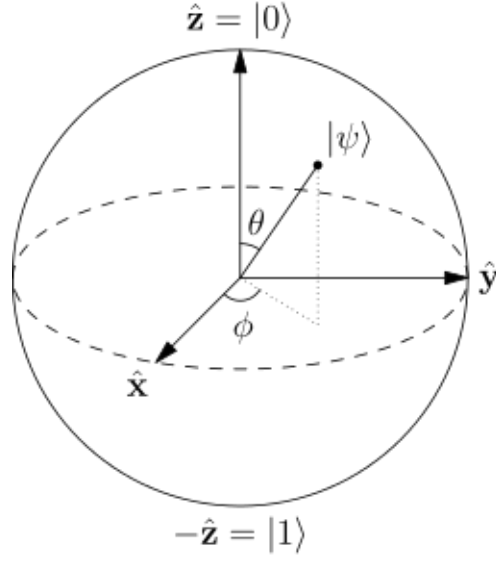


Figure 3.1.: Bloch sphere representation of a quantum state  $|\psi\rangle$ . Observe that for a time dependent azimuthal angle such as  $\phi(t) = \gamma B_0 t$ , the state precess around z-axis.

where  $\theta$  and  $\phi$  are the polar and azimuthal angles, respectively. We can identify in Equation (3.5) the time dependent azimuthal angle  $\phi(t) = \gamma B_0 t$ , so the spin precess around the z-axis with the Larmor frequency  $\omega_L = \gamma B_0$ , see Fig. 3.1.

### 3.1.2. Applying radio frequency

In NMR experiments the magnet provides the static field in the z-axis and the probe the radiofrequency field with an oscillating magnetic field with frequency  $\omega$ . The Hamiltonian of this problem is

$$H(t) = \frac{1}{2} \hbar \gamma (B_0 \sigma_z + B_1 \cos(\omega t) \sigma_x). \quad (3.6)$$

It is convenient to analyse the problem in a frame that is rotating with the Larmor frequency around z-axis. The quantum state in the new frame will be the state represented in laboratory frame times a time-dependent phase:

$$|\psi'(t)\rangle = e^{i\omega_L \sigma_z t/2} |\psi(t)\rangle. \quad (3.7)$$

Replacing the transformed state, Eq. (3.7), in the Schroedinger equation we find the transformed Hamiltonian,

$$i\hbar \frac{d}{dt} |\psi'(t)\rangle = H' |\psi'(t)\rangle, \quad (3.8)$$

where the Hamiltonian in the new frame is

$$H'(t) = \left( -\frac{\hbar\omega_L}{2} \sigma_z + e^{i\omega_L\sigma_z t/2} H(t) e^{-i\omega_L\sigma_z t/2} \right). \quad (3.9)$$

The first term in the right hand side of equation is a rotation about the z-axis, but it will be canceled as we shall see below. The last term can be calculated by replacing  $H(t)$ ,

$$\begin{aligned} e^{i\omega_L\sigma_z t/2} H(t) e^{i\omega_L\sigma_z t/2} &= \frac{\hbar\gamma}{2} e^{i\omega_L\sigma_z t/2} (B_0\sigma_z + B_1 \cos(\omega t)\sigma_x) e^{-i\omega_L\sigma_z t/2} \\ &= \frac{\hbar\gamma}{2} (B_0\sigma_z + e^{i\omega_L\sigma_z t/2} B_1 \cos(\omega t)\sigma_x e^{-i\omega_L\sigma_z t/2}) \end{aligned} \quad (3.10)$$

As we can see from Equation (3.10) the first term on the right hand is a rotation about z-axis that cancels the first term on the right hand side of Equation (3.9). The term  $\cos(\omega t)\sigma_x$  can be rewritten in terms of raising and lowering Pauli operators,

$$\begin{aligned} \cos(\omega t)\sigma_x &= \frac{1}{2} ((\cos(\omega t)\sigma_x + \sin(\omega t)\sigma_y) + (\cos(\omega t)\sigma_x - \sin(\omega t)\sigma_y)) \\ &= ((e^{-i\omega t}\sigma_+ + e^{i\omega t}\sigma_-) + (e^{i\omega t}\sigma_+ + e^{-i\omega t}\sigma_-)). \end{aligned} \quad (3.11)$$

Substituting Equation (3.11) in Eq. (3.10) and using the identity  $e^{i\alpha\sigma_z}\sigma_{\pm}e^{-i\alpha\sigma_z} = e^{2i\alpha}\sigma_{\pm}$ , we find the transformed Hamiltonian only as a function of the magnetic field and frequency of radiofrequency field. In the rotating frame, the spin precession around z-axis are not observed and the hamiltonian

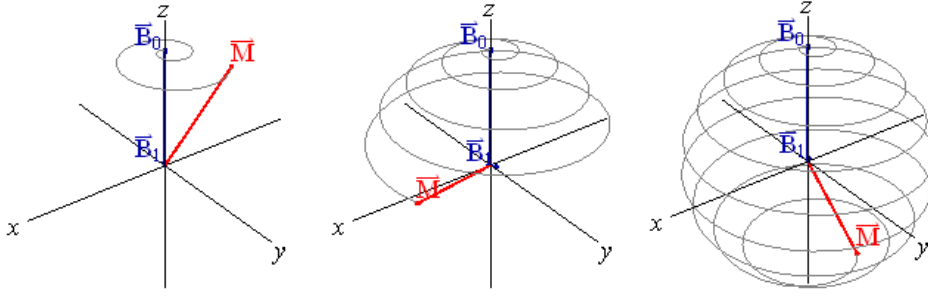


Figure 3.2.: Representation of spin state on the Bloch sphere in a resonance experiment. The states precess around z-axis due static magnetic field and rotates around x-axis due radiofrequency field.

$H'(t)$  becomes

$$H'(t) = \frac{\hbar\gamma}{2} B_1 \left( (e^{i(\omega_L - \omega)t} \sigma_+ + e^{i(\omega - \omega_L)t} \sigma_-) + (e^{i(\omega_L + \omega)t} \sigma_+ + e^{-i(\omega_L + \omega)t} \sigma_-) \right) \quad (3.12)$$

The resonance condition occurs when the frequency  $\omega$  is equal to the Larmor frequency. In this case Hamiltonian will be

$$H'(t) = \frac{\hbar\gamma}{2} B_1 \left( (\sigma_+ + \sigma_-) + (e^{2i\omega_L t} \sigma_+ + e^{-2i\omega_L t} \sigma_-) \right). \quad (3.13)$$

The second term on the second hand side of Eq. (3.13) is negligible [95] and this is called the *Rotating Wave Approximation (RWA)* [95]. Finally, in the rotating frame, in the resonance condition ( $\omega = \omega_L$ ) and with RWA approximation, the Hamiltonian becomes

$$H' = \frac{\hbar\gamma}{2} B_1 \sigma_x. \quad (3.14)$$

Hamiltonian represents a rotation about the x-axis. So in the laboratory frame, the spin precess around z-axis and rotates around x-axis; this is known as Rabi oscillation [96] (see the representation on Bloch sphere in Fig.(3.10)).

### 3.1.3. Relaxation: Bloch-Torrey equations

In petrophysics we are usually interested in the resonance of the protons of the hydrogen nucleus  $H^1$  in the pore fluid (e.g., water or hydrocarbon) [62]. The resonance effect was explained in the last section with quantum approach for one single spin. The magnetization of the fluid in porous media is a result of a huge number of spin particles. Because of this the relaxation phenomena can be explained classically as we will do in this chapter. The phenomenological equations for NMR relaxation are the Bloch-Torrey equations [94, 97], see Eq.(3.15):

$$\frac{\partial \vec{m}}{\partial t} = \gamma \vec{m} \times \vec{B}_{ext} - \begin{pmatrix} \vec{m}_{x'}/T_2 \\ \vec{m}_{y'}/T_2 \\ (\vec{m}_{z'} - \vec{m}_0)/T_1 \end{pmatrix} - \nabla(\vec{D}\nabla\vec{m}). \quad (3.15)$$

The quantity  $\vec{m} = \vec{m}(\vec{r}, t)$  is the magnetization density vector in the rotating frame of reference,  $\gamma$  is the gyromagnetic ratio of the protons,  $B_{ext}$  is the external magnetic field,  $(x', y', z')$  denotes the spatial coordinates in the rotating frame of reference, and the  $\vec{D}$  is the diffusion tensor. In the case of isotropic diffusion the tensor  $\vec{D}$  simplifies to  $D = |\vec{D}|$ . The values  $T_1$  and  $T_2$  are the longitudinal and transverse relaxation times, respectively.  $T_1$  is the characteristic time to magnetization relaxe in z-axis and  $T_2$  is the characteristic time to decay of transverse macroscopic magnetization.

The Bloch-Torrey equations are the fundamental equations of motion of the magnetic moment vector  $\vec{m}$ . They are derived from the Newton second law for angular momentum plus a damping term governing the attenuation of magnetization, and a diffusion term. We can decompose the Eq.(3.15) in the

three components:

$$\left\{ \begin{array}{l} \frac{d\vec{m}_x}{dt} = \gamma(\vec{m}_y B_z - \vec{m}_z B_y) - \vec{m}_x/T_2 - D \frac{d^2 \vec{m}_x}{dx^2} \\ \frac{d\vec{m}_y}{dt} = \gamma(\vec{m}_z B_x - \vec{m}_x B_z) - \vec{m}_y/T_2 - D \frac{d^2 \vec{m}_y}{dx^2} \\ \frac{d\vec{m}_z}{dt} = \gamma(\vec{m}_x B_y - \vec{m}_y B_x) - (\vec{m}_z - \vec{m}_0)/T_2 - D \frac{d^2 \vec{m}_z}{dx^2} \end{array} \right. \quad (3.16)$$

Is interesting to analyse the solution of Bloch-Torrey Equations (3.16) when a static field is applied in  $z$ -axis and a radio frequency field is applied in the  $xy$ -plane. The components of magnetic field are components of the

$$\begin{aligned} B_x &= B_1 \cos(\omega t) \\ B_y &= B_1 \sin(\omega t) \\ B_z &= B_0 \end{aligned} \quad (3.17)$$

First we will analyse the slow diffusion regime, so the diffusion term will be neglected. After that the fast diffusion regime will be considered. To evaluate the solution of Eqs.(3.16) with field (3.17) is conveniently transform the coordinates to rotating frame with Larmor frequency. The transformation of coordinates are

$$\begin{aligned} m_x &= m_{x'} \cos(\omega_0 t) + m_{y'} \sin(\omega_0 t) \\ m_y &= m_{x'} \sin(\omega_0 t) - m_{y'} \cos(\omega_0 t) \\ m_z &= m_{z'} \end{aligned} \quad (3.18)$$

The Bloch equations for magnetization in a rotation frame becomes

$$\left\{ \begin{array}{l} \frac{dM_x}{dt} = (\omega_0 - \omega)M_y - \frac{M_x}{T_2} \\ \frac{dM_y}{dt} = -(\omega_0 - \omega)M_x + \omega_1 M_z - \frac{M_y}{T_2} \\ \frac{dM_z}{dt} = -\omega_1 M_y - \frac{M_z - M_0}{T_1} \end{array} \right. \quad (3.19)$$

We have dropped the primes of coordinates and written the equations in magnetization variables that are the volumetric integral of magnetic moment  $M_i(t) = \int_0^\infty \vec{m}_i(x, y, z, t) dV$ . The steady state solution of Eq.(3.19) is obtained by setting the time derivative magnetizations components equal to zero,  $\frac{dM_x}{dt} = \frac{dM_y}{dt} = \frac{dM_z}{dt} = 0$ . In this regime the solutions are:

$$\begin{cases} M_x &= \frac{\omega_1 T_2^2 \delta\omega}{1 + \omega_1^2 T_1 T_2 + (T_2 \delta\omega)^2} M_0 \\ M_y &= -\frac{\omega_1 T_2}{1 + \omega_1^2 T_1 T_2 + (T_2 \delta\omega)^2} M_0 \\ M_z &= \frac{1 + T_2^2 \delta\omega^2}{1 + \omega_1^2 T_1 T_2 + (T_2 \delta\omega)^2} M_0, \end{cases} \quad (3.20)$$

In the limit where  $\omega_1$  is so small that  $\omega_1 T_2 \ll 1$ , these equation reduce to:

$$\begin{cases} M_x &= \frac{\omega_1 T_2^2 \delta\omega}{1 + (T_2 \delta\omega)^2} M_0 \\ M_y &= \frac{\omega_1 T_2}{1 + (T_2 \delta\omega)^2} M_0 \\ M_z &= M_0. \end{cases} \quad (3.21)$$

The solution for  $M_x$  (absorption mode) and  $M_y$  (dispersion mode) is represented in Fig.(3.3).

Is interesting to analyse when we apply a radio frequency pulse (r.f. pulse method) in resonance condition. The spins will precess by the angle  $\theta = \omega_1 \tau$ , where  $\tau$  is the time pulse duration. When the r.f. is switched off the longitudinal component relaxes back to its equilibrium value [98]. The transverse magnetization induces a radiofrequency field that can detected in a form of a complex signal:

$$F(t) = M_0 \sin \theta \exp(-t/T_2) \exp(i\delta t), \quad (3.22)$$

called free induction decay signal (FID) (3.4). Is possible to show that its Fourier transform have the same form of absorption and dispersion modes

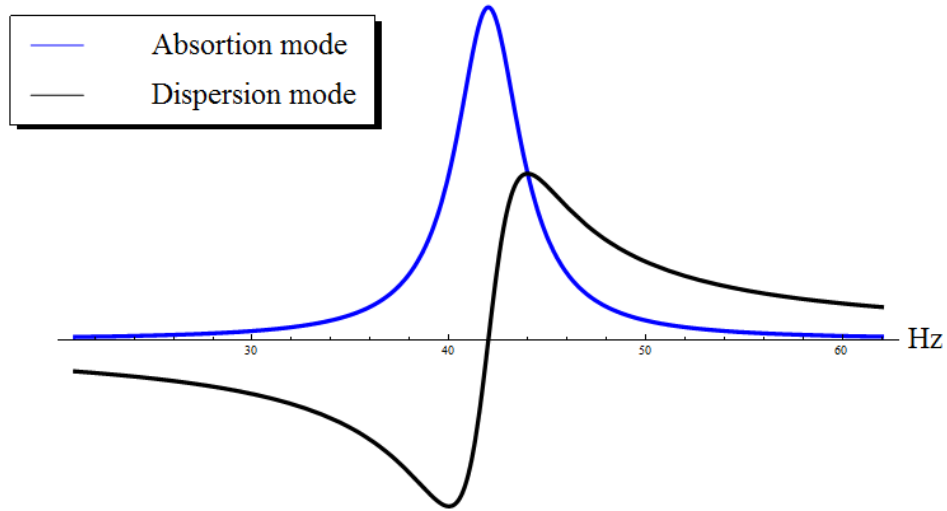


Figure 3.3.: The absorption and dispersion modes.

seen above.

#### 3.1.4. Spin echo and CPMG pulse sequence

The spin echo was discovered by Hahn in 1950 [99] and is one of the most important contributions to NMR. A spin-echo is a refocusing of the transverse magnetization, following a  $\frac{\pi}{2}$ - $\pi$  pulse sequence. The echo occurs because the magnetization is a sum of all spins in the sample and each spin feels a slightly different magnetic field  $\delta B$ . Because of this the spins will precess at different rates around the  $z$ -axis, so the relative phase is lost. When a second pulse of  $\pi$  is applied, in time  $t = \tau$ , the spins change the signal of precession and turn back to initial configuration in a time  $t = 2\tau$ , so the relative phase, between spins, tends to zero and the echo is observed (Fig.3.5).

If the sample is a fluid, the spins are in diffusion motion, and at different positions when the pulses are applied, so they feel a slightly different inhomogeneity when the  $\pi$ -pulse is applied. This means that the amplitude of echo is

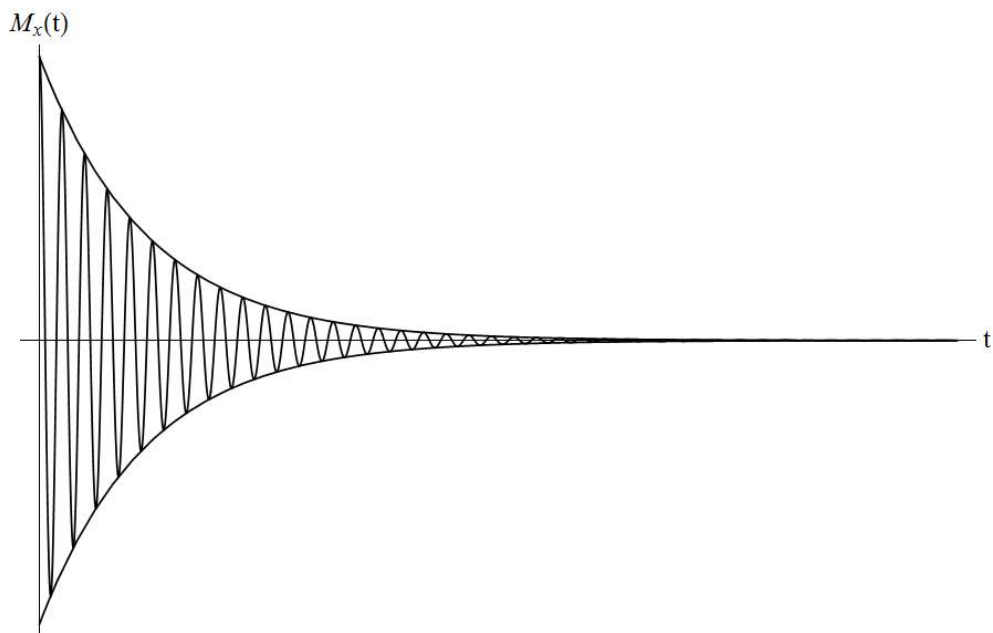


Figure 3.4.: Representation of a component of free induction decay (FID).

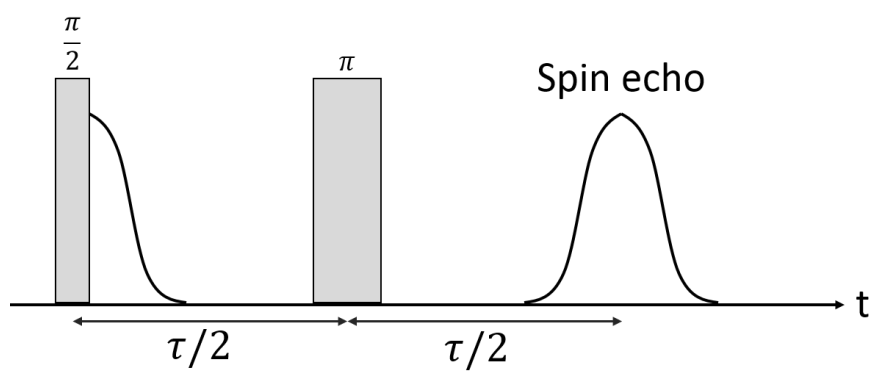


Figure 3.5.: Representation of spin echo that is a phase recovery due application of a  $\frac{\pi}{2}$ - $\pi$  pulse sequence.

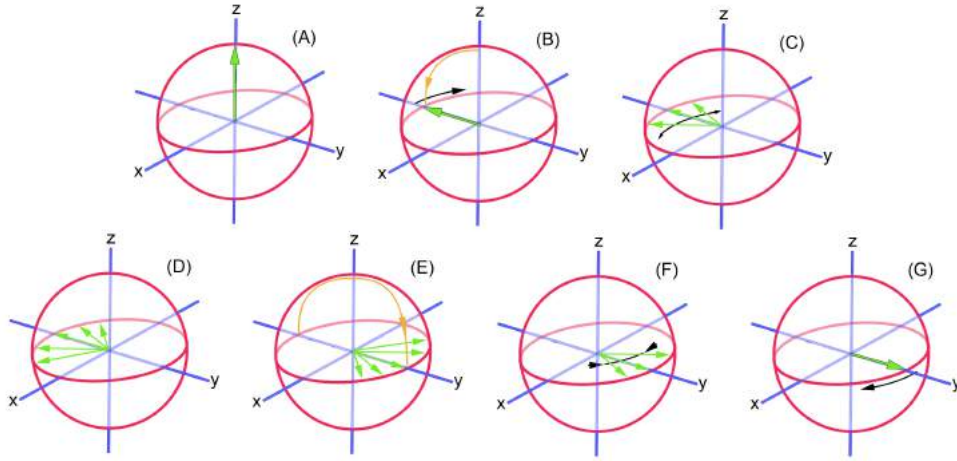


Figure 3.6.: Representation of spins in a Bloch sphere of phase recovery in a  $\frac{\pi}{2}$ - $\pi$  pulse sequence: (A) initial state; (B)  $\frac{\pi}{2}$ -pulse; (C) and (D) lost of phase; (E)  $\pi$ -pulse; (F) and (G) phase recovery.

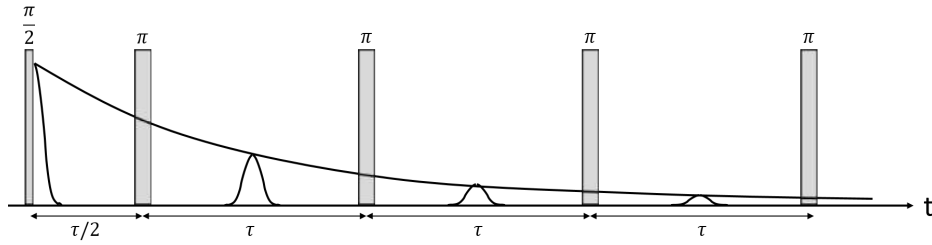


Figure 3.7.: Representation of CPMG pulse sequence. The  $T_2$  time is the mean lifetime of the transverse relaxation decay.

less than the first FID. If more than one  $\pi$ -pulse is applied, at equally spaced intervals of time  $\tau$ , we observe an echo train, as shown in Fig.(3.6). This pulse sequence is known as CPMG, and is a standard way to measure the transverse magnetization from which we can infer the  $T_2$ -distribution.

### 3.2. NMR on Porous Media

In this section we solve the Bloch-Torrey equations in a restricted domain. This is the problem of one single pore fully saturated with a fluid. The confined diffusion is an eigenvalue problem with boundary conditions, where the shape

of boundary defines the eigenvalues and the eigenvectors spectrum.

After the application of  $90^\circ$  RF pulse, the transverse magnetization in a static magnetic field is described by

$$D\nabla^2 m(\vec{r}, t) - \Gamma m(\vec{r}, t) = \frac{\partial m(\vec{r}, t)}{\partial t} \quad (3.23)$$

where  $D$  is the diffusion coefficient,  $m(\vec{r}, t)$  is the magnetization density and  $\Gamma$  is the bulk relaxation coefficient. The boundary condition associated to the surface of the pore, known as Robin condition [14], is:

$$\left( D \frac{\partial m(\vec{r}, t)}{\partial \hat{n}} + Km(\vec{r}, t) \right) \Big|_{surface} = 0 \quad (3.24)$$

where  $\hat{n}$  is a vector normal to the surface, and  $K$  is called *surface relaxivity coefficient*. The Neumann boundary condition  $\left( \frac{\partial m(\vec{r}, t)}{\partial \hat{n}} \Big|_{surface} = 0 \right)$  emerges from Robin boundary condition in the limit of  $D \gg Kl$ , where  $l$  is a characteristic length of pore size and the Dirichlet boundary condition  $(m(\vec{r}, t)|_{surface} = 0)$  applies when  $D \ll Kl$ . The Neumann and Dirichlet boundary conditions represent the fast and slow diffusion regime, respectively. The physical meaning of these two regimes is the strength of spins in the fluid coupling with spins of the solid matrix. In the slow diffusion regime (Dirichlet condition,  $D \ll Kl$ ), the spins in the fluid close to the surface have a larger strength coupling with the surface, where the spins have a random configuration of magnetization, and the magnetization will be null at the surface. In the fast diffusion regime (Neumann condition,  $D \gg Kl$ ), the coupling strength is weaker and  $m(\vec{r}, t)$  is not zero, but only its spatial derivative.

The initial condition of the magnetization density is simply:

$$m(\vec{r}, 0) = \frac{M_0}{V} \quad (3.25)$$

where  $M_0$  is the value of initial magnetization and  $V$  is the total volume of the pore. The diffusion coefficient for bulk water is  $D \approx 10^{-9}m/s$  and surface relaxivity is  $K \approx 10^{-6}m^2/s$ , for sandstones [100]. As we will see the relaxivity appears as a product with the pore radius,  $Kl$ , in the calculation of eigenvalues  $\zeta_n$  in  $T_2$  equation, so varying  $K$  is analogous to varying the radius.

The solution of Equation (3.23) can be written as a multiexponential sum [14]

$$m(\vec{r}, t) = \sum_{n=0}^{\infty} A_n F_n(\vec{r}) e^{-t/T_{2n}}, \quad (3.26)$$

where  $A_n$  are coefficients,  $F_n(\vec{r})$  are the eigenvectors, and  $T_{2n}$  is the  $n$ -th multiple transverse relaxation time, dependent on the dimensionless eigenvalue  $\zeta_n$ . Therefore, the multiexponential decay behavior is intrinsic to the solutions of the diffusion equation upon the boundary conditions specified in Eq. (3.24), even for one single pore. Replacing Eq.(3.26) into Eq.(3.23) one obtains:

$$\nabla^2 F_n(\vec{r}) = \left( \frac{\Gamma}{D} - \frac{1}{DT_{2n}} \right) F_n(\vec{r}). \quad (3.27)$$

The multiexponential solution reduces the problem to that of solving the boundary Equation (3.24) for a given geometry. Finally, to obtain the magnetization as a function of time,  $M(t)$ , it is necessary to integrate  $m(\vec{r}, t)$  over the volume domain. It can be shown [17] that the magnetization can be written as:

$$M(t) = M_0 \sum_{n=0}^{\infty} I_n e^{-t/T_{2n}}. \quad (3.28)$$

The  $I_n$  coefficients are normalised and can be calculated from volumetric integrals of eigenvectors in a pore space domain:

$$I_n = \frac{1}{V} \frac{[\int F_n(\vec{r}) d\tau]^2}{\int F_n^2(\vec{r}) d\tau}, \quad (3.29)$$

as well as the  $A_n$  coefficients:

$$A_n = \frac{M_0 \int F_n(\vec{r}) d\tau}{V \int F_n^2(\vec{r}) d\tau}. \quad (3.30)$$

It is insightful to apply the above results to a known geometry to obtain the eigenvalues spectrum, and consequently the  $T_2$  distribution for a single pore. We will discuss this problem for a spherical geometry, but it can be done for other geometries, as well [14], see Fig.(3.8). The statistical model that we want to approach is one for porous media built from spheres of different radii.

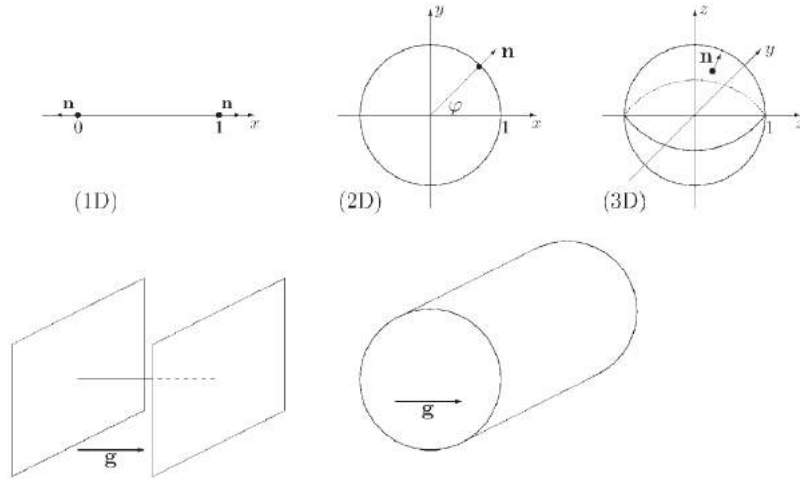


Figure 3.8.: Usual geometries to analytically solve diffusion equation with boundary conditions, and obtain a solution for transverse NMR relaxation [14].

### 3.2.1. Single spherical pore

We will consider one single spherical pore, which means that the boundary conditions will have spherical symmetry (Fig.3.9). This case is interesting because, whereas we deal with a three dimensional surface, the differential equation will be radial, and so it is a didactic example.

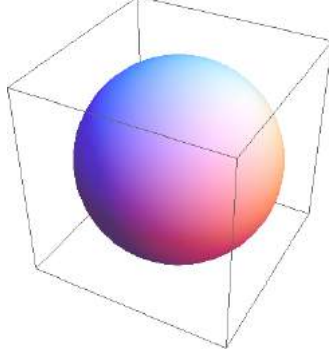


Figure 3.9.: Spherical geometry representation. This geometry has analytical solution for  $T_2$  relaxation. Considering a special sum of spherical pores is possible to predict a q-exponential decay for  $T_2$ .

The diffusion equation, Eq.(3.27), in spherical coordinates is

$$F_n''(r) + \frac{2}{r}F_n'(r) + \left(\frac{1}{T_{2n}D} - \frac{\Gamma}{D}\right)F_n(r) = 0. \quad (3.31)$$

The solutions for the eigenvectors are

$$F_n(r) = \frac{1}{r} \text{sen} \left( \frac{\zeta_n r}{l} \right), \quad (3.32)$$

where  $l$  is the radius of sphere and  $\zeta_n = l\sqrt{\frac{1}{T_{2n}D} - \frac{\Gamma}{D}}$  are the eigenvalues. The  $\zeta_n$  are calculated using the Robin boundary condition, Eq.(3.24), which leads to:

$$\cot(\zeta_n) = \left(1 - \frac{lK}{D}\right) \frac{1}{\zeta_n}. \quad (3.33)$$

The spectrum of  $T_{2n}$  as a function of eigenvalues  $\zeta_n$  are

$$T_{2n} = \frac{l^2}{D\zeta_n^2 + l^2\Gamma}. \quad (3.34)$$

The result of Eq.(3.34) was obtained for a sphere but the analytical solution of Eq.(3.23) and Eq.(3.24) for other geometries such as cubic or cylindrical, the formal result for  $T_2$  is the same as Eq.(3.34), the only difference being the

equation to calculate  $\zeta_n$ , that will no longer be Eq.(3.33). So the problem to find the  $T_2$  spectrum for one pore is reduced to solving an eigenvalue problem. The effects of surface relaxivity  $K$  are considered in  $\zeta_n$  equation. The  $T_2$  spectrum for one pore, or even  $T_2$  distribution in porous media are correlated with the pore size or pore size distribution by the function Eq.(3.34). In the asymptotic pore size regime ( $l \rightarrow \infty$ )  $T_2$  is equal the inverse of  $\Gamma$ , i.e. free diffusion.

The total magnetization is a sum of exponential functions Eq.(3.28), where each exponential are multiplied by a coefficient  $I_n$  given by Eq.(3.29). For the spherical pore the  $I_n$  coefficients are

$$I_n = \frac{12(\text{sen}\zeta_n - \zeta_n \text{cos}\zeta_n)^2}{\zeta_n^3(2\zeta_n - \text{sen}(2\zeta_n))}. \quad (3.35)$$

The magnetization solution is therefore:

$$M(t) = M_0 \sum_{n=0}^{\infty} I_n e^{-\left(\frac{D\zeta_n^2}{l^2} + \Gamma\right)t}. \quad (3.36)$$

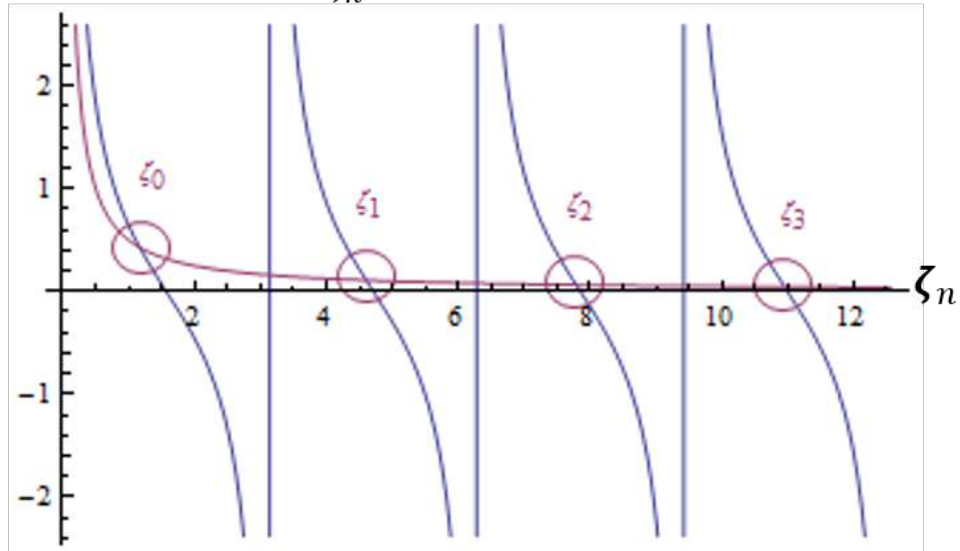
For typical values of parameters [70],  $D = 10^{-9}m/s$ ,  $K = 10^{-6}m^2/s$ ,  $l = 0.5mm$ , the eigenvalue set, numerically solved, Eq.(3.33), is  $\zeta = \{(\zeta_0 = 1.16); (\zeta_1 = 4.60); (\zeta_2 = 7.79); (\zeta_3 = 10.95); \dots\}$ . Considering  $\Gamma = 0$  the normalised magnetization decay with time given in  $ms$  will be:

$$\frac{M(t)}{M_0} = 0.996e^{-\frac{t}{184.02}} + 0.0034e^{-\frac{t}{11.79}} + 0.0004e^{-\frac{t}{4.12}} + 0.0001e^{-\frac{t}{2.08}} + \dots \quad (3.37)$$

Note that the first mode contributes with 99,6% for the total intensity.

It is instructive to analyse the modes intensities  $I_n$  as a function of the eigenvalues  $\zeta_n$ . If we choose the radius  $l = 1mm$ , the Equation (3.33), for the

$$\text{Cot}(\zeta_n); \left(1 + \frac{lK}{D}\right) \frac{1}{\zeta_n};$$



$$\text{Cot}(\zeta_n); \left(1 + \frac{lK}{D}\right) \frac{1}{\zeta_n};$$

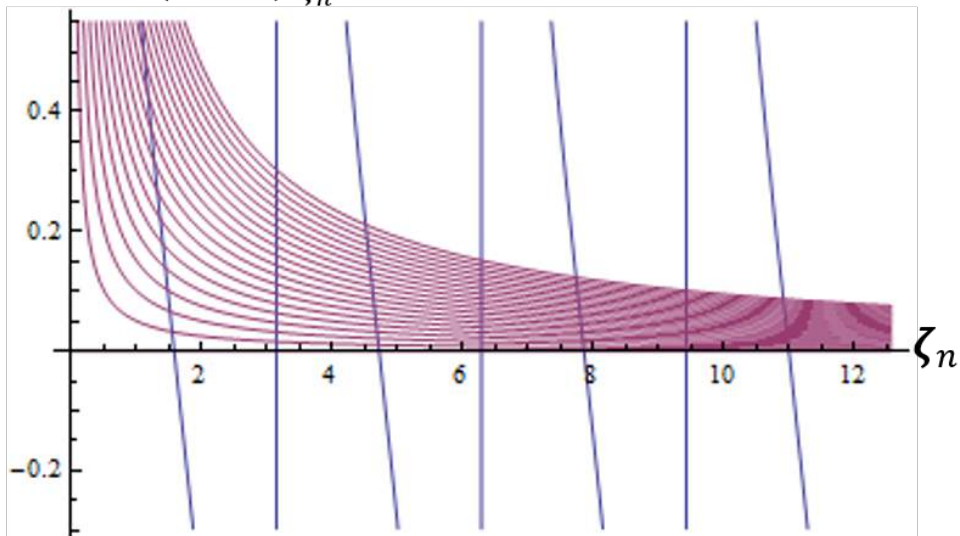


Figure 3.10.: The left figure shows the graphical solution for  $\zeta_n$  eigenvalues transcendental equation in spherical pores Eq.(3.33) for  $D = 10^{-9}m/s$ ,  $K = 10^{-6}m^2/s$  and  $l < 1mm$ . The right figure shows variations in curves intersection by change pore size  $l$ . The first eigenvalue will be always  $0 \leq \zeta_0 \leq \pi$ .

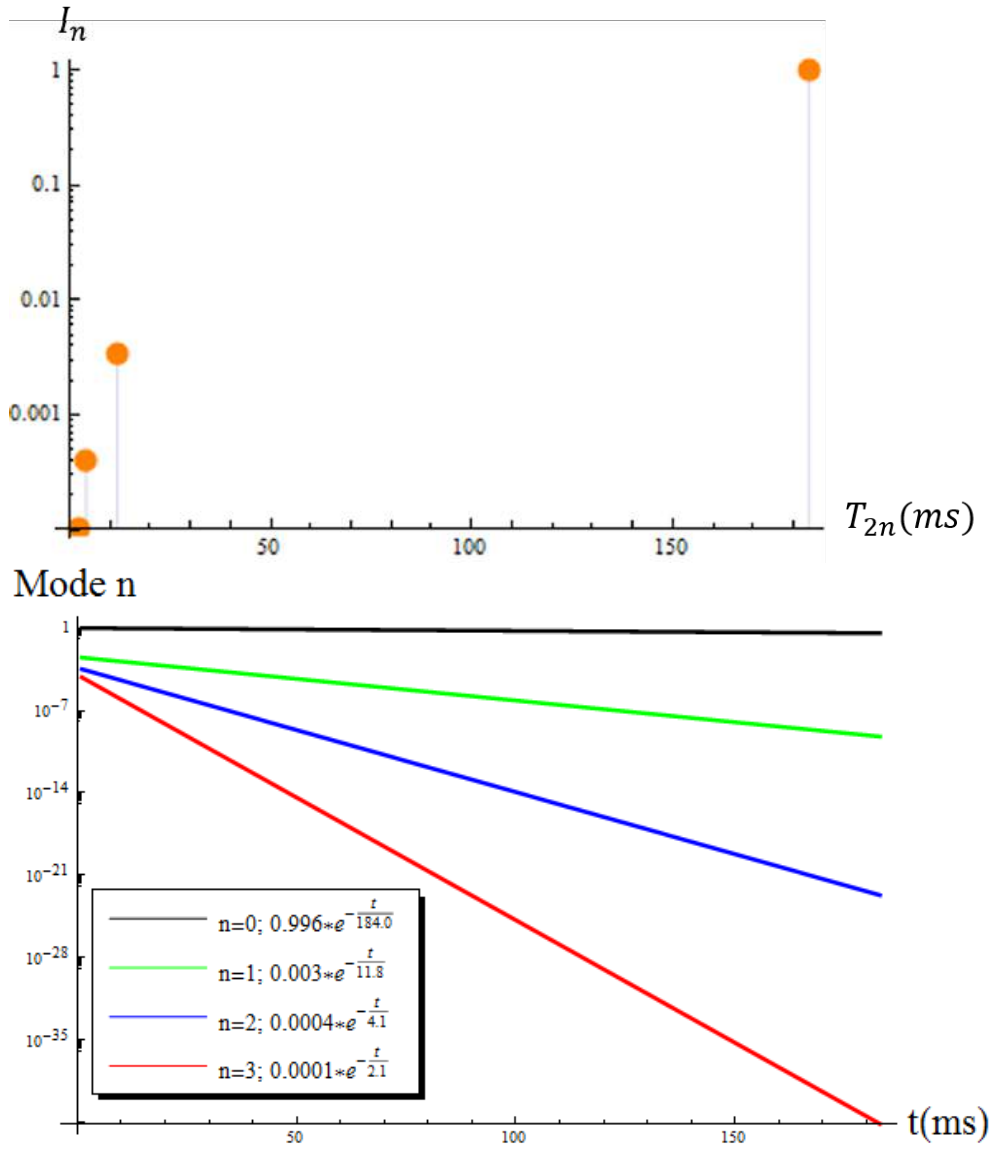


Figure 3.11.: The left figure shows the  $T_{2n}$  spectrum and the intensities modes  $I_n$  for a single spherical pore for  $D = 10^{-9}m/s$ ,  $K = 10^{-6}m^2/s$ ,  $l = 0.5mm$  and  $\Gamma = 0$ . The right figure shows the first four magnetization modes given by Eq.(3.37); the first one is the most important.

eigenvalue spectrum, will be no longer a transcendental equation:

$$\cot(\zeta_n) = \left(1 - \frac{lK}{D}\right) \frac{1}{\zeta_n} \quad (3.38)$$

$$\cot(\zeta_n) = \left(1 - \frac{10^{-3}10^{-6}}{10^{-9}}\right) \frac{1}{\zeta_n} \quad (3.39)$$

$$\cot(\zeta_n) = 0 \quad (3.40)$$

$$\zeta_n = (n + 1) \frac{\pi}{2}. \quad (3.41)$$

The first mode,  $n = 0$ , has eigenvalue  $\zeta_0 = \frac{\pi}{2}$ . In Fig. 3.12 are shown two graphics, the first one shows the intensities of modes  $I_n$  as a function of the variable  $\zeta$ , and the second one shows the variable  $\zeta$  is limited to  $\zeta = \frac{\pi}{2}$ . Note that with these values of  $D$  and  $K$ , any value of  $l$  less than 1mm implies  $\zeta_0 < \frac{\pi}{2}$ , see Fig.(3.11). From the analysis of the Fig.(3.12) it is possible to see that the first mode  $I_0$  is always larger than 0.986.

### 3.2.2. Two spherical pores

As we saw in the previous section, the solution to the decay of the magnetization in one single pore can be expressed in a multiexponential form, in which it appears an infinity and discrete set of eigenvalues. However, for typical values for the parameters, we found that the first order, that is, the first exponential in magnetization equation corresponds to more than 98% of the measured signal. Therefore, it is reasonable to assume that a pore of a given fixed radius size  $l$ , contributes with a single exponential decay to the total signal when we have a distribution of pore sizes. Before looking at the consequences of this approach, we will analyse a possible degeneracy of modes of different spheres, i.e., we will analyse if it is possible the second eigenvalue of one sphere to be comparable to the first eigenvalue of the other in a system with two spherical pores.

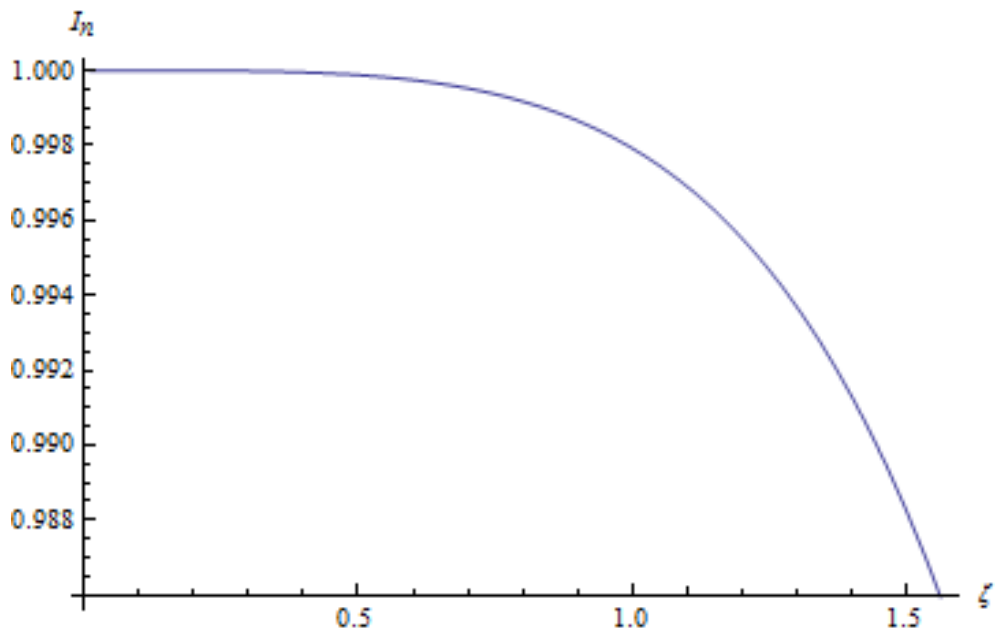
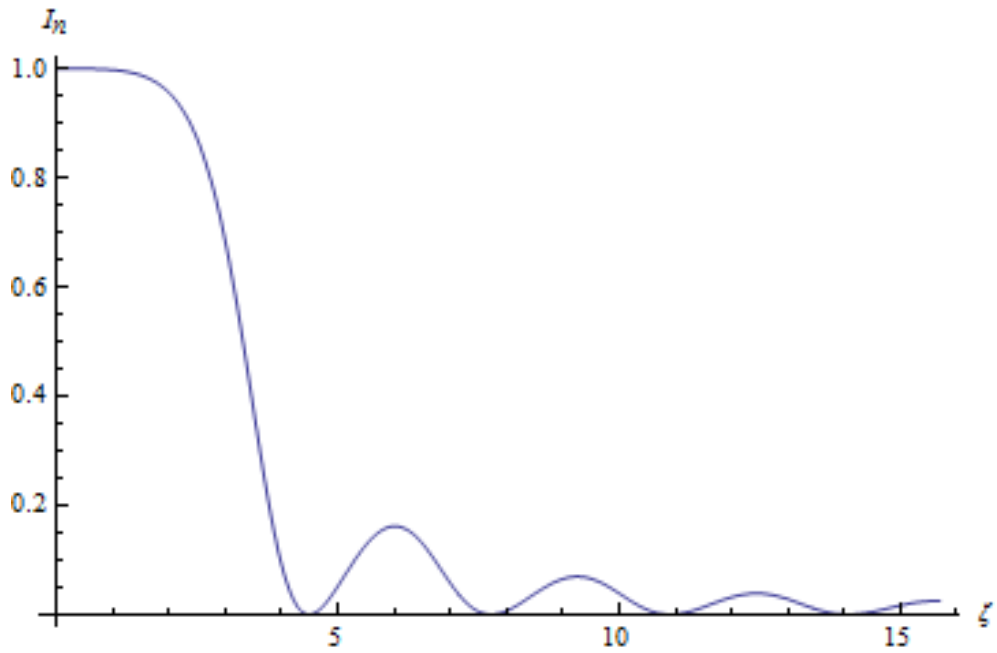


Figure 3.12.: Plots of the intensities  $I_n$ , Eq. (3.35) as function of  $\zeta_n$ . If the pore radius is  $l \leq 0.5mm$  the first mode is  $I_0 \geq 98.6\%$ .

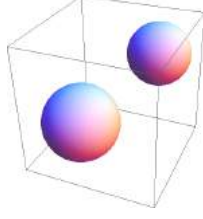


Figure 3.13.: Representation of two spherical pores with different radii with analytical solution for transverse relaxation. The total magnetization of this system will be a sum of the contribution from the two spheres.

Suppose now that we have two isolated pores, and that our measuring device will measure the signal from both (Fig.3.14). We saw in the previous section what is the response of the magnetization from each pore. The total response that our new system will be the weighted average by volume of each pore,  $v_i$ , we mean that

$$\frac{M(t)}{M_0} = \frac{1}{v_1 + v_2} (v_1 m_1(t) + v_2 m_2(t)). \quad (3.42)$$

The magnetization of each pore is given by Eq.(4.4),

$$\frac{M(t)}{M_0} = \frac{1}{v_1 + v_2} \left( v_1 \sum_{n=0}^{\infty} I_{n,1} e^{-t/T_{2n,1}} + v_2 \sum_{n=0}^{\infty} I_{n,2} e^{-t/T_{2n,2}} \right) \quad (3.43)$$

where the index after comma in  $I_{n,i}$  and  $T_{2n,i}$  is the pore index. If we change the volume  $v_i$  by the radius  $l_i$  and with the relation  $v_i = \frac{4}{3}\pi l_i^3$  we get:

$$\frac{M(t)}{M_0} = \frac{1}{l_1^3 + l_2^3} \left( l_1^3 \sum_{n=0}^{\infty} I_{n,1} e^{-t/T_{2n,1}} + l_2^3 \sum_{n=0}^{\infty} I_{n,2} e^{-t/T_{2n,2}} \right). \quad (3.44)$$

There should be values of radii  $l_1$  and  $l_2$  such that the second eigenvalue of the sphere 1 has the same value that the first eigenvalue of the pore 2. This degeneracy reveals a kind of ambiguity in the inversion of magnetization signal and therefore in the prediction of pore size distribution from  $T_2$  distribution. Let's take a concrete example. Using  $l_1 = 1mm$  and  $l_2 = 0.132mm$ , we obtain

the following the normalised magnetizations

$$m_1(t) = 0.985e^{-\frac{t}{405.28}} + \mathbf{0.012e^{-\frac{t}{45.03}}} + 0.0015e^{-\frac{t}{16.21}} + 0.0004e^{-\frac{t}{8.27}} + \dots \quad (3.45)$$

and

$$m_2(t) = \mathbf{0.9997e^{-\frac{t}{45.03}}} + 0.0002e^{-\frac{t}{0.847}} + 0.00002e^{-\frac{t}{0.145}} + \dots \quad (3.46)$$

Note that in the above equations, the second magnetization mode in Eq.(3.45) ( $0.012e^{-\frac{t}{45.03}}$ ) and the first mode in Eq.(3.46) ( $0.9997e^{-\frac{t}{45.03}}$ ), have the same value of  $T_2$ , i.e.,  $T_{21,1} = T_{20,2}$ , where the first index only indicates that we are working with the transverse relaxation  $T_2$ , the second index indicates the eigenvalue number, and the third index indicates the sphere number.

The total magnetization is given by Eq.(3.44),

$$\frac{M(t)}{M_0} = \frac{(0.985e^{-\frac{t}{405.28}} + 0.012e^{-\frac{t}{45.03}} + \dots) + (0.132)^3(0.9997e^{-\frac{t}{45.03}} + \dots)}{1 + (0.132)^3} \quad (3.47)$$

$$\frac{M(t)}{M_0} = 0.983e^{-\frac{t}{405.28}} + 0.014e^{-\frac{t}{45.03}} + 0.0015e^{-\frac{t}{16.21}} + \dots \quad (3.48)$$

If we compare Eq.(3.48), that describe the normalised transverse magnetization decay of a system with two spherical pores of radii  $l_1 = 1mm$  and  $l_2 = 0.132mm$  with Eq.(3.37), that describe one spherical pore of radius  $l = 0.5mm$ , the first magnetization mode, of each equation, correspond to 98.3% and 99.6% of the total signal measured, respectively. So in a  $T_2$  experiment the correlation between  $T_2$  times and pore sizes, and even the number of pores cannot be made directly. Of course these results are obtained without approximation and in the regime where diffusion and superficial relaxation are competing, i.e.,  $\frac{D}{l} \approx K$ . The fast diffusion regime ( $\frac{D}{l} \gg K$ ) corresponds to the Neumann boundary condition ( $\left. \frac{dF_n(r)}{dr} \right|_{r=l} = 0$ ) and the slow diffusion regime ( $\frac{D}{l} \ll K$ ) corresponds to the Dirichlet boundary condition ( $F_n(r=l) = 0$ ).

These limits will be discussed in the next section.

### 3.2.3. Spherical pore in slow and fast regimes

The Robin boundary condition, Eq.(3.24), is an intermediate case between Neumann and Dirichlet boundary conditions. The Neumann boundary conditions is the limit of Robin boundary condition when  $\frac{D}{l} \gg K$ , that correspond to the fast diffusion regime:

$$\lim_{\frac{D}{l} \gg K} \left( D \frac{\partial m(\vec{r}, t)}{\partial \hat{n}} + K m(\vec{r}, t) \right) \Big|_{surface} = D \frac{\partial m(\vec{r}, t)}{\partial \hat{n}} \Big|_{surface} = 0. \quad (3.49)$$

The Dirichlet boundary condition is the limit of Robin boundary condition when  $\frac{D}{l} \ll K$ , that correspond to the slow diffusion regime:

$$\lim_{\frac{D}{l} \ll K} \left( D \frac{\partial m(\vec{r}, t)}{\partial \hat{n}} + K m(\vec{r}, t) \right) \Big|_{surface} = K m(\vec{r}, t) \Big|_{surface} = 0. \quad (3.50)$$

The two limits represent, in spherical pores, conditions on the eigenvector  $F_n(r)$ . In the two cases the  $T_2$  spectrum can be represented formally by Eq.(3.34), rewritten here:

$$T_{2n} = \frac{l^2}{D\zeta_n^2 + l^2\Gamma}. \quad (3.51)$$

The difference is the equation to calculate the eigenvalues  $\zeta_n$  which is no longer Eq.(3.33). In the Neumann condition (fast diffusion) the eigenvalue equation is

$$\tan(\zeta_n) = \zeta_n, \quad (3.52)$$

and in the Dirichlet condition (slow diffusion) the eigenvalue equation is

$$\zeta_n = n\pi. \quad (3.53)$$

The first eigenvalue  $\zeta_0$  is a number between  $0 \leq \zeta \leq \pi$  and its exact value depends on the pore geometry and the surface relaxivity.

### 3.2.4. Cubic pore

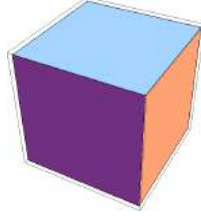


Figure 3.14.: Representation of cubic geometry. This kind of boundary for a pore surface has analytical solution for transverse NMR magnetization.

The solution of eigenvalue Equation (3.27) for the cubic symmetry is given by writing the Laplacian operator in the cartesian coordinates:

$$(\partial_x^2 + \partial_y^2 + \partial_z^2)F_{n_x n_y n_z}(x, y, z) + \left( \frac{1}{DT_2} - \frac{\Gamma}{D} \right) F_{n_x n_y n_z}(x, y, z) = 0. \quad (3.54)$$

The solution of Eq.(3.54) will depend of boundary conditions. In the fast diffusion regime ( $\frac{D}{l} \gg K$ ), or Neumann boundary condition ( $\frac{\partial}{\partial \vec{n}} F_{n_x n_y n_z}(x, y, z)|_{surface} = 0$ ), the solution will be:

$$F_{n_x n_y n_z}(x, y, z) = \cos\left(\frac{n_x \pi}{l} x\right) \cos\left(\frac{n_y \pi}{l} y\right) \cos\left(\frac{n_z \pi}{l} z\right), \quad (3.55)$$

where  $l$  is the cubic side size. The eigenvalue spectrum is

$$\zeta_{n_x n_y n_z}^2 = \pi^2(n_x^2 + n_y^2 + n_z^2) \quad (3.56)$$

In the slow diffusion regime ( $\frac{D}{l} \ll K$ ), or Dirichlet boundary condition

$\left( F_{n_x n_y n_z}(x, y, z) \Big|_{surface} = 0 \right)$ , the solution will be:

$$F_{n_x n_y n_z}(x, y, z) = \sin\left(\frac{n_x \pi}{l} x\right) \sin\left(\frac{n_y \pi}{l} y\right) \sin\left(\frac{n_z \pi}{l} z\right), \quad (3.57)$$

where  $l$  is the cubic side size. The eigenvalue spectrum is

$$\zeta_{n_x n_y n_z}^2 = \pi^2(n_x^2 + n_y^2 + n_z^2). \quad (3.58)$$

In the two cases the  $T_2$  spectrum is:

$$T_2 = \frac{l^2}{D\pi^2(n_x^2 + n_y^2 + n_z^2) + l^2\Gamma} \quad (3.59)$$

Observe that Eq.(3.59) has the same form as Eq.(3.34).

The solution for eigenvectors  $F_{n_x n_y n_z}(x, y, z)$  with Robin boundary conditions is a linear combination of sines and cosines. The eigenvalues will be:

$$\cot(\zeta_{n_i}) = \frac{D\zeta_{n_i} - lK}{D\zeta_{n_i} + lK}, \quad (3.60)$$

where  $i = (x, y, z)$  and the  $\zeta_{n_x n_y n_z}^2 = \zeta_x^2 + \zeta_y^2 + \zeta_z^2$ . The  $T_2$  spectrum is given by Eq.(3.34).

### 3.2.5. Bimodal distribution of spherical pores

Let us now consider a bimodal distribution of spherical pores (Fig.3.15). Consider a sphere of radius  $l_1$  and  $n$  spheres of radius  $l_2$ , the magnetization is

$$\frac{M(t)}{M_0} = \frac{1}{l_1^3 + nl_2^3} \left( l_1^3 \sum_{n=0}^{\infty} I_{n,1} e^{-t/T_{2n,1}} + nl_2^3 \sum_{n=0}^{\infty} I_{n,2} e^{-t/T_{2n,2}} \right). \quad (3.61)$$

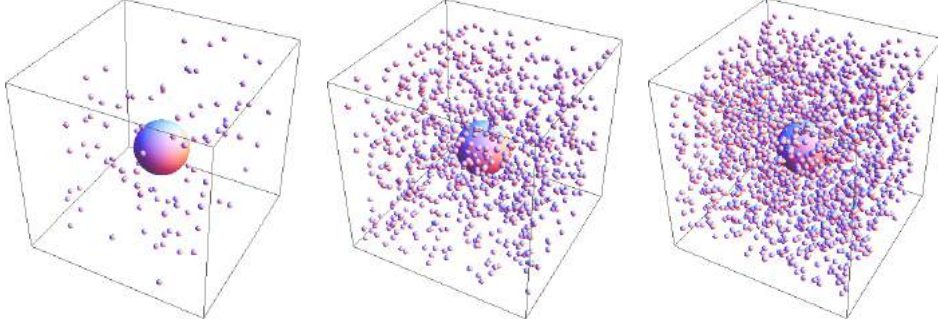


Figure 3.15.: Representation of a system with one big pore and many small pores. Depending of the number of small pores, the relaxation can be dominated by them.

With the approximation that only the first mode contributes to the magnetization decay, the solution can be written as

$$\frac{M(t)}{M_0} \approx \frac{1}{a_1^3 + na_2^3} \left( a_1^3 I_{0,1} e^{-t/T_{20,1}} + na_2^3 I_{0,2} e^{-t/T_{20,2}} \right). \quad (3.62)$$

If we chose  $D = 10^{-9} m^2/s$ ,  $K = 10^{-6} m/s$ ,  $\Gamma = 0$ ,  $l_1 = 1mm$  and  $l_2 = 0.132mm$ , is possible to write the transverse magnetization function of the number of small pores  $n$ :

$$\frac{M(t)}{M_0} \approx \frac{1}{1 + 0.002n} \left( 0.98 \times e^{-\frac{t}{405.28}} + (0.012 + 0.002n) \times e^{-\frac{t}{45.03}} \right). \quad (3.63)$$

Figure 3.16 shows the behavior of magnetization,  $T_2$  and pore radius distributions when the small pore number  $n$  vary about three orders of magnitude.

### 3.3. NMR Petrophysics

The NMR relaxation measurements of rocks with fluid content can yield information about porosity, pore-size distribution, bound water and permeability. It has been observed that fluid in porous media exhibit transverse and longitudinal relaxation faster than their bulk value (Figure 3.17). Observe that in

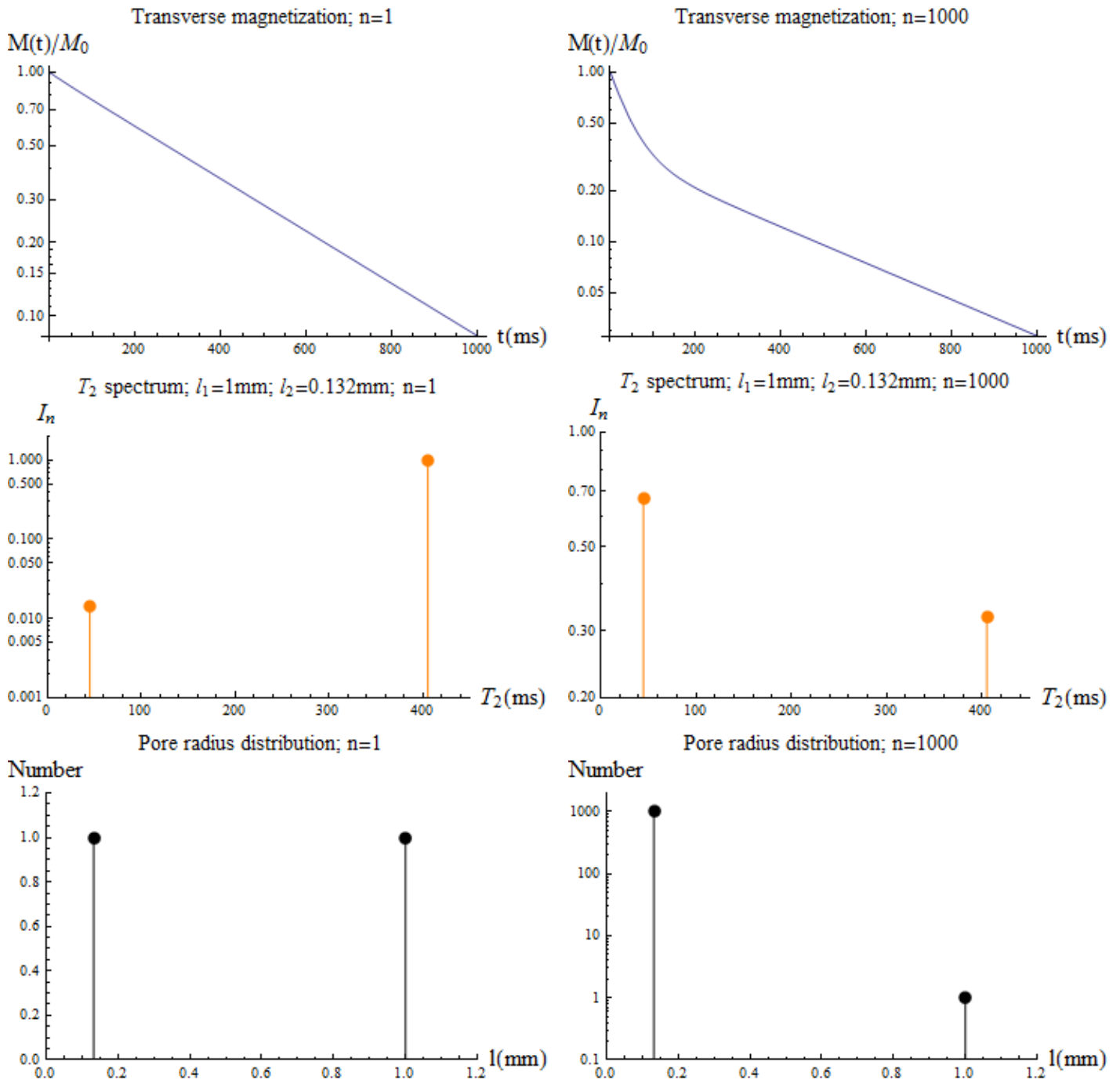


Figure 3.16.: The three figures on the left show the behavior of the magnetization,  $T_2$  and pore radius distributions for  $n = 1$ . The three figures on the right show the behavior of the magnetization,  $T_2$  and pore radius distribution for  $n = 1000$ . It is necessary three orders of magnitude in the number of small pores, relative to the big pore, for fast relaxation to be evident in magnetization signal and consequently in  $T_2$  distribution.

the second graphics of Figure 3.17, the oil doesn't change their time relaxation if it is in sandstone or in bulk form. The petrophysical model explains this result by the interaction of fluid with pore walls. If the rock has a residual water saturation and is saturated by oil, the interaction of this oil with the pore walls are not present and so the time relaxation are not affected.

The petrophysical model for relaxation is based on three mechanisms: *i*) the surface relaxation; *ii*) the bulk relaxation; and *iii*) relaxation by diffusion in a gradient field, (Fig. 3.18). For the transverse relaxation  $T_2$  all the three mechanisms are present, and the longitudinal relaxation is not affected by relaxation due diffusion in a gradient field. The equations are:

$$\frac{1}{T_2} = \frac{1}{T_{2S}} + \frac{1}{T_{2B}} + \frac{1}{T_{2DG}} \quad (3.64)$$

and

$$\frac{1}{T_1} = \frac{1}{T_{1S}} + \frac{1}{T_{1B}}. \quad (3.65)$$

The surface relaxation is due the interaction of the spin fluid with pore walls. The paramagnetic ions present in pore surface cause a faster relaxation of spin fluid. All the molecular characteristics of pore surface are modelled by the relaxivity surface  $K$  term, that describes the capacity of the surface to cause relaxation. The surface relaxation time is related to the surface-volume ratio:

$$\frac{1}{T_S} = K \frac{S}{V}, \quad (3.66)$$

where the  $T_S$  time is either the transverse or longitudinal time,  $S$  is the pore surface area and  $V$  is the pore volume. Essentially, the ratio  $V/S$  has dimension of size, so when the term of surface relaxation is the most important in relaxation process, the  $T_2$  or  $T_1$  time is linear with pore size.

The time for a particle to diffuse across the pore is  $T_d = l^2/D$ . The fast diffusion regime is given when  $T_d \ll T_S$  and in this regime, the  $T_S$  is the most

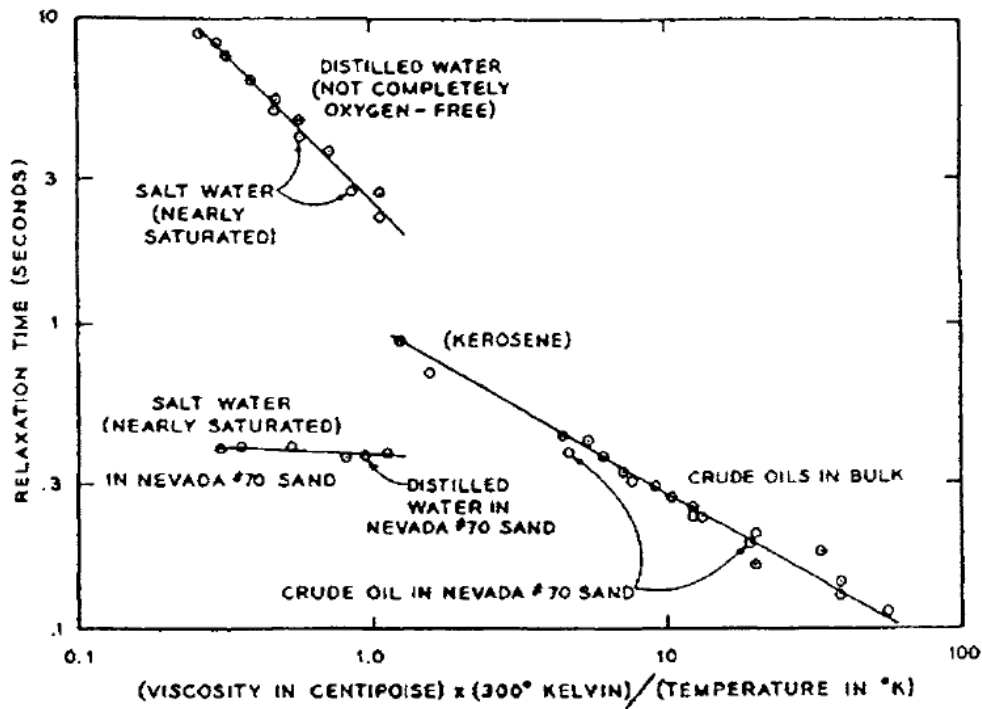
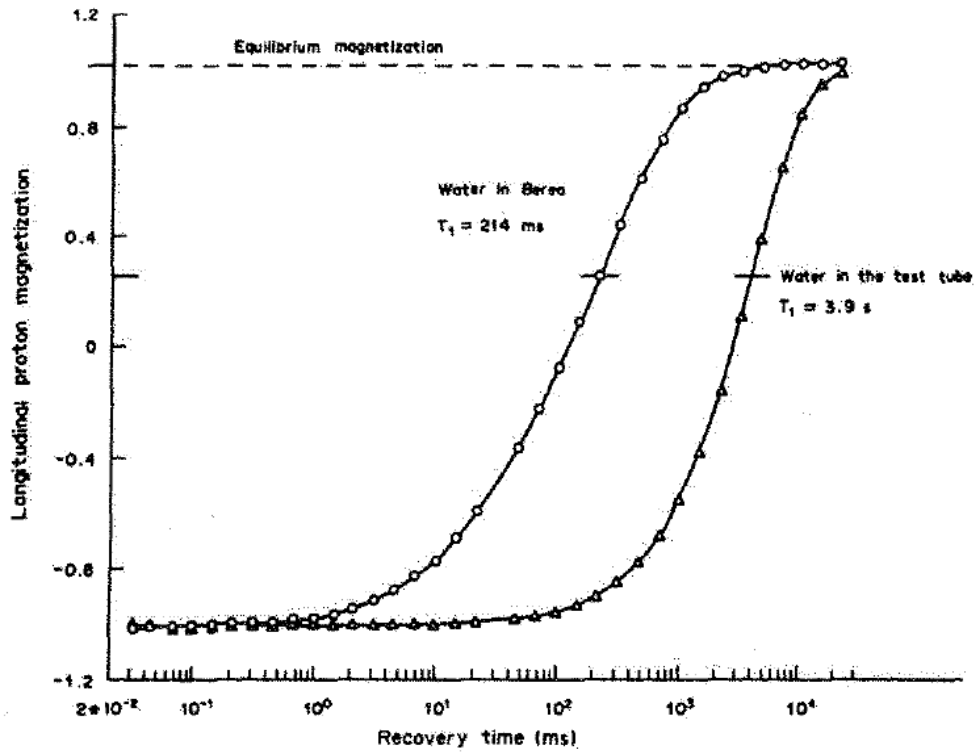


Figure 3.17.: The figure on the top is from Kenyon [15] and shows the longitudinal NMR data to extract  $T_1$  time. When water is in the Berea sandstone the  $T_1$  value is 214ms and their bulk value is 3.9s. The second figure [16] shows relaxation time as a function of the ratio viscosity/temperature. When water is present in sandstone the relaxation time is smaller.

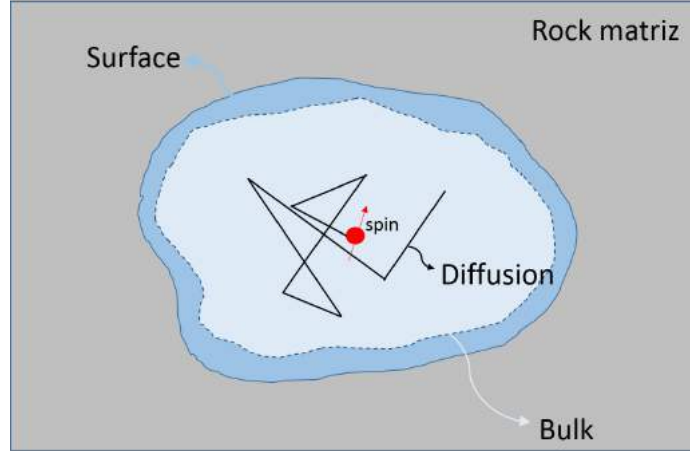


Figure 3.18.: Schematic representation of diffusive spin inside a pore. The relaxation is due three mechanisms, surface, bulk and diffusion (see text).

important mechanism of relaxation and so the time relaxation is linear with pore size. The fast diffusion regime is:

$$\frac{T_d}{T_S} = \frac{l^2/D}{l/K} = \frac{lK}{D} \ll 1. \quad (3.67)$$

The relaxation time decay for one pore is associated to one single exponential in the fast diffusion regime in the NMR petrophysical model. Because of this, the porous media can be modelled by a sum of exponentials, where each pore contribute with one single exponential:

$$M(T) = \sum_i^{N_{pore}} a_i e^{-\frac{t}{T_i}}, \quad (3.68)$$

where  $a_i$  is a number proportional to the total number of excited spins in each pore. Observe that the NMR petrophysical model has no considerations about statistics of pores. With this model the problem to find the relaxation time distribution is given by the inversion of the data decay to find the exponential modes that explain the data. In the next section we will discuss how to invert

the data with a regularization procedure.

### 3.3.1. The inversion of $T_2$ decay

The inversion of NMR transverse relaxation data from porous media is an ill-posed problem [101] in which noise can severely affect the prediction of the transverse relaxation time,  $T_2$ , distribution. The standard way to give a solution to an ill-posed problem is introduce some kind of regularization [102]. When the data is too noisy, the regularization parameter,  $\alpha$ , will be large and the solution can be far from the initial problem proposed. To minimize the effects of noise, high-field NMR experiments can be applied in order to validate new models, subsequently applied to noisy low-field experiments. Discussion about the characteristics of high- vs. low-field NMR experiments in porous media can be found in references [103,104].

We propose a method to describe NMR transverse relaxation based on the superstatistics of Beck-Cohen [74]. Different from standard inversion methods in which single exponentials and regularization parameters priori fix  $T_2$  values to calculate numerically the coefficients of the expansion, our method assumes a distribution for  $T_2$  given by an analytical function, and a least-square fit yields the statistical parameters. The main advantage of the method is to eliminate common numerical flaws, and to yield analytical function for  $T_2$  distributions, from which the fluid contents and petrophysical properties can be easily obtained.

The multiexponential is a non-linear function and, given a set of data  $d_i$ , the best solution is the set of values  $(T_{2i}, a_i)$  that minimize the function:

$$\left| \sum_{j=1}^{Ndata} \left( \sum_{i=1}^{Nexp} a_i e^{-\frac{t_j}{T_{2i}}} - d_j \right) \right|^2, \quad (3.69)$$

where  $Ndata$  is the experimental sampling size,  $Nexp$  is the number of expo-

nentials chosen and the set  $(T_{2i}, a_i)$  is the  $T_2$  distribution. In general, company services of NMR well log provide data with  $Nexp \geq 32$  and NMR petrophysical laboratories generally uses  $Nexp \geq 100$ . Analysis about the number of exponentials can be found in literature [105]. With this large value for  $Nexp$  it is impossible to find the minimum of Eq. (3.69), and at this point a regularization procedure is introduced to the least-square problem:

$$\min \left\{ \left| \sum_{j=1}^{Ndata} \left( \sum_{i=1}^{Nexp} a_i e^{-\frac{t_j}{T_{2i}}} - d_j \right) \right|^2 + \alpha \sum_{i=1}^{Nexp} |a_i|^2 \right\}, \quad (3.70)$$

where the second term is the Tikhonov zero order regularization. Now the set of non-linear variables  $T_{2i}$  is fixed and log spaced, the least-square problem is linear and it consists of finding the  $a_i$  set values for a given  $\alpha$ . The regularization stabilizes the numerical problem and is based only in mathematical assumptions. Our proposal is to use a non-linear least-square fit in which each parameter involved has a physical interpretation, see Section(4.1).

## 4. Results

### 4.1. $q$ -Exponential model for magnetization decay

In the Section 3.2.1 we analysed the solution of diffusion equation with boundary conditions for one single sphere. The solution for parallel plates and cylinder can be found in [14]. It is possible to show that, independently of the geometry, the first eigenvalue  $\zeta_0$  will be the most relevant when the fast diffusion regime is satisfied ( $D \gg lK$ ). Let us consider the fast diffusion condition and analyse a statistical model with this consideration.

For three different kinds of geometries given by cartesian, cylindrical and spherical coordinates, is possible to solve analytically the diffusion equation with boundary conditions. The dependence of  $T_2$  time with pore size is given by Equation (3.34), rewritten here:

$$T_{2n} = \frac{l^2}{D\zeta_n + l^2\Gamma}. \quad (4.1)$$

If we consider that only the first eigenvalue is needed to describe  $T_2$  the NMR transverse relaxation, will be:

$$T_2 = \frac{l^2}{D\zeta_0 + l^2\Gamma}. \quad (4.2)$$

This result is not new and can be found in Brownstein and Tarr 1979 [14]. The novelty in this thesis is a construction of a statistical model using analytical

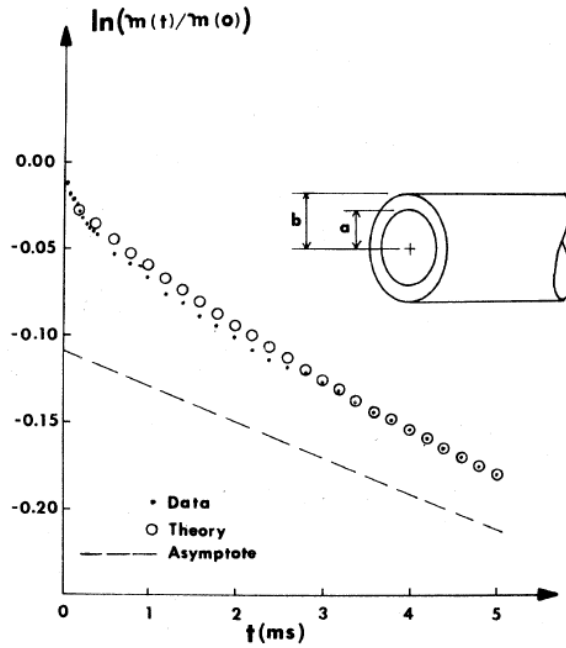


Figure 4.1.: Geometrical model of Brownstein and Tarr 1979 [14] applied to explain data of rat gastronemius muscle NMR decay. An annular cylinder geometry is assumed and the ratio of radius  $R = b/a$  is tuned to give the best fit.

results of [14].

In Brownstein and Tarr 1979 paper [14], they search for the best geometry to explain data from NMR decay of rat gastronemius muscle and found that the best model is an annular cylinder with one free parameter  $R = b/a$ , where  $b$  and  $a$  are the outer and inner cylinder radius, (Figure 4.1). Other conclusion is that the system is in slow diffusion regime, because they found  $\frac{aK}{D} \approx 4.9$  for  $R = 3$ ,  $a$  being related with  $l$  pore size parameter, as previously discussed.

The work of Tangyan *et.al.* 2012 [17] uses a sphere-cylinder model to explain data of NMR decay from porous rock saturated by oil and water and the result is a model with three exponential functions to describe fine, middle and macro pores, (Figure 4.2).

We advocate that it is not necessary to know exactly the shape of pore geometry, but if we consider that each pore has a random geometry and con-

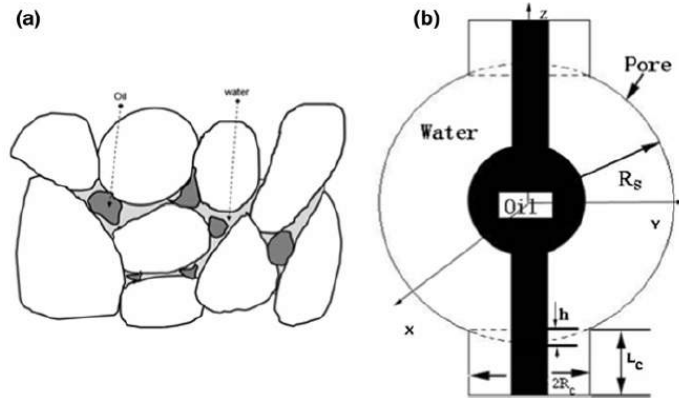


Figure 4.2.: Geometrical model of Tangyan *et. al.* 2012 [17] to describe porous rock saturated by oil and water.

sequently a random  $\zeta_0$ , the time of magnetization decay will be a large sum of all randomic  $T_2$  time of each pore. All the complication about geometry and even the surface relaxivity will be given by one value of the first eigenvalue  $\zeta_0$  that is a number between  $0 \leq \zeta_0 \leq \pi$ . If the assumption of the fast diffusion regime is not valid, the further eigenvalues can be considered, and the model refined. In this thesis we will construct the most simple statistical model and will apply it to successfully explain NMR data decay in porous media.

In order to construct a statistical model for NMR data decay we will suppose, at first, that only the first eigenvalue contribute to  $T_2$ . Suppose that Eq.(4.2) describes  $T_2$  for one single pore given, independently of its geometry. The magnetization such a this pore is:

$$\frac{m(t)}{m_0} = I_0 e^{-\beta_0 t}. \quad (4.3)$$

where  $\beta_0 = \frac{D\zeta_0}{l^2} + \Gamma$ , the zero index refers to the first eigenvalue. For a discrete distribution of pores, the total magnetization will be:

$$\frac{M(t)}{M_0} = \sum_{i=1}^{N_{pore}} I_{0i} e^{-\beta_{0i} t}, \quad (4.4)$$

where the  $i$  index refers to each pore in the sample. Observe that the set  $(I_{0j}, T_{2i})$ , where  $T_{2i} = \beta_{0j}^{-1}$ , defines a discrete  $T_2$  distribution, where the fast relaxation given by small values of  $T_2$  represent small pores and the slow relaxation the big pores.

We can generalize the result of Eq.(4.4) for a continuous distribution of pores:

$$\frac{M(t)}{M_0} = \int_0^\infty d\beta f(\beta) e^{-\beta t}, \quad (4.5)$$

where  $f(\beta)$  is a probability density function. Each pore of the sample will contribute with a value of  $\beta$ . As we saw in Chapter 2, the  $\beta$  value can be consider a sum of squared Gaussian random variables

$$\beta = \sum_j^\nu X_j^2, \quad (4.6)$$

$\beta$  must be positive because it is the inverse of  $T_2$  time. Also, as we see in Chapter 2, the distribution of  $\beta$  variable given by Eq.(4.6) will be  $\chi^2$ -distribution given by Eq.(2.6). The total magnetization will be therefore:

$$\frac{M(t)}{M_0} = \int_0^\infty d\beta \chi_{q, \beta_0}^2(\beta) e^{-\beta t}, \quad (4.7)$$

where  $\beta_0 = \langle \beta \rangle$  is the mean of distribution. The result of magnetization is a  $q$ -exponential

$$M(t) = M_0 e_q^{-\beta_0 t}. \quad (4.8)$$

Equation (4.8) is an analytical model for magnetization decay from NMR experiments, based on statistical assumption that the  $\beta$  variable is a sum of squared Gaussian random variables, or in other words, the  $\beta = \frac{1}{T_2}$  distribution for porous media, the  $f(\beta)$ , is a  $\chi^2$ -distribution.

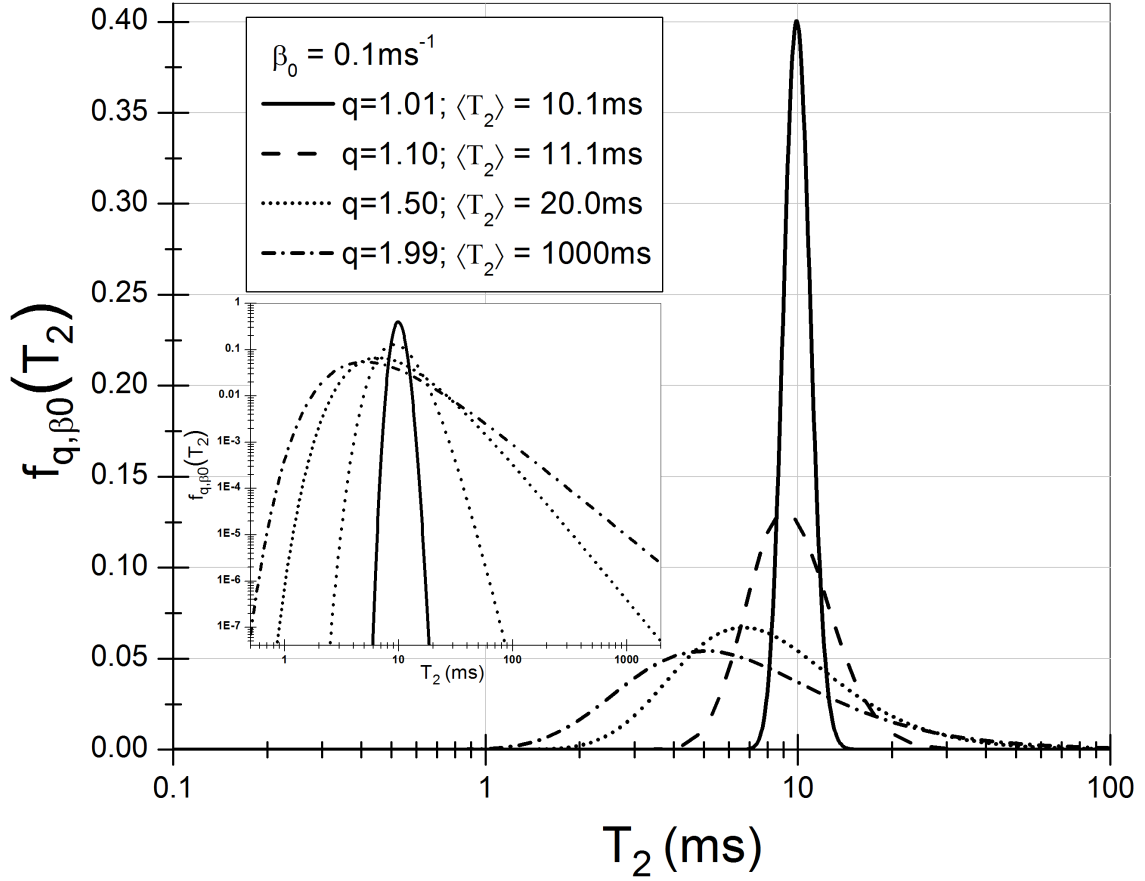


Figure 4.3.: Analytical function for  $T_2$  distribution used in NMR experiments on porous media. In the limit of  $q \rightarrow 1$ ,  $f_{q, \beta_0}(T_2)$  tends to a distribution highly concentrated around in  $\langle T_2 \rangle$ , and recovers one single exponential for the magnetization. The inset a log-log plot showing the tail behavior of distributions.

The  $q$  parameter as a function of  $T_2$  is

$$q = 2 - \frac{1}{\left\langle \frac{1}{T_2} \right\rangle \langle T_2 \rangle}, \quad (4.9)$$

and the  $T_2$  distribution is

$$f_{q,\beta_0}(T_2) = \frac{\left(\frac{1}{(q-1)\beta_0}\right)^{\frac{1}{q-1}}}{\Gamma\left(\frac{1}{q-1}\right)} T_2^{\frac{q}{1-q}} e^{-\frac{1}{(q-1)\beta_0} \frac{1}{T_2}}. \quad (4.10)$$

In the limit  $q \rightarrow 1$ , the analytical distribution for  $T_2$  Eq.(4.10) tends to a Dirac delta-like distribution, as can be seen qualitatively in Figure (4.3). The relation between the chi-square distribution of  $\beta$ s and  $T_2$  distribution is

$$f_{q,\beta_0}(T_2) = \frac{1}{T_2^2} \chi_{q,\beta_0}^2 \left( \frac{1}{T_2} \right), \quad (4.11)$$

where  $\beta = \frac{1}{T_2}$  and  $\beta_0 = \langle \frac{1}{T_2} \rangle$ . The area under  $f_{q,\beta_0}(T_2)$  represents the total amount of fluid in the porous media. In order to compare curves from different models, we must normalize the curves to the same area. In what follows it is important to observe that the higher the value of  $\langle T_2 \rangle$ , the smaller will appear the peak of  $f_{q,\beta_0}(T_2)$ . It is important to keep in mind, however, that the curves have all the same normalised area, as exemplified in Fig. (4.4).

## 4.2. NMR High-field experiments

The petrophysics NMR data has, in general, a large amount of noise, in particular log well data, (Fig 4.5). The presence of large noise in data can makes the inversion problem unstable and, to circumvent this problem, a large value of regularization is needed. For testing a new model it is specially important, if possible, that the experimental data to have a minimum amount of noise and samples need to be well behaved. On this direction, we performed

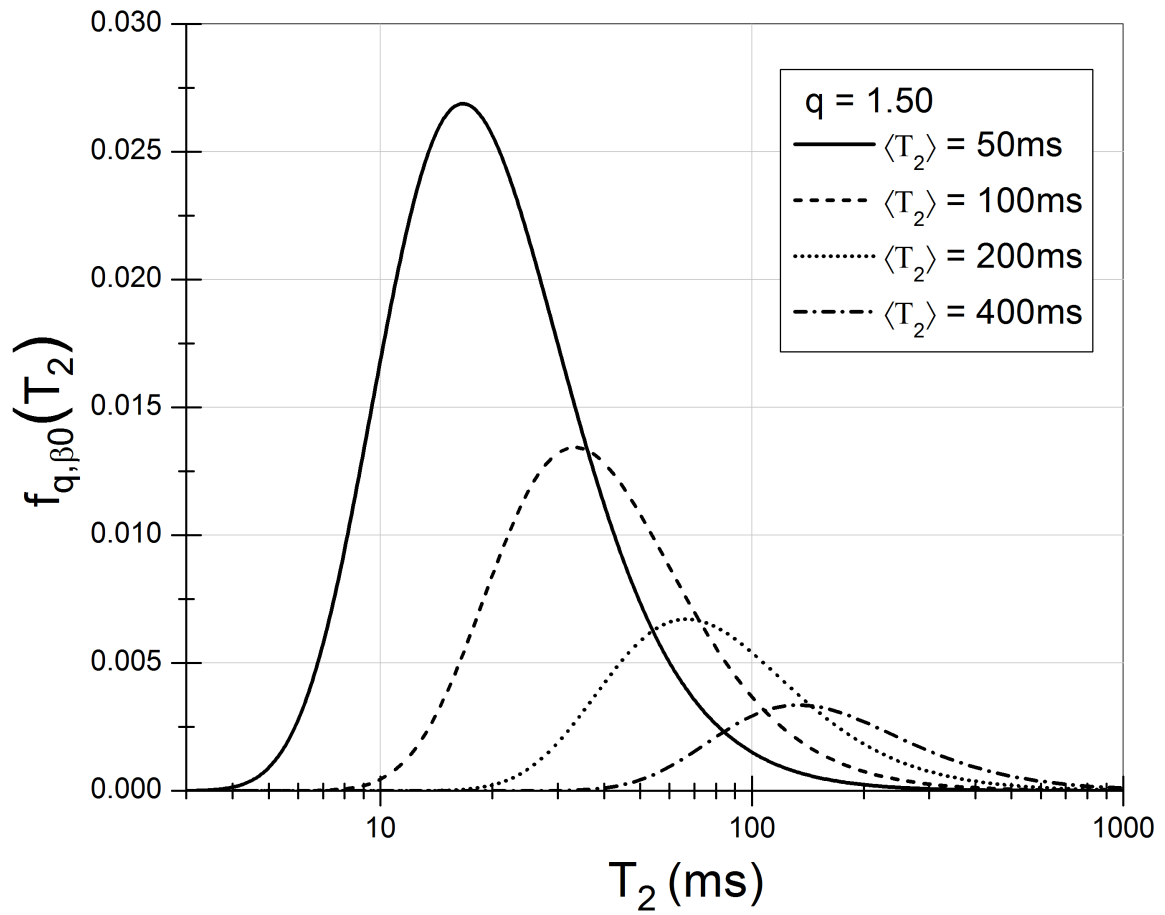


Figure 4.4.: The area under each curve in the graphics is equal to one, and the  $q$  parameter is chosen  $q = 1.5$  for this example. Because the logarithm scale, the peak of the distribution becomes smaller as  $\langle T_2 \rangle$  increases.

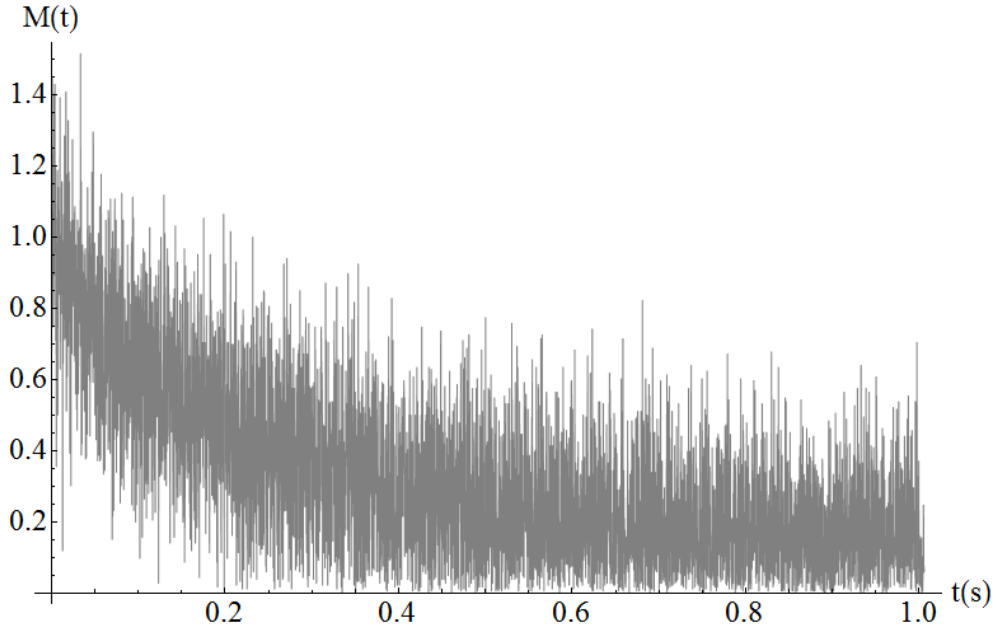


Figure 4.5.: Example of typical NMR log well data with a large amount of noise.

high-field NMR experiments on a VARIAN Shielded 500 MHz spectrometer at the Brazilian Center for Research in Physics. The CPMG sequence was applied to measure transverse relaxation times decay of  $^1H$  in water imbibed on microspheres glass with different granulometries ranges.

We used two sets of glass microsphere with five different ranges of two different companies, the Multiesferas and Cospheric, and three samples of outcrop rocks. The Multiesferas set is of soda lime glass and the spheres radii are in the following ranges: A (425-600 $\mu m$ ); B (250-425 $\mu m$ ); C (106-212 $\mu m$ ); D (75-125 $\mu m$ ); and E (45-90 $\mu m$ ). The Cospheric's microspheres are in the following ranges: A (710-850 $\mu m$ ); B (425-500 $\mu m$ ); C (212-250 $\mu m$ ); D (106-125 $\mu m$ ); and E (45-53 $\mu m$ ); see the Fig. 4.6. The outcrops rocks used were the Berea and the Buff Berea sandstone, and the Indiana Limestone, (Fig.4.7).

The samples from the Microesfera set can be view in Fig. 4.8. We have used a NMR probe of 10mm in the experiment, which means that we have a tube of 10mm of external diameter to pack the glass microspheres. In Fig. 4.8

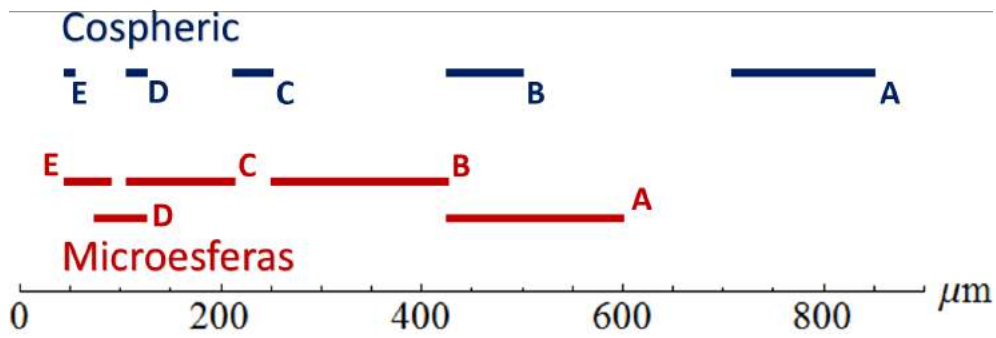


Figure 4.6.: The colored bars represent the diameter size range of ten samples of soda lime glass microsphere from two different companies. The Cospheric's microspheres have the follow ranges: A (710-850 $\mu\text{m}$ ); B (425-500 $\mu\text{m}$ ); C (212-250 $\mu\text{m}$ ); D (106-125 $\mu\text{m}$ ); and E (45-53 $\mu\text{m}$ ); and the Microesferas sample have the follow ranges: A (425-600 $\mu\text{m}$ ); B (250-425 $\mu\text{m}$ ); C (106-212 $\mu\text{m}$ ); D (75-125 $\mu\text{m}$ ); and E (45-90 $\mu\text{m}$ ).



Figure 4.7.: Outcrop rocks used in high-field NMR experiments. From left to right is the Buff Berea Sandstone, Berea Sandstone and Indiana Limestone.

the left tube contains the finest grains (45-90 $\mu m$ ), and in crescent order the last one at right has the largest grains (425-600 $\mu m$ ). Figs. 4.8 and 4.9 show a x-ray microtomography ( $\mu CT$ ), made in one of the samples. The  $\mu CT$  image was performed in PETROBRAS/CENPES  $\mu CT$  lab.

#### 4.2.1. Microesferas A: 425-600 $\mu m$ range diameter

In order to compare the different models, in this case the multiexponential and the q-exponential models, it is necessary to analyse the values of the regularization parameter  $\alpha$  used in the multiexponential model. There are many methods and discussions about how to choose the regularization parameter [101,106]. For the glass microspheres pack of Microesferas A, the result of the  $\alpha$  parameter value on the  $T_2$  distribution in the multiexponential model can be seen in Fig.4.10. Observe that when the  $\alpha$  parameter is decreasing, the  $T_2$  distribution tends to spike the distributions, and the fast relaxation domain becomes more pronounced.

On the other hand, the fitting model of three q-exponentials yields

$$M(t) = 89336.7 \times e_{1.39}^{-\frac{t}{62.9}} + 276036.0 \times e_{1.15}^{-\frac{t}{412.3}} + 29979.2 \times e_{1.16}^{-\frac{t}{1695.3}}, \quad (4.12)$$

or in terms of initial magnetization:

$$\frac{M(t)}{M_0} = 0.226 \times e_{1.39}^{-\frac{t}{62.9}} + 0.698 \times e_{1.15}^{-\frac{t}{412.3}} + 0.076 \times e_{1.16}^{-\frac{t}{1695.3}}. \quad (4.13)$$

The above result means that the magnetization decay is composed by three q-exponential modes. The first, and fastest, contributes with 22.6% of signal, and has  $q_{fast} = 1.39$  and  $\beta_0^{-1} = 62.9ms$ . The second mode contributes with 69.8%,  $q_{medium} = 1.15$  and  $\beta_0^{-1} = 412.3ms$ . The third mode has 7.6%,  $q_{slow} = 1.16$  and  $\beta_0^{-1} = 1695.3ms$ . The error calculated from Eq.(4.14) and associated to the fit models are  $Error_{\alpha=0.1} = 0.002$ ,  $Error_{\alpha=1} = 0.01$  and  $Error_{q-exp} =$

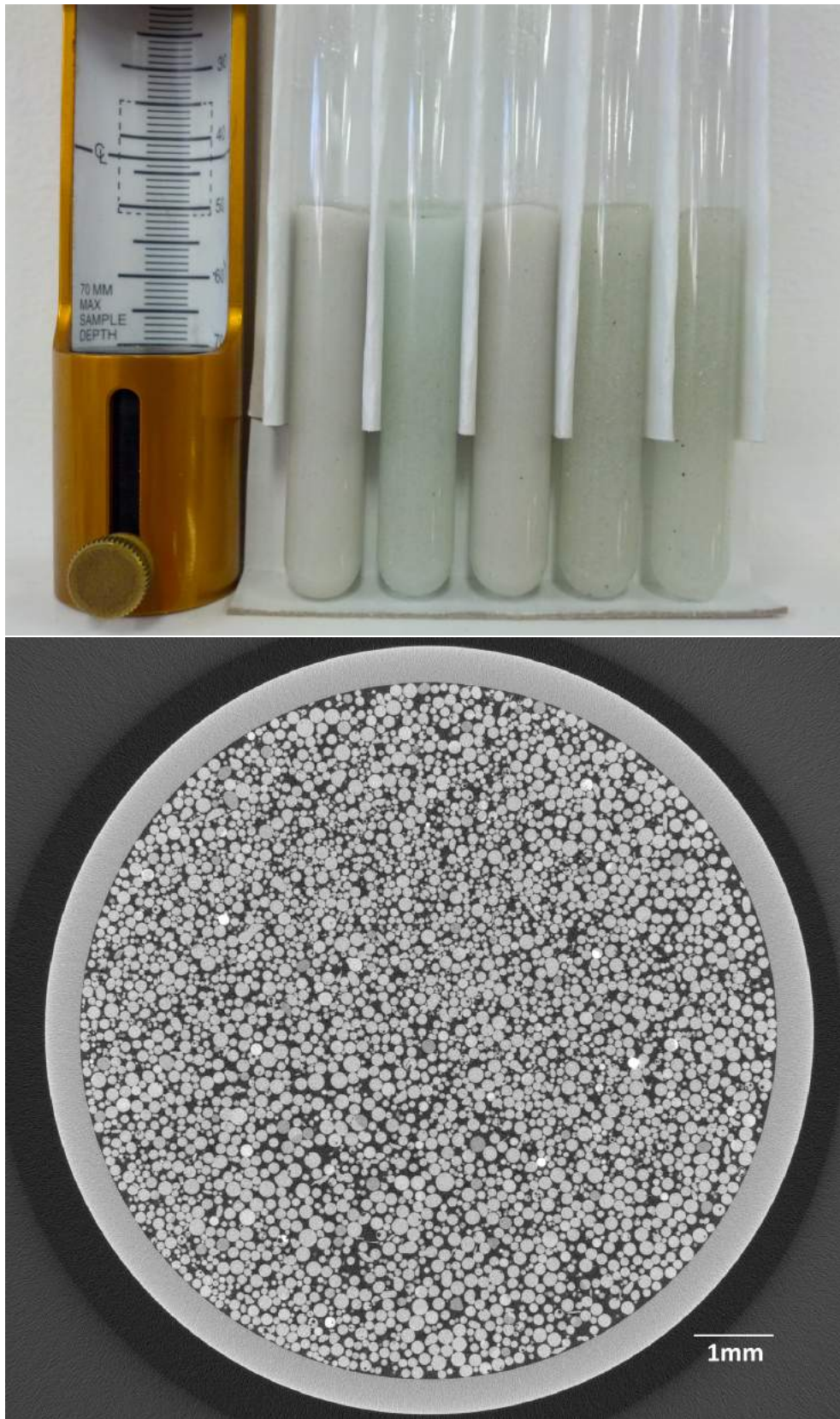


Figure 4.8.: The figure on top shows the soda-lime glass microspheres set of samples with five different diameter ranges inside 10mm tubes, imbibed on water for perform NMR experiments. The figure on the bottom shows one raw image of the x-ray microtomography of the glass microsphere sample of range 106-212 $\mu\text{m}$  diameter of Microesfera.

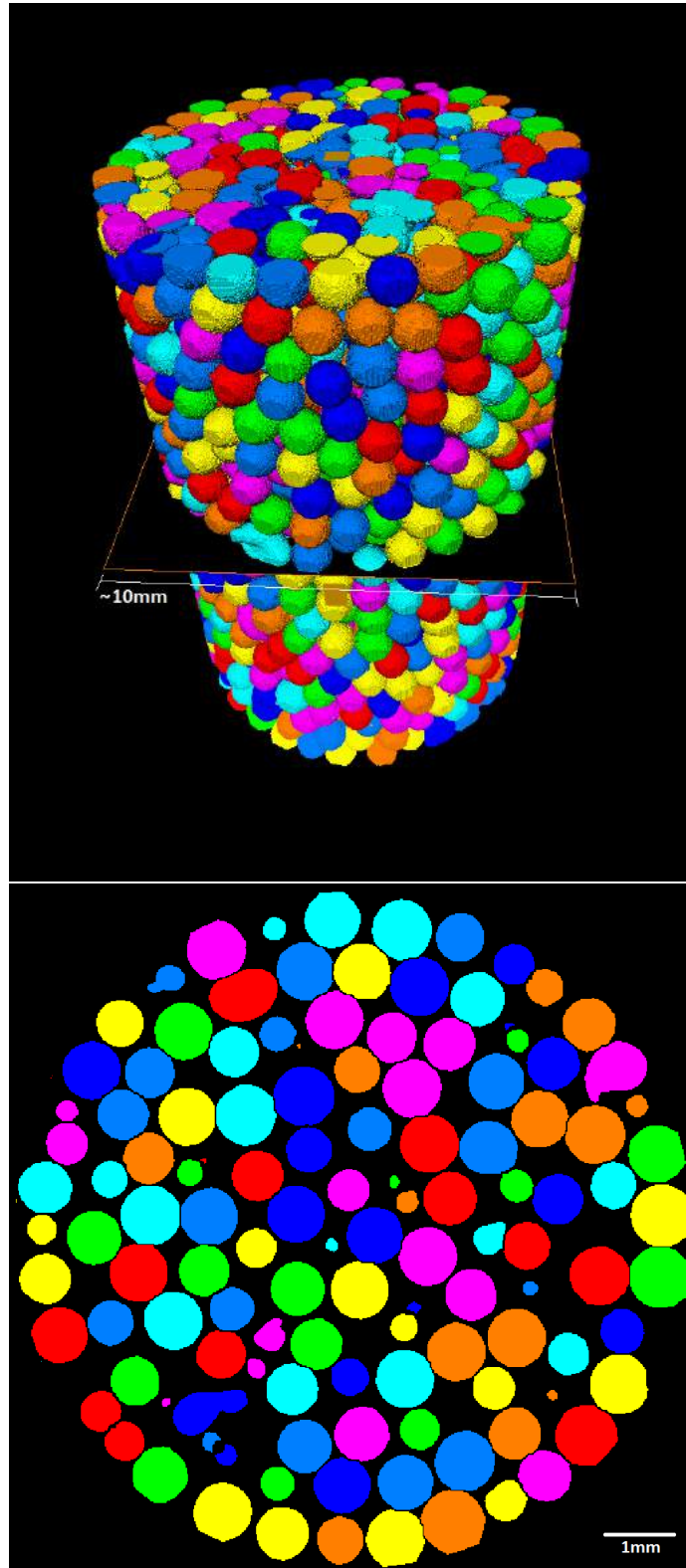


Figure 4.9.: The figure on top shows the rendered 3D volume of microtomography images of soda-lime glass microspheres from Cospheric with range of  $710\text{-}850\mu\text{m}$ . The figure on the bottom shows one horizontal 2D slice of the first image.

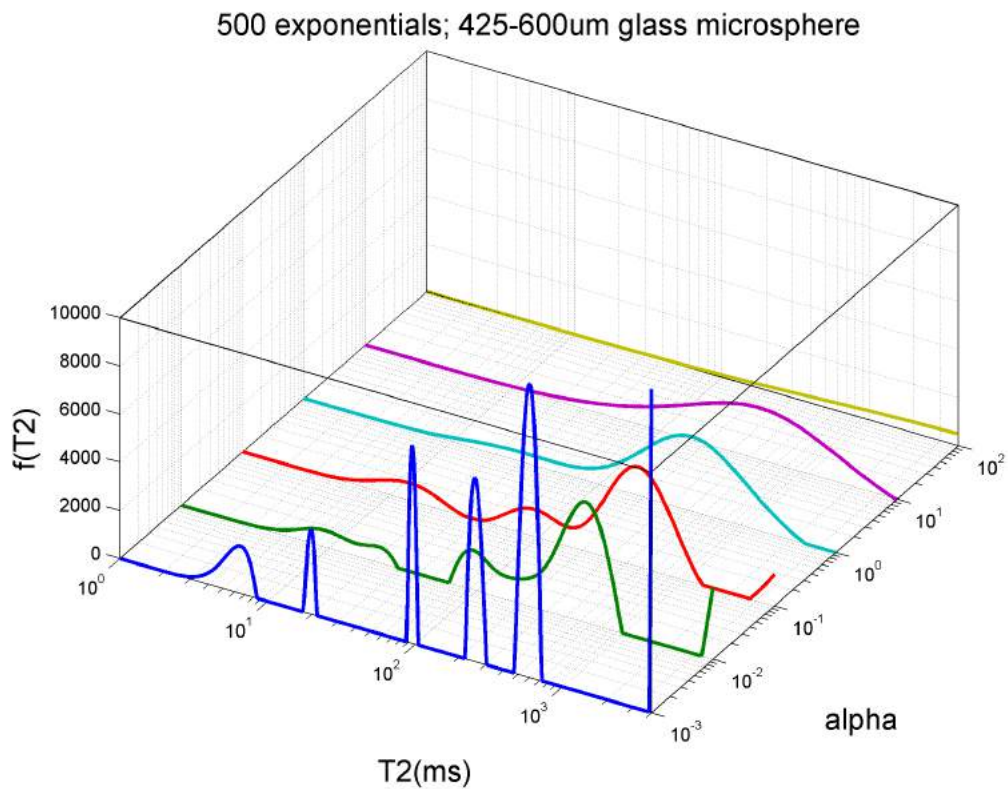
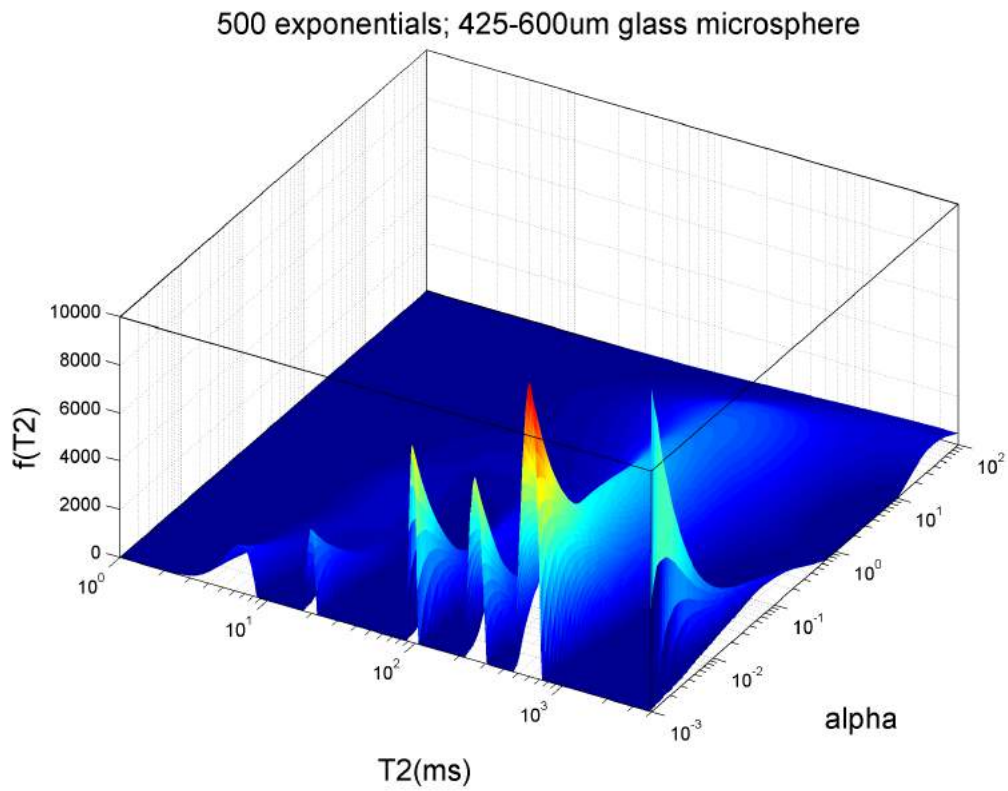


Figure 4.10.: Analyses of the regularization parameter effect,  $\alpha$ , on the  $T_2$  distribution for Microesferas sample A.

0.002.

$$\text{Error} = \frac{1}{N} \sum_{i=1}^N \frac{|Model(i) - Data(i)|}{Data(i)} \quad (4.14)$$

The relation between model parameters  $q$  and  $\beta_0^{-1}$  with the mean  $\langle T_2 \rangle$  and standard deviation  $\sigma$  of the distribution  $f_{q,\beta_0}(T_2)$  is given by

$$\langle T_2 \rangle = \frac{\beta_0^{-1}}{2 - q} \quad (4.15)$$

and

$$\sigma = \sqrt{\frac{q - 1}{3 - 2q}} \langle T_2 \rangle. \quad (4.16)$$

The values of  $q$ ,  $\beta_0^{-1}$ ,  $\langle T_2 \rangle$  and  $\sigma$  for the microesferas sample A can be seen in table 4.1.

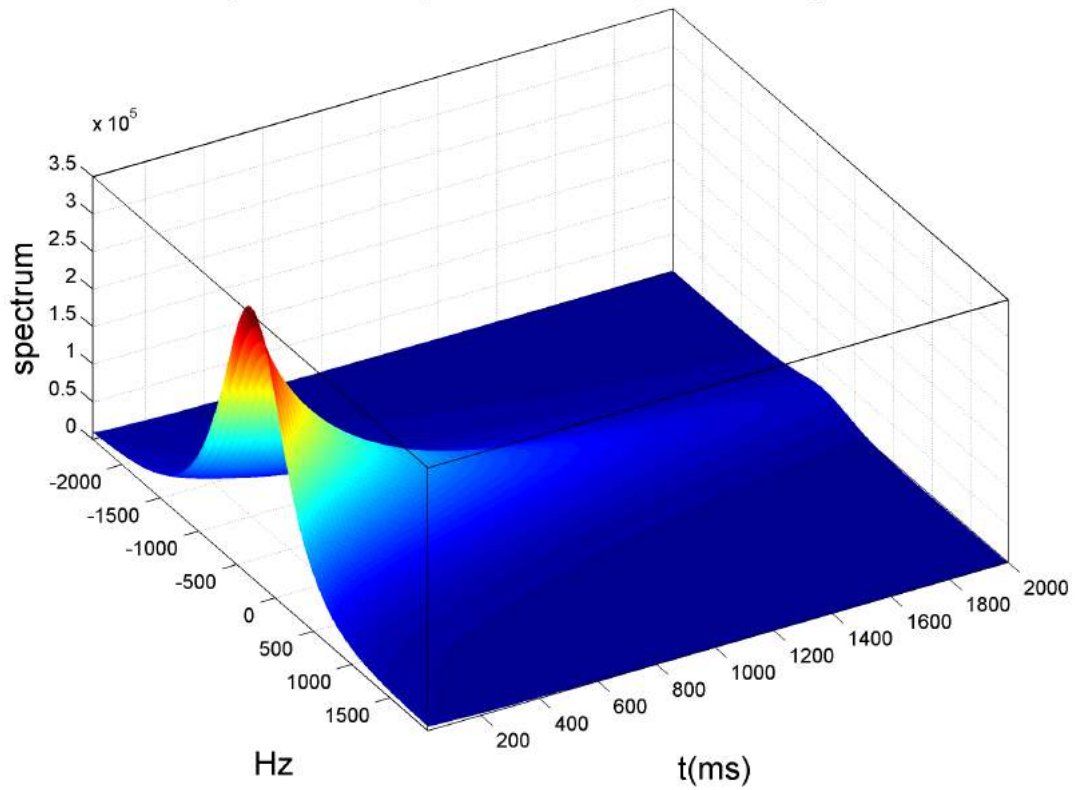
	fast	medium	slow
Intensity (%)	22.6	69.8	7.6
q	1.39	1.15	1.16
$\beta_0^{-1}$ (ms)	62.9	412.3	1695.3
$\langle T_2 \rangle$ (ms)	103.1	485.1	2012.1
$\sigma$ (ms)	137.3	224.6	964.0

Table 4.1.: Statistical parameters of three q-exponentials model for Microesferas sample A.

The  $T_2$  distribution associated to three q-exponential model and multiexponential model with regularization parameter  $\alpha$  can be view in Fig.(4.12). Is possible to observe a smoothing in the multiexponential distribution for larger  $\alpha$  parameters. The analytical model for  $T_2$  distribution is composed by three  $f_{q,\beta_0}(T_2)$  and the statistical parameters of distribution is given by nonlinear model fit procedure. The equation of black solid line in Fig. 4.12 is:

$$F(T_2) = 0.226f_{1.39,62.9}(T_2) + 0.698f_{1.15,412.3}(T_2) + 0.076f_{1.16,1695.3}(T_2), \quad (4.17)$$

Spectrum decay; 425-600um glass microsphere



Microesferas A; 425–600 $\mu$ m

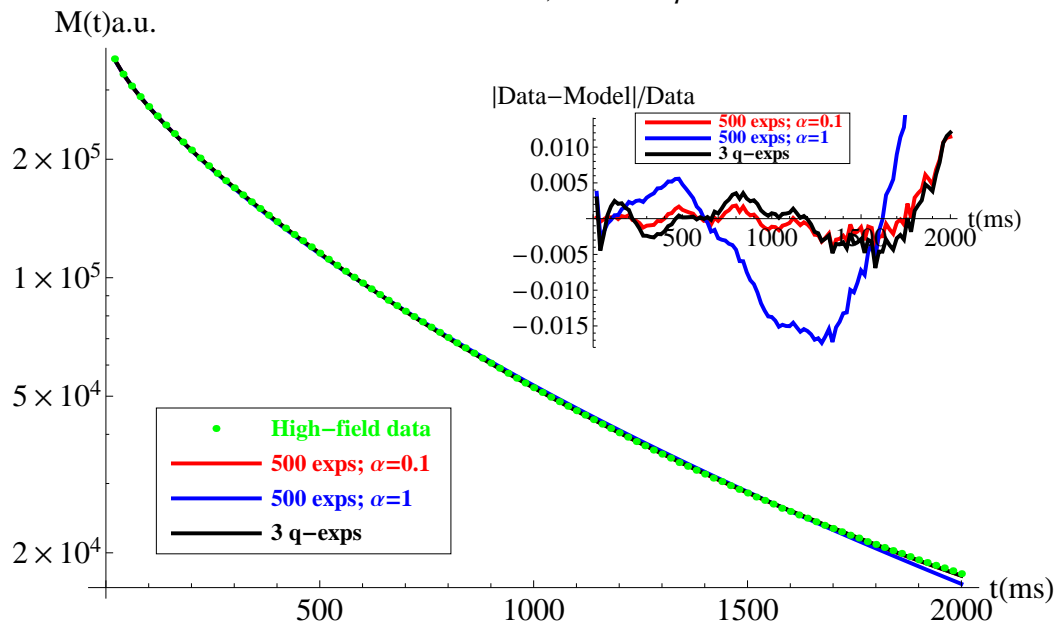


Figure 4.11.: The figure on top shows the spectrum decay in CPMG pulse sequence. The figure on bottom shows the comparison between the q-exponential and multiexponential models decay to prediction of  $T_2$  distribution in Microesferas sample A.

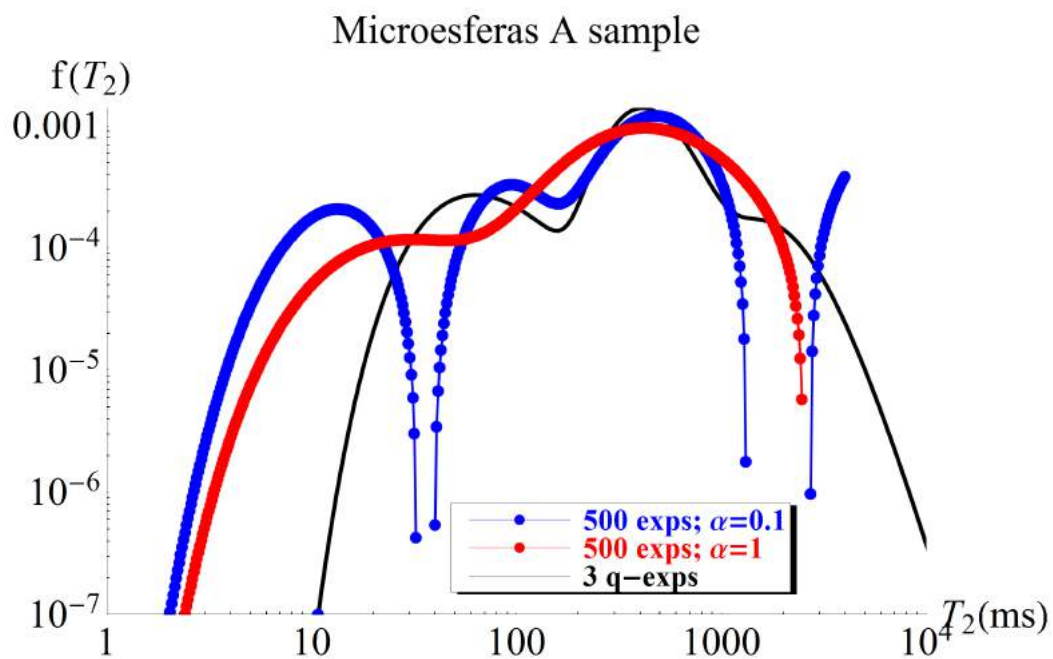
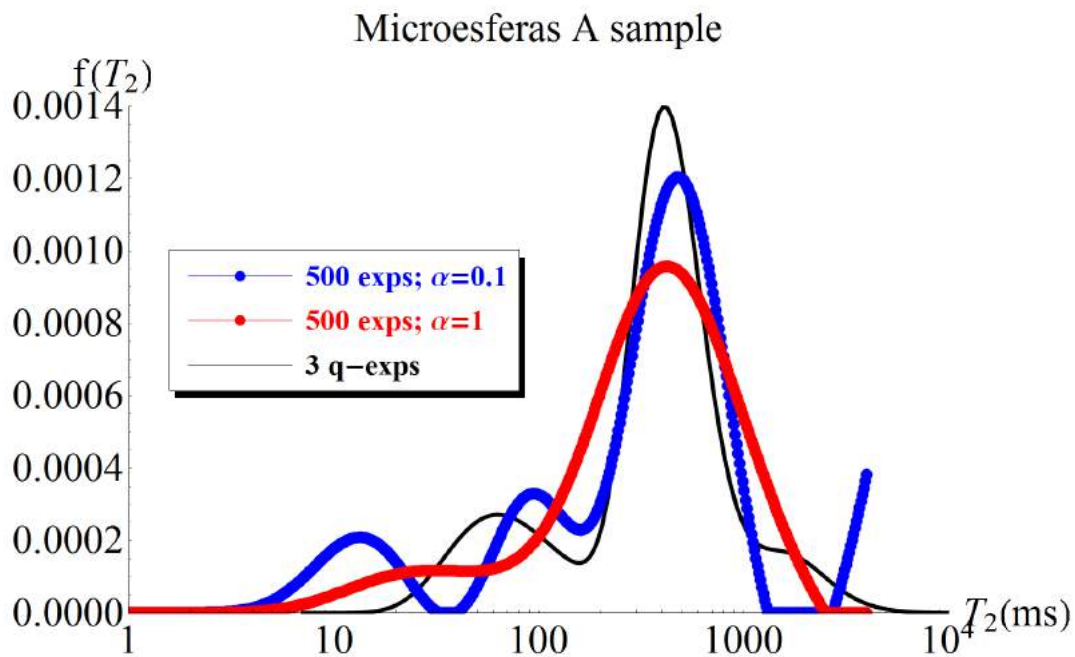


Figure 4.12.: Comparison of  $T_2$  distribution given by q-exponential model and multiexponential model in Microesferas sample A.

where each  $f_{q,\beta_0}(T_2)$  is given by Eq.(4.10) and represent fast, medium and slow relaxation respectively.

Observe in Fig.4.12 that the most pronounced mode in the three distribution is close to each other around  $T_2 = 400ms$ . In the log-log plot is possible to see that some zero values of  $T_2$ , from multiexponential modes, disappear when  $\alpha$  change from  $\alpha = 0.1$  to  $\alpha = 1$ , in times closed to  $T_2 = 40ms$  and  $T_2 = 2000ms$ . The  $T_2$  relaxation time is related to real physical dynamics of spin in porous space and in multiexponential model this time are biased by the regularization parameter value. The q-exponential model give analytical and continuous distribution for  $T_2$  with statistical parameter for each spin behavior regime, (Table 4.1). In general the  $T_2$  distribution modes in multiexponential model tends to be broader than than q-exponential model. This behavior is due to the fact that the multiexponential model has a finite range on the  $T_2$  axis, and therefore do not present long tail behavior.

### 4.2.2. Microesferas B: 250-425 $\mu\text{m}$ range diameter

The values of statistical parameters for the q-exponential model applied to NMR relaxation  $T_2$  experiment of Microesferas B (250-425 $\mu\text{m}$ ) can be viewed in Table 4.2. Most of the signal comes from the medium relaxation, and corresponds to the 70.7% of the total signal, with  $\langle T_2 \rangle_{\text{medium}} = 499.3\text{ms}$  and  $\sigma_{\text{medium}} = 256.1\text{ms}$ .

	fast	medium	slow
Intensity (%)	22.6	70.7	6.7
q	1.32	1.17	1.07
$\beta_0^{-1}$ (ms)	69.0	413.2	1631.6
$\langle T_2 \rangle$ (ms)	101.3	499.3	1764.2
$\sigma$ (ms)	95.2	256.1	524.7

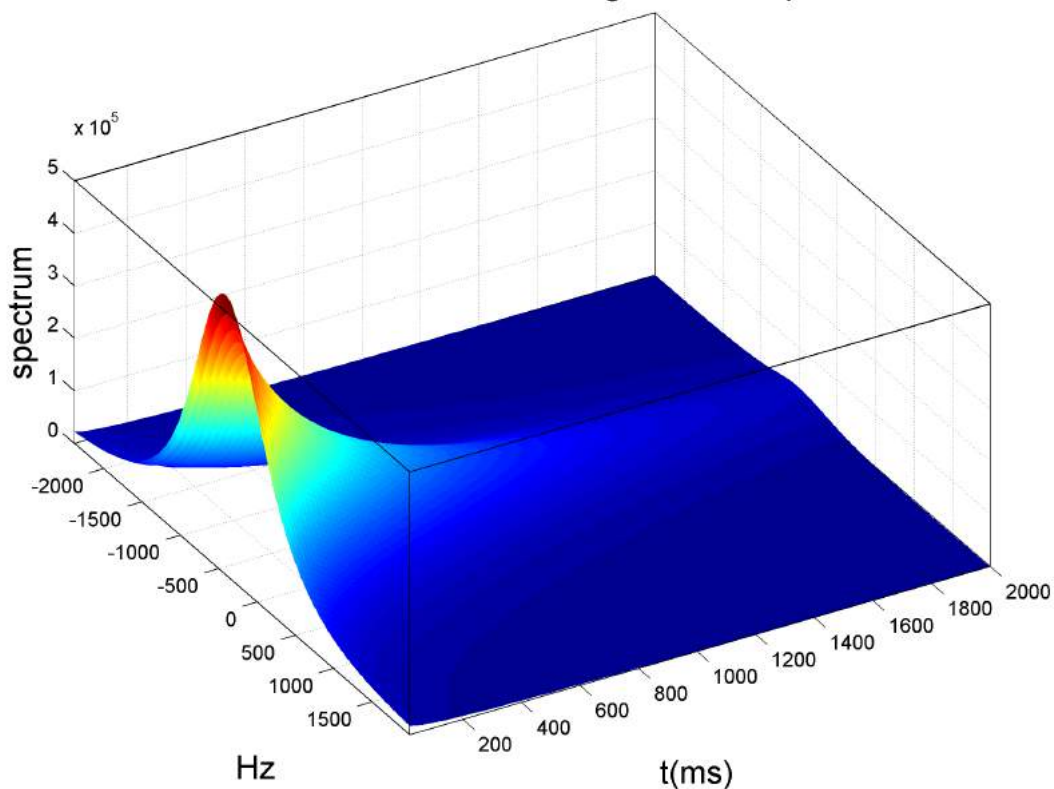
Table 4.2.: Statistical parameters of three q-exponentials model for Microesferas sample B.

The comparison between the q-exponential model and multiexponential can be viewed in Fig. 4.13. We choose two values of regularization parameter,  $\alpha = 0.1$  and  $\alpha = 1$  for the multiexponential fit. The error calculated by Eq.(4.14) and associated to the fit models are  $Error_{\alpha=0.1} = 0.002$ ,  $Error_{\alpha=1} = 0.009$  and  $Error_{q-exp} = 0.003$ . All the three fits have comparable errors and the best fit is the multiexponential with  $\alpha = 0.1$ , however the  $T_2$  distribution associated with it exhibits artefacts for long times decay due finite size effect of  $T_2$  range chosen (Fig.4.15). For smaller values of  $\alpha$ , the  $T_2$  distribution exhibit non-zero values for fast relaxation that maybe not be related to the dynamics of spins in the porous space, (Fig.4.14), but with inversion artefacts.

The multiexponential fit gives a continuous  $T_2$  distribution defined from zero to infinite, and exhibit long tail behavior. The multiexponential model for  $T_2$  is very depending on the regularization parameter  $\alpha$ . The behavior of  $T_2$  distribution with  $\alpha$  can be viewed in Fig.4.14.

The experimental results, as well as their analisis, for Microesferas samples

Microesferas B; 250-425 $\mu\text{m}$  glass microsphere



Microesferas B; 250-425 $\mu\text{m}$

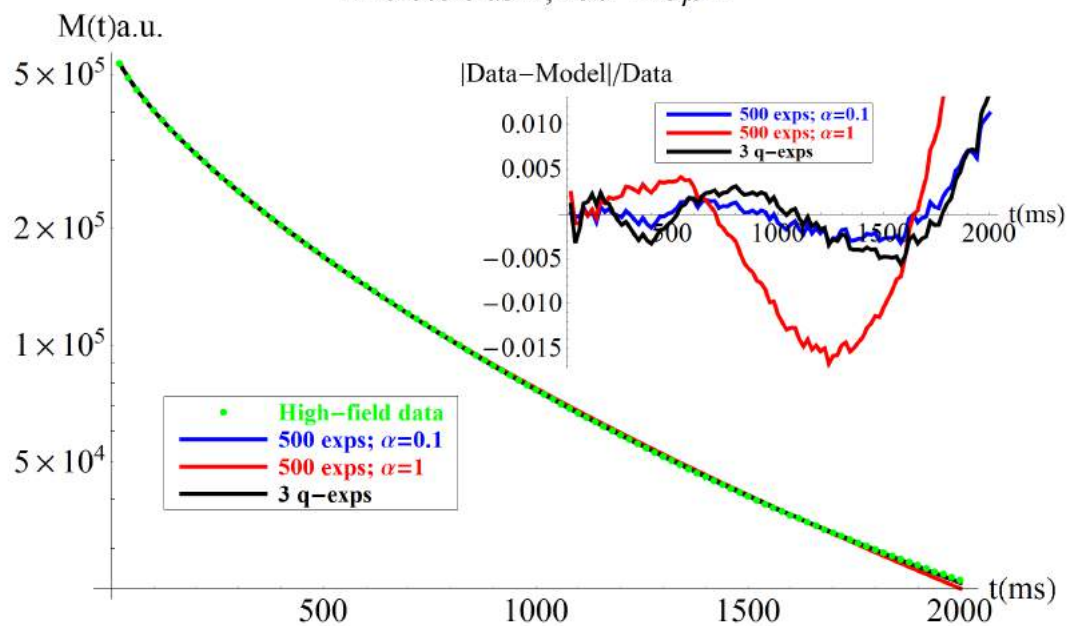


Figure 4.13.: The figure on top shows the spectrum decay in CPMG pulse sequence. The figure on bottom shows the comparison between the q-exponential and multiexponential models for the of  $T_2$  distribution in Microesferas sample B.

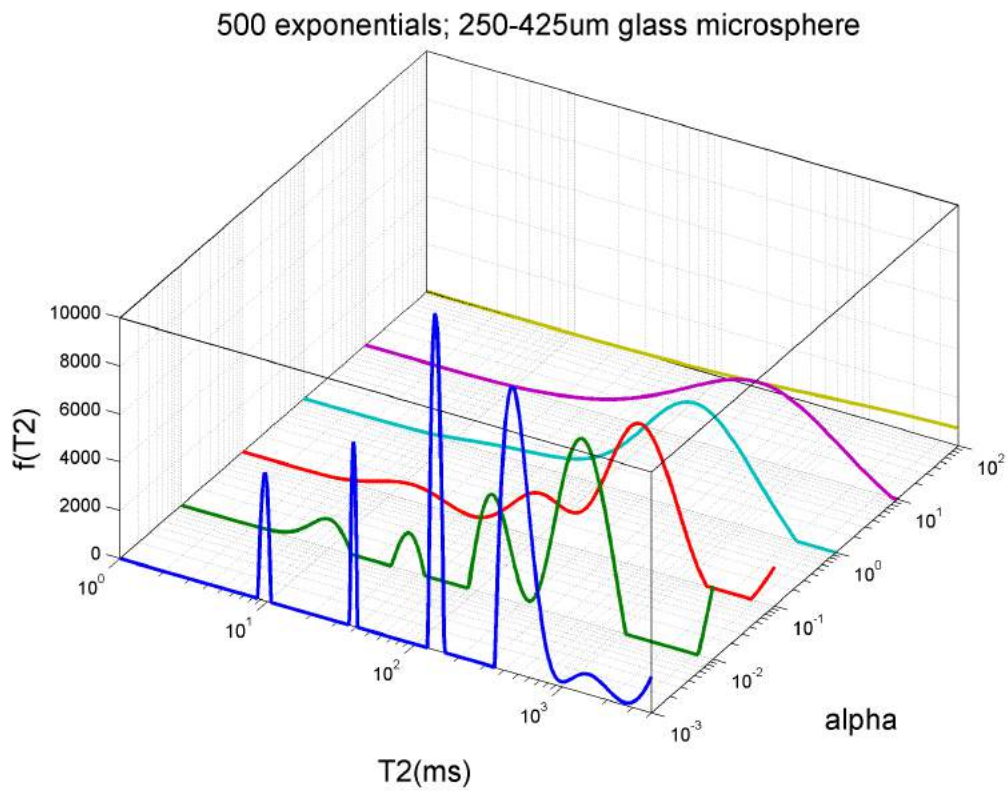
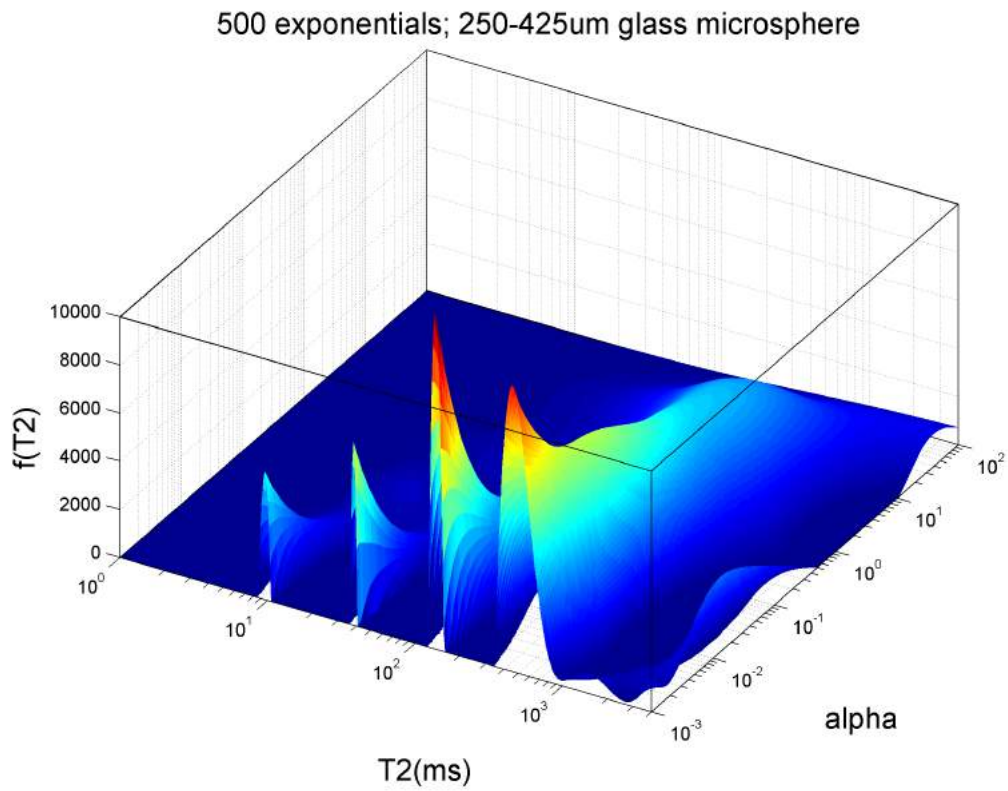


Figure 4.14.: Analyses of the regularization parameter effect,  $\alpha$ , on the  $T_2$  distribution for Microesferas sample B.

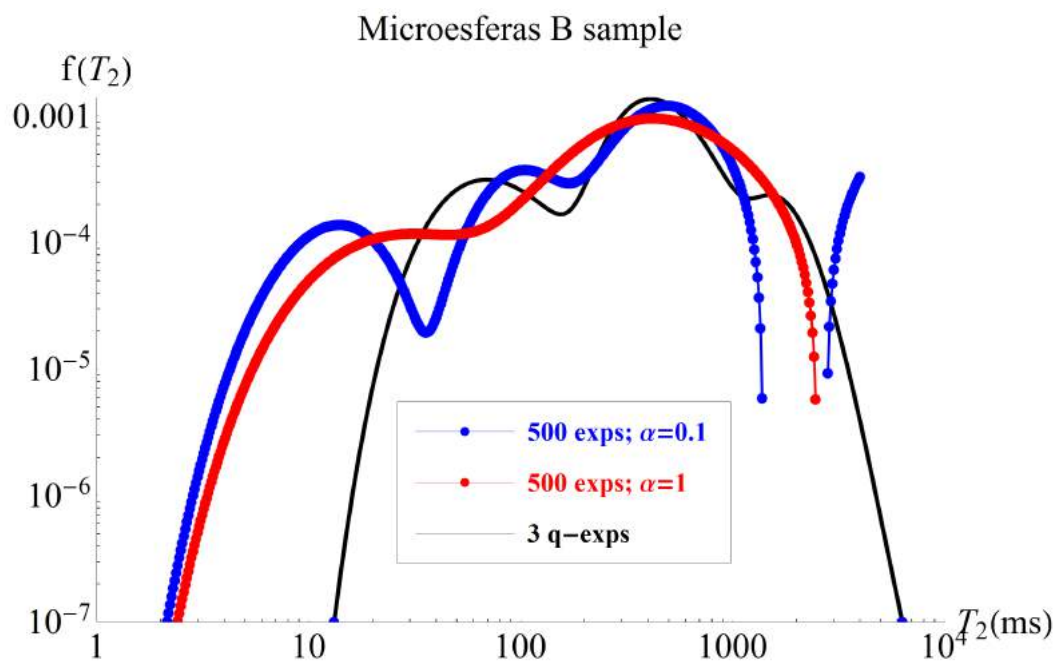
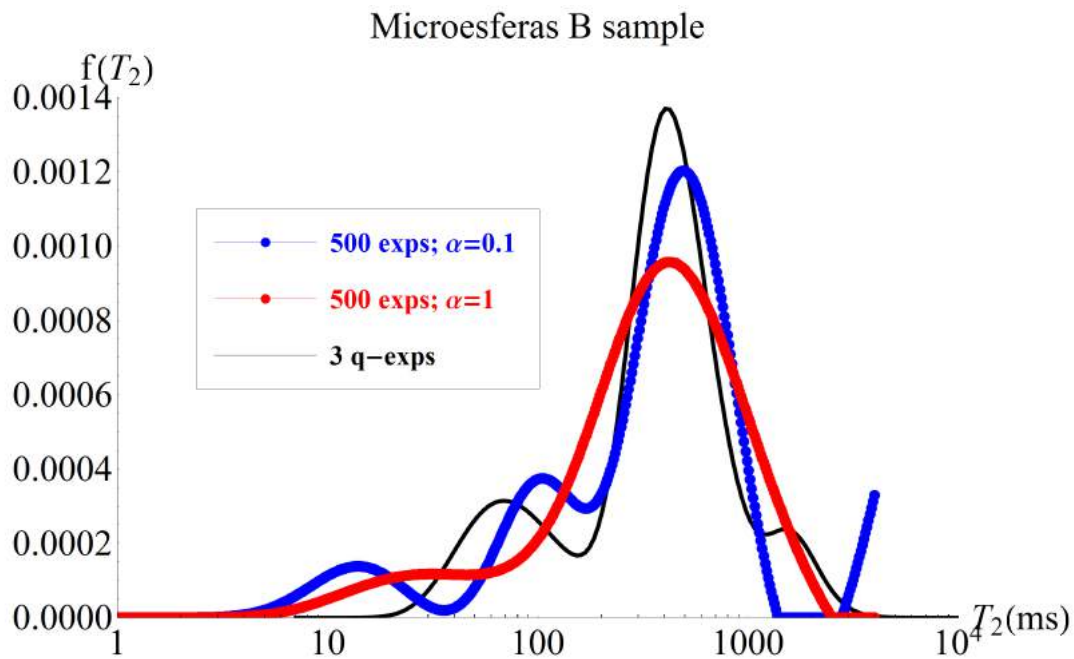


Figure 4.15.: Comparison of  $T_2$  distribution given by q-exponential model and multiexponential model decay.

C, D and E are described in Appendix A. We will now describe the results for some Cospheric samples and rocks.

### 4.2.3. Cospheric A: 710-850 $\mu m$ range diameter

Fig.4.16 shows the multiexponential and q-exponential fit models for Cospheric sample C A (710-850 $\mu m$ ), the inset shows the error along the decay, between the model and the measured data. The  $\alpha$  parameters chosen were  $\alpha = 0.1$  and  $\alpha = 1$ . The errors associated with fits are: i)  $Error_{\alpha=0.1} = 0.0008$ ; ii)  $Error_{\alpha=1} = 0.003$ ; and iii)  $Error_{q-exp} = 0.001$ . The statistical parameters associated with q-exponential model can be viewed in Table 4.3.

	fast	medium	slow
Intensity (%)	12.4	–	87.5
q	1.5	–	1.35
$\beta_0^{-1}$ (ms)	175.1	–	1892.1
$\langle T_2 \rangle$ (ms)	350.2	–	2929.7
$\sigma$ (ms)	39773.8	–	3228.1

Table 4.3.: Statistical parameters of two q-exponentials model for Cospheric sample A.

The Fig.(4.17) shows the behavior of  $T_2$  distribution, given by multiexponential model, with  $\alpha$  regularization parameter. In the Fig.(4.18) is possible to see the comparison between the  $T_2$  distributions of multiexponential model, with two values of  $\alpha$  parameter, and the  $f_{q,\beta_0}(T_2)$  model proposed.

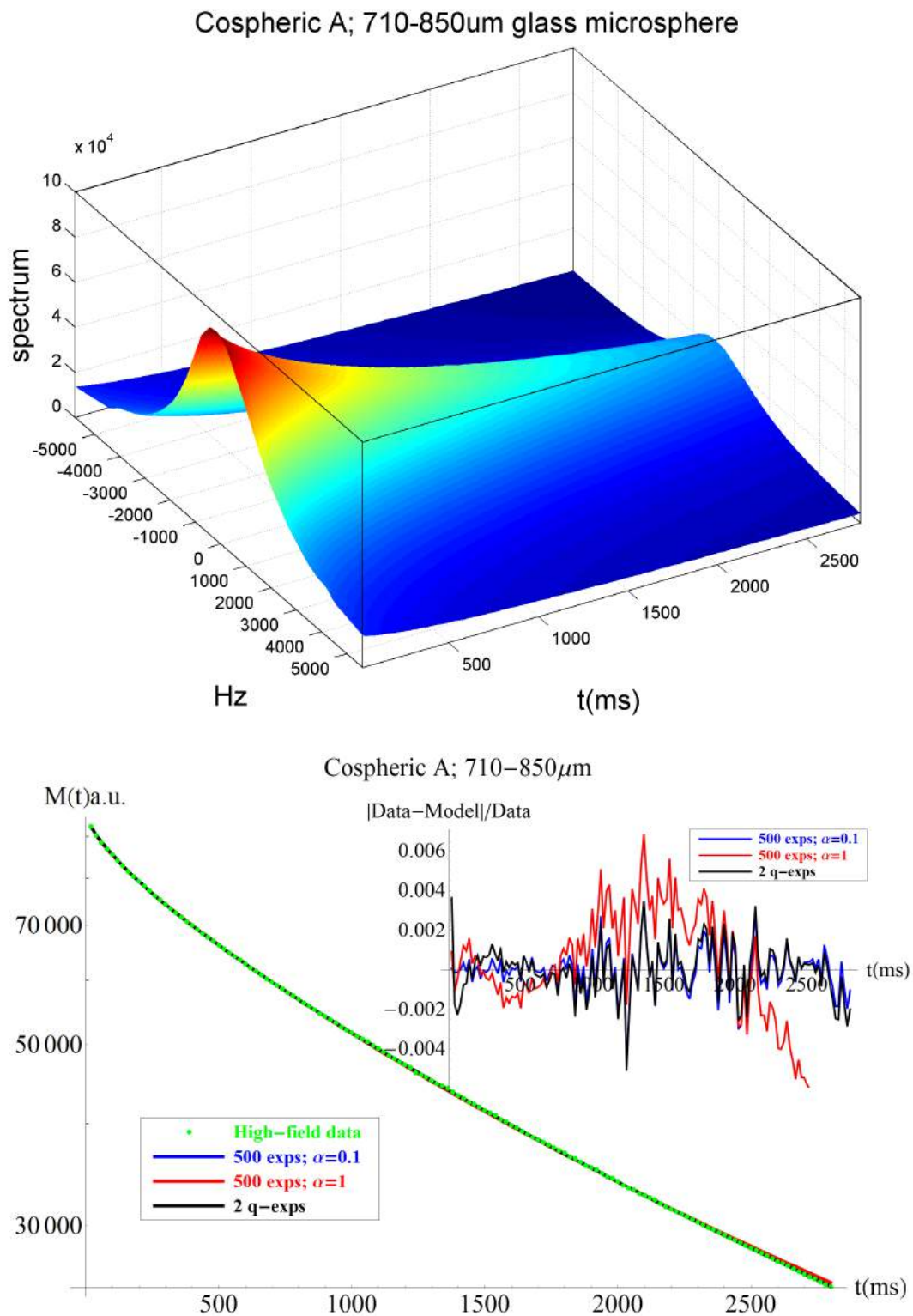


Figure 4.16.: The figure on top shows the spectrum decay in CPMG pulse sequence. The figure on bottom shows the comparison between the q-exponential and multiexponential models for the of  $T_2$  distribution in Cospheric sample A.

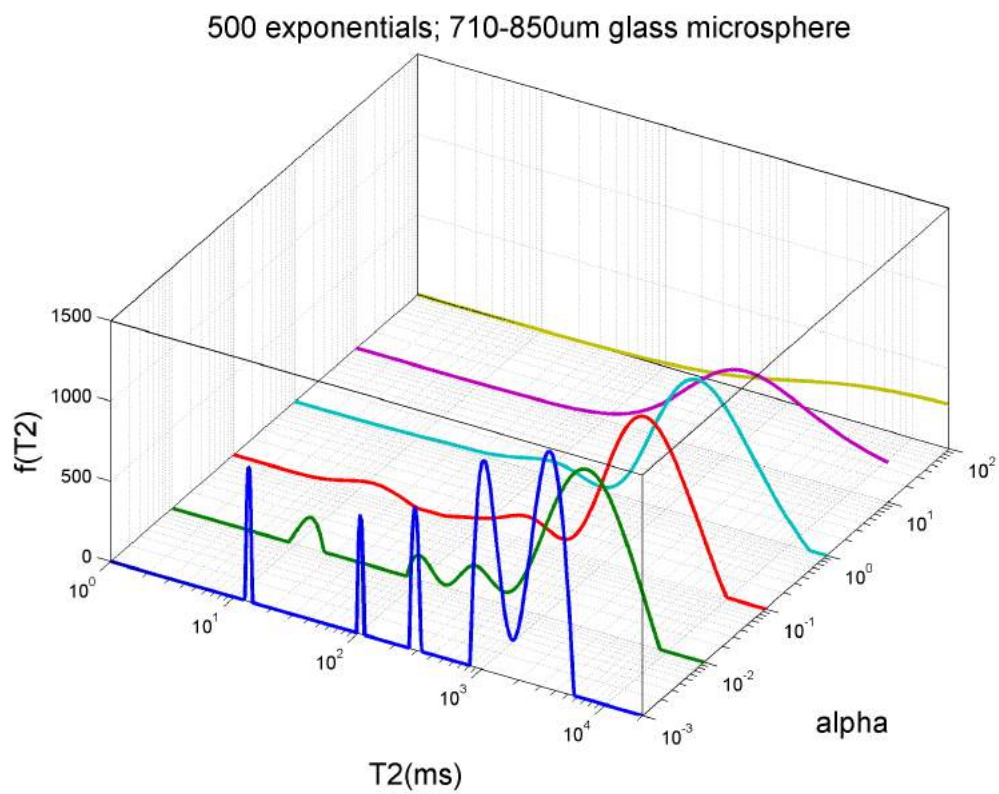
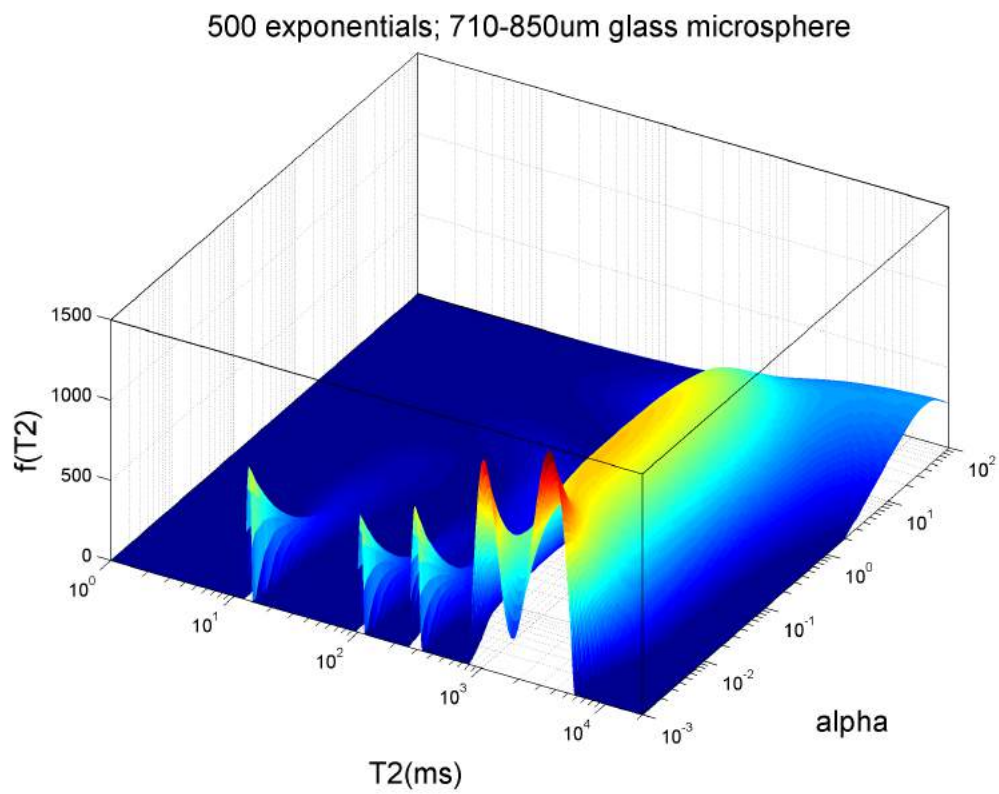


Figure 4.17.: Analyses of the regularization parameter effect,  $\alpha$ , on the  $T_2$  distribution for Cospherisample C A.

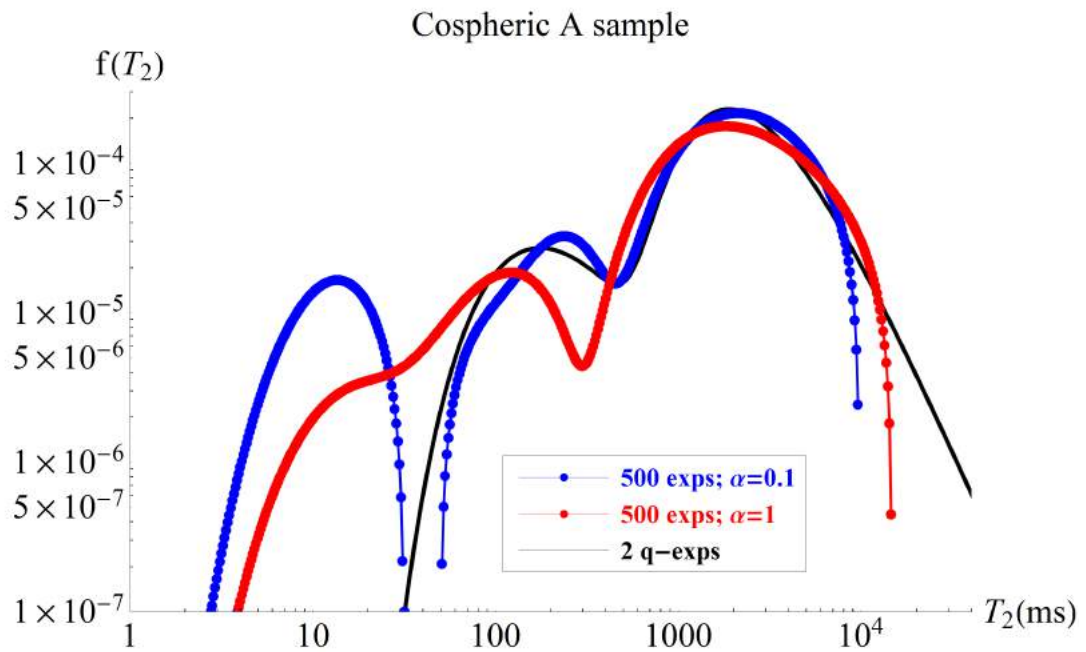
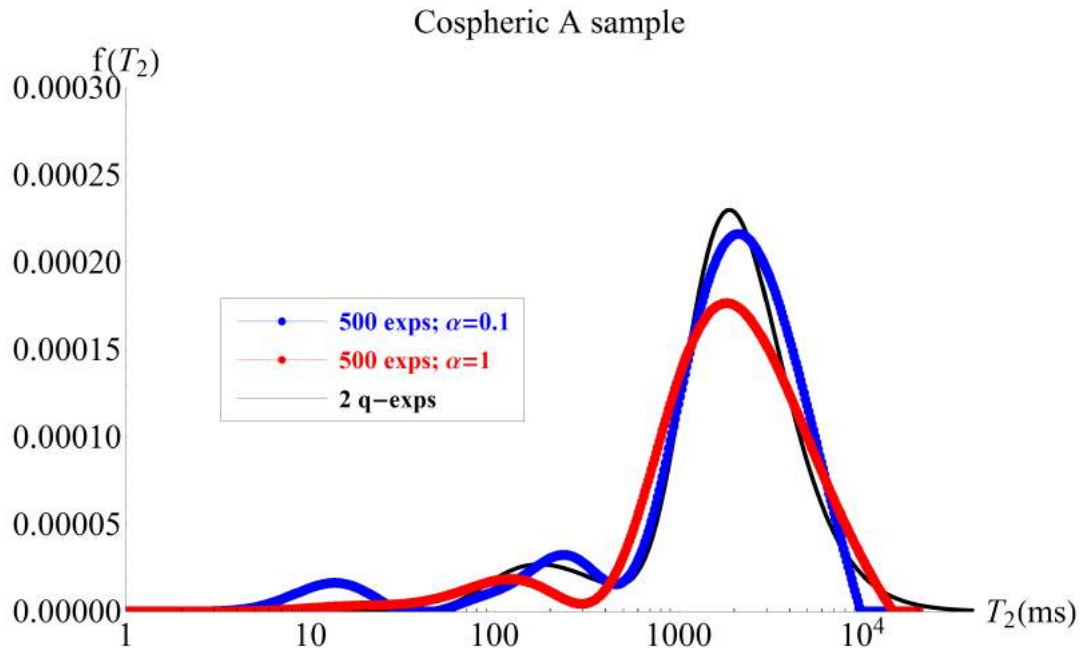


Figure 4.18.: Comparison of the  $T_2$  distributions given by q-exponential and multiexponential models.

#### 4.2.4. Cospheric B: 425-500 $\mu m$ range diameter

Fig.4.19 shows the multiexponential and q-exponential fit models for Microesfera sample C (425-500 $\mu m$ ), the inset shows the error along the decay, between the model and the measured data. The  $\alpha$  parameters chosen were  $\alpha = 0.1$  and  $\alpha = 1$ . The errors associated with fits are: i)  $Error_{\alpha=0.1} = 0.001$ ; ii)  $Error_{\alpha=1} = 0.008$ ; and iii)  $Error_{q-exp} = 0.002$ . The statistical parameters associated with q-exponential model can be viewed in Table 4.4.

	fast	medium	slow
Intensity (%)	27.6	61.9	10.5
q	1.40	1.10	1.30
$\beta_0^{-1}$ (ms)	149.5	638.2	5736.8
$\langle T_2 \rangle$ (ms)	249.1	707.6	8147.6
$\sigma$ (ms)	351.9	247.3	6936.4

Table 4.4.: Statistical parameters of three q-exponentials model for Cospherisample C B.

The Fig.(4.20) shows the behavior of  $T_2$  distribution, given by multiexponential model, with  $\alpha$  regularization parameter. In the Fig.(4.21) is possible to see the comparison between the  $T_2$  distributions of multiexponential model, with two values of  $\alpha$  parameter, and the  $f_{q,\beta_0}(T_2)$  model proposed.

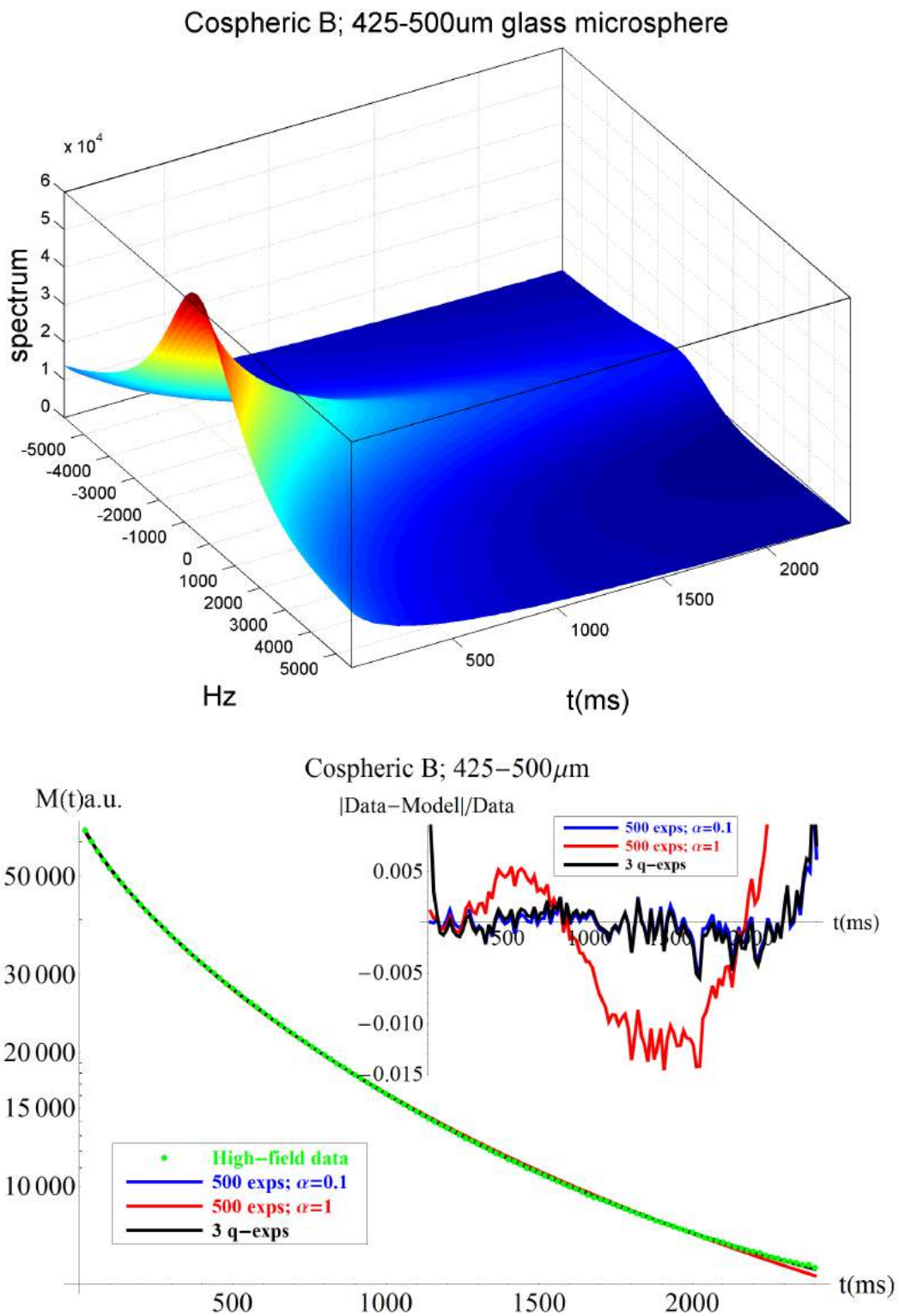


Figure 4.19.: The figure on top shows the spectrum decay in CPMG pulse sequence. The figure on bottom shows the comparison between the q-exponential and multiexponential models for the of  $T_2$  distribution in Cospheric sample B.

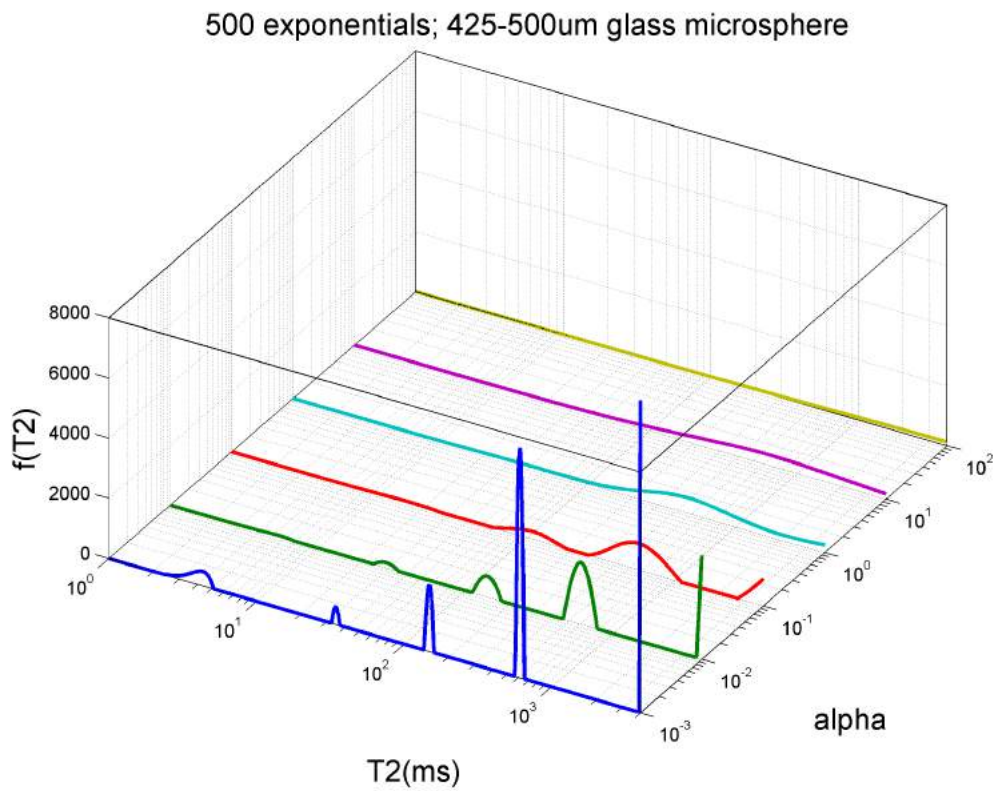
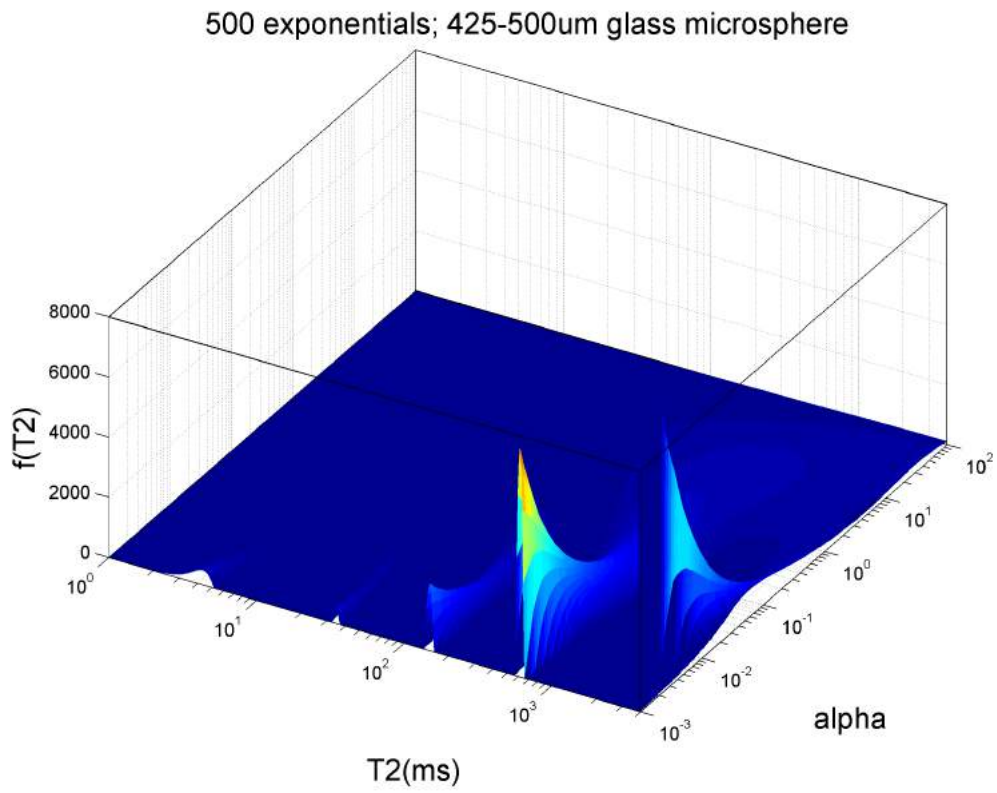


Figure 4.20.: Analyses of the regularization parameter effect,  $\alpha$ , on the  $T_2$  distribution for Cospherisample C B.

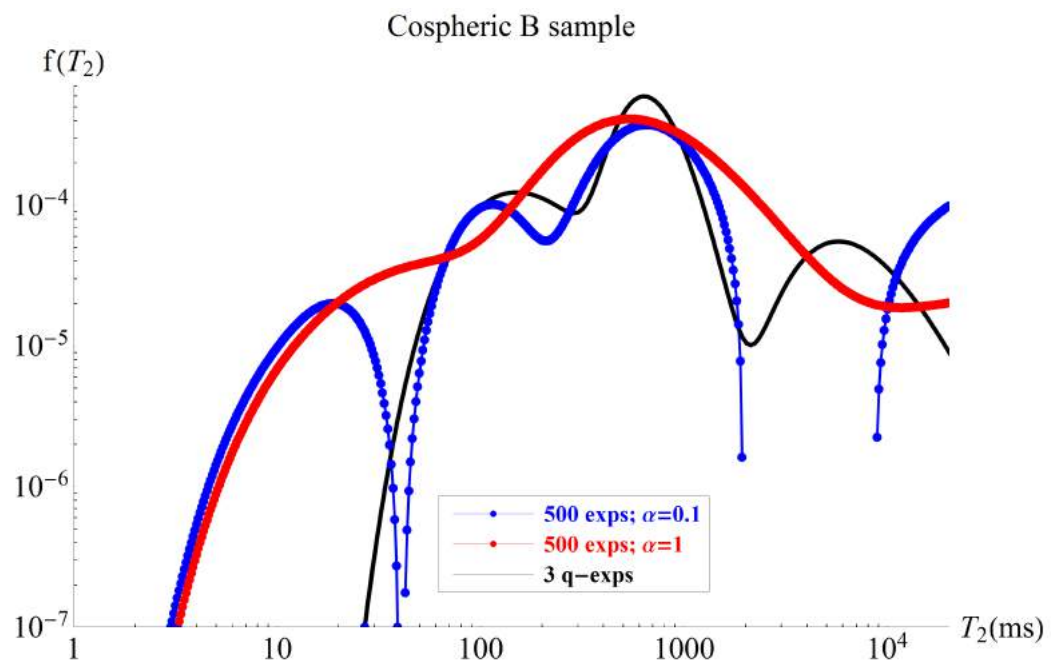
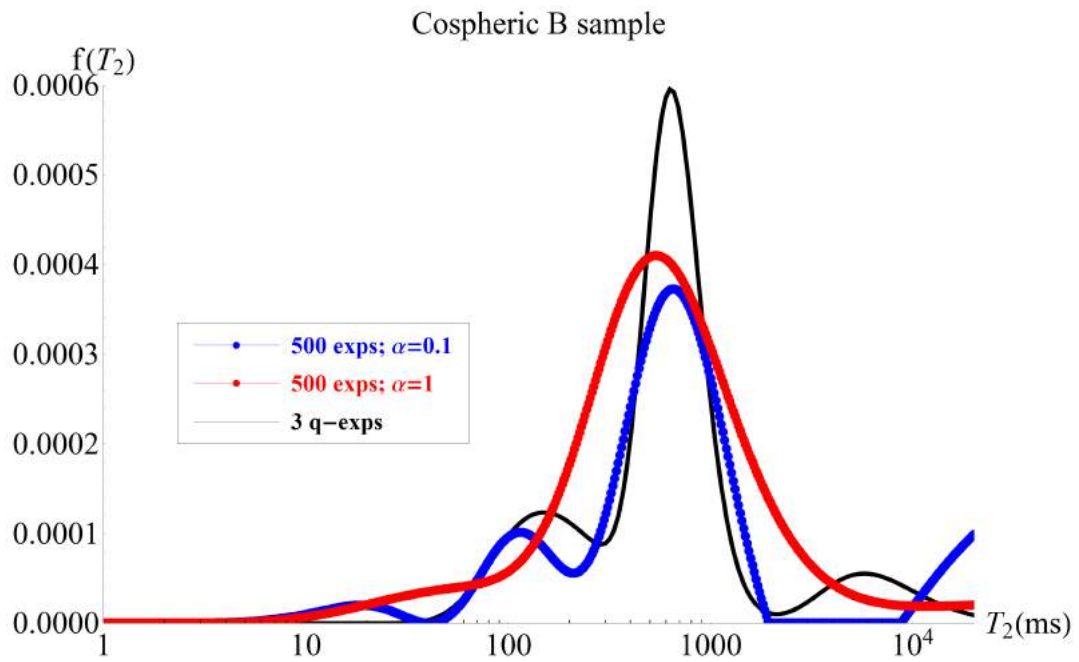


Figure 4.21.: Comparison of  $T_2$  distribution given by q-exponential model and multiexponential model.

#### 4.2.5. Berea Sandstone

Fig.4.22 shows the multiexponential and q-exponential fit models for Berea Sandstone, the inset shows the error along the decay, between the model and the measured data. The  $\alpha$  parameter chosen were  $\alpha = 0.1$  and  $\alpha = 1$ . The errors associated with fits are: i)  $Error_{\alpha=0.1} = 0.003$ ; ii)  $Error_{\alpha=1} = 0.02$ ; and iii)  $Error_{q-exp} = 0.005$ . The statistical parameters associated with q-exponential model can be viewed in Table 4.5.

	fast	medium	slow
Intensity (%)	37.3	58.8	3.8
q	1.15	1.18	1.04
$\beta_0^{-1}$ (ms)	7.15	122.3	731.5
$\langle T_2 \rangle$ (ms)	8.46	149.3	759.7
$\sigma$ (ms)	4.0	79.5	152.1

Table 4.5.: Statistical parameters of three q-exponentials model for Berea Sandstone.

The Fig.(4.23) shows the behavior of  $T_2$  distribution, given by multiexponential model, with  $\alpha$  regularization parameter. In the Fig.(4.24) is possible to see the comparison between the  $T_2$  distributions of multiexponential model, with two values of  $\alpha$  parameter, and the  $f_{q,\beta_0}(T_2)$  model proposed.

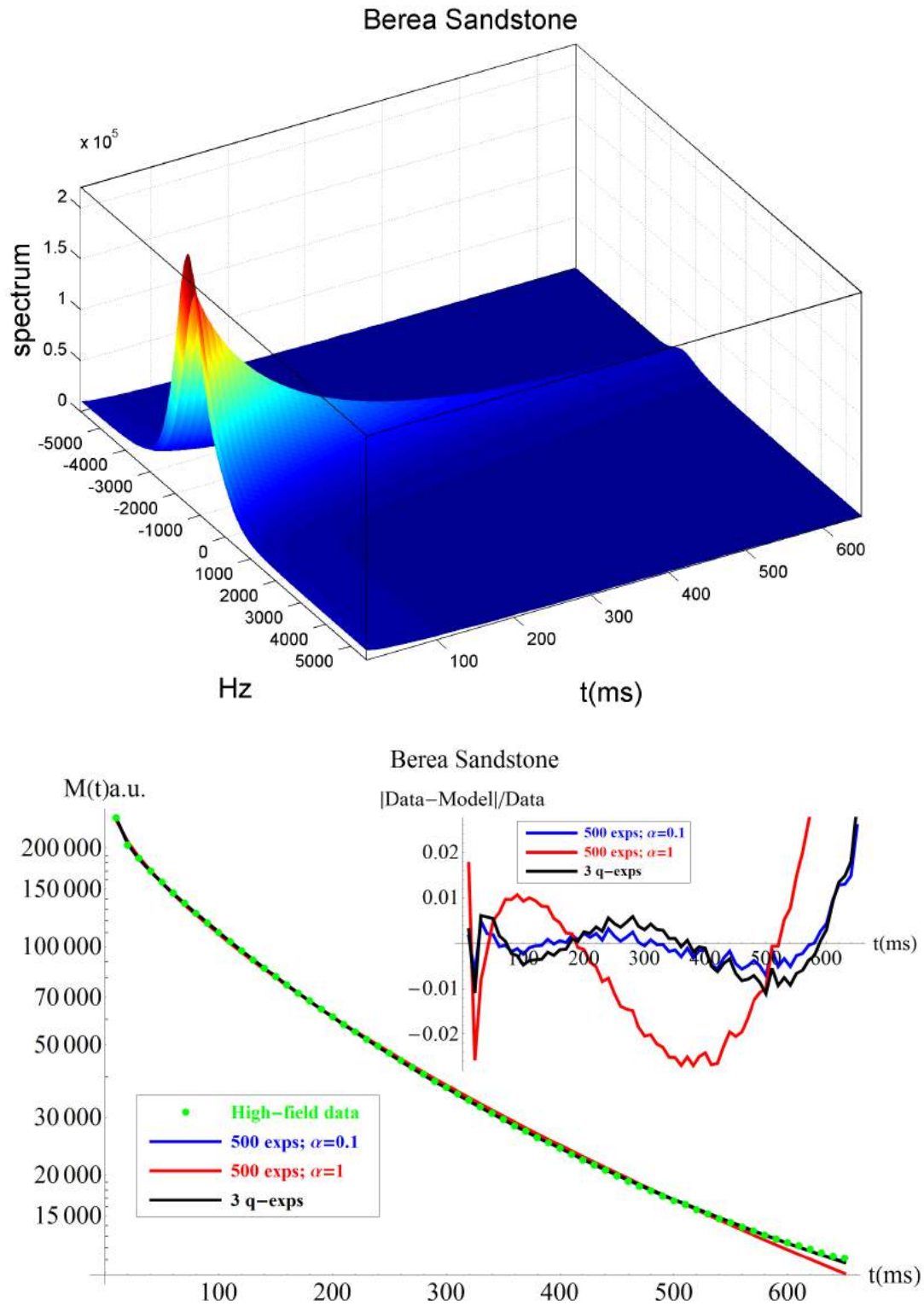


Figure 4.22.: The figure on top shows the spectrum decay in CPMG pulse sequence. The figure on bottom shows the comparison between the q-exponential and multiexponential models for the of  $T_2$  distribution in Berea Sandstone.

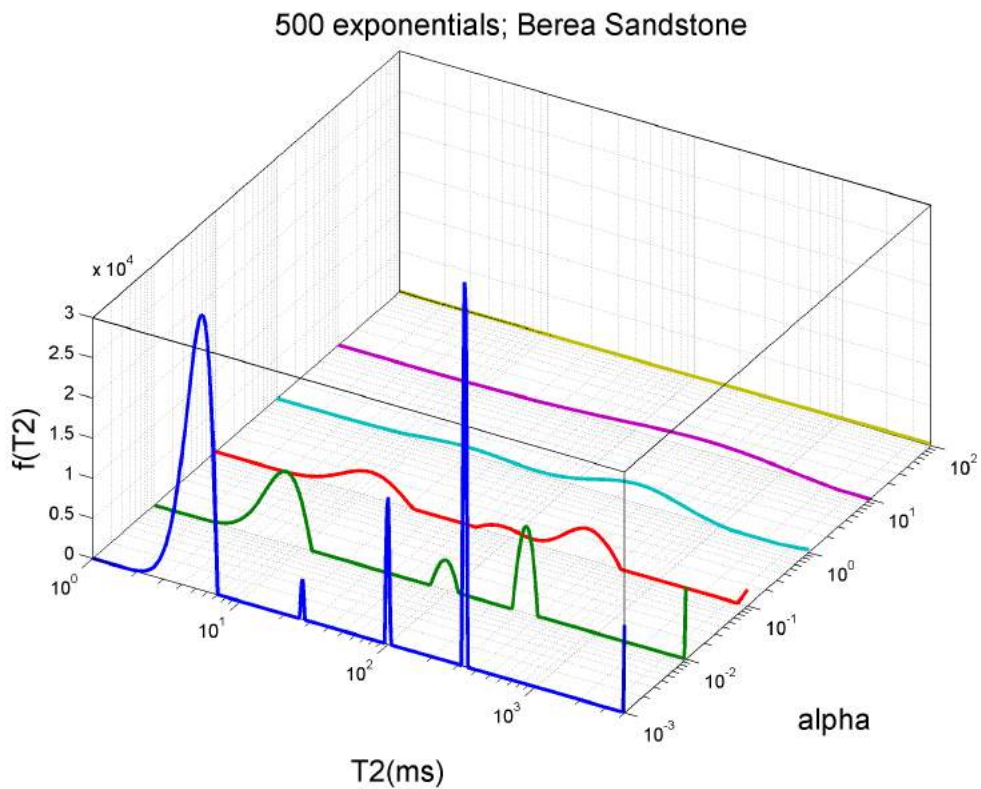
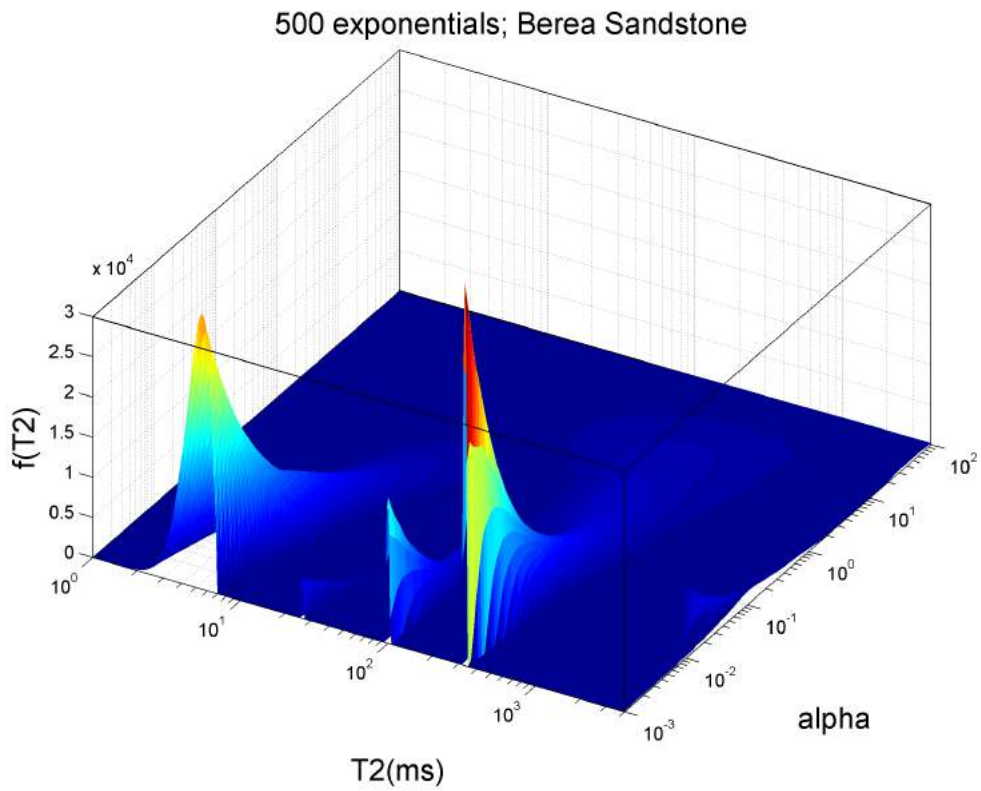


Figure 4.23.: Analyses of the regularization parameter effect,  $\alpha$ , on the  $T_2$  distribution for Berea Sandstone.

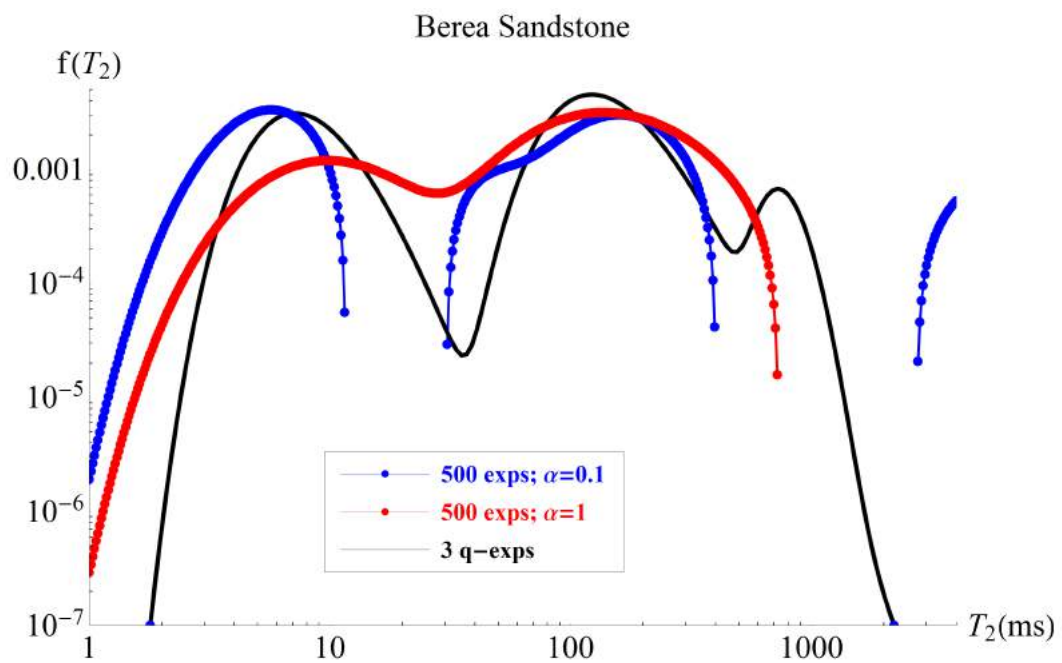
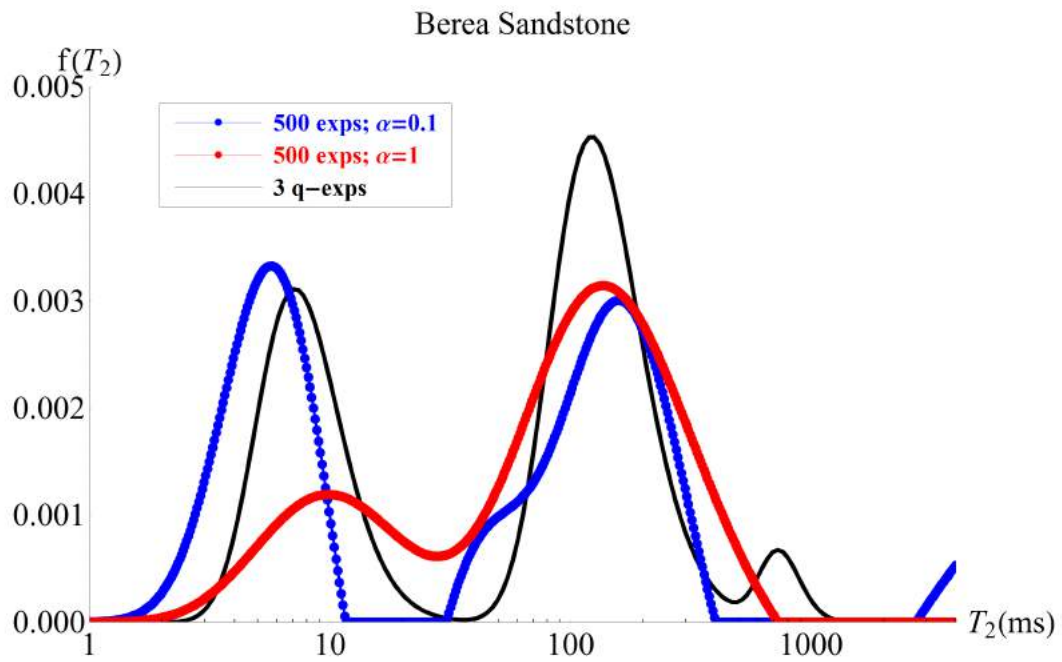


Figure 4.24.: Comparison of the  $T_2$  distributions given by q-exponential and multiexponential models.

#### 4.2.6. Buff Berea Sandstone

Fig.4.25 shows the multiexponential and q-exponential fit models for Buff Berea Sandstone, the inset shows the error along the decay, between the model and the measured data. The  $\alpha$  parameter chosen were  $\alpha = 0.1$  and  $\alpha = 1$ . The errors associated with fits are: i)  $Error_{\alpha=0.01} = 0.008$ ; ii)  $Error_{\alpha=0.1} = 0.04$ ; and iii)  $Error_{q-exp} = 0.01$ . The statistical parameters associated with q-exponential model can be viewed in Table 4.6.

	fast	medium	slow
Intensity (%)	52.4	43.9	3.7
q	1.47	1.04	1.48
$\beta_0^{-1}$ (ms)	8.97	56.6	326.0
$\langle T_2 \rangle$ (ms)	16.8	59.9	627.8
$\sigma$ (ms)	44.6	12.5	2213.1

Table 4.6.: Statistical parameters of three q-exponentials model for Buff Berea Sandstone.

The Fig.(4.26) shows the behavior of  $T_2$  distribution, given by multiexponential model, with  $\alpha$  regularization parameter. In the Fig.(4.27) is possible to see the comparison between the  $T_2$  distributions of multiexponential model, with two values of  $\alpha$  parameter, and the  $f_{q,\beta_0}(T_2)$  model proposed.

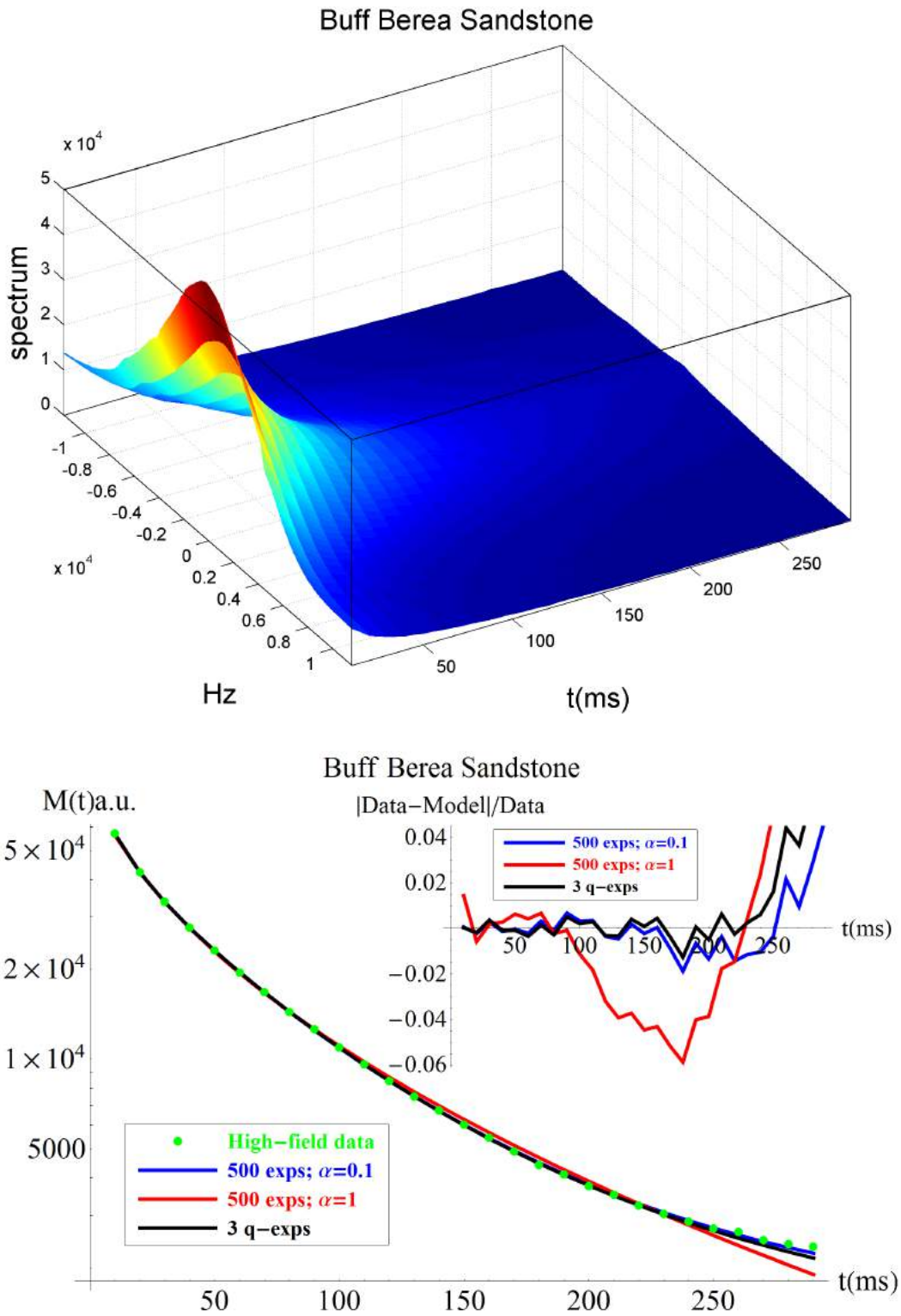


Figure 4.25.: The figure on top shows the spectrum decay in CPMG pulse sequence. The figure on bottom shows the comparison between the q-exponential and multiexponential models for the of  $T_2$  distribution in Buff Berea Sandstone.

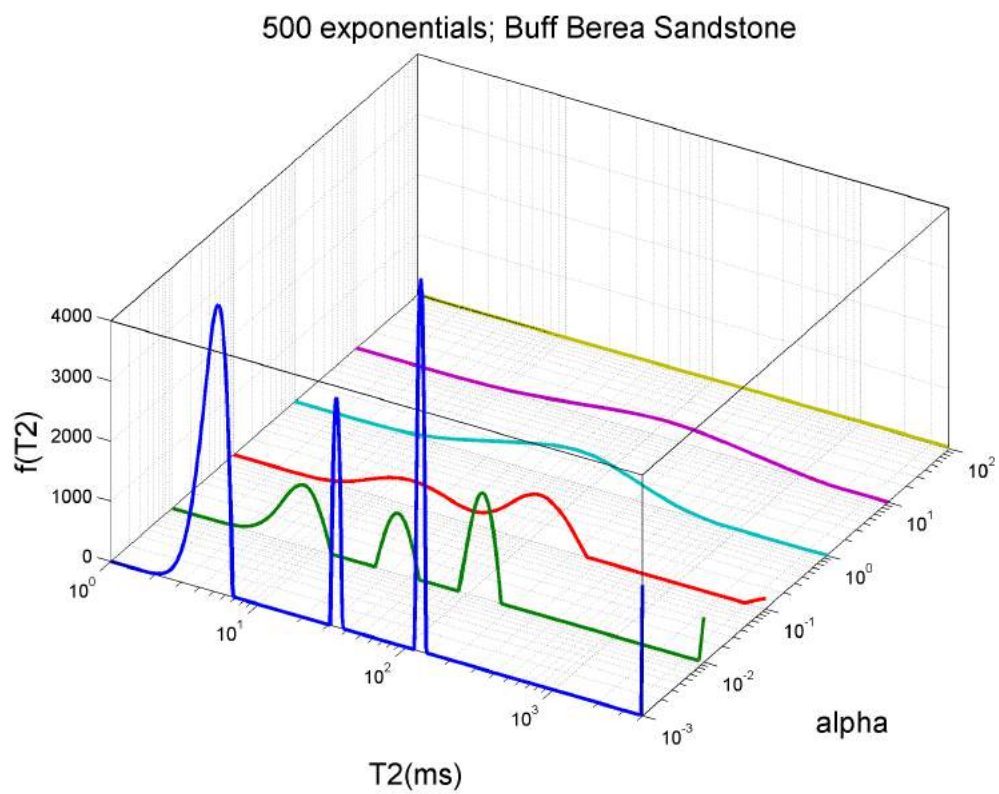
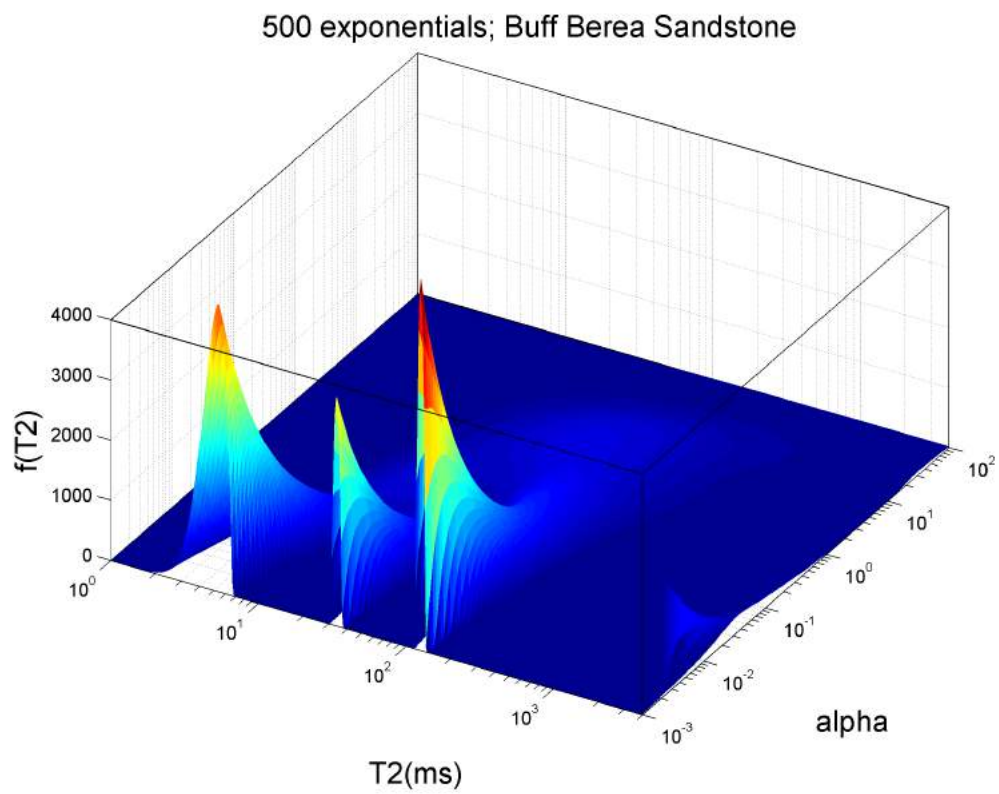


Figure 4.26.: Analyses of the regularization parameter effect,  $\alpha$ , on the  $T_2$  distribution for Buff Berea Sandstone.

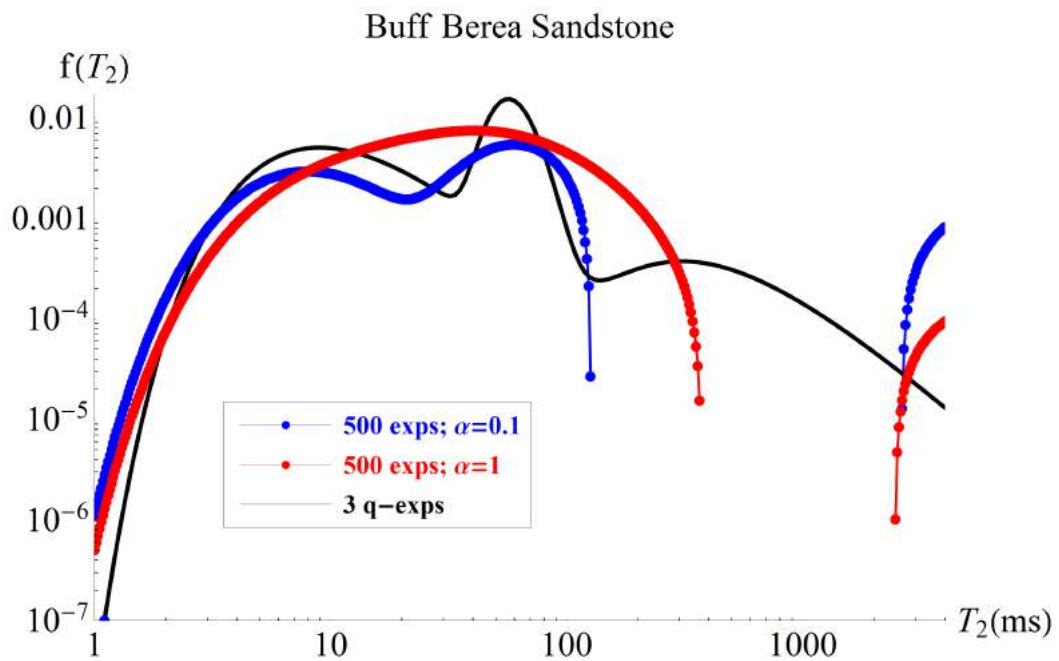
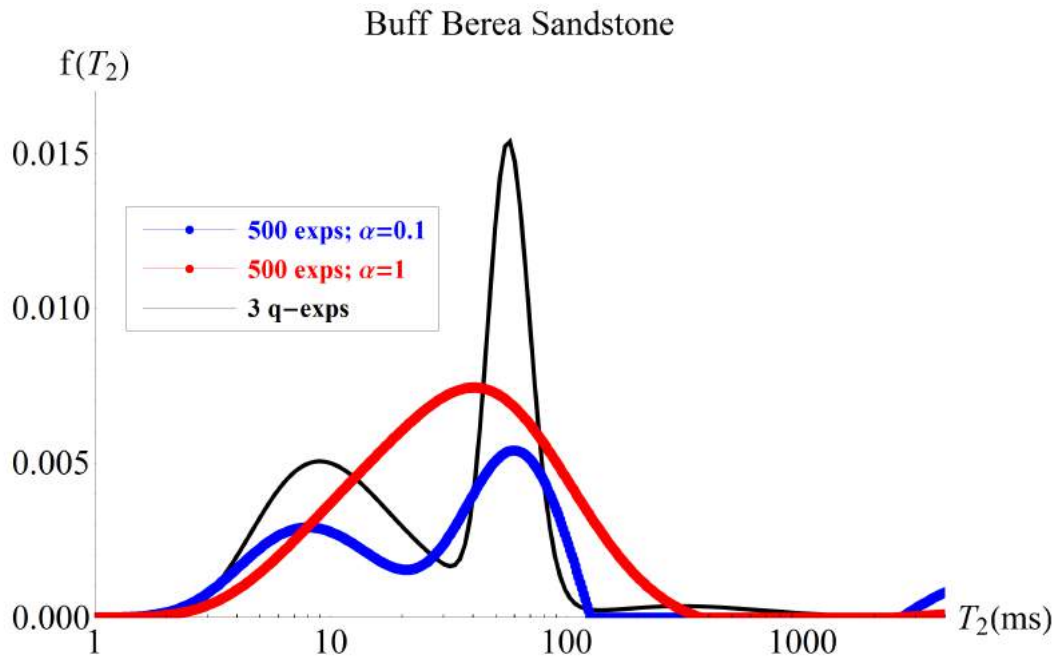


Figure 4.27.: Comparison of the  $T_2$  distributions given by q-exponential and multiexponential models.

### 4.2.7. Indiana Limestone

Fig.4.28 shows the multiexponential and q-exponential fit models for Indiana Limestone, the inset shows the error along the decay, between the model and the measured data. The  $\alpha$  parameter chosen were  $\alpha = 0.1$  and  $\alpha = 1$ . The errors associated with fits are: i)  $Error_{\alpha=0.1} = 0.002$ ; ii)  $Error_{\alpha=1} = 0.004$ ; and iii)  $Error_{q-exp} = 0.004$ . The statistical parameters associated with q-exponential model can be viewed in Table 4.7.

	fast	medium	slow
Intensity (%)	46.9	32.9	21.1
q	1.49	1.06	1.40
$\beta_0^{-1}$ (ms)	4.26	28.3	123.0
$\langle T_2 \rangle$ (ms)	8.48	30.0	206.5
$\sigma$ (ms)	94.0	7.7	299.7

Table 4.7.: Statistical parameters of three q-exponentials model for Indiana Limestone.

The Fig.(4.29) shows the behavior of  $T_2$  distribution, given by multiexponential model, with  $\alpha$  regularization parameter. In the Fig.(4.30) is possible to see the comparison between the  $T_2$  distributions of multiexponential model, with two values of  $\alpha$  parameter, and the  $f_{q,\beta_0}(T_2)$  model proposed.

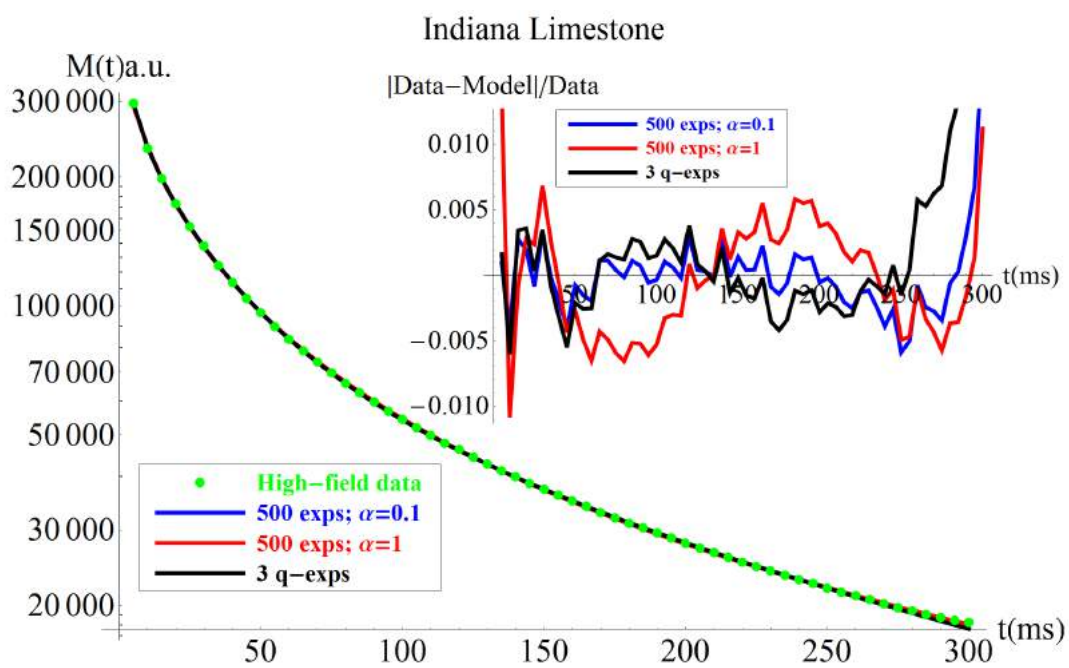
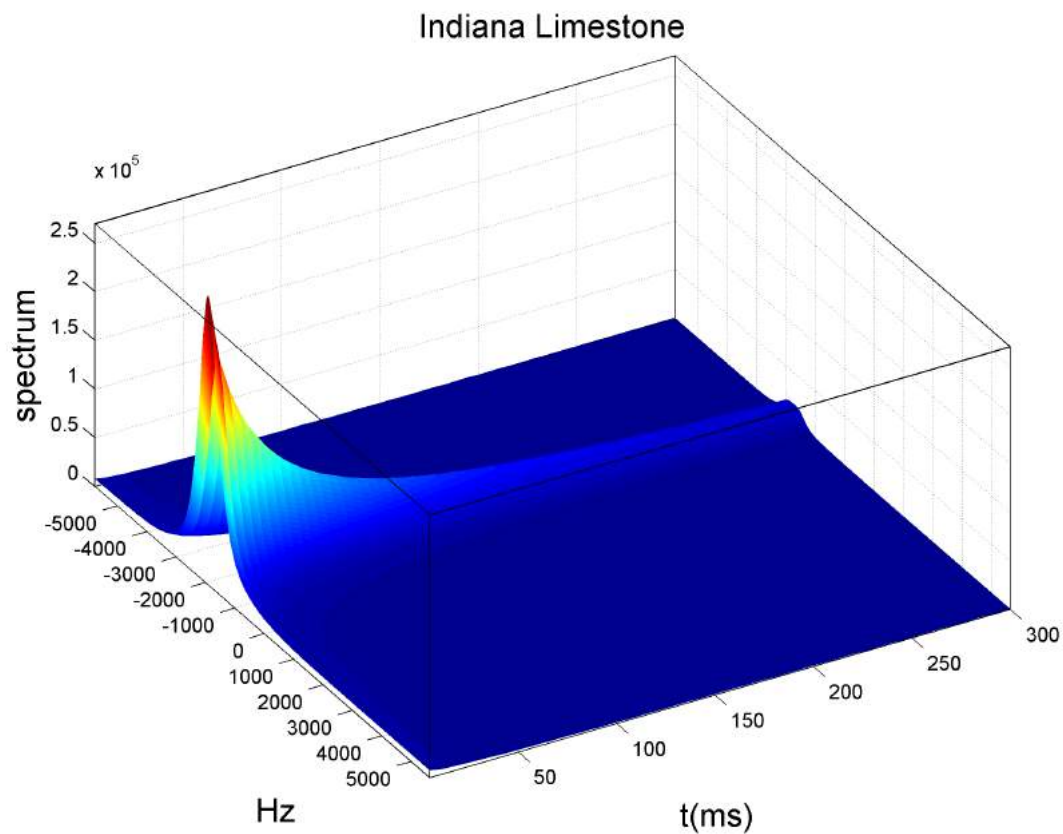


Figure 4.28.: The figure on top shows the spectrum decay in CPMG pulse sequence. The figure on bottom shows the comparison between the q-exponential and multiexponential models for the of  $T_2$  distribution for Indiana Limestone.

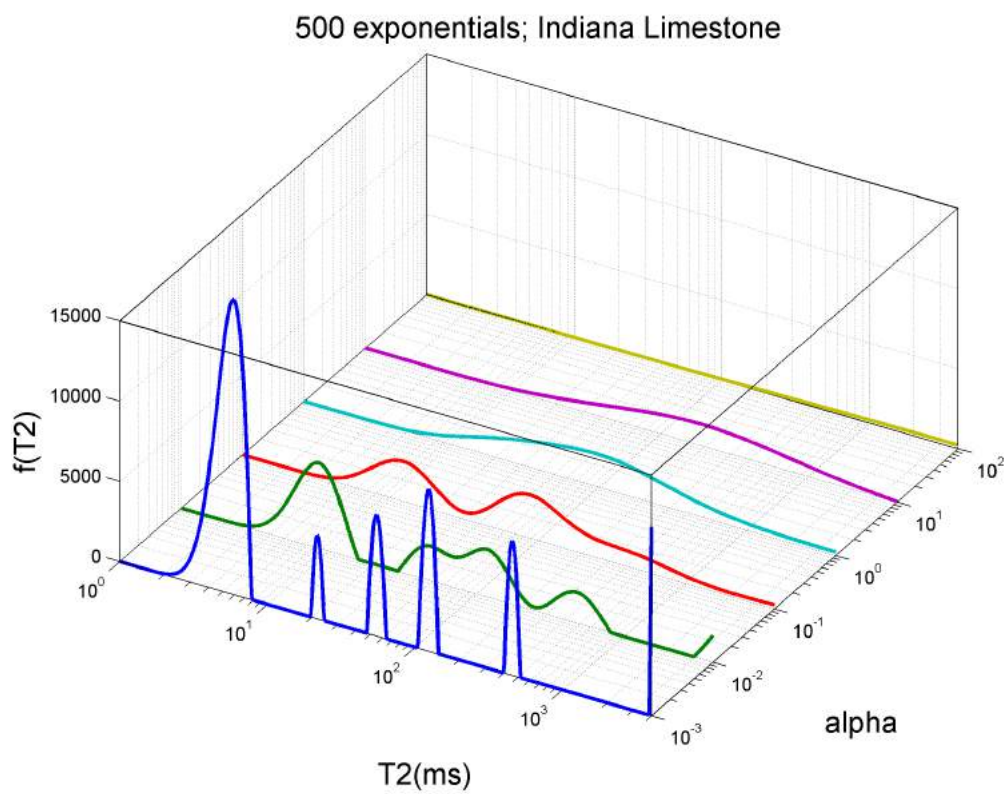
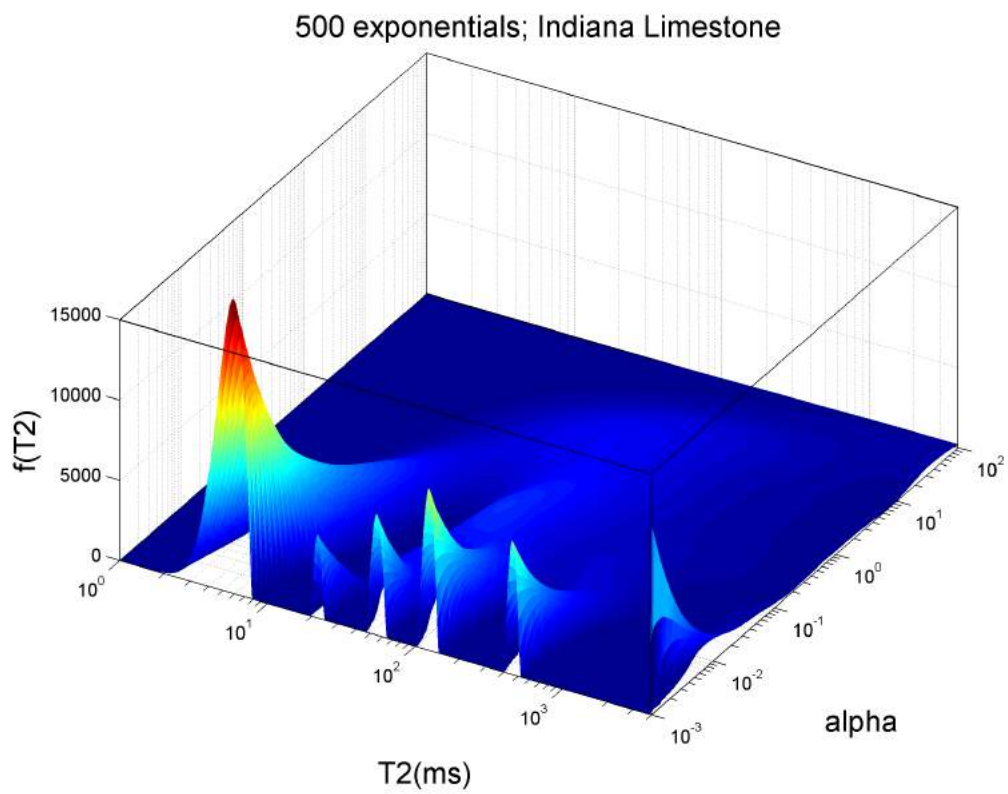


Figure 4.29.: Analyses of the regularization parameter effect,  $\alpha$ , on the  $T_2$  distribution for Indiana Limestone.

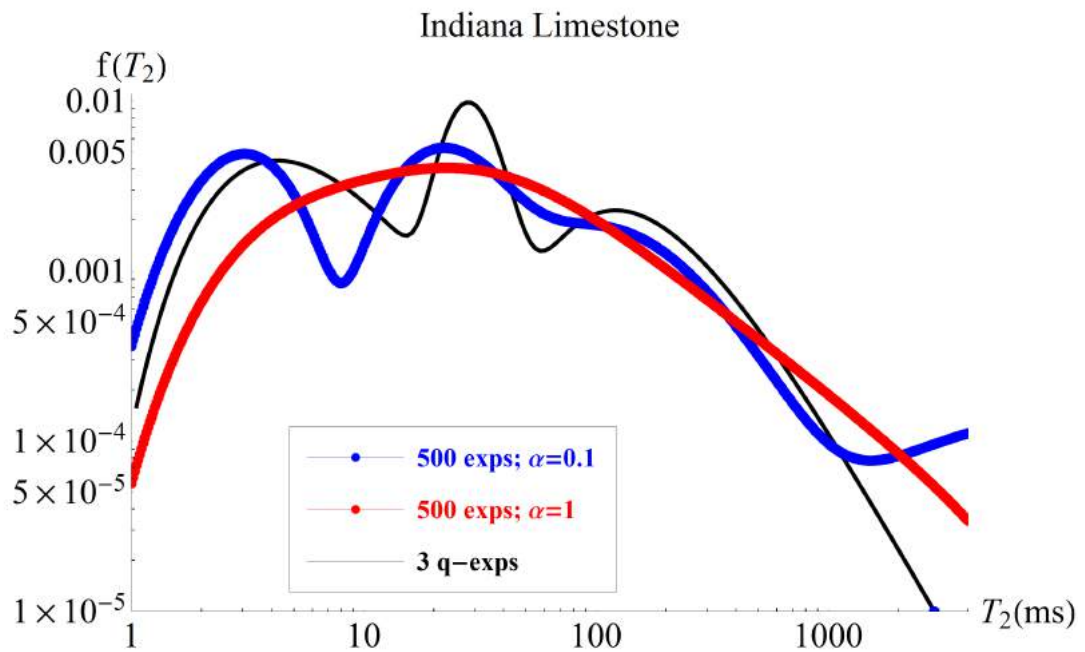
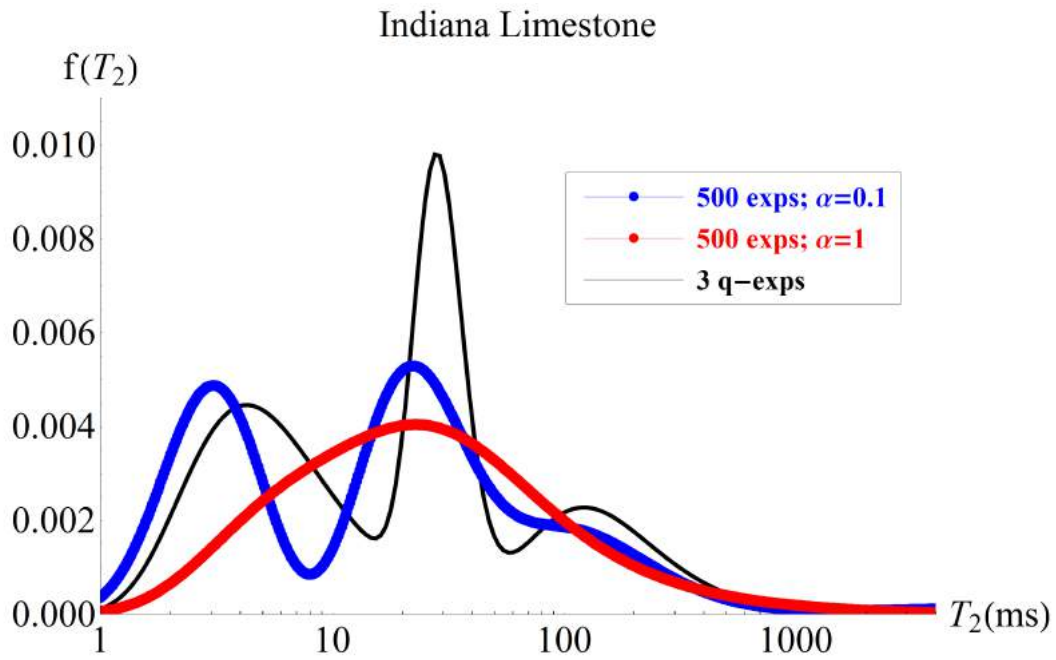


Figure 4.30.: Comparison of  $T_2$  distribution q-exponential model and multiexponential model decay.

## 5. Conclusions and Discussions

### 5.1. Prediction of pore sizes

The fast relaxation can be analytically modelled by  $n$  small pores. This suggests to use the  $T_2$  spectrum, given by Eq.(3.34), to be used in digital petrophysics where a size attribute can be extracted for each pore of sample from x-ray microtomography images. The surface relaxivity  $K$  and geometry of pore will contribute to determine the exact value of  $\zeta_0$  that is a dimensionless number between  $0 \leq \zeta \leq \pi$ . With the approximation by the first eigenvalue  $\zeta_0$  to the calculation of  $T_2$  we can explicit the dependency of pore size distribution,  $g(l)$ , and  $T_2$  distribution  $f(T_2)$ :

$$f(T_2)dT_2 = g(l)dl, \quad (5.1)$$

which leads to

$$g(l) = f(T_2)\frac{dT_2}{dl}, \quad (5.2)$$

and using Eq.(3.34), we find

$$g(l) = \frac{2Dl\zeta_0}{(D\zeta_0^2 + l^2\Gamma)^2} f\left(\frac{l^2}{D\zeta_0^2 + l^2\Gamma}\right). \quad (5.3)$$

Equation (5.3) is an analytical pore size distribution that emerge from q-exponential model for NMR transverse decay on porous media. The only problem of that model is to estimate the real value of  $\zeta_0$ , that is function of  $D$ ,

$l$  and  $K$  in a non trivial manner,  $\zeta_0 = \zeta_0(D, K, l)$ . However, the  $\zeta_0$  eigenvalue is a number between  $0 < \zeta_0 < \pi$ , and can be estimated by high resolution image analysis of microtomography, comparing with pore size distribution of 3D images. Of course that there are many assumptions in this approach, but it is an analytical function with statistical assumptions and can be used to extract petrophysical information of porous media.

In order to analyse the prediction of pore sizes from  $T_2$  measures we use a multiexponential model without inversion, using a nonlinear fit. The number of exponentials are chosen based in the spike that appear in  $T_2$  distribution with inversion when regularization parameter is low. In Fig. 4.10 is possible to see six spikes in  $T_2$  distribution when  $\alpha = 0.001$ . This spikes is in general interpreted like inversion artefacts, although this values of  $T_2$  can be related to discrete eigenvalues of diffusion equation for pore structure. If this is true, the model with six exponential with  $T_2$  values close to the values of the spikes, can describe well the data. However if the six exponential fit well the data, it is not a proof that these values are the pore structure eigenvalues.

The fit of one six exponentials model and three q-exponentials is shown in Fig.5.1. The two models were found by one nonlinear fit and not by regularization procedure. The error associated to the  $T_2$  decay is around 0.1% and is less than thick plot bullet. It impossible to distinguish visually the difference between the data decay and the two models. One plot of the ratio *model/data* was shown too in the Fig.5.1 for multiexponential model with regularization procedure, with nonlinear fit and q-exponential model with nonlinear fit. All models fit well the data with acceptable error.

The model with six exponentials for magnetization decay found is:

$$M(t) = 31496.2 \times e^{-\frac{t}{9.86}} + 22838.8 \times e^{-\frac{t}{22.3}} + 75287.2 \times e^{-\frac{t}{111.2}} + 184812.0 \times e^{-\frac{t}{384.4}} + 94527.2 \times e^{-\frac{t}{796.0}} + 15973.0 \times e^{-\frac{t}{3414.8}}. \quad (5.4)$$

It is most convenient to write the magnetization in terms of the initial magnetization:

$$\frac{M(t)}{M_0} = 0.074 \times e^{-\frac{t}{9.86}} + 0.054 \times e^{-\frac{t}{22.3}} + 0.177 \times e^{-\frac{t}{111.2}} + 0.435 \times e^{-\frac{t}{384.4}} + 0.222 \times e^{-\frac{t}{796.0}} + 0.038 \times e^{-\frac{t}{3414.8}}. \quad (5.5)$$

The above equation means that the decay  $M(t)$  have six modes with relative intensities of 7.4%, 5.4%, 17.7%, 43.5%, 22.2% and 3.8%. In the approximation of the fast diffusion, only the first eigenvalue of each pore is representative for the magnetization signal, so consequently the only one exponential is correspondent to each pore. This assumptions leads to a interpretation of that the pore structure of Microesferas sample A is composed by only six pore sizes. Using Equation (5.1) we can estimate the pore diameters associated to these relaxation  $T_2$  times. The pore diameter associated to one  $T_2$  time is:

$$l = \sqrt{\frac{D\zeta_0^2 T_2}{1 + T_2 \Gamma}}. \quad (5.6)$$

Using  $\Gamma \rightarrow 0$ ,  $D = 10^{-9} m^2/s$  and  $\zeta_0 = \pi/2$ , we found the following pore diameters with relative percent value for total volume: 7.4% of  $3.93 \mu m$ , 5.4% of  $5.92 \mu m$ , 17.7% of  $13.2 \mu m$ , 43.5% of  $24.6 \mu m$ , 22.2% of  $35.9 \mu m$  and 3.8% of  $73.2 \mu m$ .

When we predict pore sizes from  $T_2$  times, we are supposing implicitly a value for surface relaxivity  $K$ . The value of  $K$  will influence in value of eigenvalue  $\zeta_0$ . The eigenvalue  $\zeta_0$  is function of diffusion coefficient  $D$ , surface relaxivity  $K$  and geometry of that can be simplified by the pore size attribute  $l$ ,  $\zeta_0 = \zeta_0(D, K, l)$ . However, as we seen before, the  $\zeta_0$  is a dimensionless number between  $0 \leq \zeta_0 \leq \pi$ . The pore diameters estimation by magnetization decay and function of eigenvalue  $\zeta_0$  can be view in Fig.5.2.

This spikes can be related to the eigenvalues of pore structure, but to prove

Microesferas A; 425–600 $\mu\text{m}$

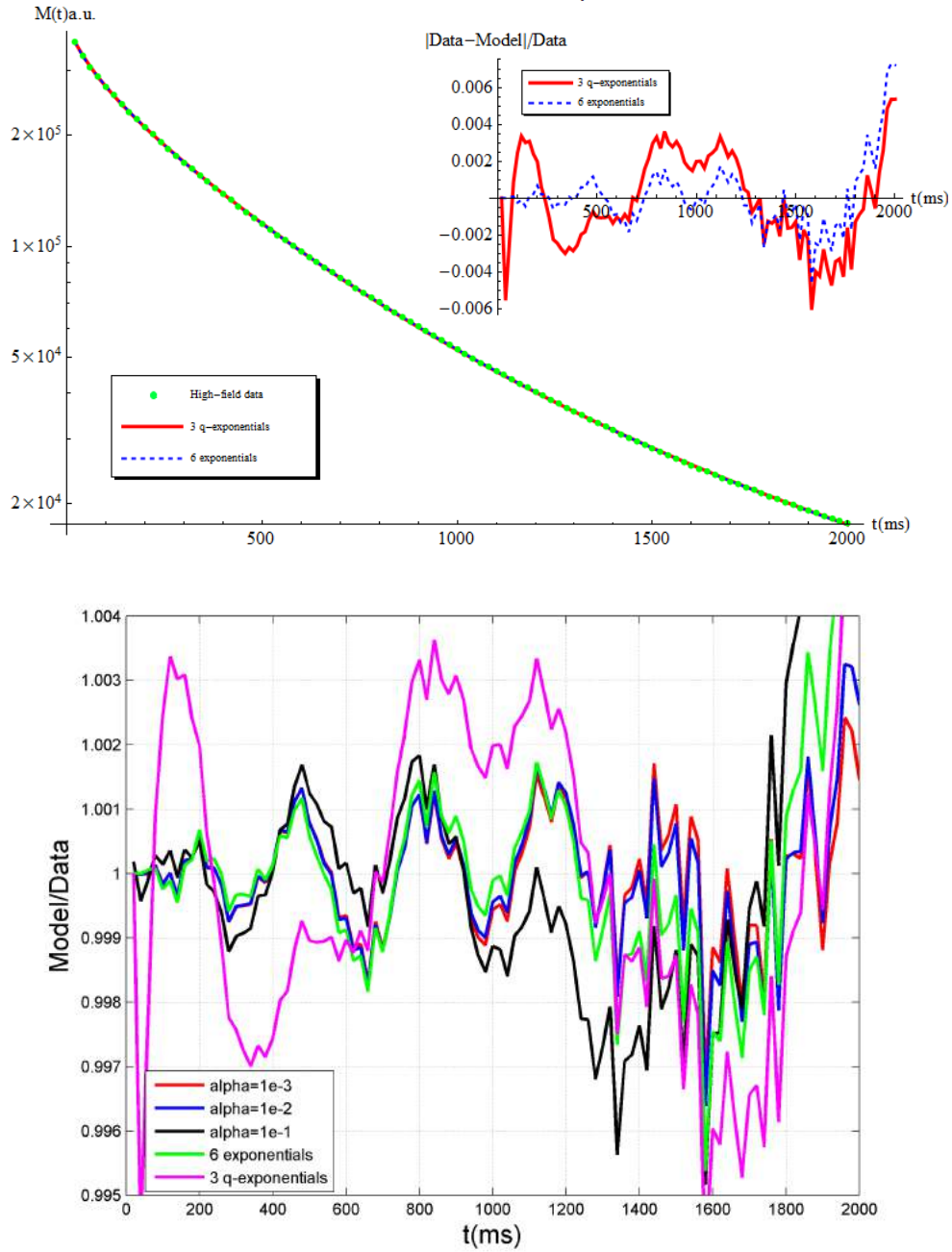


Figure 5.1.: The figure on top show the model fit of six exponentials and three q-exponentials. The bottom figure show the ratio  $model/data$  to analyse the quality of fit. All models fit well with less than 0.4% of error.

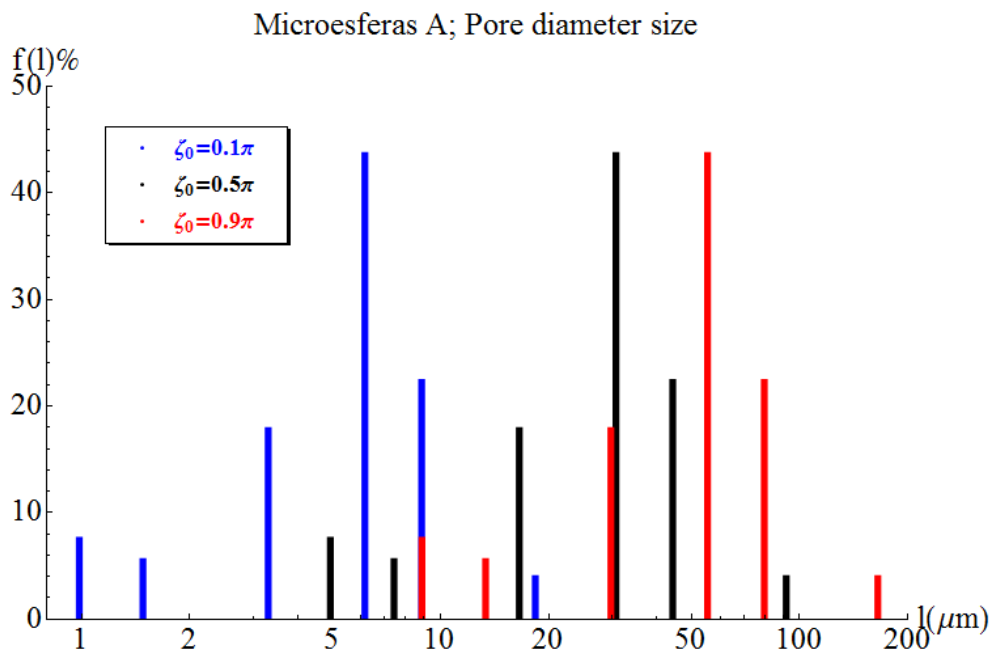


Figure 5.2.: Discrete distribution of six exponentials model in function of eigenvalue  $\zeta_0$ . The blue lines are the distribution of pore diameters for  $\zeta_0 = 0.1\pi$ , the black lines for  $\zeta_0 = 0.5\pi$  and red is for  $\zeta_0 = 0.9\pi$ . The pore size diameter is linear with the eigenvalue  $\zeta_0$ .

or disprove this statement, more investigation is needed. One way to treat this problem and possibly elucidate this point, is numerically solve diffusion equation with boundary condition in a  $3D$  microtomography image.

## 5.2. Concluding remarks

Prediction of  $T_2$  distribution from transverse relaxation decay in NMR experiments on porous media is an ill-posed problem [1, 14], but the diffusion equation with boundary and initial conditions, commonly used to describe this phenomenon, is a well-posed problem [107]. Well-posedness means that solution exists, is unique, and changes continuously with initial condition [108]. Porous media is composed by many pores of different sizes and shapes, and the total transverse magnetization signal is a statistical sum of the signal from each pore. In each one the magnetization is described by the diffusion equation with boundary and initial conditions, but due to the statistical nature of the signal response, the inversion of transverse relaxation data of a porous media becomes an ill-posed problem. There are yet other difficulties associated to the description of NMR on porous media, such as the distance of correlation between the spin in the fluid and the spin in the matrix, contributing to superficial relaxation, superficial mineralogical spatial distribution, which results in a distribution of values for the superficial relaxation parameter, effects of paramagnetic impurities, which may be present in the fluid and in the solid, and so on.

The multiexponential model emerges naturally from the concept that each pore contributes with one single exponential, so the total signal can be approximated by a finite sum of exponentials. The Robin boundary condition, considers that the relaxation in one pore has a contribution from diffusion, driven by diffusion coefficient  $D$ , and another from the surface driven by surface relaxativity  $K$ . By solving the analytical problem for only one spherical

pore, it is possible to see that the solution is a discrete infinite sum of exponentials Eq. (4.4), and that the second eigenvalue  $\zeta_1$  contributes less than 0.4% to the intensity in Eq. (3.37) if compared to the first eigenvalue  $\zeta_0$ , when the radius of sphere is less than 0.5mm, and  $D = 10^{-9}\text{m}^2/\text{s}$  and  $K = 10^{-6}\text{m}/\text{s}$  [70].

The superstatistical model proposed for transverse relaxation decay, yields an analytical function for  $T_2$  distribution, and therefore is free from numerical artefacts. Basically, the model is an *infinite* sum of exponentials with a known distribution. For  $\chi^2$  distributions, the sum is represented by the so-called  $q$ -exponentials. We illustrated the model with  $\chi^2$ -distribution for inverse of  $T_2$  and this leads naturally to a new basis function  $f_{q,\beta_0}(T_2)$ , Eq. (4.10). For  $q \rightarrow 1$  the distribution is a Dirac delta-like:  $f_{1,\beta_0}(T_2) \propto \delta(T_2 - \langle T_2 \rangle)$ . Therefore, the superstatistical model can be viewed as a generalization of a multiexponential basis. The main advantages of this model are: (i) with only two  $f_{q,\beta_0}(T_2)$  functions it is possible to solve non-linear least squares problem and obtain a good description of porous media, without introducing the bias of regularization; (ii) the function  $f_{q,\beta_0}(T_2)$  yields information about a population of spins with a well defined mean and standard deviation of  $T_2$ , describing naturally collective and statistical behavior; (iii) this function is defined in all positive domain of real numbers and goes to zero when  $T_2 \rightarrow \infty$ , so it does not have artefacts from finite size effect; iv) small number of non-linear parameters and physical interpretation of each one.

In order to verify the applicability of the model to the routine of a porous media laboratory, we used low-field data from PETROBRAS NMR Laboratory in CENPES of Indiana Limestone. Figure 5.3 shows the decay of the magnetization. We see that from 500ms onwards the noise becomes rather important. This amount of noise is yet not comparable to well log data, but in this last case our methodology can also be applied, as well. The data were

fitted by the two models, three multiexponentials with different regularization parameters  $\alpha$ , and two  $q$ -exponentials with no regularization at all. The three sets of two hundred exponentials are close to each other for most of the time interval. The  $q$ -exponential model is comparable to the others up to  $t \cong 1200\text{ms}$ , after which a small divergence can be observed. However, from Fig 5.4, it is possible to see how regularization can lead to spiky distributions. An important statistical parameter to compare distribution is the logarithmic mean  $T_{2LM}$  [109] and for the distribution of Fig. (5.4) the  $q$ -exponential yields  $T_{2LM} = 130.3\text{ms}$ , whereas for the multiexponentials  $T_{2LM} = 107.8\text{ms}$ ,  $107.3\text{ms}$  and  $111.1\text{ms}$  for  $\alpha = 0.01$ ;  $0.1$ ; and  $1$ , respectively, which are in good agreement with each other. The  $q$ -exponential provides average slightly larger due long tail behavior of distribution, i.e., the  $q$ -exponential model has infinite and continuous spectrum of exponentials while multiexponential model has finite spectrum of exponentials.

The minimization of non-linear least square in a two  $q$ -exponential model,

$$M(t) = I_1 e_{q_1}^{-\beta_{01}t} + I_2 e_{q_2}^{-\beta_{02}t}, \quad (5.7)$$

yields directly the statistical parameters of the analytical distribution of  $T_2$ :

$$g(T_2) = I_1 f_{q_1, \beta_{01}}(T_2) + I_2 f_{q_2, \beta_{02}}(T_2), \quad (5.8)$$

where  $f_{q, \beta_0}(T_2)$  is given by Equation (4.10). Note that the normalization coefficients of the distributions  $g(T_2)$ , and the amplitudes of the multiexponential functions, Eq. (3.69), are given by initial magnetization  $M_0$ :

$$I_1 + I_2 = \sum_{i=1}^{N_{exp}} a_i = M_0. \quad (5.9)$$

In summary, we have presented a method which allows the analysis  $T_2$  decay

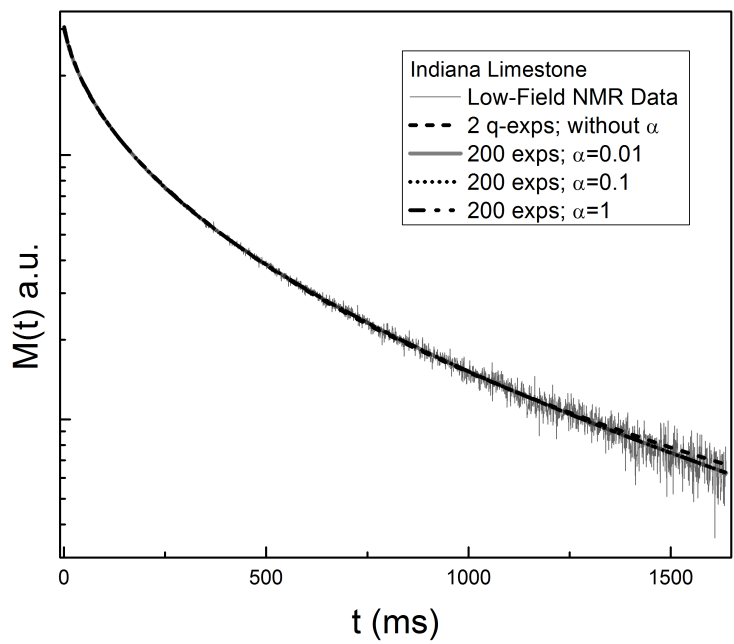


Figure 5.3.: Low-field NMR transverse data decay for Indiana Limestone sample. We have fitted four curves, three multiexponentials with different values for Tikhonov regularization, and a two  $q$ -exponentials curves.

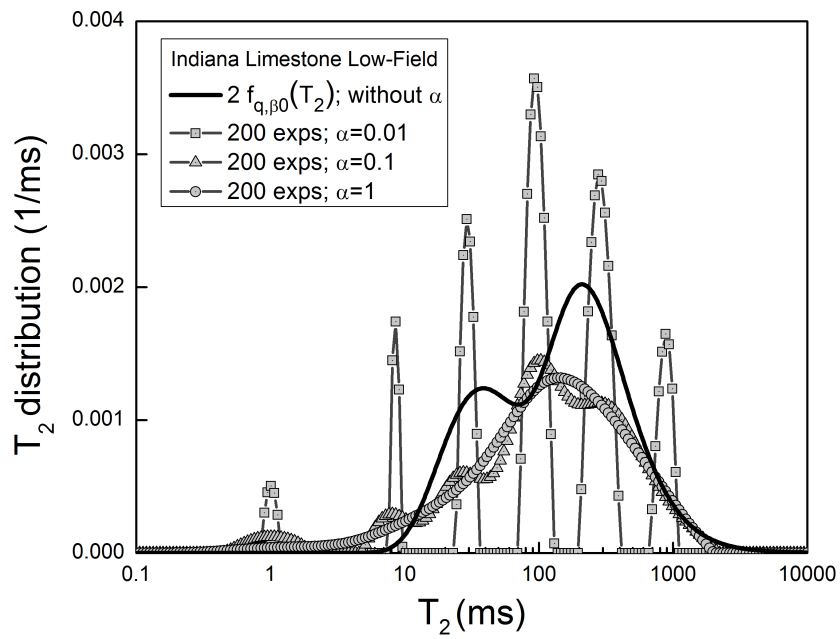


Figure 5.4.: Normalised four distributions of  $T_2$  NMR low-field data decay of Indiana Limestone. The squares obtained from the multiexponential model with low value of regularization, and exhibits a non-physical oscillating behavior.

on porous media based on superstatistics. It would be interesting to attempt the method using distributions other than  $\chi^2$ . Among the petrophysical information which can be obtained with the analytical function  $f_{q,\beta_0}(T_2)$  are the same one with multiexponential analysis: i) fluid content (gas, water or oil) in geological reservoir; ii) permeability and porosity analysis; iii) volumes of free and bound fluid and etc. Analysis of other petrophysical parameters, such as  $T_{2cutoff}$ , can be improved using the method. If we identify the parameters  $I_1$  and  $I_2$  in Eq. (5.8) with the Bound Volume Index (BVI) and the Free Volume Index (FVI), the model can predict the  $T_{2cutoff}$  directly from the data of only one experiment. The transcendental equation for  $T_{2cutoff}$  prediction will be:

$$\int_0^{T_{2cutoff}} [BVI f_{q_1, \beta_{01}}(T_2) + FFI f_{q_2, \beta_{02}}(T_2)] dT_2 = BVI, \quad (5.10)$$

which leads to

$$BVI \frac{\Gamma\left(\frac{1}{q_1-1}, \frac{1}{(q_1-1)\beta_{01}T_{2cutoff}}\right)}{\Gamma\left(\frac{1}{q_1-1}\right)} + FFI \frac{\Gamma\left(\frac{1}{q_2-1}, \frac{1}{(q_2-1)\beta_{02}T_{2cutoff}}\right)}{\Gamma\left(\frac{1}{q_2-1}\right)} = BVI. \quad (5.11)$$

All the parameters in Eq. (5.11) are obtained from the fitting procedure, and the  $T_{2cutoff}$  can be easily calculated from this expression. The presence of Clay Bound Water (CBW) can be taken into account by using three  $q$ -exponentials:

$$g(T_2) = CBW f_{q_1, \beta_{01}}(T_2) + BVI f_{q_2, \beta_{02}}(T_2) + FFI f_{q_3, \beta_{03}}(T_2). \quad (5.12)$$

These possibilities will be exploited in future works.

# A. Microesferas samples C, D and E

## A.1. Microesferas C: 106-212 $\mu m$ range diameter

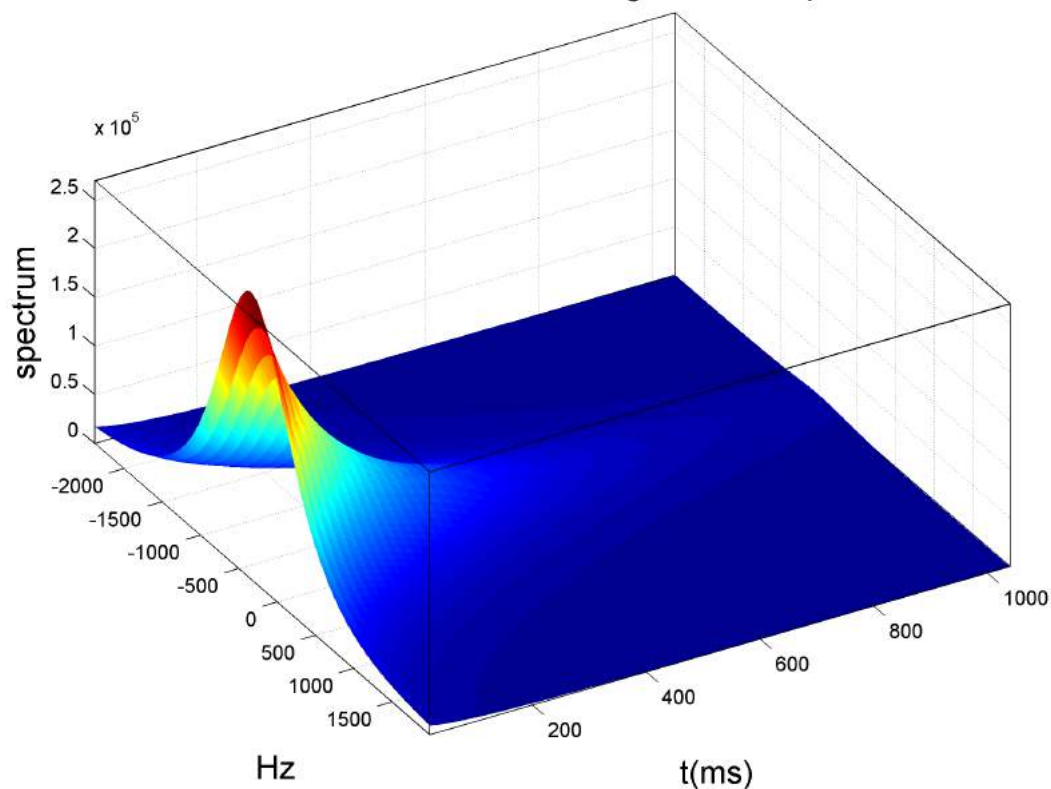
Fig.A.1 shows the multiexponential and q-exponential fit models for Microesfera sample C (106-212 $\mu m$ ), the inset shows the error along the decay, between the model and the measured data. The  $\alpha$  parameters chosen were  $\alpha = 0.01$  and  $\alpha = 0.1$ . The errors associated with fits are: i)  $Error_{\alpha=0.01} = 0.0007$ ; ii)  $Error_{\alpha=0.1} = 0.003$ ; and iii)  $Error_{q-exp} = 0.004$ . The statistical parameters associated with q-exponential model can be viewed in Table A.1.

	fast	medium	slow
Intensity (%)	23.2	64.0	12.8
q	1.31	1.07	1.18
$\beta_0^{-1}$ (ms)	42.5	165.3	344.4
$\langle T_2 \rangle$ (ms)	61.7	178.6	422.4
$\sigma$ (ms)	56.0	52.9	228.6

Table A.1.: Statistical parameters of three q-exponentials model for Microesferas sample C.

The Fig.(A.2) shows the behavior of  $T_2$  distribution, given by multiexponential model, with  $\alpha$  regularization parameter. In the Fig.(A.3) is possible to see the comparison between the  $T_2$  distributions of multiexponential model, with two values of  $\alpha$  parameter, and the  $f_{q,\beta_0}(T_2)$  model proposed. The multiexponential model predicts a regime of very fast decay, with values close to

Microesferas C; 106-212 $\mu$ m glass microsphere



Microesferas C; 106-212 $\mu$ m

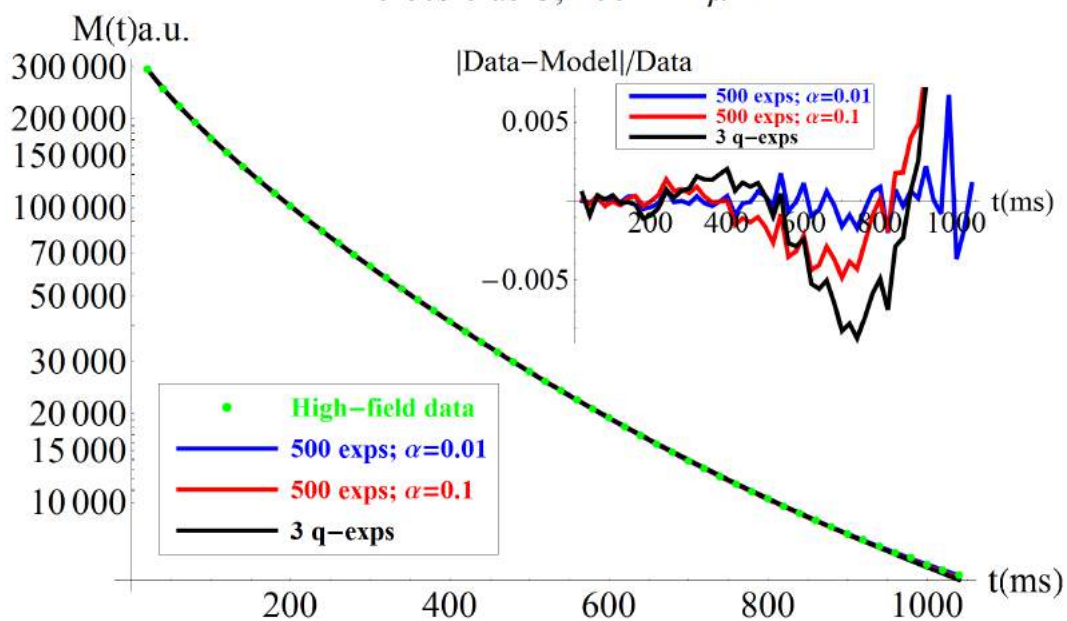


Figure A.1.: The figure on top shows the spectrum decay in CPMG pulse sequence. The figure on bottom shows the comparison between the q-exponential and multiexponential models for the  $T_2$  distribution in Microesferas sample C.

$T_2 = 10ms$ . The most part of spins decay with time close to  $T_2 = 200ms$  for all the three fit models.

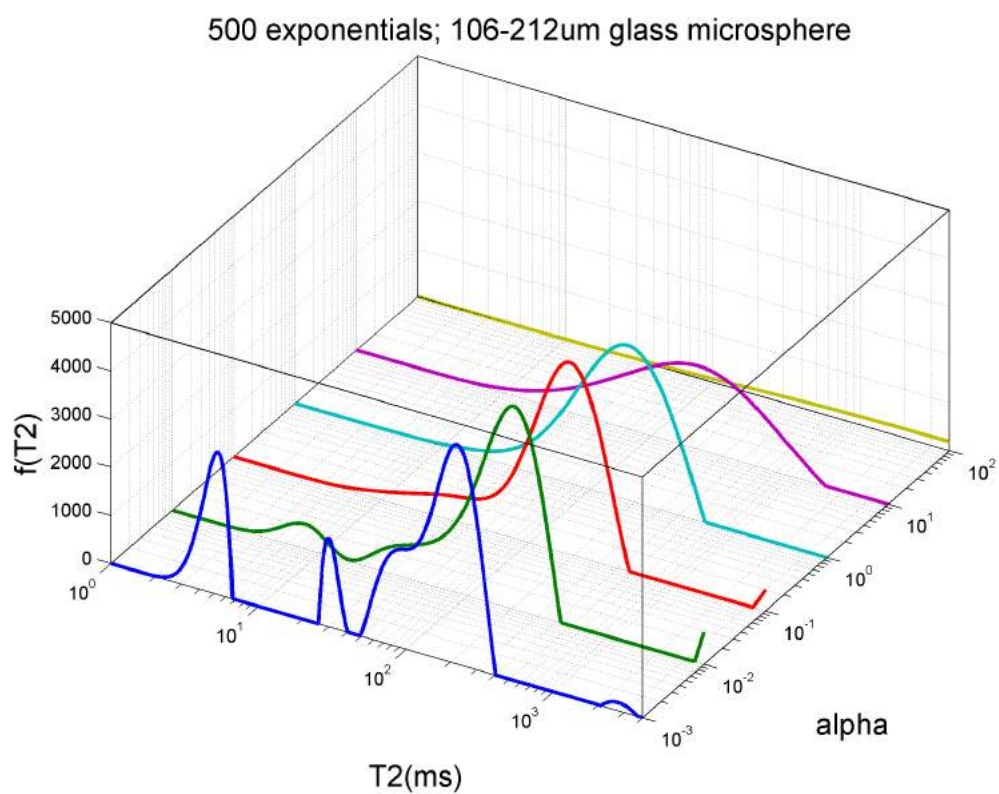
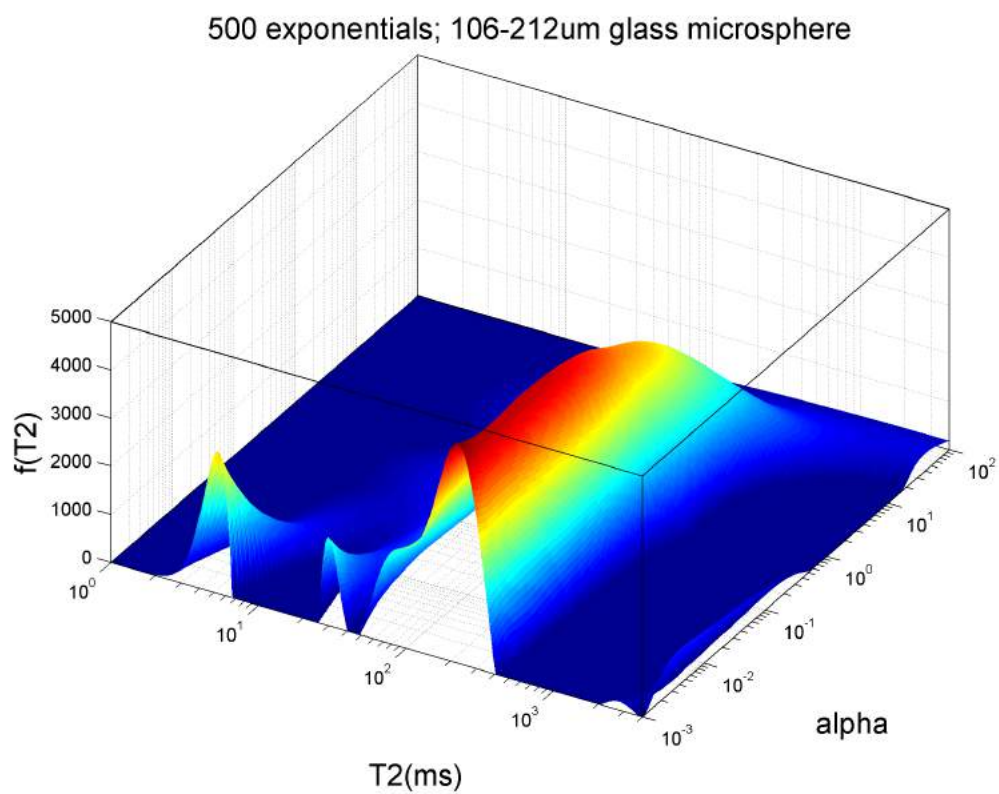


Figure A.2.: Analyses of the regularization parameter effect,  $\alpha$ , effect on the  $T_2$  distribution for Microesferas sample C.

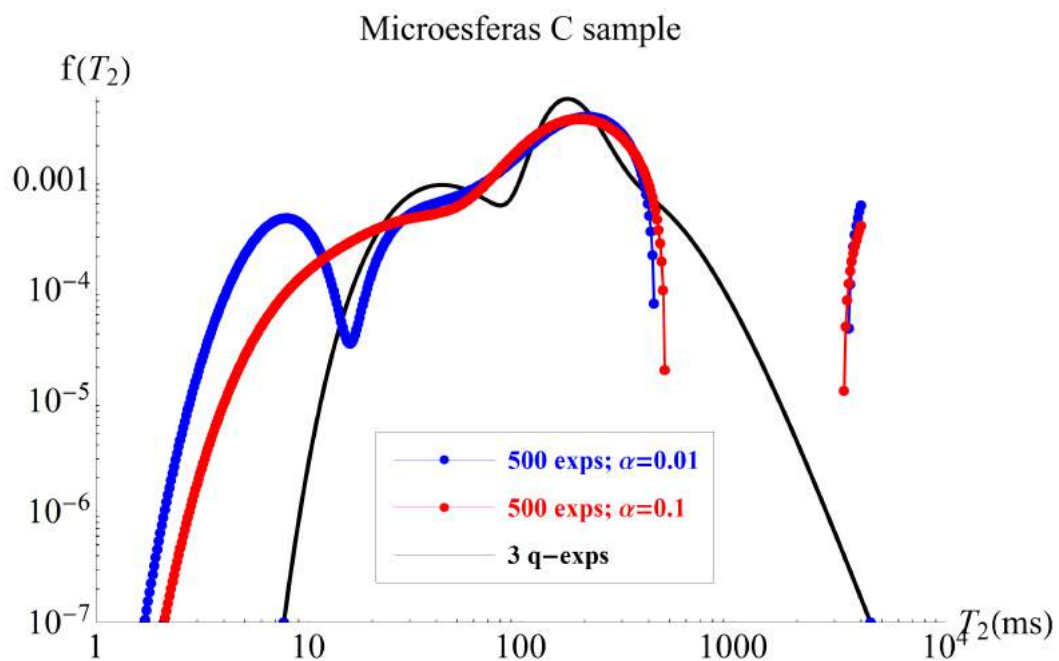
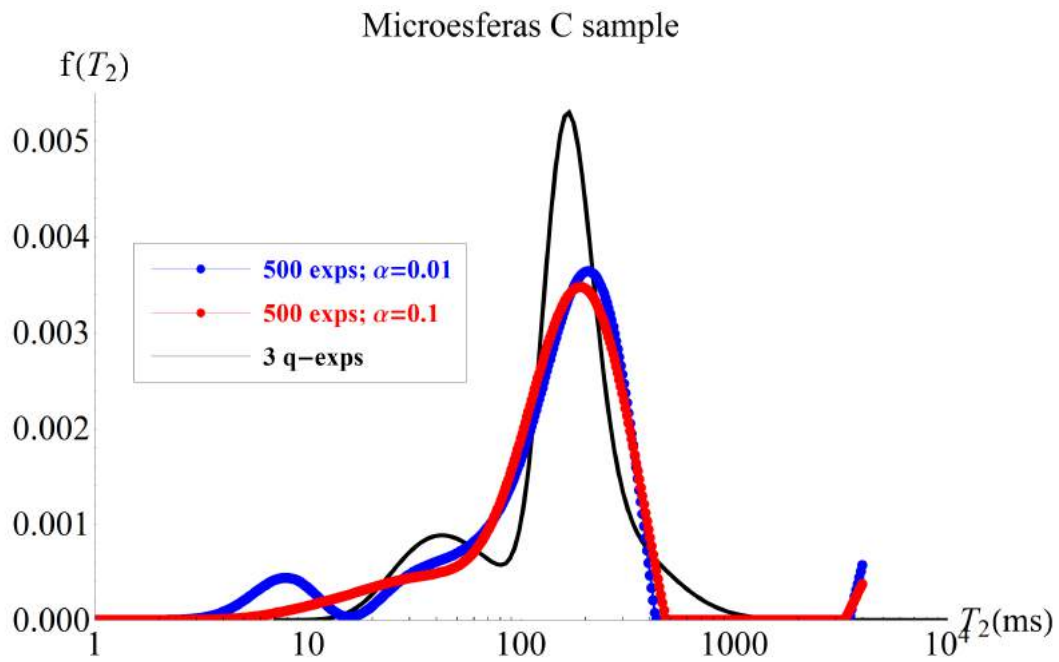


Figure A.3.: Comparison of the  $T_2$  distributions given by q-exponential and multiexponential models.

## A.2. Microesferas D: 75-125 $\mu m$ range diameter

Fig.A.4 shows the multiexponential and q-exponential fit models for Microesfera sample D (75-125 $\mu m$ ), the inset shows the error along the decay, between the model and the measured data. The  $\alpha$  parameter chosen were  $\alpha = 0.1$  and  $\alpha = 1$ . The errors associated with fits are: i)  $Error_{\alpha=0.1} = 0.005$ ; ii)  $Error_{\alpha=1} = 0.03$ ; and iii)  $Error_{q-exp} = 0.006$ . The statistical parameters associated with q-exponential model can be viewed in Table A.2.

	fast	medium	slow
Intensity (%)	33.2	59.3	7.4
q	1.34	1.04	1.30
$\beta_0^{-1}$ (ms)	50.8	242.2	802.6
$\langle T_2 \rangle$ (ms)	77.4	253.2	1144.6
$\sigma$ (ms)	80.7	55.0	986.3

Table A.2.: Statistical parameters of three q-exponentials model for Microesferas sample D.

The Fig.(A.5) shows the behavior of  $T_2$  distribution, given by multiexponential model, with  $\alpha$  regularization parameter. In the Fig.(A.6) is possible to see the comparison between the  $T_2$  distributions of multiexponential model, with two values of  $\alpha$  parameter, and the  $f_{q,\beta_0}(T_2)$  model proposed.

Microesferas D; 75-125um glass microsphere

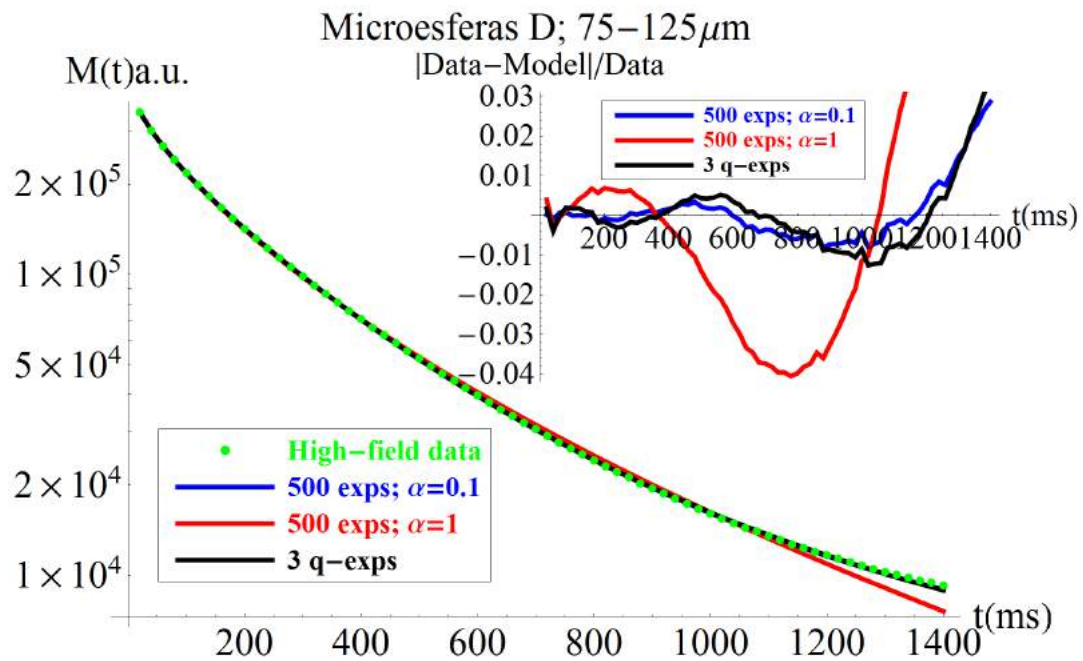
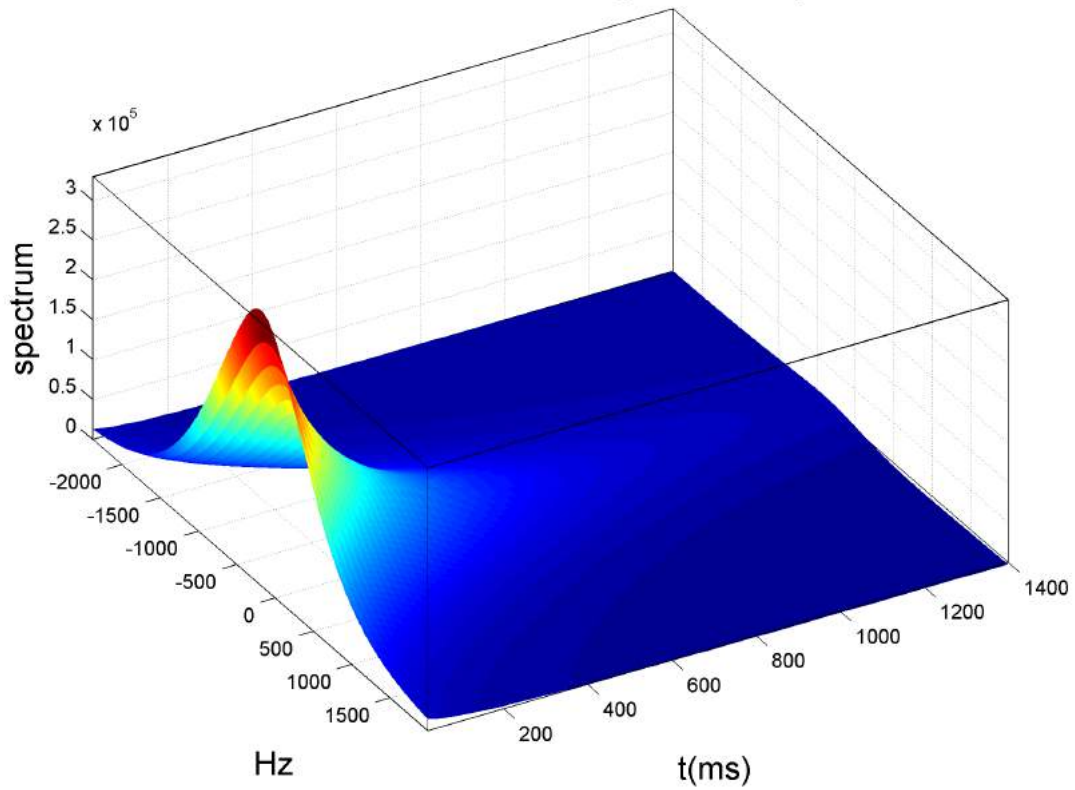


Figure A.4.: The figure on top shows the spectrum decay in CPMG pulse sequence. The figure on bottom shows the comparison between the q-exponential and multiexponential models for the of  $T_2$  distribution in Microesferas sample D.

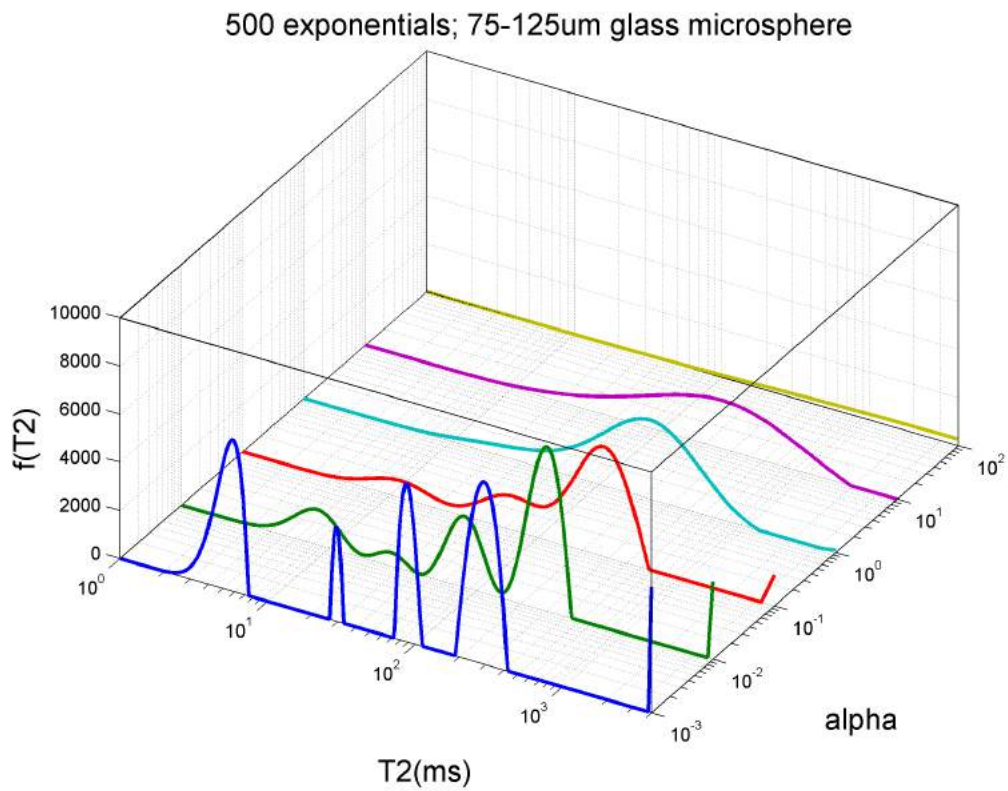
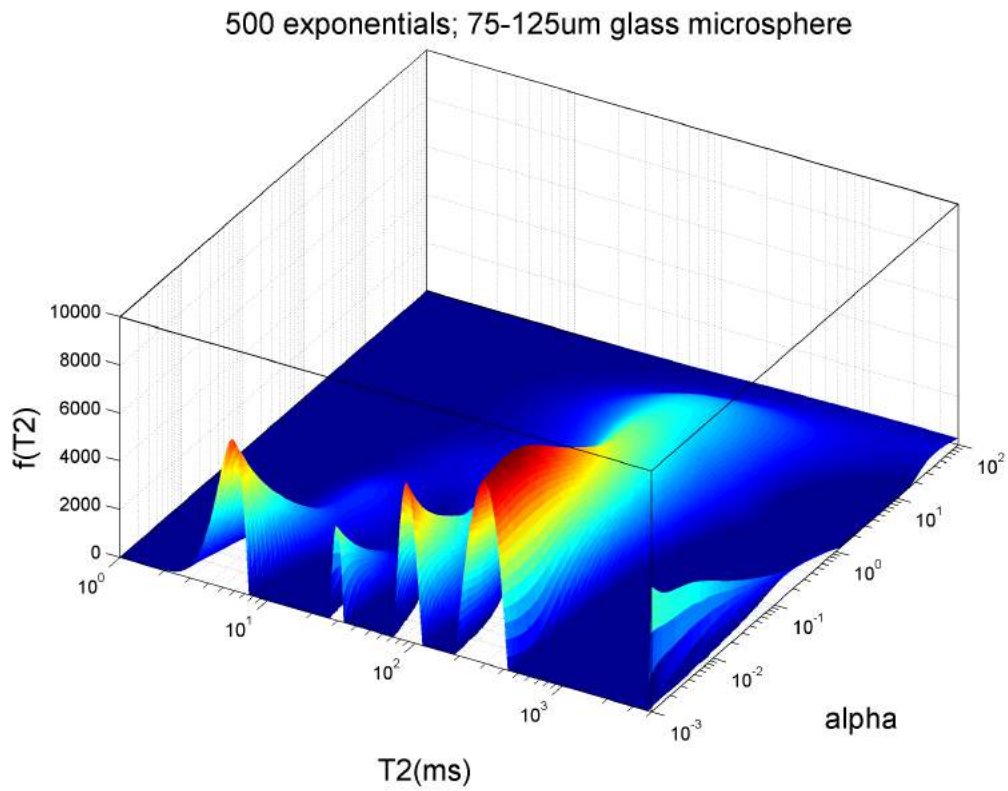


Figure A.5.: Analyses of the regularization parameter effect,  $\alpha$ , on the  $T_2$  distribution for Microesferas sample D.

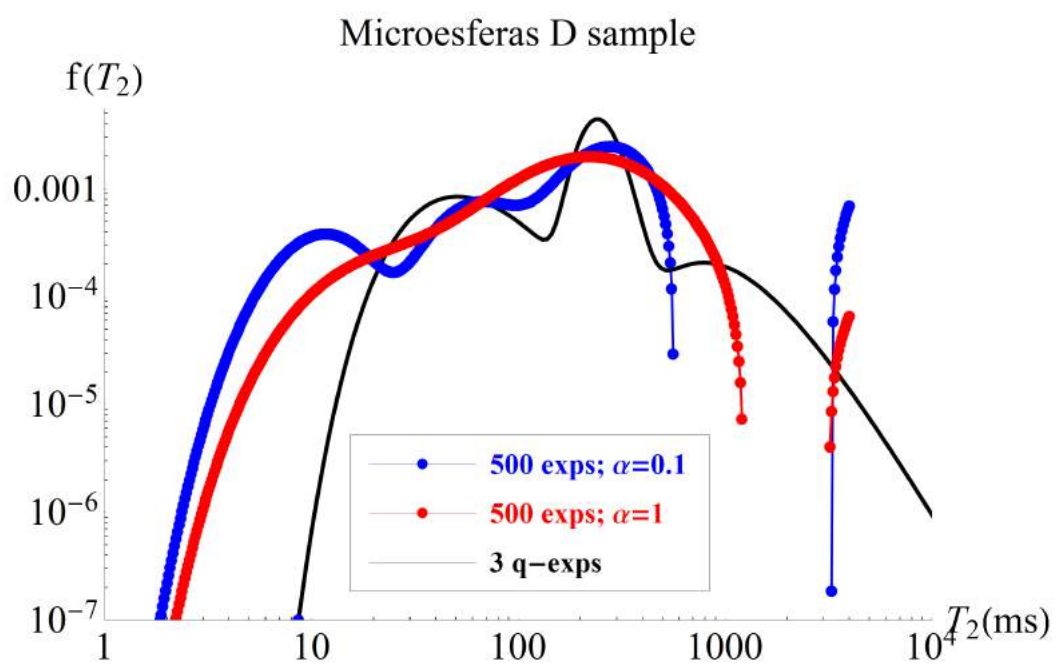
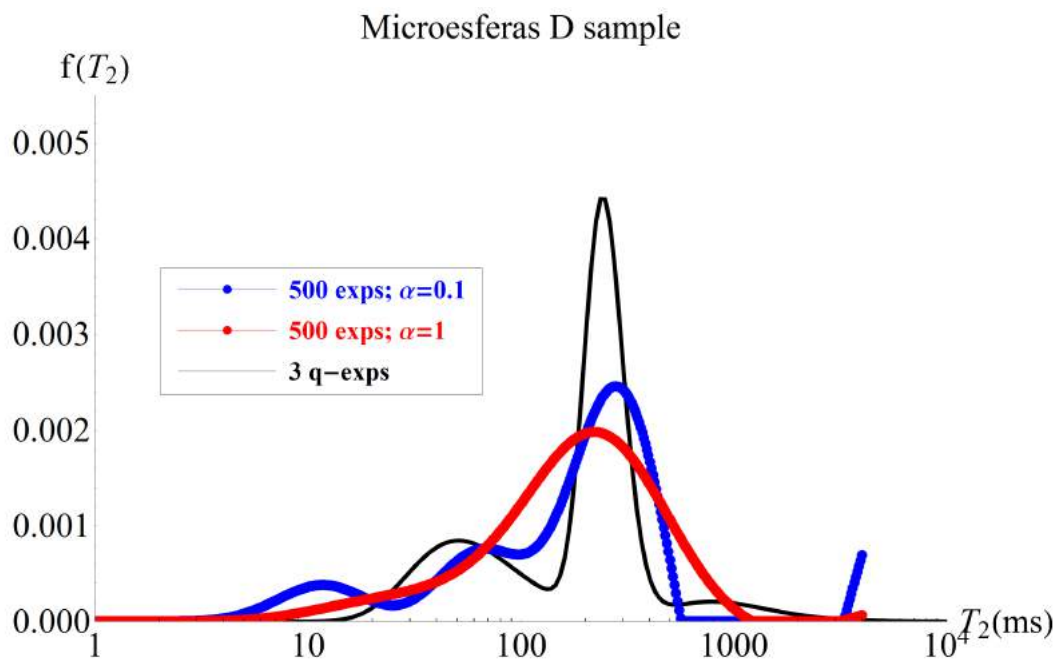


Figure A.6.: Comparison of the  $T_2$  distributions given by q-exponential and multiexponential models.

### A.3. Microesferas E: 45-90 $\mu m$ range diameter

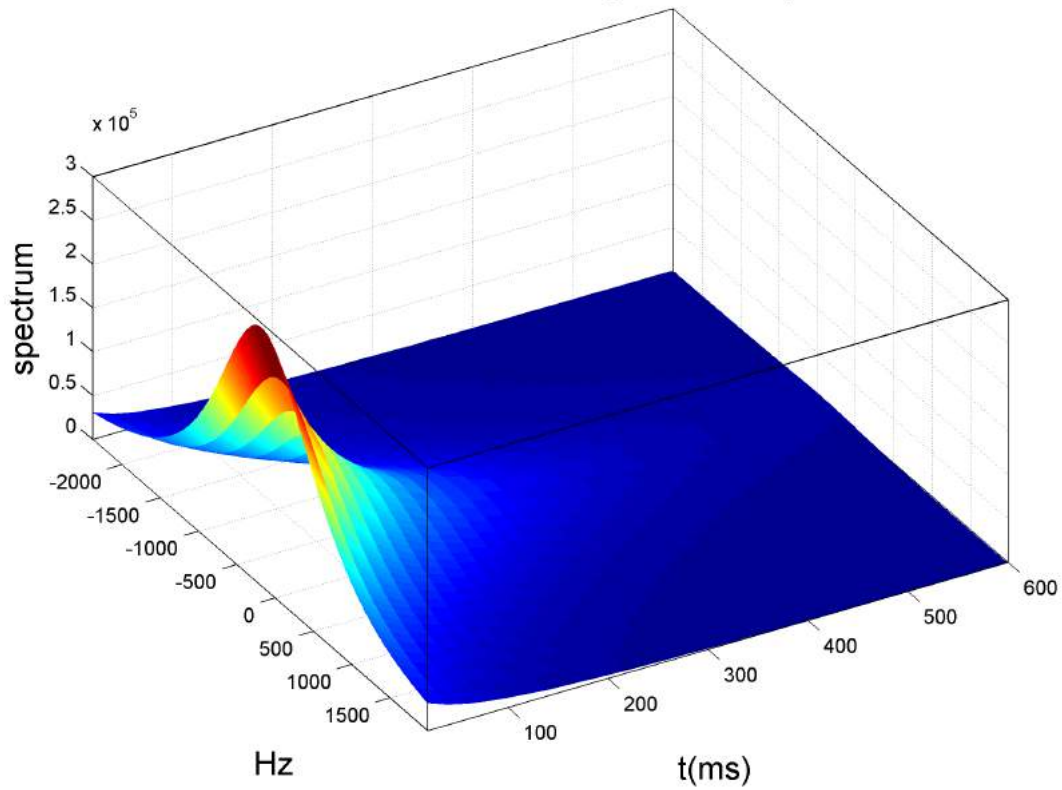
Fig.A.7 shows the multiexponential and q-exponential fit models for Microesfera sample E (45-90 $\mu m$ ), the inset shows the error along the decay, between the model and the measured data. The  $\alpha$  parameter chosen were  $\alpha = 0.1$  and  $\alpha = 1$ . The errors associated with fits are: i)  $Error_{\alpha=0.1} = 0.005$ ; ii)  $Error_{\alpha=1} = 0.041$ ; and iii)  $Error_{q-exp} = 0.002$ . The statistical parameters associated with q-exponential model can be viewed in Table A.3.

	fast	medium	slow
Intensity (%)	41.2	56.9	1.9
q	1.21	1.04	1.32
$\beta_0^{-1}$ (ms)	38.3	111.9	493.9
$\langle T_2 \rangle$ (ms)	48.4	116.8	731.8
$\sigma$ (ms)	28.9	24.8	705.6

Table A.3.: Statistical parameters of three q-exponentials model for Microesferas sample E.

The Fig.(A.8) shows the behavior of  $T_2$  distribution, given by multiexponential model, with  $\alpha$  regularization parameter. In the Fig.(A.9) is possible to see the comparison between the  $T_2$  distributions of multiexponential model, with two values of  $\alpha$  parameter, and the  $f_{q,\beta_0}(T_2)$  model proposed.

Microesferas E; 45-90 $\mu$ m glass microsphere



Microesferas E; 45-90 $\mu$ m

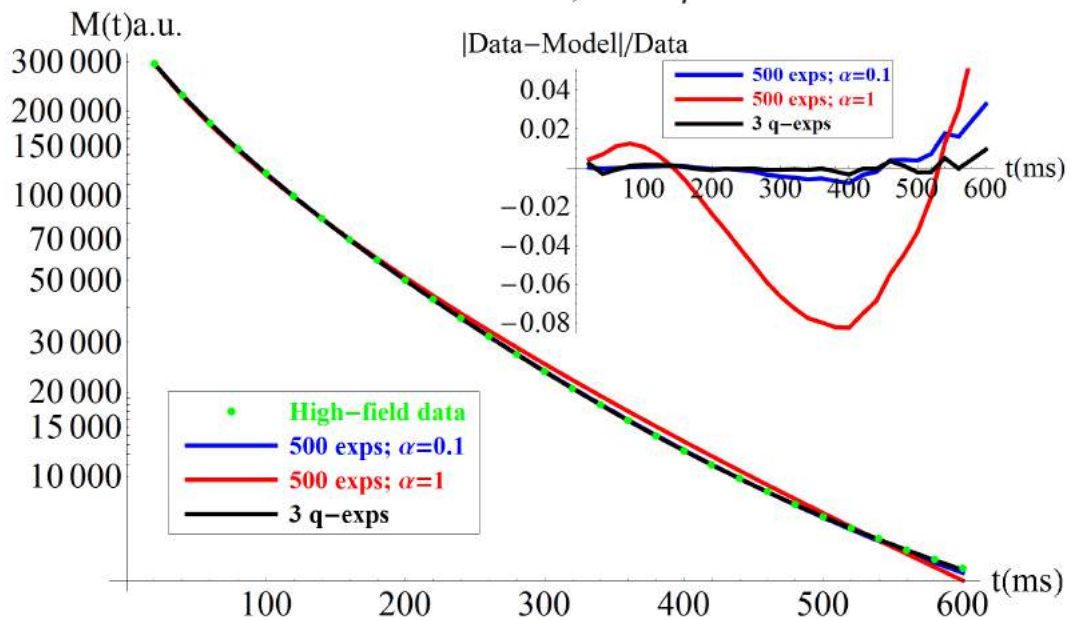


Figure A.7.: The figure on top shows the spectrum decay in CPMG pulse sequence. The figure on bottom shows the comparison between the q-exponential and multiexponential models for the of  $T_2$  distribution in Microesferas sample E.

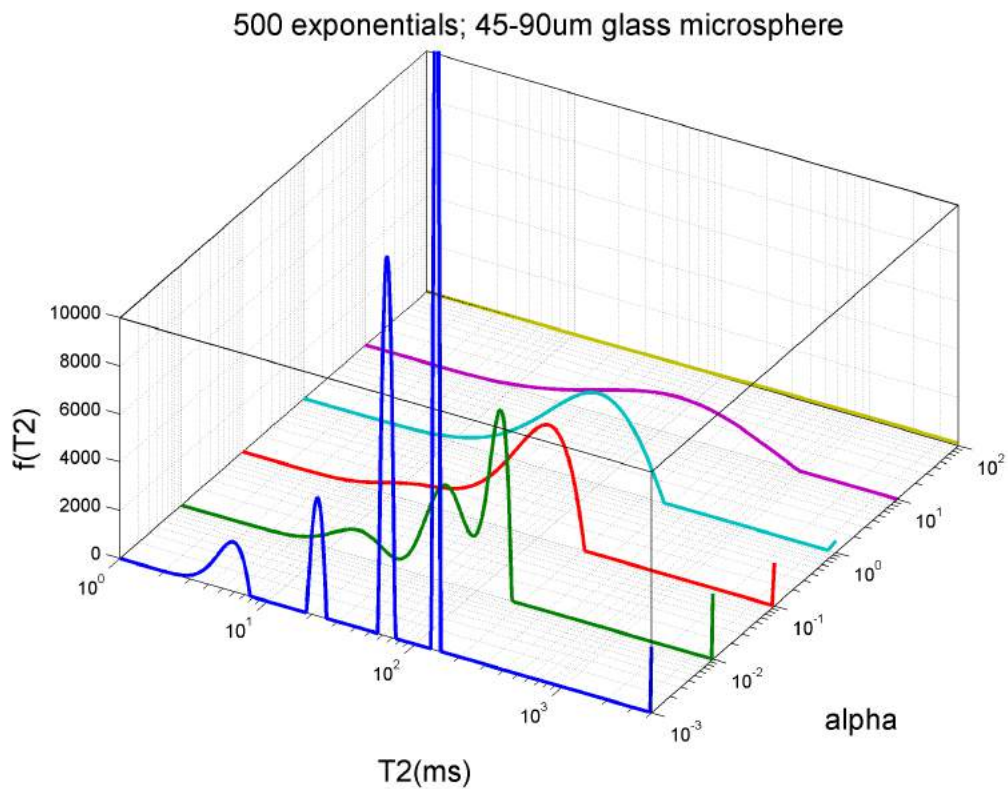
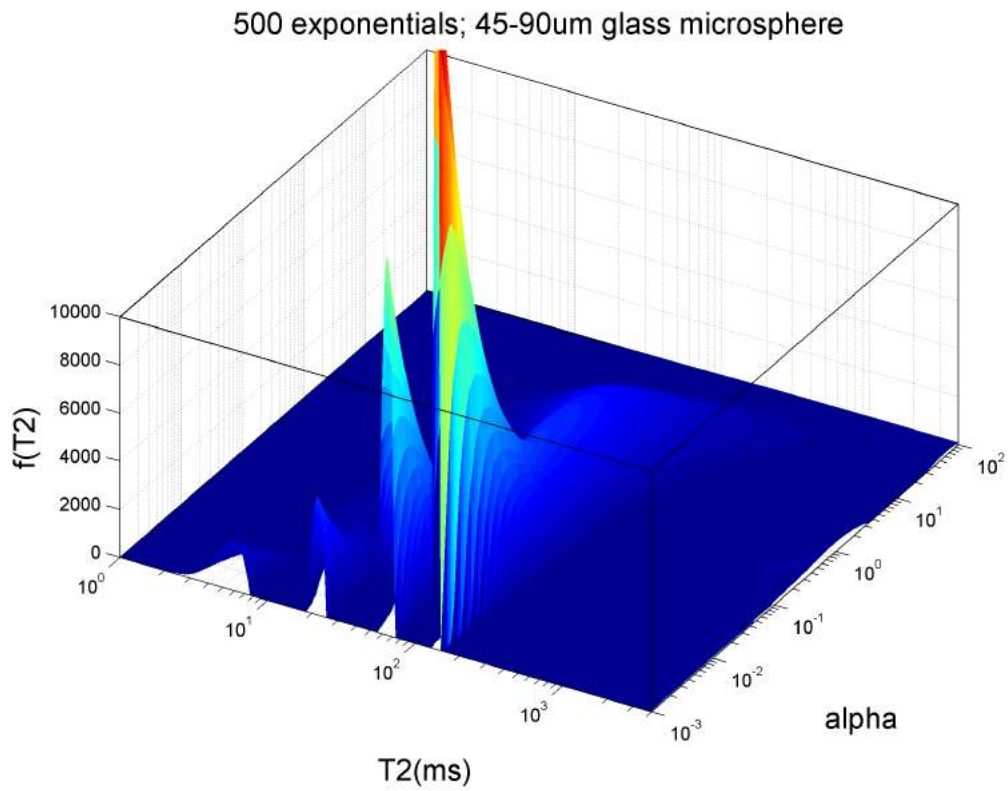


Figure A.8.: Analyses of the regularization parameter effect,  $\alpha$ , on the  $T_2$  distribution for Microesferas sample E.

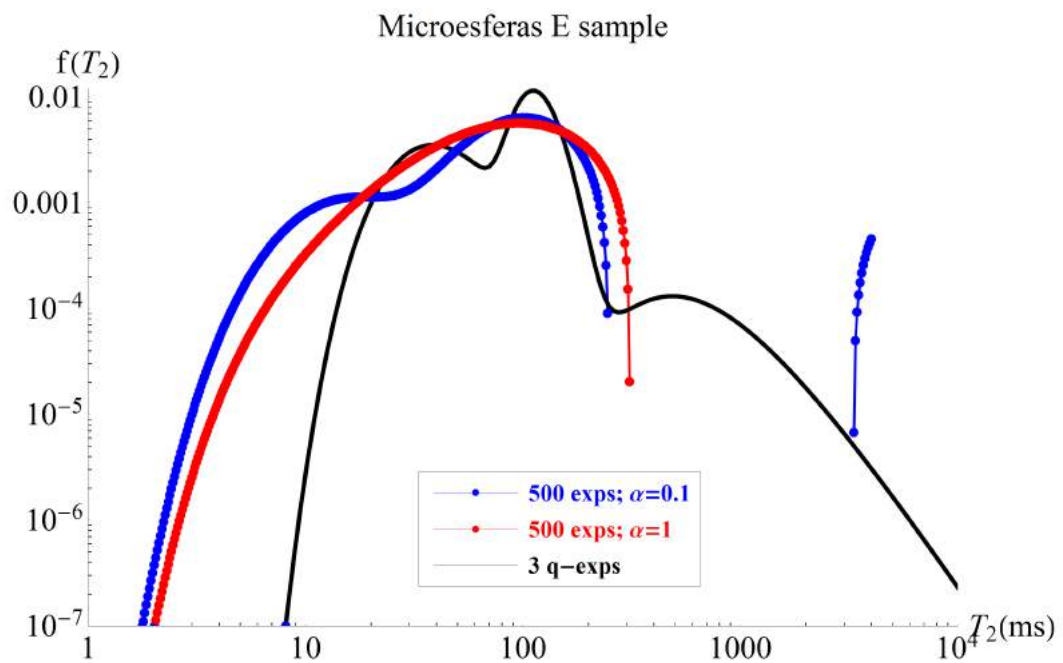
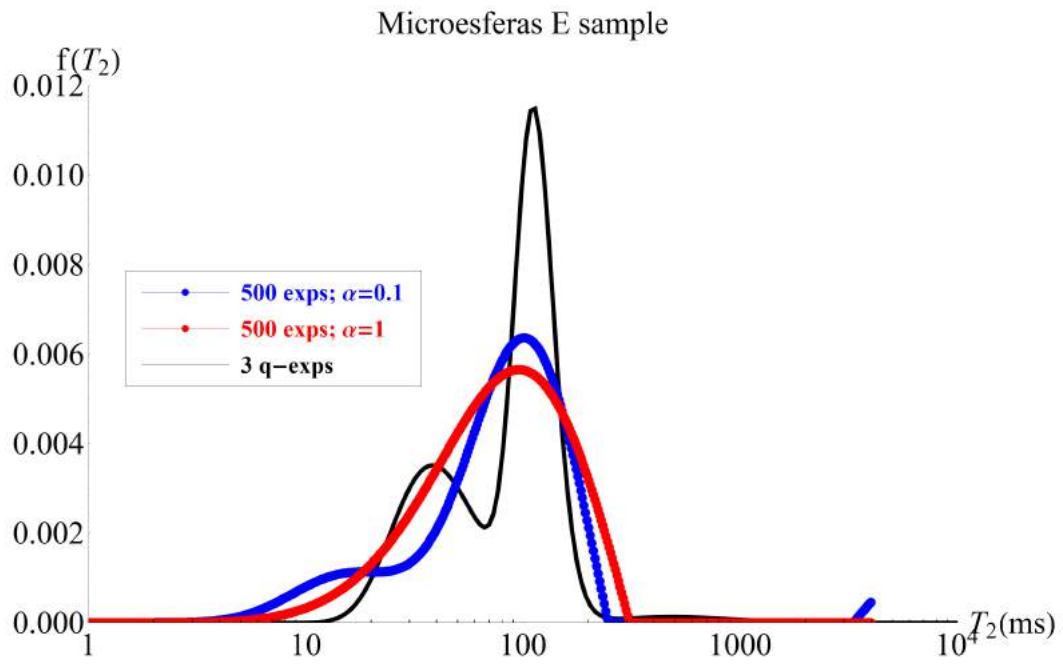


Figure A.9.: Comparison of the  $T_2$  distributions given by q-exponential and multiexponential models.

## B. Cospheric samples C, D and E

### B.1. Cospheric C: 212-250 $\mu m$ range diameter

Fig.B.1 shows the multiexponential and q-exponential fit models for Cospheric sample C (212-250 $\mu m$ ), the inset shows the error along the decay, between the model and the measured data. The  $\alpha$  parameter chosen were  $\alpha = 0.1$  and  $\alpha = 1$ . The errors associated with fits are: i)  $Error_{\alpha=0.1} = 0.002$ ; ii)  $Error_{\alpha=1} = 0.02$ ; and iii)  $Error_{q-exp} = 0.002$ . The statistical parameters associated with q-exponential model can be viewed in Table B.1.

	fast	medium	slow
Intensity (%)	24.4	70.4	5.2
q	1.37	1.13	1.29
$\beta_0^{-1}$ (ms)	56.8	279.7	3507.9
$\langle T_2 \rangle$ (ms)	90.7	320.5	4974.4
$\sigma$ (ms)	109.8	132.4	4216.1

Table B.1.: Statistical parameters of three q-exponentials model for Cospheric sample C.

The Fig.(B.2) shows the behavior of  $T_2$  distribution, given by multiexponential model, with  $\alpha$  regularization parameter. In the Fig.(B.3) is possible to see the comparison between the  $T_2$  distributions of multiexponential model, with two values of  $\alpha$  parameter, and the  $f_{q,\beta_0}(T_2)$  model proposed.

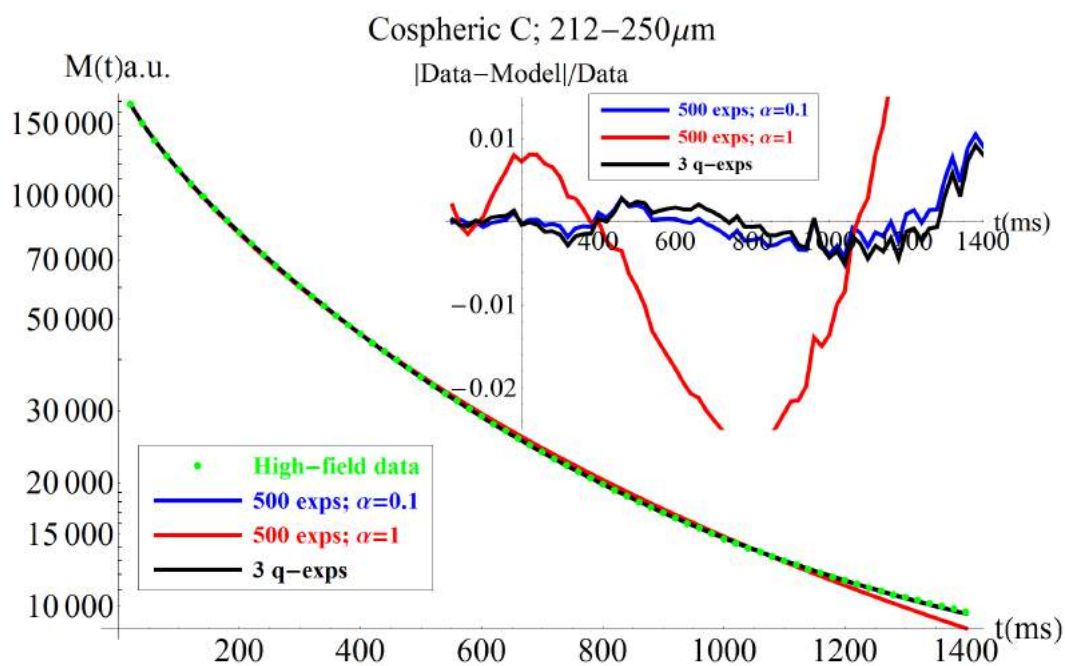
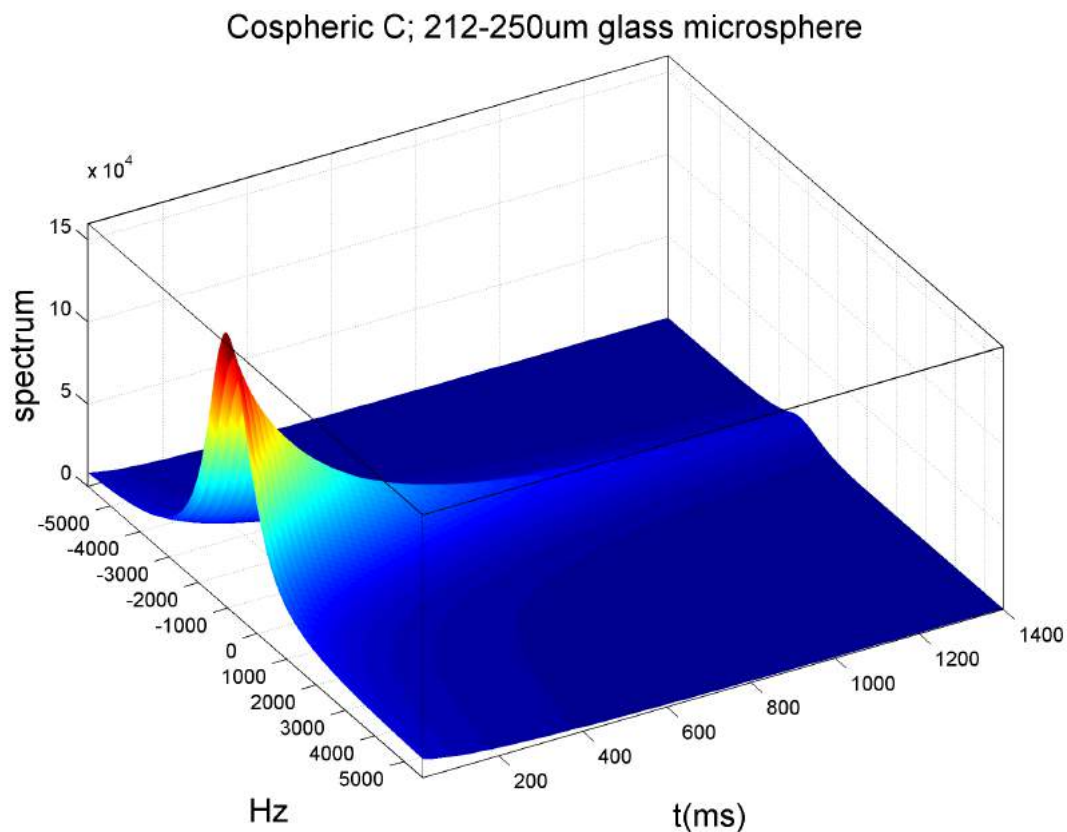


Figure B.1.: The figure on top shows the spectrum decay in CPMG pulse sequence. The figure on bottom shows the comparison between the q-exponential and multiexponential models for the of  $T_2$  distribution in Cospheric sample C.

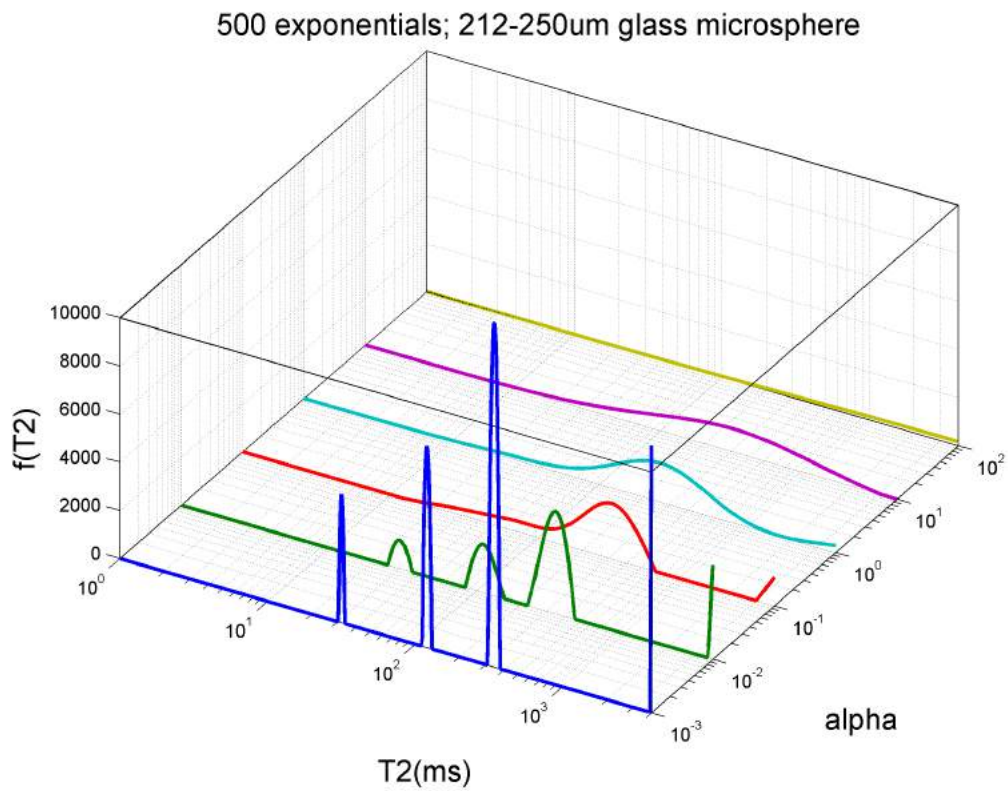
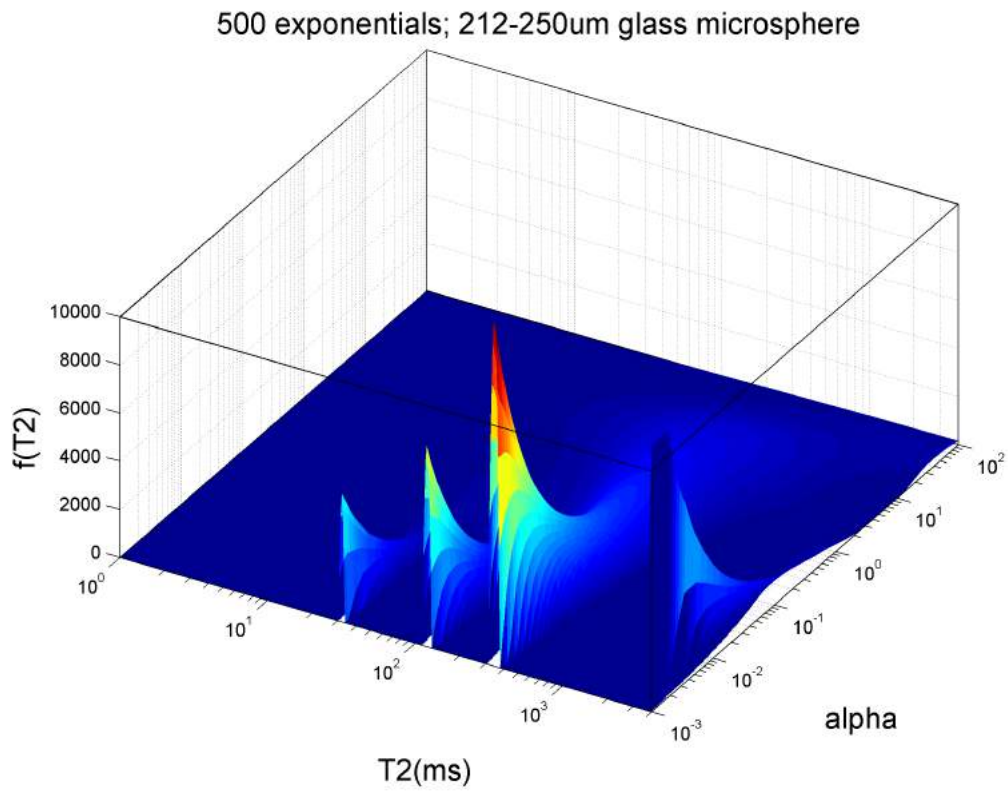


Figure B.2.: Analyses of the regularization parameter effect,  $\alpha$ , on the  $T_2$  distribution for Cospheric sample C.

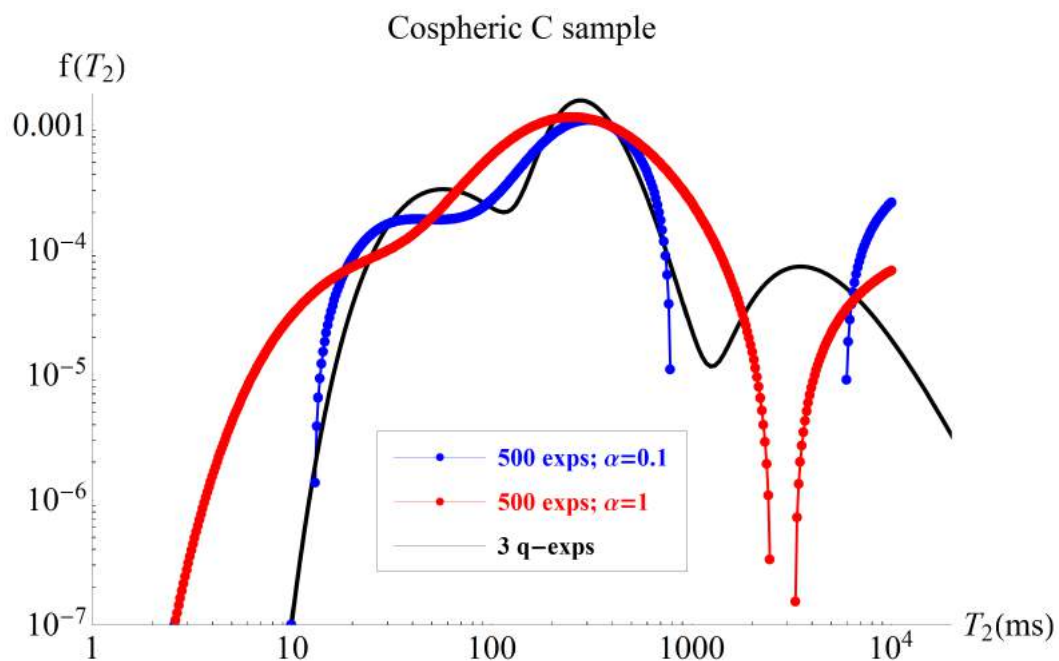
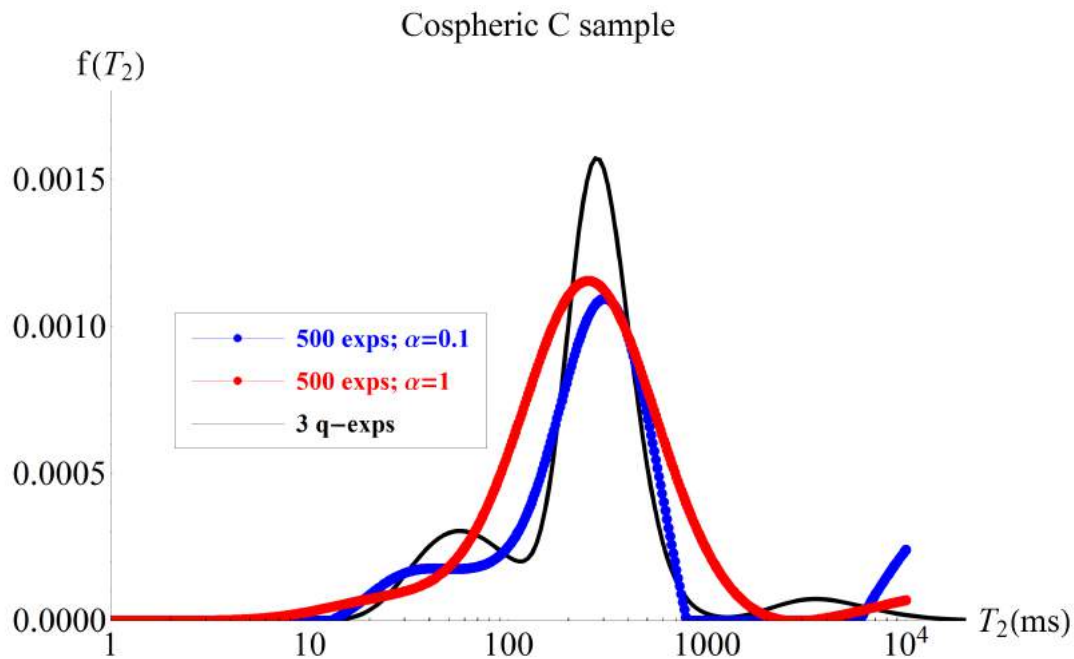


Figure B.3.: Comparison of the  $T_2$  distributions given by q-exponential and multiexponential models.

## B.2. Cospheric D: 106-125 $\mu m$ range diameter

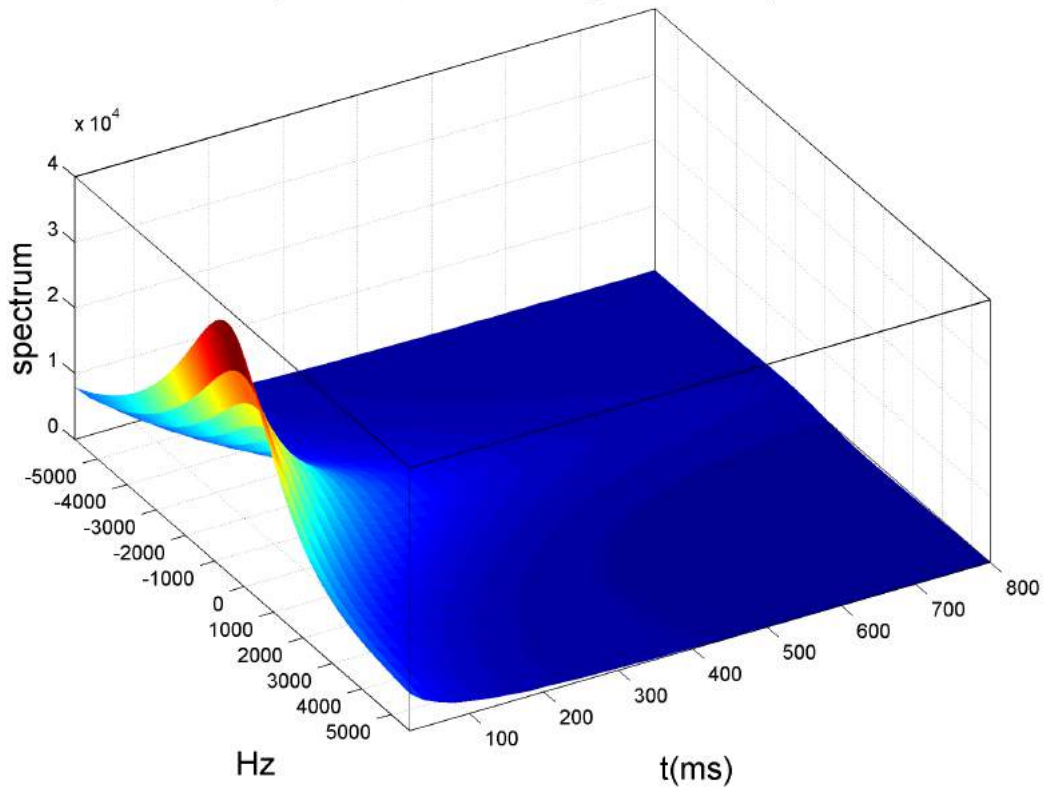
Fig.B.4 shows the multiexponential and q-exponential fit models for Cospheric sample D (106-212 $\mu m$ ), the inset shows the error along the decay, between the model and the measured data. The  $\alpha$  parameter chosen were  $\alpha = 0.1$  and  $\alpha = 1$ . The errors associated with fits are: i)  $Error_{\alpha=0.1} = 0.007$ ; ii)  $Error_{\alpha=1} = 0.07$ ; and iii)  $Error_{q-exp} = 0.007$ . The statistical parameters associated with q-exponential model can be viewed in Table B.2.

	fast	medium	slow
Intensity (%)	44.3	52.5	3.1
q	1.28	1.01	1.37
$\beta_0^{-1}$ (ms)	35.5	119.6	772.2
$\langle T_2 \rangle$ (ms)	49.4	121.2	1218.9
$\sigma$ (ms)	39.6	14.0	1427.9

Table B.2.: Statistical parameters of three q-exponentials model for Cospheric sample D.

The Fig.(B.5) shows the behavior of  $T_2$  distribution, given by multiexponential model, with  $\alpha$  regularization parameter. In the Fig.(B.6) is possible to see the comparison between the  $T_2$  distributions of multiexponential model, with two values of  $\alpha$  parameter, and the  $f_{q,\beta_0}(T_2)$  model proposed.

Cospheric D; 106-125 $\mu\text{m}$  glass microsphere



Cospheric D; 106–125 $\mu\text{m}$

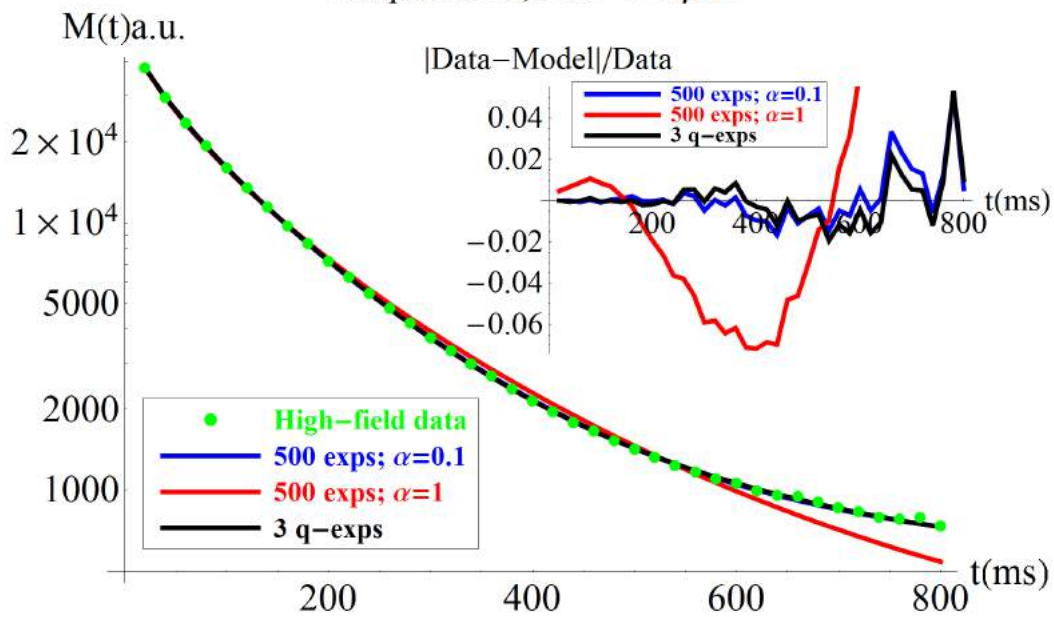


Figure B.4.: The figure on top shows the spectrum decay in CPMG pulse sequence. The figure on bottom shows the comparison between the q-exponential and multiexponential models for the of  $T_2$  distribution in Cospheric sample D.

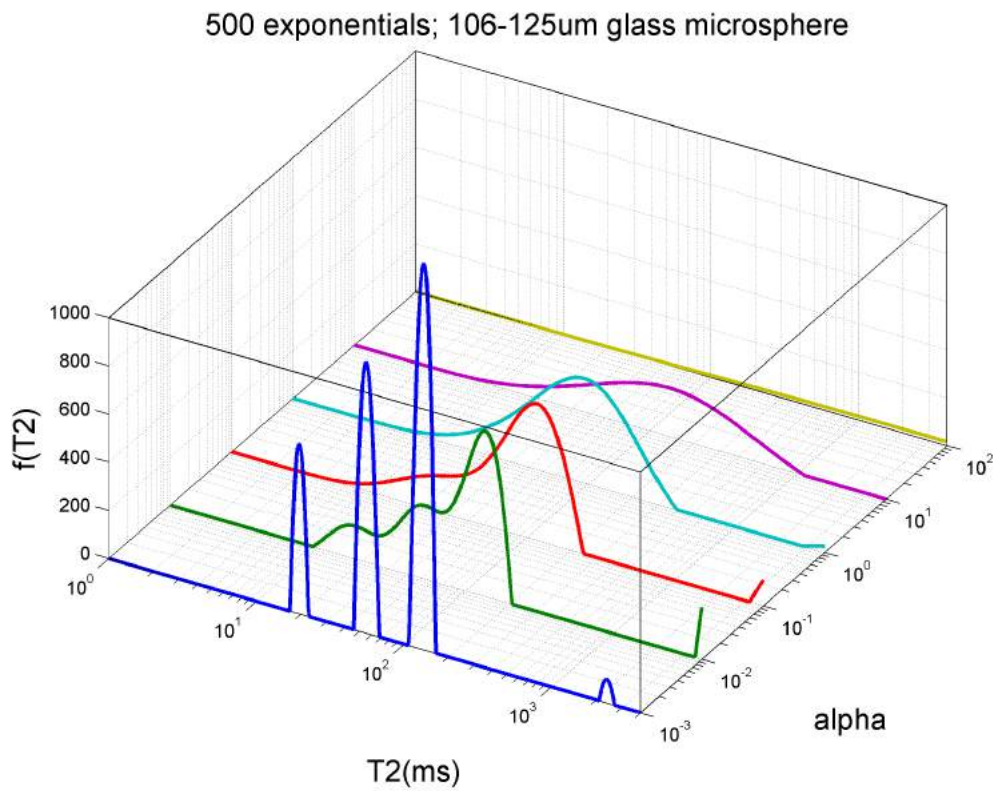
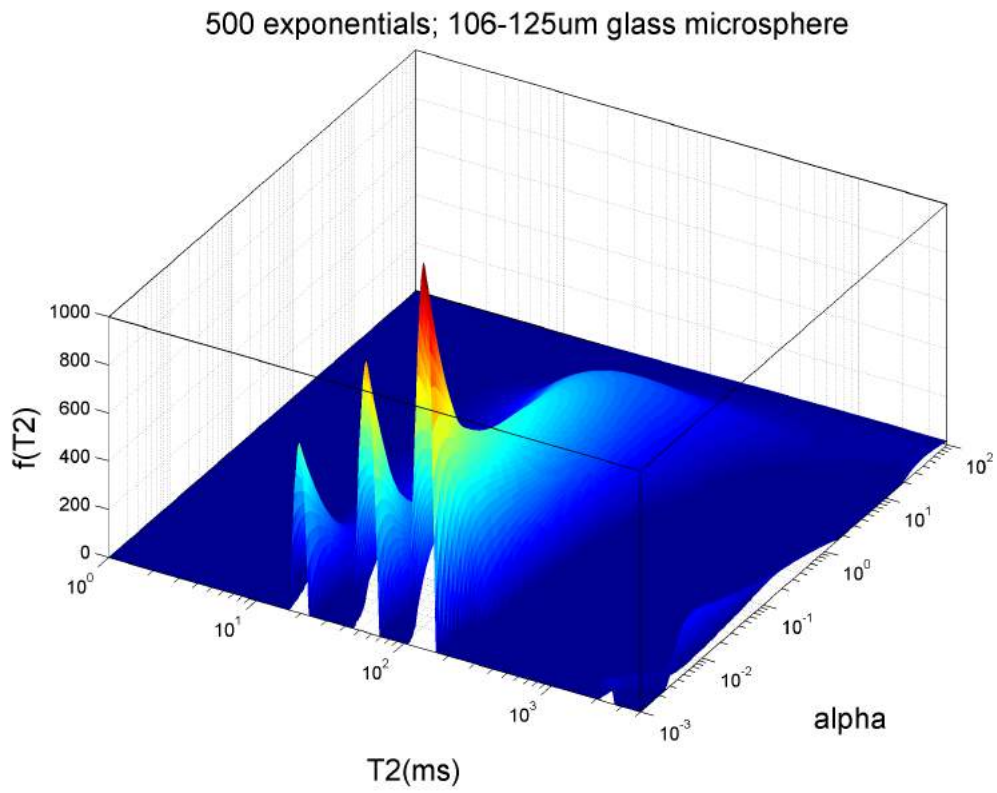


Figure B.5.: Analyses of the regularization parameter effect,  $\alpha$ , on the  $T_2$  distribution for Cospheric sample D.

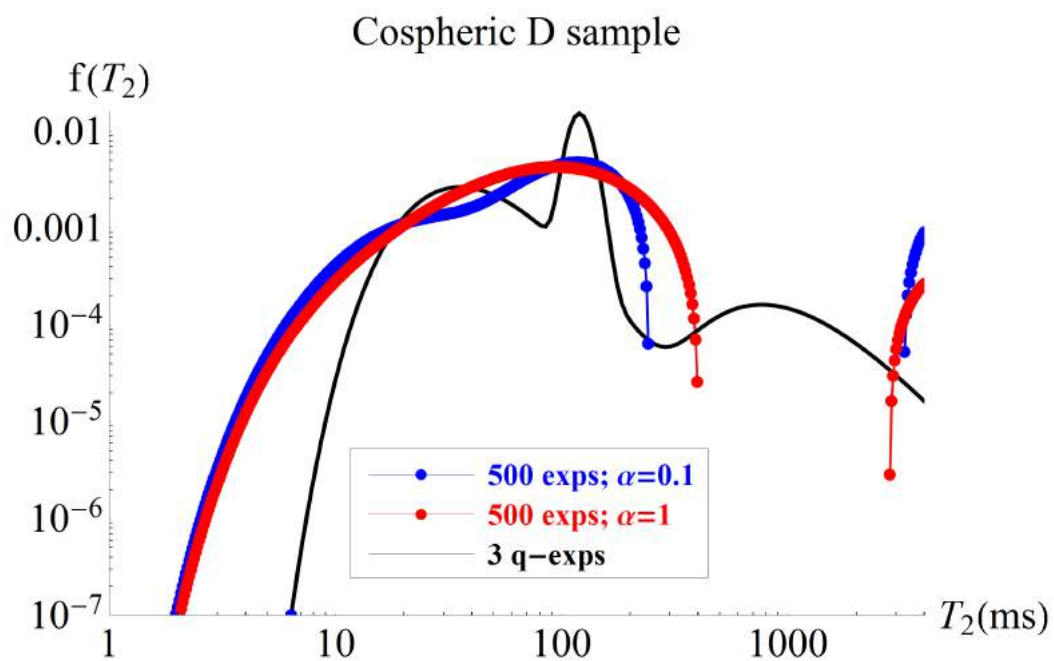
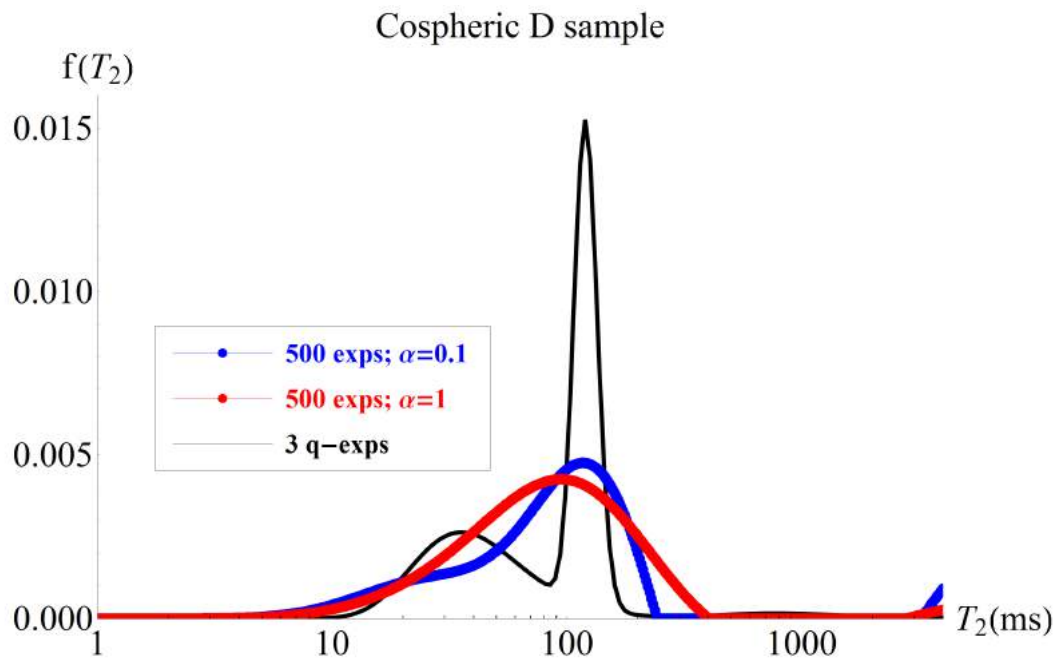


Figure B.6.: Comparison of the  $T_2$  distributions given by q-exponential and multiexponential models.

### B.3. Cospheric E: 45-53 $\mu\text{m}$ range diameter

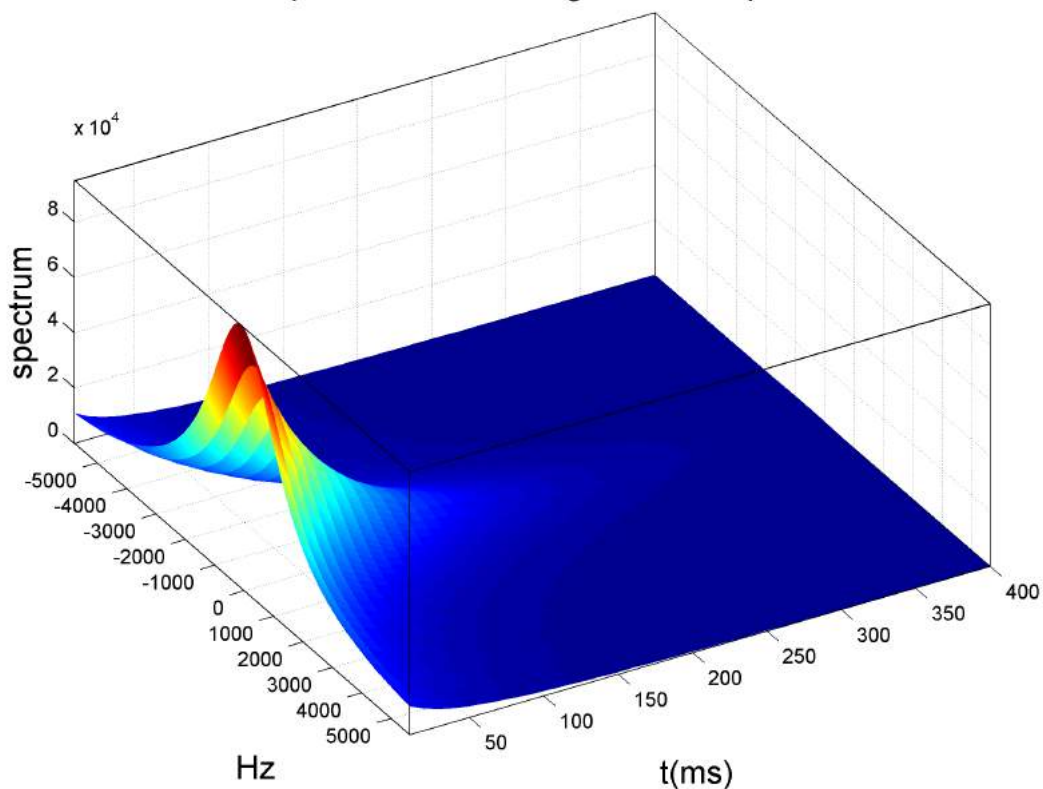
Fig.B.7 shows the multiexponential and q-exponential fit models for Cospheric sample E (45-53 $\mu\text{m}$ ), the inset shows the error along the decay, between the model and the measured data. The  $\alpha$  parameter chosen were  $\alpha = 0.01$  and  $\alpha = 0.1$ . The errors associated with fits are: i)  $Error_{\alpha=0.01} = 0.02$ ; ii)  $Error_{\alpha=0.1} = 0.1$ ; and iii)  $Error_{q-exp} = 0.006$ . The statistical parameters associated with q-exponential model can be viewed in Table B.3.

	fast	medium	slow
Intensity (%)	36.0	–	63.9
q	1.40	–	1.02
$\beta_0^{-1}$ (ms)	27.1	–	66.5
$\langle T_2 \rangle$ (ms)	45.5	–	67.7
$\sigma$ (ms)	66.3	–	9.1

Table B.3.: Statistical parameters of three q-exponentials model for Cospheric sample E.

The Fig.(B.8) shows the behavior of  $T_2$  distribution, given by multiexponential model, with  $\alpha$  regularization parameter. In the Fig.(B.9) is possible to see the comparison between the  $T_2$  distributions of multiexponential model, with two values of  $\alpha$  parameter, and the  $f_{q,\beta_0}(T_2)$  model proposed.

### Cospheric E; 45-53um glass microsphere



### Cospheric E; 45-90 $\mu$ m

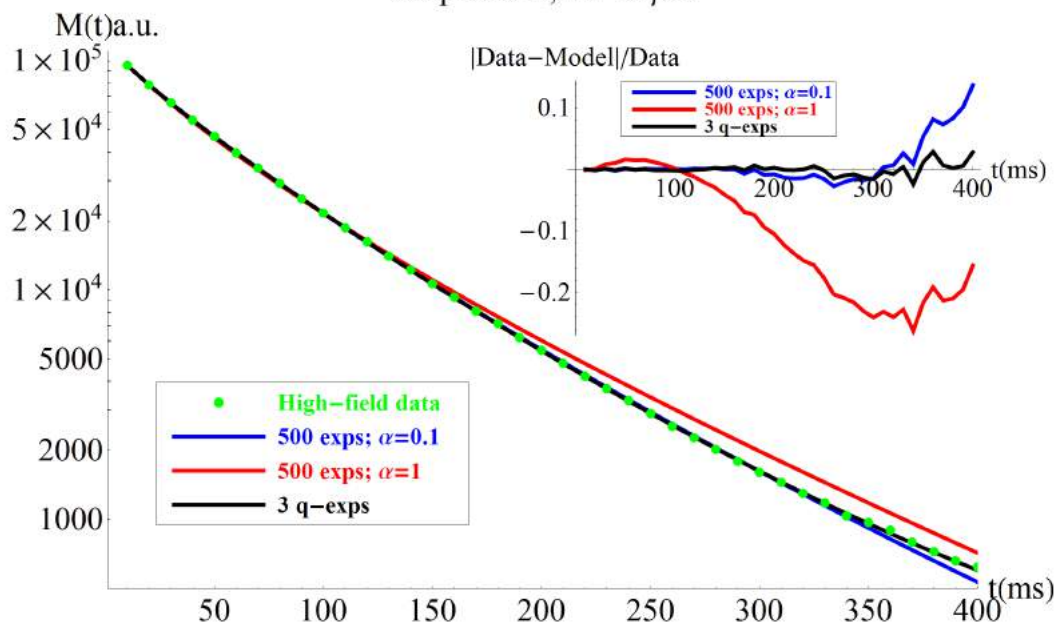


Figure B.7.: The figure on top shows the spectrum decay in CPMG pulse sequence. The figure on bottom shows the comparison between the q-exponential and multiexponential models for the of  $T_2$  distribution in Cospheric sample E.

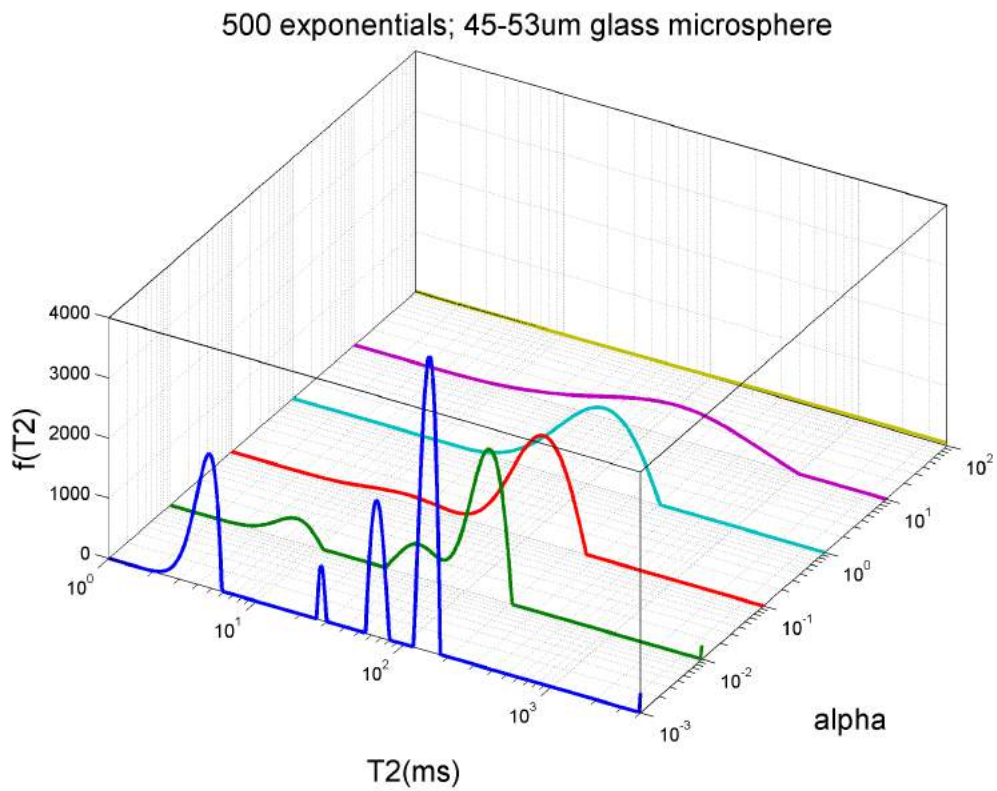
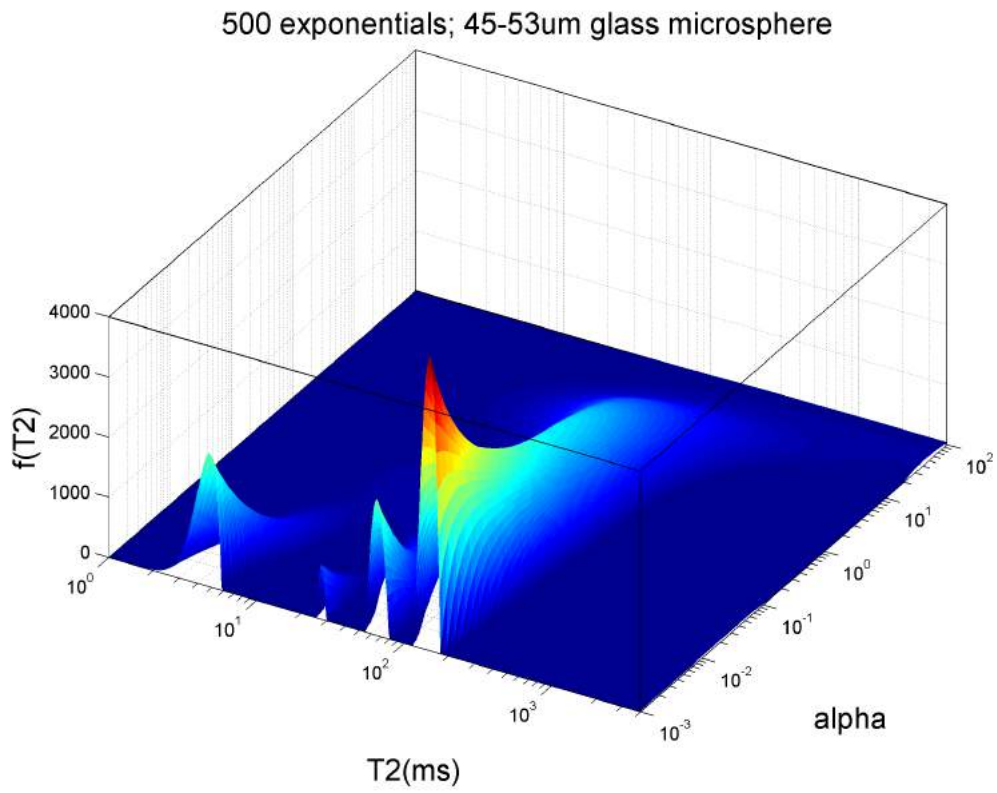


Figure B.8.: Analyses of the regularization parameter effect,  $\alpha$ , on the  $T_2$  distribution for Cospheric sample E.

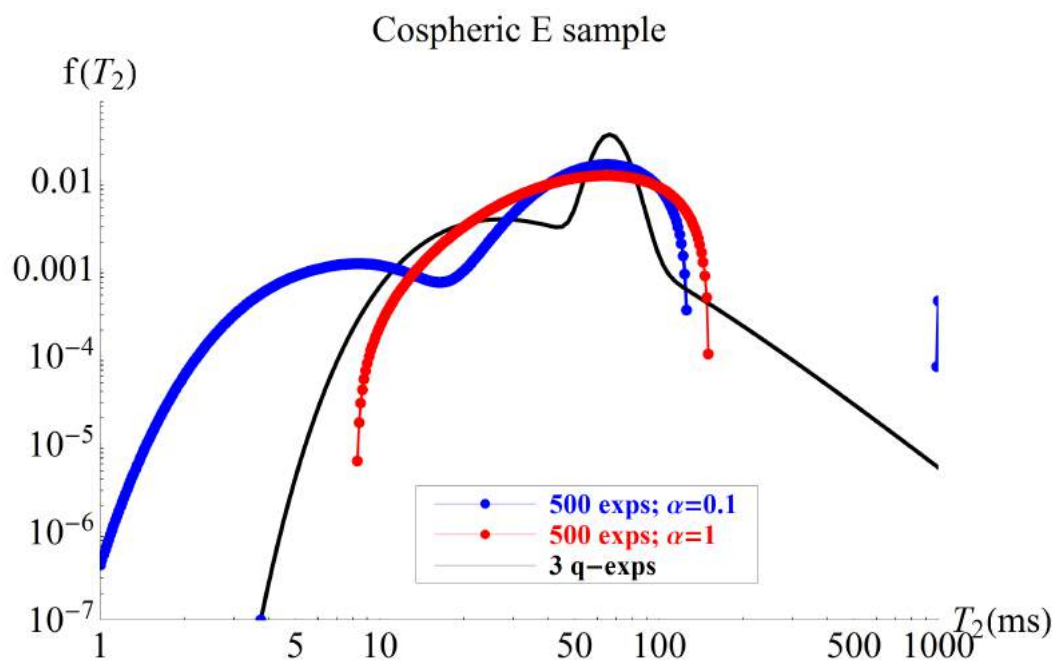
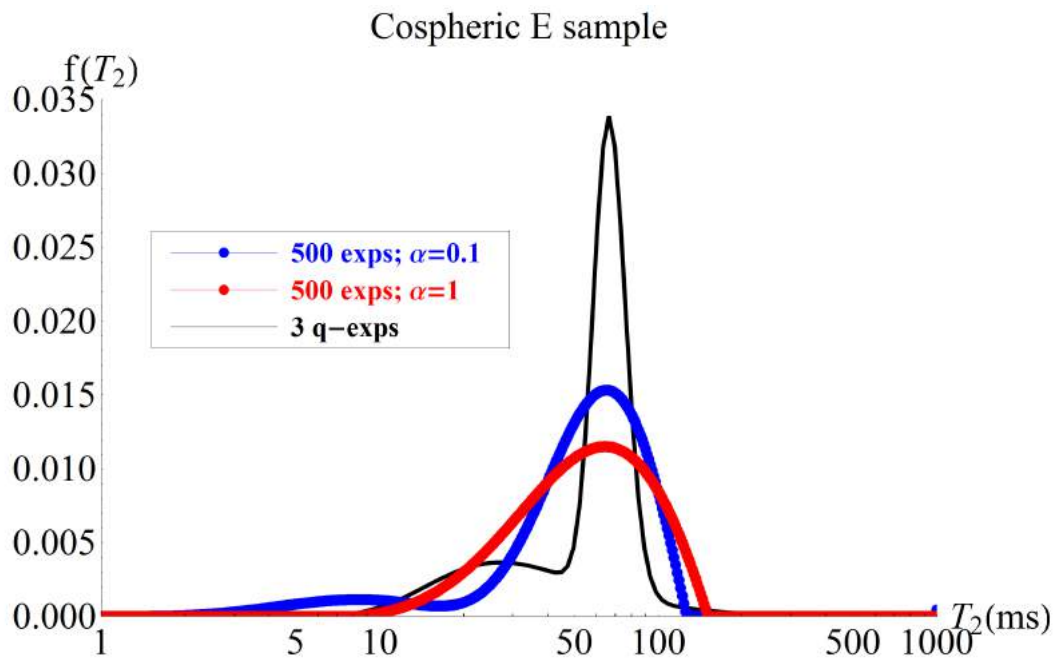


Figure B.9.: Comparison of the  $T_2$  distributions given by q-exponential and multiexponential models.

# Bibliography

- [1] Yi-Qiao Song. Magnetic resonance of porous media (mrpm): A perspective. *Journal of Magnetic Resonance*, 229(0):12 – 24, 2013.
- [2] André Alves de Souza. *Estudo de propriedades petrofísicas de rochas sedimentares por Ressonância Magnética*. Doutorado, Ciência e Engenharia de Materiais - USP, São Carlos, 2012.
- [3] L. Buryakovsky and G.V. Chilingar. *Fundamentals of the Petrophysics of Oil and Gas Reservoirs*. Co-published by John Wiley & Sons, Inc. Hoboken, New Jersey, and Scrivener Publishing LLC, Salem, Massachusetts, 2012. ISBN 978-1-118-34447-7.
- [4] Jude O Amaefule, Mehmet Altunbay, Djebbar Tiab, David G Kersey, Dare K Keelan, et al. Enhanced reservoir description: using core and log data to identify hydraulic (flow) units and predict permeability in uncored intervals wells. In *SPE Annual Technical Conference and Exhibition*. Society of Petroleum Engineers, 1993.
- [5] Alexandre Nassim Cotait. *Caracterização petrofísica e petrologia das fácies retrabalhadas, formação Barra Velha, bacia de Santos*, 2014.
- [6] B. Zinszer and F.M. Pellerin. *Petrophysics: Theory and Practice of Measuring Reservoir Rock and Fluid Transport Properties*. Editions TECHNIP, 2007. ISBN 978-2-7108-0899-2.

- [7] <http://www.blueflameenergy.com/operations/completion/>. [Online; accessed 30-november-2014].
- [8] <http://www.ogs.ou.edu/oilgasfaq.php>. [Online; accessed 30-november-2014].
- [9] Christian Beck. Superstatistics: Theoretical concepts and physical applications. *arXiv:0705.3832v1*.
- [10] Constantino Tsallis. *Introduction to Nonextensive Statistical Mechanics: Approaching a Complex World*. Springer New York, New York, NY ;, 2009.
- [11] Constantino Tsallis, Murray Gell-Mann, and Yuzuru Sato. Asymptotically scale-invariant occupancy of phase space makes the entropy sq extensive. *Proceedings of the National Academy of Sciences of the United States of America*, 102(43):15377–15382, 2005.
- [12] Filippo Caruso and Constantino Tsallis. Nonadditive entropy reconciles the area law in quantum systems with classical thermodynamics. *Physical Review E*, 78:021102, 2008.
- [13] Hansgeorg Pape, Joachim E. Tillich, and Manfred Holz. Pore geometry of sandstone derived from pulsed field gradient NMR. *Journal of Applied Geophysics*, 58(3):232 – 252, 2006.
- [14] K. R. Brownstein and C. E. Tarr. Importance of classical diffusion in NMR studies of water in biological cells. *Phys. Rev. A*, 19:2446–2453, Jun 1979.
- [15] Kenyon W. E. Petrophysical principles of applications of NMR logging. *The Log Analyst*, 38:21–43, 1997.
- [16] Brown R. J. S. *Magn. Reson. Imaging*, 14:811, 1996.

- [17] Liu Tangyan, Jun Yan, Jie Yan, Xu Feng, and Ma Zaitian. Theoretical mechanism and application of sphere-cylinder model in NMR for oil-water porous media. *Pure and Applied Geophysics*, 169(7):1257–1267, 2012.
- [18] Jair C. C. Freitas, Edson C. Passamani, Marcos T. D. Orlando, Francisco G. Emmerich, Flávio Garcia, Luiz C. Sampaio, and Tito J. Bonagamba. Effects of ferromagnetic inclusions on  $^{13}\text{C}$  MAS NMR spectra of heat-treated peat samples. *Energy Fuels*, 16(5):1068–1075, 2002.
- [19] E.H.C.P Sinnecker, I.S Oliveira, P Tiberto, and A.P Guimar aes. Magnetic and structural properties of Cu-Co granular alloys measured with NMR. *Journal of Magnetism and Magnetic Materials*, 218(2?3):132 – 136, 2000.
- [20] A. Gambardella. *Science and Innovation: The US Pharmaceutical Industry During the 1980s*. OCLC Upload. Cambridge University Press, 1995. ISBN 9780521451185. LCCN lc95147721.
- [21] B. Carlsson. *Technological Systems in the Bio Industries: An International Study*. Economics of Science, Technology and Innovation. Springer US, 2002. ISBN 9780792376330. LCCN 2001057979.
- [22] G.B. Asquith and C.R. Gibson. *Basic well log analysis for geologists*. Methods in exploration series. American Association of Petroleum Geologists, 1982. ISBN 9780891816522. LCCN 82073052.
- [23] F. van de Velde, S.H. Knutsen, A.I. Usov, H.S. Rollema, and A.S. Cerezo.  $^1\text{H}$  and  $^{13}\text{C}$  high resolution NMR spectroscopy of carrageenans: application in research and industry. *Trends in Food Science Technology*, 13(3):73 – 92, 2002.

- [24] C.P. Slichter. *Principles of Magnetic Resonance*. Lecture Notes in Computer Science. World Publishing Company, 1990. ISBN 9783540501572. LCCN 96142868.
- [25] Bruce L. Miller. A review of chemical issues in 1h NMR spectroscopy: N-acetyl-l-aspartate, creatine and choline. *NMR in Biomedicine*, 4(2): 47–52, 1991.
- [26] Varanavasi Govindaraju, Karl Young, and Andrew A. Maudsley. Proton NMR chemical shifts and coupling constants for brain metabolites. *NMR in Biomedicine*, 13(3):129–153, 2000.
- [27] M.A. Wilson. *N.M.R. techniques and applications in geochemistry and soil chemistry*. Pergamon Press, 1987. ISBN 9780080348520. LCCN 87035940.
- [28] Burkhard Rost. Review: Protein secondary structure prediction continues to rise. *Journal of Structural Biology*, 134(23):204 – 218, 2001.
- [29] Lewis E Kay. Protein dynamics from NMR. *Biochemistry and Cell Biology*, 76(2-3):145–152, 1998.
- [30] R.S. Macomber. *A complete introduction to modern NMR spectroscopy*. Wiley-Interscience publication. Wiley, 1998. ISBN 9780471157366. LCCN 97017106.
- [31] A. G. Araujo Ferreira, C. A. Brasil, D. O. Soares Pinto, E. R. Azevedo, T. J. Bonagamba, and J. Teles. Quantum state tomography and quantum logical operations in a three qubits NMR quadrupolar system. *International Journal of Quantum Information*, 10(02):1250016, 2012.
- [32] L. M. K. Vandersypen and I. L. Chuang. NMR techniques for quantum control and computation. *Rev. Mod. Phys.*, 76:1037–1069, Jan 2005.

- [33] S. L. Braunstein, C. M. Caves, R. Jozsa, N. Linden, S. Popescu, and R. Schack. Separability of very noisy mixed states and implications for nmr quantum computing. *Phys. Rev. Lett.*, 83:1054–1057, Aug 1999.
- [34] I.S. Oliveira. *Física Moderna para iniciados, inter. e afic. vol 2*. LIVRARIA DA FISICA, 2005. ISBN 9788588325449.
- [35] R. M. Serra and I. S. Oliveira. Nuclear magnetic resonance quantum information processing. *Philosophical Transactions of the Royal Society A: Mathematical, Physical and Engineering Sciences*, 370(1976):4615–4619, 2012.
- [36] Jan O. Walbrecker and Ahmad A. Behroozmand. Surface NMR measurements of the longitudinal relaxation time T1 in a homogeneous sand aquifer in skive, Denmark. *Journal of Applied Geophysics*, 87(0):46 – 52, 2012.
- [37] Asif Muhammad and Rodrigo Bagueira de Vasconcellos Azeredo. 1h NMR spectroscopy and low-field relaxometry for predicting viscosity and API gravity of brazilian crude oils a comparative study. *Fuel*, 130(0): 126 – 134, 2014.
- [38] Jeffrey L. Paulsen and Yi-Qiao Song. Two-dimensional diffusion time correlation experiment using a single direction gradient. *Journal of Magnetic Resonance*, 244(0):6 – 11, 2014.
- [39] M.D. Correia, A.M. Souza, J.P. Sinnecker, R.S. Sarthour, B.C.C. Santos, W. Trevizan, and I.S. Oliveira. Superstatistics model for distribution in NMR experiments on porous media. *Journal of Magnetic Resonance*, 244(0):12 – 17, 2014.
- [40] P A Bottomley. Human in vivo nmr spectroscopy in diagnostic medicine:

- clinical tool or research probe? *Radiology*, 170(1):1–15, 1989. PMID: 2642336.
- [41] Paul A. Bottomley, Thomas H. Foster, Raymond E. Argersinger, and Leah M. Pfeifer. A review of normal tissue hydrogen nmr relaxation times and relaxation mechanisms from 1100 mhz: Dependence on tissue type, nmr frequency, temperature, species, excision, and age. *Medical Physics*, 11(4), 1984.
- [42] Robert Turner. Gradient coil design: A review of methods. *Magnetic Resonance Imaging*, 11(7):903 – 920, 1993.
- [43] Peter J. Basser and Derek K. Jones. Diffusion-tensor MRI: theory, experimental design and data analysis a technical review. *NMR in Biomedicine*, 15(7-8):456–467, 2002.
- [44] C. Beck and E.G.D. Cohen. Superstatistics. *Physica A: Statistical Mechanics and its Applications*, 322(0):267 – 275, 2003.
- [45] Christian Beck, Ezechiel G. D. Cohen, and Harry L. Swinney. From time series to superstatistics. *Phys. Rev. E*, 72:056133, Nov 2005.
- [46] Hugo Touchette and Christian Beck. Asymptotics of superstatistics. *Phys. Rev. E*, 71:016131, Jan 2005.
- [47] Constantino Tsallis and Andre M. C. Souza. Constructing a statistical mechanics for Beck-Cohen superstatistics. *Phys. Rev. E*, 67:026106, Feb 2003.
- [48] A. Y. Abul-Magd. Modeling highway-traffic headway distributions using superstatistics. *Phys. Rev. E*, 76:057101, Nov 2007.
- [49] Petr Jizba and Hagen Kleinert. Superstatistics approach to path integral for a relativistic particle. *Phys. Rev. D*, 82:085016, Oct 2010.

- [50] Denis Nikolaevich Sob'yanin. Generalization of the Beck-Cohen superstatistics. *Phys. Rev. E*, 84:051128, Nov 2011.
- [51] Christian Beck. Superstatistics in hydrodynamic turbulence. *Physica D: Nonlinear Phenomena*, 193(14):195 – 207, 2004. Anomalous distributions, nonlinear dynamics, and nonextensivity.
- [52] A.M. Mathai and H.J. Haubold. Pathway model, superstatistics, tsallis statistics, and a generalized measure of entropy. *Physica A: Statistical Mechanics and its Applications*, 375(1):110 – 122, 2007.
- [53] C. Beck. Superstatistics: theory and applications. *Continuum Mechanics and Thermodynamics*, 16(3):293–304, 2004.
- [54] Christian Beck. Stretched exponentials from superstatistics. *Physica A: Statistical Mechanics and its Applications*, 365(1):96 – 101, 2006.
- [55] Sumiyoshi Abe, Christian Beck, and Ezechieel G. D. Cohen. Superstatistics, thermodynamics, and fluctuations. *Phys. Rev. E*, 76:031102, Sep 2007.
- [56] Gustave Erdman Archie. Introduction to petrophysics of reservoir rocks. *AAPG Bulletin*, 34(5):943–961, 1950.
- [57] D. Tiab and E.C. Donaldson. *Petrophysics: Theory and Practice of Measuring Reservoir Rock and Fluid Transport Properties*. Elsevier Science, 2011. ISBN 9780123838490.
- [58] Stefan M. Luthi. History of logging. In *Geological Well Logs*, pages 12–20. Springer Berlin Heidelberg, 2001. ISBN 978-3-662-04629-6.
- [59] Gavin Bridge and Andrew Wood. Geographies of knowledge, practices of globalization: learning from the oil exploration and production industry. *Area*, 37(2):199–208, 2005.

- [60] Robert L. Kleinberg. Nmr well logging at schlumberger. *Concepts in Magnetic Resonance*, 13(6):396–403, 2001.
- [61] E.C. Thomas. 50th anniversary of the Archie equation: Archie left more than just an equation. *The Log Analyst*, May-June:199, 1992.
- [62] O Mohnke and N Klitzsch. Microscale simulations of nmr relaxation in porous media considering internal field gradients. *UNKNOWN*, 9(4): 846–857, 2010.
- [63] Djebbar Tiab and Erle C Donaldson. *Petrophysics: theory and practice of measuring reservoir rock and fluid transport properties*. Gulf professional publishing, 2011.
- [64] Dianne Rahm. Regulating hydraulic fracturing in shale gas plays: The case of texas. *Energy Policy*, 39(5):2974–2981, 2011.
- [65] Louis Caryl Gratton and HJ Fraser. Systematic packing of spheres: with particular relation to porosity and permeability. *The Journal of Geology*, pages 785–909, 1935.
- [66] H. M. Jaeger and S. R. Nagel. Physics of granular states. *Science*, 255: 1524, 1992.
- [67] K. Keating. The effect of surface area and grain size of glass bead packs on nmr relaxation rates. *In press in Near Surface Geophysics*.
- [68] Henry Darcy. *Les fontaines publiques de la ville de Dijon: exposition et application...* Victor Dalmont, 1856.
- [69] Josef Kozeny. *Über kapillare Leitung des Wassers im Boden:(Aufstieg, Versickerung und Anwendung auf die Bewässerung)*. Hölder-Pichler-Tempsky, 1927.

- [70] K. J. Dunn, D.D.J. Bergman, and G.G.A. Latorraca. *Nuclear Magnetic Resonance: Petrophysical and Logging Applications*. Handbook of Geophysical Exploration Ser: Seismic Exploration Series. Pergamon [Imprint], 2002. ISBN 9780080438801. LCCN 01058543.
- [71] A Kumar, CL Farmer, GR Jerauld, and D Li. Efficient upscaling from cores to simulation models. In *SPE annual technical conference*, pages 257–272, 1997.
- [72] Christian Beck. Dynamical foundations of nonextensive statistical mechanics. *Phys. Rev. Lett.*, 87:180601, Oct 2001.
- [73] Constantino Tsallis, Evaldo M.F. Curado, Maria do Socorro de Souza, Vera L. Elias, Claudio Bettini, Maximiano S. Scuta, and Rodolfo Beer. Generalized Archie law: application to petroleum reservoirs. *Physica A: Statistical Mechanics and its Applications*, 191(1?4):277 – 283, 1992.
- [74] C. Beck and E.G.D. Cohen. Superstatistics. *Physica A: Statistical Mechanics and its Applications*, 322(0):267 – 275, 2003.
- [75] Christian Beck. Recent developments in superstatistics. *Brazilian Journal of Physics*, 39:357 – 363, 08 2009.
- [76] Christian Beck, Ezechiele G. D. Cohen, and Harry L. Swinney. From time series to superstatistics. *Phys. Rev. E*, 72:056133, Nov 2005.
- [77] Ken Kiyono and Hidetoshi Konno. Log-amplitude statistics for Beck-Cohen superstatistics. *Phys. Rev. E*, 87:052104, May 2013.
- [78] Constantino Tsallis. Possible generalization of Boltzmann-Gibbs statistics. *Journal of Statistical Physics*, 52(1-2):479–487, 1988.
- [79] D O Soares-Pinto, M S Reis, R S Sarthour, and I S Oliveira. Spin waves

- in a complex magnetic system: a nonextensive approach. *Journal of Statistical Mechanics: Theory and Experiment*, 2007(08):P08011, 2007.
- [80] P.M. Adler and J.-F. Thovert. Fractal porous media. *Transport in Porous Media*, 13(1):41–78, 1993.
- [81] Yu Boming. Analysis of flow in fractal porous media. *Appl. Mech. Rev.*, 61:050801, 2008.
- [82] John H. Cushman. On diffusion in fractal porous media. *Water Resources Research*, 27(4):643–644, 1991.
- [83] F.A.L. Dullien and H. Brenner. *Porous Media: Fluid Transport and Pore Structure*. Elsevier Science, 1991. ISBN 9780323139335.
- [84] C.G. Jacquin and P.M. Adler. Fractal porous media ii: Geometry of porous geological structures. *Transport in Porous Media*, 2(6):571–596, 1987.
- [85] BOMING YU and JIANHUA LI. Some fractal characters of porous media. *Fractals*, 09(03):365–372, 2001.
- [86] Sean P. Rigby and Lynn F. Gladden. The prediction of transport properties of porous media using fractal models and NMR experimental techniques. *Chemical Engineering Science*, 54(15-16):3503 – 3512, 1999.
- [87] S.P. Rigby and L.F. Gladden. NMR and fractal modelling studies of transport in porous media. *Chemical Engineering Science*, 51(10):2263 – 2272, 1996. *Chemical Reaction Engineering: From Fundamentals to Commercial Plants and Products*.
- [88] James P. Hyslip and Luis E. Vallejo. Fractal analysis of the roughness and size distribution of granular materials. *Engineering Geology*, 48(3-4): 231 – 244, 1997. *Fractals in Engineering Geology*.

- [89] Paul G. Okubo and Keiiti Aki. Fractal geometry in the san andreas fault system. *Journal of Geophysical Research: Solid Earth*, 92(B1):345–355, 1987.
- [90] D.L. Turcotte. *Fractals and Chaos in Geology and Geophysics*. Cambridge University Press, 1997. ISBN 9780521567336. LCCN 96031558.
- [91] JIANCHAO CAI, FERNANDO SAN JOS MARTNEZ, MIGUEL ANGEL MARTN, and EDMUND PERFECT. An introduction to flow and transport in fractal models of porous media: Part i. *Fractals*, 22(03):1402001, 2014.
- [92] V. Schwmmle, F. D. Nobre, and C. Tsallis. q-gaussians in the porous-medium equation: stability and time evolution. *The European Physical Journal B*, 66(4):537–546, 2008.
- [93] G. NyambuyaBridge. General spin dirac equation (ii). *Journal of Modern Physics*, 4(8):1050–1058, 2013.
- [94] Felix Bloch. Nuclear induction. *Physical review*, 70(7-8):460, 1946.
- [95] Kazuyuki Fujii. Introduction to the rotating wave approximation (RWA) : Two coherent oscillations. 2013.
- [96] Thilo Bauch and Goran Johansson. lectures in quantum informatics. 2011.
- [97] Henry C Torrey. Bloch equations with diffusion terms. *Physical Review*, 104(3):563, 1956.
- [98] M. Goldman. *Quantum description of high-resolution NMR in liquids*. International series of monographs on chemistry. Clarendon Press, 1988. ISBN 9780198556398. LCCN 88001668.
- [99] Erwin L Hahn. Spin echoes. *Physical Review*, 80(4):580, 1950.

- [100] K-J Dunn, David J Bergman, and Gerald A LaTorraca. *Nuclear magnetic resonance: petrophysical and logging applications*. Elsevier, 2002.
- [101] Iain J. Day. On the inversion of diffusion NMR data: Tikhonov regularization and optimal choice of the regularization parameter. *Journal of Magnetic Resonance*, 211(2):178 – 185, 2011.
- [102] Andrey N. Tikhonov and Vasilii Y. Arsenin. *Solutions of ill-posed problems*. V. H. Winston & Sons, Washington, D.C.: John Wiley & Sons, New York, 1977. xiii+258 pp. Translated from the Russian, Preface by translation editor Fritz John, Scripta Series in Mathematics.
- [103] J. Mitchell, T. C. Chandrasekera, and L. F. Gladden. Obtaining true transverse relaxation time distributions in high-field NMR measurements of saturated porous media: Removing the influence of internal gradients. *The Journal of Chemical Physics*, 132(24), 2010.
- [104] L. R. Stingaciu, A. Pohlmeier, P. Blümmler, L. Weihermüller, D. van Dusschoten, S. Stapf, and H. Vereecken. Characterization of unsaturated porous media by high-field and low-field nmr relaxometry. *Water Resources Research*, 45(8):n/a–n/a, 2009.
- [105] Guang-Zhi LIAO, Li-Zhi XIAO, Ran-Hong XIE, and Juan-Juan FU. Influence factors of multi-exponential inversion of nmr relaxation measurement in porous media. *Chinese Journal of Geophysics*, 50(3):796–802, 2007.
- [106] Per Christian Hansen, Toke Koldborg Jensen, and Giuseppe Rodriguez. An adaptive pruning algorithm for the discrete l-curve criterion. *Journal of Computational and Applied Mathematics*, 198(2):483 – 492, 2007.
- [107] W. L. Miranker. A well posed problem for the backward heat equation. *Proc. Amer. Math. Soc.*, 12:243–247, 1961.

- [108] Jacques Hadamard. Sur les problèmes aux dérivées partielles et leur signification physique. *Princeton University Bulletin*, 13:49–52, 1902.
- [109] Lalitha Venkataramanan, Tarek M. Habashy, Denise E. Freed, and Fred K. Gruber. Continuous moment estimation of CPMG data using mellin transform. *Journal of Magnetic Resonance*, 216(0):43 – 52, 2012.